EVALUATION OF A DIFFRACTION-ENHANCED IMAGING (DEI) PROTOTYPE AND EXPLORATION OF NOVEL APPLICATIONS FOR CLINICAL IMPLEMENTATION OF DEI

Laura Suzanne Faulconer

A dissertation submitted to the faculty of the University of North Carolina at Chapel Hill in partial fulfillment of the requirements for the degree of Doctor of Philosophy in the Department of Biomedical Engineering (Medical Imaging).

Chapel Hill
2009

Approved By:

Advisor: Etta Pisano

Reader: Caterina Gallippi

Reader: David Lalush

Reader: Mark Tommerdahl

Reader: Zhong Zhong

ABSTRACT

LAURA FAULCONER: Evaluation of a Diffraction-Enhanced Imaging (DEI) Prototype and Exploration of Novel Applications for Clinical Implementation of DEI
(Under the direction of Etta Pisano)

Conventional mammographic image contrast is derived from x-ray absorption, resulting in breast structure visualization due to density gradients that attenuate radiation without distinction between transmitted, scattered, or refracted x-rays. Diffraction-enhanced imaging (DEI) allows for increased contrast with decreased radiation dose compared to conventional mammographic imaging due to monochromatic x-rays, its unique refraction-based contrast mechanism, and excellent scatter rejection. Although laboratory breast imaging studies have demonstrated excellent breast imaging, important clinical translation and application studies are needed before the DEI system can be established as a useful breast imaging modality. This dissertation focuses on several important studies toward the development of a clinical DEI system.

First, contrast-enhanced DEI was explored using commercially available contrast agents. Phantoms were imaged at a range of x-ray energies and relevant contrast agent concentrations. Second, we performed a reader study to determine if superior DEI contrast mechanisms preserve image quality as tissue thickness increases. Breast specimens were imaged at several thicknesses, and radiologist perception of lesion visibility was recorded. Lastly, a prototype DEI system utilizing an x-ray tube source was evaluated through a reader study. Breast tissue specimens were imaged on the traditional and prototype DEI systems, and expert radiologists evaluated image quality and pathology correlation.

This dissertation will demonstrate proof-of-principle for contrast-enhanced DEI, establishing the feasibility of contrast-enhanced DEI using commercially available contrast agents. Further, it will show that DEI might be able to reduce breast compression, and thus the perception of pain during mammography, without significantly decreasing breast lesion visibility. Finally, this research shows the successful implementation of a DEI prototype, displaying breast features with approximately statistically equivalent visibility to the traditional DEI system. Together, this research is an important step toward the clinical translation of DEI, a technology with the potential to facilitate early breast cancer detection and diagnosis.

In recognition of their unending support through this journey, I dedicate this doctoral dissertation to my parents, Charles Jr. and Susan Faulconer. They provided me with an education and fostered a sense of drive and determination that led me to scientific research. I would also like to thank my twin sister, Emily, for always keeping up the competitive spirit that encouraged me forward. Without their support I may have never reached the level of success I have already achieved and never known the possibilities the future holds.

ACKNOWLEDGEMENTS

Dr. Christopher Parham at the University of California at San Francisco

Dr. Dean M. Connor at Brookhaven National Laboratory

Elodia Cole at the University of North Carolina at Chapel Hill

Dr. Larken Euliss at HRL Laboratories LLC

Dr. Zhong Zhong at Brookhaven National Laboratory

Dr. Avraham Dilmanian at Brookhaven National Laboratory

Dr. Cherie Kuzmiak at the University of North Carolina at Chapel Hill

Dr. Marcia Koomen at the University of North Carolina at Chapel Hill

Dr. Yeonhee Lee at the University of North Carolina at Chapel Hill

Dr. Josh Rafoth at the University of North Carolina at Chapel Hill

Dr. Kyu Cho at the University of North Carolina at Chapel Hill

Dr. Chad Livasy at the University of North Carolina at Chapel Hill

Dr. Paul Dayton at the University of North Carolina at Chapel Hill

Lee Mullin at the University of North Carolina at Chapel Hill

James Tsuruta at the University of North Carolina at Chapel Hill

Dr. Jim Hainfeld at Brookhaven National Laboratory

Dr. Eunhee Kim at the University of North Carolina at Chapel Hill

Dr. Donglin Zeng at the University of North Carolina at Chapel Hill

Ann Sherman at the University of North Carolina at Chapel Hill

Lori Smith at the University of North Carolina at Chapel Hill

Dr. Andrea Kasko at the University of California in Los Angeles

Ken Lin at the University of California in Los Angeles

Doreen Steed at the University of North Carolina at Chapel Hill

Mammography Clinic Radiation Technicians at University of North Carolina Hospitals

TABLE OF CONTENTS

LIST OF TABLES

Table

LIST OF FIGURES

Figures

LIST OF ABBREVIATIONS AND SYMBOLS

A	Atomic Mass
ADH	Atypical Ductal Hyperplasia
AI	Aromatase Inhibitor
Al	Aluminum
ALH	Atypical Lobular Hyperplasia
AUC	Area Under the Receiver-Operator Characteristic Curve
BI-RADS	Breast Imaging-Reporting and Data System
BMI	Body Mass Index
c	Speed of Light
CAD	Computer-Aided Diagnosis
CE-DEI	Contrast-Enhanced Diffraction-Enhanced Imaging
CLS	Compact Light Source
CT	Computed Tomography
CTF	Contrast Transfer Function
DCIS	Ductal Carcinoma *In Situ*
DEI	Diffraction-Enhanced Imaging
DEI-CT	Diffraction-Enhanced Imaging-Computed Tomography
DEI-PR	Diffraction-Enhanced Imaging Prototype with an X-Ray Tube Source
DEI-SR	Diffraction-Enhanced Imaging with a Synchrotron Radiation Source
DEI-TS	Diffraction-Enhanced Imaging-Tomosynthesis
del	Detector Element
DLR	Diagnostic Likelihood Ratio

DM	Digital Mammography
DMIST	Digital Mammographic Imaging Screening Trial
DOT	Diffuse Optical Tomography
DQE	Detective Quantum Efficiency
($dR / d\theta$)	Gradient of the Rocking Curve at the Respective Angle
DW-MRI	Diffusion-Weighted Magnetic Resonance Imaging
E	Energy
E_K	Kinetic Energy
$E_B(K)$	Binding Energy of K-Shell Electron
EIT	Electrical Impedance Tomography
EPR	Enhanced Permeability and Retention
ER (+/-)	Estrogen Receptor (Positive / Negative)
ESF	Edge Spread Function
FBP	Filtered Back-Projection
FDA	Federal Drug Administration
FDG-PET	Fluorodeoxyglucose Positron Emission Mammography
FN	False Negative
FP	False Positive
FWHM	Full Width at Half Maximum
GE	General Electric
GEE	Generalized Estimating Equation
h	Planck's Constant
hv	Photon Energy

H and D	Hunter and Driffield (curve)
HRT	Hormone Replacement Therapy
HU	Hounsfield Unit
HVL	Half-Value Layer
I	Intensity; Current
I_0	Initial Intensity
I_H	Intensity Diffracted from the Analyzer
I_L	Intensity Diffracted from the analyzer at the $-½ W_D$
I_R	Intensity Diffracted from the analyzer at the $+½ W_D$
IDL	Interactive Data Language
IR	Infrared Radiation
LCIS	Lobular Carcinoma *In Situ*
LD_{50}	Lethal Dose for 50% of the Exposed Population
LET	Linear Energy Transfer
LN	Lymph Node
LOH	Loss of Heterozygosity
LSF	Line Spread Function
ME	Myoepithelial
MIR	Multiple Image Radiography
Mo	Molybdenum
MQSA	Mammography Quality Standards Act
MRA	Magnetic Resonance Angiography
MRE	Magnetic Resonance Elastography

MRI	Magnetic Resonance Imaging
MRS	Magnetic Resonance Spectroscopy
MTF	Modulation Transfer Function
n	Number of Photons Removed from Incident Beam; order of reflection; refractive index
N	Number of Electrons per Unit Volume
N_0	Number of Incident Photons
N_A	Avagadro's Number
N_{back}	Number of Photons Detected within a Background Region
N_{det}	Number of Photons Detected within Specific Pixel
N_{ROI}	Number of Photons Detected within Specific Region of Interest
NMR	Nuclear Magnetic Resonance
NPV	Negative Predictive Value
NSABP	National Surgical Adjuvant Breast and Bowel Project
OCT	Optical Coherence Tomography
P_D	Power Deposited
P_R	Power Radiated
PAT	Photoacoustic Tomography
PEM	Positron Emission Mammography
PET	Positron Emission Tomography
pixel	Picture Element
PPV	Positive Predictive Value
PR (+/-)	Progesterone Receptor (Positive / Negative)
PSF	Point Spread Function

r_e	Classical Electron Radius
RAL	Raloxifene
rf	Radiofrequency
Rh	Rhodium
rms	Root Mean Square
$R(\theta_0)$	Rocking Curve at a Specific Angular Position of the Analyzer Crystal
ROC	Receiver-Operator Characteristic
RS	Raman Spectroscopy
SAXS	Small Angle Scatter
SDNR	Signal Difference to Noise Ratio
SFM	Screen-Film Mammography
SM	Scintimammography
SNR	Signal to Noise Ratio
SNR_{diff}	Differential SNR
SPECT	Single Photon Emission Computed Tomography
SR	Synchrotron Radiation
SYRMEP	Synchrotron Radiation for Medical Physics
t	Time
TAM	Tamoxifen
TAT	Thermoacoustic Tomography
TDLU	Terminal Duct Lobular Unit
TN	True Negative
TP	True Positive

TS	Tomosynthesis
UNC	University of North Carolina
UNC-CH	University of North Carolina at Chapel Hill
uPAR	Urokinase Plasminogen Activator Receptor
US	Ultrasound
USAXS	Ultra Small Angle Scatter
UV	Ultraviolet
ν	Frequency
V	Voltage
voxel	Volume Element
W	Tungsten
WAXS	Wide Angle Scatter
W_D	Darwin Width
XDFI	X-Ray Dark-Field Imaging
Z	Atomic Number
Z_{eff}	Effective Atomic Number
β	X-Ray Absorption
δ	Phase Shift Due to Scattering
$\Delta\theta_z$	Deflection Angle in the Vertical Plane
η	Quantum Efficiency
θ	Angle
θ_B	Angle of Bragg Reflection
κ	Pair Production

λ	Wavelength
λ_s	Scattering Mean Free Path
μ	Linear Attenuation Coefficient
μ_{eff}	Effective Linear Attenuation Coefficient
π	Photodisintegration
ρ	Physical Density
σ	Compton Scatter; Noise
σ_{back}	Noise within the Background
σ_{ROI}	Noise within a Specific Region of Interest
τ	Photoelectric Absorption
φ	Photon Flux
Φ	Photon Fluence
ω	Coherent Scatter; Amount of Energy Required to Produce and Element of Signal

CHAPTER 1: INTRODUCTION

1.1 Overview

Screen-film mammography (SFM) and digital mammography (DM) have been optimized and have thus become relatively low-dose imaging modalities with moderate sensitivity and specificity. However, despite their widespread utilization for breast cancer screening, approximately 10 to 15% of cancers remain mammographically occult (Meyer 1990). In addition, there is a substantial risk of the induction of breast cancer or other radiation exposure-related disease because of the use of mammography (Kopans 2007). Cancer imparts distinct and measurable changes in breast tissue at a cellular level, yet attenuation contrast based on the spatial distribution of x-ray attenuation does not always provide sufficient contrast in a mammographic image, primarily due to the often minimal differences in physical density between normal and cancerous tissues.

However, such microscopic and macroscopic aberrations associated with early small cancers may cause refraction, minute changes in the direction of x-ray propagation. These subtle changes can be exploited by the use of diffraction-enhanced imaging (DEI). DEI obtains images based on absorption contrast as well as the unique contrast mechanisms of refraction and extinction, with the potential for greatly reduced radiation dose (Chapman 1997, Zhong 2000, Parham 2006). The application of DEI to breast imaging has consistently provided superior contrast and signal-to-noise (SNR) ratios when compared with conventional radiographic images (Pisano 2000, Kiss 2003, Kiss

2004, Chapman 1996, Chapman 1997, Chapman 1998, Hasnah 2002b, Fiedler 2004, Liu 2007a, Fernández 2005, Lewis 2003, Pagot 2005).

Contrast-enhanced mammography is under investigation, either as an adjunct or replacement for conventional mammography (Dromain 2006, Jong 2003, Diekmann 2003, Lewin 2003). Limited research has been conducted evaluating the potential of contrast-enhanced DEI (CE-DEI). Thus, theoretical prediction of absorption and refraction contrast was performed for a variety of potential x-ray contrast agents considering physical density amenable to absorption-based contrast and electron-density that could potentially create refraction contrast. DEI phantom imaging of several commercially available contrast agents established the feasibility of CE-DEI.

Furthermore, in this dissertation we demonstrate that DEI has a major advantage over conventional mammography in that the x-ray energy used can be set higher, thus lowering patient dose. Conventional mammography must use lower energies because there is a rapid decrease in the photoelectric effect as x-ray energy increases, resulting in a dramatic loss of absorption contrast. At higher energies, refraction contrast persists. Thus, DEI can harness higher imaging energies while conserving refraction contrast. High energy monochromatic x-rays result in reduced patient radiation and overcome path length limitations requiring breast compression in a conventional system. It follows that DEI may not require breast compression in order to obtain an image that contains information important for clinical diagnosis. This could offer a dramatic improvement for patient comfort and could potentially increase the number of women willing to undergo annual screening mammography.

Until recently, the largest drawback to the implementation of DEI for breast imaging has been the difficulty in translating this technology into a clinical setting using available incoherent source x-ray tube technology (Förster 1980, Davis 1995, Ingal 1998, Wang 2006b, Kim 2007b, Vine 2007). Nonetheless, our group recently constructed an x-ray tube-based DEI system (DEI-PR) that successfully acquired refraction images (Parham 2009). This dissertation demonstrates that the DEI-PR system can provide images comparable to the synchrotron-based DEI system in spite of obstacles to such a demonstration, such as design flaws that were unavoidable at the time of development. We developed a reference set of data, with expert radiologists evaluating the correlation of DEI image features with known histological findings. A second-generation DEI-PR currently under development will utilize a more powerful x-ray tube and an optimized digital detector with a reduced source-to-detector distance. When the second-generation DEI-PR has been developed, allowing a fair receiver-operator characteristic (ROC) analysis study, its performance can be compared to these correlation data.

DEI might have the potential to revolutionize mammography and early-stage breast cancer detection. As DEI research continually makes strides demonstrating the ability to acquire images with excellent soft tissue contrast, particularly within breast tissues, one must also consider real issues involving the translation of this imaging modality into a clinical setting. This research addresses several issues critical to the development of DEI as a clinically relevant imaging modality such as the evolution of a contrast-enhanced DEI protocol, the reduction of breast compression for increased patient comfort, and the development of a standalone DEI system for preclinical development.

1.2 Objectives

Aim 1: To determine the feasibility of contrast-enhanced DEI.

A. Predict absorption and refraction contrast for potential DEI contrast agents at clinically viable concentrations

B. Obtain or synthesize contrast agents for phantom studies
1. Iodine, molecular
2. Gadolinium, molecular
3. Ferric Oxide, nanoparticle
6. Microbubble

C. Implement phantom DEI imaging to measure refraction and absorption contrast
1. Several x-ray energies
2. Multiple rocking curve positions
3. Range of concentrations

Aim 2: To determine if breast compression significantly affects DEI image quality.

A. Image human breast tissue specimens with DEI
1. Image at three compression levels
2. Image at multiple rocking curve positions
3. Obtain pathologic diagnosis for regions of interest

B. Develop DEI training set for expert radiologists

C. Conduct reader study evaluating lesion characteristic visibility of various tissue thicknesses using synchrotron-based DEI

Aim 3: To demonstrate the prototype DEI system as roughly equivalent with the synchrotron-based DEI.

A. Image full-thickness human breast tissue specimens with DEI
1. Image on prototype x-ray tube-based DEI system, traditional synchrotron-based DEI system, and digital mammography
2. Image at multiple rocking curve positions
3. Obtain pathologic diagnosis for regions of interest

B. Develop DEI training set for expert radiologists

C. Conduct reader study evaluating lesion benign/malignant appearance and lesion characteristic visibility using the synchrotron- and x-ray tube-based DEI

1.3 Dissertation Organization

In order for readers of widely varied backgrounds to understand DEI as applied to breast imaging, chapter 2 describes the anatomy of the human breast and discusses cancers of the breast as well as risk factors for breast cancer development. Chapter 3 reviews methods of x-ray generation and how x-rays interact with breast structures. Chapter 4 covers issues affecting radiographic image quality. Conventional and digital mammography are detailed in chapter 5. Other preclinical and clinical breast imaging modalities are briefly detailed in chapter 6. Chapter 7 reviews how laboratory and clinical trials are used to demonstrate clinical utility of an emerging breast imaging technology. A thorough explanation of DEI and its cousin DEI-computed tomography (DEI-CT) is presented in chapter 8. Although much research has explored DEI for breast imaging applications, chapter 9 explores additional potential medical imaging applications of DEI. Chapter 10 investigates the novel area of contrast-enhanced DEI. Chapter 11 considers the effects of the reduction of breast compression on DEI image quality. Chapter 12 discusses the prototype DEI device with comparison to both traditional DEI and digital mammography standards. Finally, chapter 13 reviews the findings presented throughout this dissertation and suggests future directions for continued research.

CHAPTER 2: THE HUMAN BREAST AND BREAST CANCER

2.1 Overview

Breast cancer is currently the second most common cancer in the world, and the second leading cause of death among women in the United States (Jemal 2007, Parkin 2001). The implementation of dedicated mammography units, improved x-ray beam quality, effective breast compression, and exposure control during imaging have dramatically improved breast cancer detection (Haus 1990). This chapter addresses the normal human breast structure and anatomy, followed by a discussion of the cellular and molecular basis of breast cancer. Together, these create a foundation for understanding the changes induced by benign and cancerous conditions of the breast, followed by discussion of breast cancer risk factors and the potential for breast cancer prevention.

2.2 Human Female Breast Structure and Anatomy

The intricate structure of the human female breast undergoes cyclical changes with the menstrual cycle, dramatic changes with life events such as pregnancy and menopause, and gradual changes associated with aging. Ovulation induces cellular proliferation and swelling due to increased sex steroid levels. Pregnancy causes lobules to multiply and fill the breast, and lactation engorges and fills the lobules. Aging and menopause usually cause dense breast tissue to become replaced with fatty tissue and a decline in endogenous sex-steroids. For simplicity, this discussion will only address normal and pathological issues concerning the mature, non-lactating female breast, summarized in Figure 2.1.

Breasts are rarely bilaterally symmetrical. Breast parenchyma is composed of a mixture of glandular and stromal tissue. Stroma comprises approximately 80% of the breast volume, and is made up of fatty tissue, dense interlobular connective tissue, and loose intralobular connective tissue. Hormone-sensitive specialized glandular tissue surrounds the milk-producing alveolar glands that terminate the branching ductal system, referred to as terminal ductal lobular units (TDLU). The lobules are lined by cuboidal epithelial cells loosely supported by myoepithelial cells. (Winchester 2005, Kopans 2007, Rosen 2001, Ronnov-Jessen 1996)

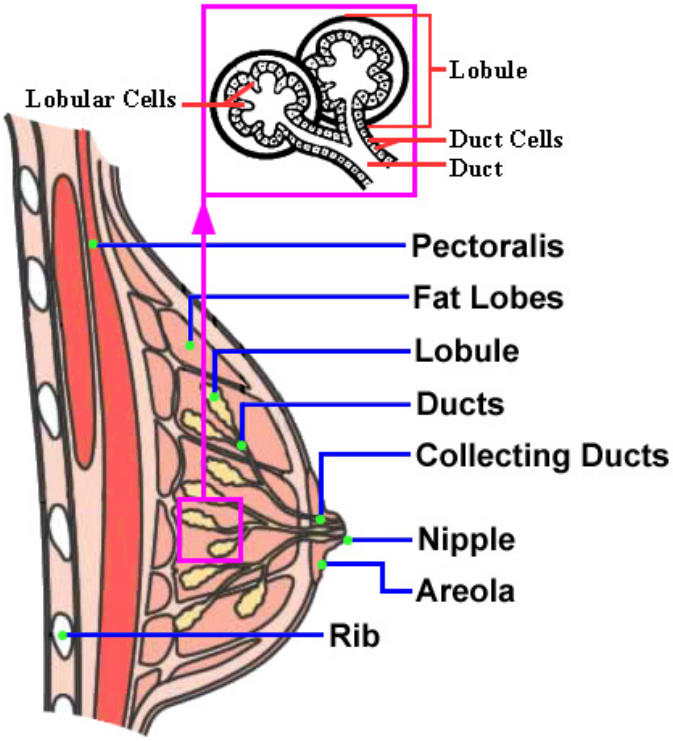

FIGURE 2.1: Structure and Anatomy of the Human Breast. The human breast is part of the female reproductive system, containing milk-producing glandular tissue and an extensive ductal system situated within a collagenous and fatty matrix. These breast structures are surrounded by the stromal breast component and supported by fibrous Cooper's ligaments, which anchor to the skin and chest wall. The breast stroma contains connective tissues, vasculature, and lymphatics. Although attached to the pectoralis muscle, the breast only contains small muscles of its own in the nipple and surrounding pigmented region of skin called the areola. (Reprinted with kind permission from http://diane.ponpines.com/images/breast_structure.jpg)

Each TDLU is attached to an extralobular duct system. The lactiferous ducts terminate at secretory pores in the nipple and form asymmetric branching structures of variable diameter arranged in distinct ductal networks. These ducts are lined by columnar epithelium formed by two types of cells: columnar cells that line the lumen and basal cells. These basal cells can differentiate into either columnar or myoepithelial cells. This ductal epithelium is supported by myoepithelial cells, basement membrane, and elastic fibers. (Winchester 2005, Kopans 2007, Rosen 2001, Ronnov-Jessen 1996)

These lobular structures undergo dramatic structural changes associated with the menstrual cycle, pregnancy, lactation, exogenous hormone use, and menopause. Menopause has the most considerable lasting effect on breast anatomy. The characteristic decrease in estrogen and progesterone, with maintenance of testosterone levels, induces structural changes in the hormone-sensitive lobules. Epithelial cells, and to a lesser extent myoepithelial cells, undergo atrophy, causing a loss of cellularity in the lobules. The basement membrane thickens, collagen content in the stromal tissue within the lobules increases, and the quantity of elastic fibers decreases. (Rosen 2001)

The breast contains approximately 15 separate ductal tracts, referred to as lobes. These lobes are not morphologically evident, but can be appreciated via dye injection into a single ductal system, although isolated shunts between distinct lobes do sometimes exist. The amount of tissue drained by a particular lobe is variable. Duct diameter tends to increase as the lactiferous ducts converge to deliver milk to the nipple through a lactiferous duct orifice secretory pore. The nipple contains sebaceous glands, and is surrounded by a region of pigmented skin called the areola, which contains modified sebaceous glands of Montgomery. The nipple and areola contain smooth muscle, which

constitutes the only muscle tissue contained in the breast. (Winchester 2005, Kopans 2007, Rosen 2001)

The lobular and ductal systems are surrounded by a collagenous and fatty stromal matrix that contains vasculature, lymphatics, and connective tissues. Breast elements are supported by collagenous Cooper's ligaments throughout the stroma that anchor to the skin and chest wall. Quantities of stromal fatty tissue and collagen vary widely between individuals as well as over a lifetime due to weight change and fatty replacement of dense parenchyma associated with aging. It is this combination of stromal and epithelial structures that leads to the radiographic appearance of breast tissue. (Rosen 2001)

The primary breast blood supply is provided by the axillary and internal mammary arteries. Lymphatic drainage of the breast occurs predominantly through the axillary lymph node (LN) chain, but drainage also occurs through the internal mammary, posterior intercostal, and supraclavicular LN chains. The lymphatic systems of each breast are interconnected, but flow to the contralateral breast typically only occurs in the case of lymphatic obstruction. A sentinel LN is the first node in the lymphatic drainage path of a particular region in the breast. There can be multiple sentinel LNs that drain a particular region (Wong 2001). (Winchester 2005, Kopans 2007, Rosen 2001)

2.3 Cellular Biology of Breast Cancer

The ductal network is the site of origination of most cancers. Ducts are composed of two main epithelial cell types- luminal epithelial and myoepithelial. Luminal epithelial cells function to excrete milk during lactation. The vast majority of cancers express markers consistent with origin from luminal epithelial cells. Myoepithelial (ME) cells can be either luminal or acinar in form. Luminal ME cells form a contractile layer around the

luminal epithelial cells. Acinar ME cells form a network around, but do not always continuously surround, the luminal epithelium. Although ME cells rarely undergo malignant transformation, they are involved in the carcinogenic process. ME cells are aberrant in *in situ* cancers, and largely absent in invasive cancers. Although the mechanisms are not fully understood, loss of ME function is associated with breast cancer development and metastasis. This is likely due in part to basement membrane and extracellular matrix proteins produced by ME cells, as well as tumor suppressor gene expression. (Adriance 2005, Lakhani 2001)

It is believed that breast cancer typically takes several years to develop into clinically detectable disease. Mammographic density of normal and abnormal tissue is often very similar, while necrosis and invasion into surrounding tissue are easily overlooked or miscategorized. Most cancers originate in the ducts, but form in other structures as well. Fibrotic tissue occasionally forms around a cancer. This process is referred to as "desmoplastic response." A tumor is often 90% stroma, with stromal tissues demonstrating abnormalities both near and far from the tumor (Ronnov-Jessen 1996). (Ikeda 2004, Winchester 2005, Harris 1991)

In situ carcinomas are locally contained collections of cancerous cells, bound inside the lobule or duct by the basement membrane. Sometimes these cells undergo changes that allow invasion of local and/or distant sites. With local invasion, basement membranes are disrupted and cancerous cells sometimes spread along collagen fibrils which subsequently display increased turnover rates and abnormal bundling (Kauppila 1998). Distant metastases originate by spread through vasculature or lymphatics. The

most common sites for distant metastatic breast cancer include the LNs, lung, liver, and bone. (Harris 1991, Winchester 2005)

Increased metabolic demand dictates an increased supply of oxygen- and nutrient-rich blood. Cancers initiate angiogenesis, creating a hypervascular network to supply increasing energy demands and overcome their diffusion-limited size, above which simple diffusion can not provide enough energy to meet the metabolic demands for continued growth and self-sustenance. These vascular networks are abnormal and lack appropriate restrictions for exchange across the vascular wall. However, angiogenesis is not exclusive to cancer. Benign proliferative lesions can also demonstrate hypervascularity due to increased metabolic demands, with increased vascularity proportional to the pathologic severity of the lesion (Heffelfinger 1996). (Harris 1991, Winchester 2005)

Tumor-involved lymphatics become crushed and nonfunctional with increasing tumor size, but the surrounding network will continue to filter and drain breast lymph and offers a route for metastatic spread of invasive breast cancer (Wilking 1992). While the axillary LNs are more commonly evaluated clinically, evaluation of the internal mammary LNs identifies metastatic spread in approximately 30% of patients diagnosed with invasive carcinoma and negative axillary LNs (Heuts 2009). For this reason, identification of sentinel LNs is an important method of assessing the metastatic spread of cancer. (Harris 1991, Winchester 2005)

Because the sentinel LNs are the most likely initial sites of metastatic spread, their status correlates with the status of subsequent LNs in the chain (Kamath 2001). If the sentinel LN contains metastatic disease, subsequent LNs in the chain have a 40-50%

chance of containing metastatic disease (Jakub 2003, Albertini 1996). However, sentinel LNs are bypassed in lymphatic metastases in approximately 1 to 4% of cases (Weaver 2000, Jakub 2003, Albertini 1996). Sentinel LN mapping has rapidly gained widespread clinical implementation because *in situ* tumors are sometimes found to have an undetected invasive component and because thorough pathologic evaluation of sentinel LN biopsy sometimes leads to upstaging, and thus a different course of treatment, for 10 to 20% of breast cancer patients (Albertini 1996, Cox 2001, Kelly 2003).

2.4 Molecular Basis of Human Breast Cancer

Breast cancer can occur spontaneously, in response to an environmental insult, or from a genetic predisposition to cancer where normal cellular control mechanisms are unable to prevent neoplastic transformation. Genetic influence depends on the actual genetic code as well as epigenetics, where heritable information in the form of DNA methylation patterns influences transcriptional products and genetic stability. Survivable mutations are passed on to daughter cells, typically involving cell cycle control, DNA repair, cell death pathways, angiogenesis, and cell adhesion. The carcinogenic process is summarized in Figure 2.2. Although the genetic profile of cancers is highly variable between individuals, the profile from different tumors within the same patient typically varies very little. (Alberts 2002, Ross 2005)

Cancer growth depends on self-sufficient development of growth signals while ignoring signals inhibitory to continued growth, avoiding senescence and apoptosis, and developing provisions for continually increasing energy demands by angiogenesis. When cells divide quickly, there is less time for DNA checking or repair of damage and mistakes, allowing an accumulation of errors. Abnormal cell-cell contact inhibits proper

communication with normal cells that might otherwise allow some regulation. Some tumors possess the ability to invade surrounding parenchyma as well as metastasize to distant sites in the body when cells lose normal adhesion properties and enter the blood stream or lymphatic system. Many genes are involved in the carcinogenic process, some of which are summarized in Table 2.1. Because currently understood genetics do not fully explain the extent of risk, it is highly likely that additional genes exist that confer breast cancer risk. (Winchester 2005, Ross 2005, Mihich 1996)

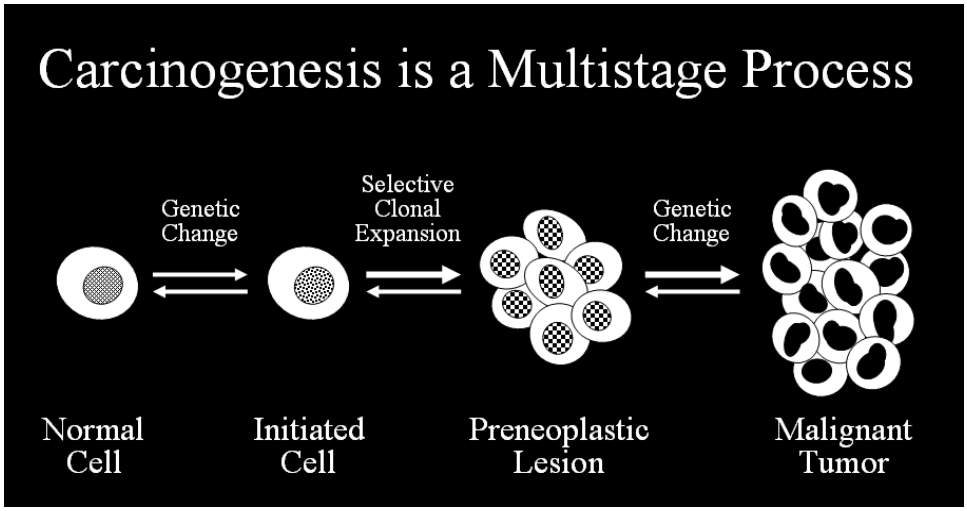

FIGURE 2.2: Carcinogenesis. Carcinogenesis occurs in four stages: initiation, promotion, conversion, and progression. Cells are primed for neoplastic transformation when an initiating event directly affects DNA. Exposures to chemical carcinogens or x-rays are examples of initiating events. Identifying an initiated cell is exceptionally difficult. Continued progression down the carcinogenic pathway involves hyperplasia and the linear evolution of an increasingly aberrant and aggressive collection of abnormal cells with loss of normal control mechanisms.

BRCA1 and BRCA2 mutations confer an increased risk of breast cancer due to loss of proper DNA repair, cell cycle control, and ubiquitination processes. BRCA mutations also result in an increased risk of developing cancer in other tissues, such as ovaries, fallopian tubes, pancreas, pharynx, stomach, gallbladder, bile ducts, and colon. Women with mutations in BRCA1 and BRCA2 have a 65% and 39% chance of developing breast cancer by the age of 70, respectively (Antoniou 2003). Hereditary

breast cancers due to BRCA mutations have unique phenotypes and often express basal-like markers. BRCA genes are rarely mutated in sporadic cancers. Cancers with BRCA1 mutations tend to have lost p53 control and do not often overexpress HER-2. The same has not been demonstrated for BRCA2 mutations. (Hall 1990, Narod 2004, Phillips 2001)

	Gene	Controls	Interacts With
Tumor Suppressor Gene	BRCA1	DNA repair, cell cycle control, ubiquitination	Rad51, TP53, Myc, E2F, BAP1
	BRCA2	DNA repair, cell cycle control, ubiquitination	Rad51, TP53
	Rad51	DNA repair	BRCA1, BRCA2
	TP53	Cell cycle control, DNA repair, apoptosis	MDM2, p16
	RB1	Cell cycle control	E2F, TFs, cyclins
	PTEN	Cell cycle control, apoptosis	AKT
	p16	Cell cycle control	CDK4, TP53
	CHEK2	Cell cycle control, DNA repair, apoptosis	TP53, BRCA1
	RIN1	Cell migration	Ras
Oncogene	HER-2/*neu*	Cell growth, differentiation	GRB7
	Myc	Proliferation, cell growth, apoptosis, differentiation	HATs, Miz-1, MAPK
	Ras	Signal transduction, cell adhesion and migration, proliferation, apoptosis	GEF, GAPs
	Fos	Proliferation, differentiation cell damage repair	Jun, growth factors, MAPK, PKA PKC, cdc2
	Jun	Regulate gene expression	Fos, JNKs
	MDM2	Negative TP53 regulator	TP53, Ras
	GRB7	Cell migration	EGFR, FAK
Other	Bcl-2	Apoptosis	Btf
	HSP27	Stress survival, apoptosis, signal transduction, differentiation	Actin, IFs, NF-κB
	FGF	Angiogenesis, proliferation	Heparin
	NCOA3	Transcription	Histones, ERα, PR, TP53, NF-κB
	BRAF	Cell cycle control	MEK
	CD44	Cell adhesion, cell migration	Hyaluronan
	Cadherin	Cell adhesion	Calcium
	ATM	Cell cycle control, DNA repair, apoptosis	TP53, CHEK2, BRCA1

TABLE 2.1 Genes Involved in Breast Cancer. Many genes involved in breast cancer have been discovered, while many more are under investigation. Mutations interact (directly or indirectly) with many other proteins, enzymes and entire pathways. These interconnections are only beginning to be elucidated. (Winchester 2005, Ross 2005, Milstein 2007, Burwinkel 2005, Mihich 1996)

The HER-2/*neu* gene is expressed in all breast epithelial cells, but is overexpressed in 10 to 34% of human breast cancers, and is highly correlated with breast cancer pathogenesis and prognosis (Slamon 1989, Ross 2003, Camp 2003). HER-2/*neu* is important for proper cell growth and differentiation processes. While there is no known ligand for HER-2/*neu*, it is the preferred heterodimerization partner for other family members, resulting in a strong signaling cascade (Ross 2003). Women with HER-2/*neu* overexpression and proliferative benign changes (typical or atypical) have a significantly increased risk of breast cancer development (Stark 2000). A tumor overexpressing HER-2/*neu* will also demonstrate amplification in its metastatic sites (Niehans 1993). Moreover, the extracellular membrane receptor location makes this an optimal target for active targeting through receptor-mediated endocytosis for imaging and therapeutic agents.

The estrogen receptor (ER) is expressed in only 10% of healthy breast tissue, while many cancerous tissues express ER at much higher percentages. Activation of the ER signaling pathway occurs in coordination with heat shock proteins, estrogen response elements, cyclin D, and several coactivators and corepressors. The ER is located internally, and binding stimulates cellular proliferation. Estrogen is mitogenic and it is generally believed that increasing levels of exposure to this hormone will increase breast cancer risk. Similarly, binding of the hormone progesterone to its receptor (PR) mediates cellular proliferation. The role of progesterone in breast cancer is controversial with researchers finding that PR is protective, has no effect, or even that it promotes the carcinogenic process. (Anderson 2002, Winchester 2005, Ross 2005, Althuis 2004, Pasqualini 2007)

Mutations in other genes such as p53, CHEK2, PTEN, ATM, CASP8, PBRL, BRIP1, bcl-2, cyclin D1, telomerase, and various growth factors are further examples of aberrant expression in many hyperplastic lesions and breast cancers (Gasco 2002, Nadler 2008, Roy 2006, Baykal 2004, Klijn 1992, Bradbury 2007). A single mutation is not enough to cause cancer. Further mutation, along with loss of heterozygosity (LOH), is common among invasive cancers, but has also been found to be present within *in situ* cancers, atypical lobular hyperplasia, non-atypical hyperplasia, and in normal tissue. LOH was found more often in patients with breast cancer than those with benign breast tissue. Together, this suggests that genetic changes are likely more widespread than currently believed. LOH detected in both luminal and ME cells suggest a common aberrant stem cell progenitor, yet ME breast tumors are far more rare than those of luminal origin. (Lakhani 1995a, Lakhani 1995b, Lakhani 1996, Lakhani 1999)

Once tumors have developed vasculature, they begin releasing proteins, and sometimes cells, into the bloodstream. Several such circulating biomarkers[1] have been identified that can assist in the detection and characterization of breast cancer. Interestingly, metastatic development does not induce a large change in the biomarker profile, suggesting that the potential for metastatic transformation is already present within the primary breast cancer. Very few biomarkers have found their way into routine clinical screening or diagnostic evaluation. The only regularly tested biomarkers include HER-2/*neu*, ER, and PR, largely because these biomarkers are also targets for therapeutic treatments using pharmacologic agents such as Herceptin, Tamoxifen, Fareston, Femara, Aromasin, Evista, and Megace (Profiles of Breast Cancer Drugs 2008). Recently, a 21-

1. Several circulating biomarkers have been identified which assist in the detection and characterization of breast cancer, including: HER-2/*neu*, ER, PR, Ki-67, p53, cyclin D1, cyclin E, cyclin B, uroplasminogen activator, cathepsin D, matrix metalloproteinases, carbohydrate antigen 15.3 (CA 15.3), CA 27.29, carcinoembryonic antigen, α-fetoprotein, urokinase plasminogen activator receptor and autobodies to breast cancer proteins.

gene assay scoring the likelihood of metastasis has been developed (Paik 2004). (Ross 2005)

2.5 Benign and Cancerous Diseases of the Breast

Differences between normal and abnormal breast tissue are often subtle, characterized by cellular features (typical versus atypical) and growth patterns (proliferative versus nonproliferative). Many of these features are important for mammographic detection and appropriate characterization of lesions. Several benign and atypical conditions are shown in Tables 2.2 and 2.3, respectively. Nonproliferative benign conditions are growths of disregulated cells, typically only harmful if the location disrupts normal function, such as blockage of proper lymphatic drainage. Some neoplasms do confer an increased risk for cancer development, usually classified as atypical or proliferative. (Jacobs 1999, Ikeda 2004, Hartmann 2005, Harris 1991)

	Calcifications	Features
Duct Ectasia	Yes	Wide, hard ducts sometimes forming a mass
Oil Cyst	Some	Well-circumscribed round, oil-filled mass
Fat Necrosis	Some	Round, fatty mass (occasionally spiculated, cystic)
Hamartoma	Some	Uncommon circumscribed, fatty/fibrotic mass
Papillary Apocrine Change	None	Proliferation of ductal epithelial cells
Fibrocystic Disease	Some	Proliferative, palpable mass with multiple cysts, stromal fibrosis, apocrine metaplasia
Fibroadenoma	Some	Common well-circumscribed, solid mass
Fibromatosis	Rare	Locally invasive mass of fibroblast proliferation
Benign Vascular Lesions	Some	Hemangioma, angiolipoma
Granular Cell Tumor	None	Uncommon palpable, poorly circumscribed mass
Lipoma	Some	Circumscribed, hard fatty mass
Papilloma	Some	Individual or multiple well-circumscribed ductal mass(es), often with intraductal hyperplasia, sclerosing adenosis
Phyllodes Tumor	Rare	Round, dense fibrotic mass
Mastitis	Yes	Inflammation

TABLE 2.2: Benign Breast Conditions. Although this is not an exhaustive discussion of benign breast diseases, several common conditions are listed. Typical clinical and mammographic presentations are noted, including whether calcifications are usually associated with the condition. (Rosen 2001)

Common benign inflammatory and reactive diseases include duct ectasia and fat necrosis. Mammary duct ectasia is characterized by dilation of the ducts with inflammatory changes within the ducts and surrounding tissues that sometimes becomes fibrotic or cystic. Fat necrosis typically results from an injury to the tissue from trauma, surgery or high radiation exposure. These masses are usually small and sometimes contain calcifications or cysts. (Rosen 2001)

	Calcifications	Features
Lobular Neoplasia (LCIS)	None	Proliferation of lobular cells (often with ALH)
Atypical Ductal / Lobular Hyperplasia (ADH, ALH)	Yes	Proliferation of ductal or lobular epithelial cells
Radial Scar (RS)	Yes	Irregular, proliferative mass with atrophic center, often occurring in multiples or with cysts, DCIS, ADH, SA
Sclerosing Adenosis (SA)	Yes	Proliferation of glandular and stromal cells into fibrotic mass

TABLE 2.3: Atypical Breast Lesions. Some benign conditions are considered atypical and proliferative, and confer an increased risk of subsequent cancer development. These lesions are often considered to be precancerous or closely associated with the presence of cancer. (Rosen 2001)

Several benign tumors are closely associated with the presence of cancer or are considered precancerous lesions. Although papillomas are benign masses in the ductal epithelium, papillary carcinoma is often associated with areas of benign papillomas. Multiple papillomas tend to have greater precancerous potential. Phyllodes tumors arise from stroma surrounding the ducts to become benign, low-grade malignant, or high-grade malignant tumors, and are sometimes associated with LCIS or invasive ductal carcinoma. (Rosen 2001)

Neoplasia is a proliferative lesion with atypia and carries a risk of breast cancer development. Lobular carcinoma *in situ* (LCIS) is a non-malignant, high-risk lesion which is difficult to detect through mammographic screening due to its growth pattern and typical absence of calcifications. Abnormal cells tend to grow around the TDLU

lumens instead of within them. Interestingly, LCIS is most often associated with invasive ductal carcinoma. Proliferative and atypical lesions are often associated with, or develop into, cancerous lesions. (Rosen 2001)

Ductal and lobular hyperplasias are proliferative lesions that are considered precancerous. Sclerosing lobular hyperplasia is often associated with a fibroadenoma. Radial scars are considered precancerous by some experts because they are proliferative in nature and are found more often in women with breast cancer than those without. LCIS lesions are often associated with radial scars. However, most radial scars are too small to be reliably detected by clinical exam or mammography. Sclerosing adenosis is a proliferative lesion of the TDLU. Although fibroadenomas are generally benign tumors, they sometimes develop adenosis, which carries a risk of breast cancer development. Even though nonproliferative fibrocystic change does not convey increased breast cancer risk, the proliferative variant is composed of several disease processes that each conveys increased risk, such as ductal hyperplasia and sclerosing adenosis. (Rosen 2001)

Several common breast cancers are summarized in Table 2.4. Ductal carcinoma *in situ* (DCIS) is a non-malignant lesion originating in the TDLU. Although DCIS sometimes develops metastatic potential, it typically has an excellent prognosis. Papillary, tubular, and mucinous carcinomas are additional cancers that are associated with good prognoses. Invasive ductal carcinomas represent 65-80% of malignant breast cancer diagnoses. Medullary carcinoma is a rapidly-growing receptor negative cancer more common among women with BRCA mutations, and is associated with a poor prognosis. (Rosen 2001)

	Invasive	Features
Ductal Carcinoma *in Situ*	No	Ductal mass often with necrosis, calcifications
Papillary Carcinoma	Not Often	Individual or multiple slow-growing, round ductal mass(es), sometimes with inflammation, fibrosis, cysts, hemorrhage
Invasive Ductal Carcinoma	Yes	Irregular, spiculated ductal mass often with necrosis, hemorrhage
Invasive Lobular Carcinoma	Yes	Single-cell lines of lobular cancer cells or irregular mass
Medullary Carcinoma	Yes	Circumscribed, rapidly-growing, poorly-differentiated mass
Tubular Cancer	Yes	Slow-growing, irregular, spiculated mass, often with DCIS, RS
Inflammatory Carcinoma	Yes	Mastitis, skin thicknening
Mucinous Carcinoma	Yes	Slow-growing, soft mass in mucinous picket, often with DCIS
Adenoid Cystic Carcinoma	Yes	Rare, slow-growing mass with excessive mucin
Sarcoma	Yes	Well-circumscribed mass
Lymphoma	Yes	Often well-circumscribed

TABLE 2.4: Malignancies of the Breast. Although this is not an exhaustive list, it summarizes some of the more common breast cancers. Common clinical and mammographic presentations are listed, with indication of whether the lesion represents a lesion capable of invading surrounding tissue and metastasizing to distant sites within the body. (Rosen 2001)

2.6 Breast Cancer Risk Factors

Currently, an American woman has a 12% chance of being diagnosed with breast cancer in her entire lifetime (Ries 2007). Regardless of a rapidly growing understanding of factors contributing to breast cancer risk, the exhaustively verified Claus and Gail risk assessment models and the standardized classification of clinical findings of breast cancer, clinicians can not specifically determine which women will actually develop cancer (Costantino 1999, Rockhill 2001, Weik 2005). However, it is generally accepted that factors affecting circulating levels of female sex hormones will influence breast cancer risk directly and indirectly through incompletely understood mechanisms. Risk factors include gender, age, genetic abnormalities, breast pathologies, history of breast cancer, ethnicity, exogenous hormone use, weight, lifestyle, initiation and cessation of menstruation, parity, *in utero* events, and radiation exposure.

Because men have significantly lower levels of circulating estrogen and less breast tissue in general, simply being a woman presents a substantial risk of breast cancer

development (Fentiman 2006, Nahleh 2006). Additionally, age is an important indicator of breast cancer risk due to percent breast density and accumulation of DNA damage (Boyd 2007, Milanese 2006, Vachon 2007, Key 2001, Torres-Mejía 2005, Palomares 2006). Although breast density varies widely between women and through the course of a lifetime, young women typically have dense breasts. Breasts generally become fatty replaced with aging, with involution rate being approximately 65% heritable (Stone 2006).

Fatty involution allows better visualization of breast features, but aging also allows DNA damage accumulation, particularly if repair pathways are not functioning properly. This means older women have more unhealthy cells primed for carcinogenic transformation, and thus a higher risk of breast cancer than younger women, even allowing for differences in breast density. Menopause influences breast cancer risk through a characteric and significant change in endogenous levels of sex hormones such as estrogen, androgen, and progesterone concentrations (Missmer 2004).

Several hereditary genetic mutations in genes governing functions such as steroid hormone metabolism, carcinogen metabolism, cell cycle control, and DNA repair pathways increase the chance of breast cancer development, particularly of early onset cancer, shown in Table 2.5 (Ross 2005). Women with these mutations are considered to be at high risk for breast cancer development, spurring the recent push for better adjunctive imaging procedures to screen for and diagnose cancers. Magnetic resonance imaging (MRI) and ultrasound (US) are attractive options as they do not deliver a radiation dose that could initiate tumors in women with compromised pathways that process such insults (Patani 2008, Berg 2008). While these systems are not presently

considered ideal for the general screening population, the risk-benefit ratio for high-risk women may justify their use as screening modalities (Patani 2008, Berg 2008).

Syndrome	Mutated Gene
Hereditary Breast Ovarian Cancer Syndrome	BRCA1, BRCA2
Li-Fraumeni Syndrome	p53
Cowden Syndrome	pTEN
Peutz-Jeghers Syndrome	STK11/LKB1
Ataxia-Telangiectasia Syndrome	ATM
Blooms Syndrome	General

TABLE 2.5: Genetic Abnormalities Commonly Resulting in Breast Cancer. BRCA1, BRCA2 and STK11/LKB1 mutations each confer a 50 to 85% risk of breast cancer development within a lifetime. Mutations in the p53 gene, resulting in Li-Fraumeni syndrome, convey a 60% risk of breast cancer development over a lifetime. There is a 25 to 50% risk of breast cancer for women with mutations in the pTEN gene. A mutation in the ATM gene doubles the lifetime risk of breast cancer. Blooms syndrome creates susceptibility to all cancers, vastly increasing the chance of developing a wide range of cancers. (Ross 2005)

With the exception of cysts, both typical and nonproliferative benign breast pathologies only impart minimally increased breast cancer risk (Key 2001, Hartmann 2005, Wang 2004). Atypia and proliferative benign conditions increase early-onset breast cancer risk, with some conditions such as LCIS increasing risk up to ten-fold (Hartmann 2005, Wang 2004, Ikeda 2004, Jacobs 1999). A woman who has had breast cancer has a greater risk of developing a second incidence of breast cancer in either breast. This risk is increased by additional factors, such as breast conserving therapy instead of full mastectomy. (Ikeda 2004)

Risk is increased two- to three-fold with a family history of breast cancer (Claus 1998, Pharoah 1997, Basham 2002). The influence of family history on a woman's breast cancer risk varies. Factors that influence breast cancer risk imposed by a family history of breast cancer include the degree of the affected family member, the number of family

members who develop breast or ovarian cancers, the age of family member at the time of cancer diagnosis, and racial differences within the family (Yang 1998). However, only 25% of women with familial breast cancer have BRCA1 or BRCA2 mutations (Shih 2002). A family history of breast cancer could indicate aggregation of risk factors such as genetics, lifestyle, and environmental exposures (Lalloo 2006, Claus 1998).

Breast cancer risk demonstrates racially distinct patterns, shown in Figure 2.3. Many race and ethnicity factors potentially influence such disparities in breast cancer incidence and mortality, including genetics, societal factors such as insurance status and availability of high quality mammographic systems in a facility with well-trained physicians, and environmental influences such as diet. Race can be further broken into ethnicity subgroups. For example, Ashkenazi Jewish white women have higher breast cancer incidence than that calculated for the entire white population of the United States. (American Cancer Society 2008)

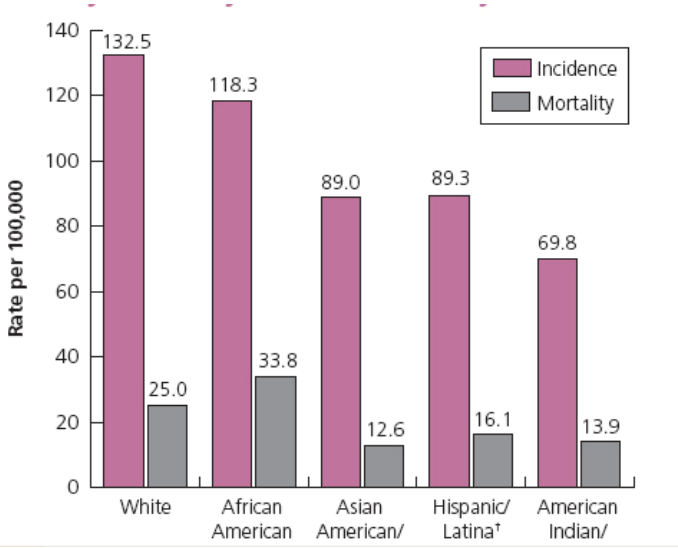

FIGURE 2.3: Incidence and Mortality of Breast Cancer by Race in the United States. As seen in the most recently compiled statistics, there are significant disparities in breast cancer incidence and mortality when analyzed by race. Reprinted with kind permission from the American Cancer Society. *Breast Cancer Facts and Figures 2007-2008*. Atlanta: American Cancer Society, Inc.

Recently, gene expression studies identified several subtypes of breast cancer important for prognosis and guiding therapy, with subtype prevalence differing based on race (Carey 2006). The basal-like subtype has low ER and HER-2/*neu* expression levels, and is associated with poor outcome (Carey 2006). This subtype occurs with dramatically increased frequency in African American women and in women carrying the BRCA1 mutation (Carey 2006).

However, neither BRCA1 mutation nor adjustment for higher prevalence of breast cancer subtypes with unfavorable prognoses fully explains the disparity in mortality between Caucasian women and African American women. This indicates the contribution of undiscovered genetic trends as well as societal factors such as insurance status and availability of high quality mammographic systems in a facility with well-trained physicians (Carey 2006). Furthermore, environmental influences, such as diet differences, could be important in explaining these disparities. (American Cancer Society 2008, Simon 2005b, Chu 2001, Weir 2003, Shavers 2002, Althuis 2004, Ikeda 2004, Ries 2007)

Recent hormonal oral contraceptive use is thought to only minimally increase breast cancer risk because it imitates normal hormonal processes and is typically used in younger women whose background risk levels are relatively low (Bernstein 2002, Key 2001, Althuis 2004). Cessation of use will gradually decrease risk to normal or to minimally elevated levels relative to background risk (Key 2001). The use of fertility drugs also has the potential to increase breast cancer risk, but current data is limited (Key 2001). After menopause, some women choose to undergo hormone replacement therapy (HRT), which increases risk because HRT use causes higher circulating hormone levels when levels would normally be decreased, and often increases breast density (Tamimi

2005, Greendale 2003, Torres-Mejía 2005, Key 2001, Magnusson 1999). Elevated risk diminishes gradually with HRT cessation (Tamimi 2005, Greendale 2003, Torres-Mejía 2005, Key 2001, Magnusson 1999).

Obesity can result from poor lifestyle choices, genetic conditions, or both. Postmenopausal obesity increases cancer risk because after menopause, sex hormones are primarily produced in fatty tissue, extending the length of exposure to high levels of hormones at a time beyond which the body naturally possesses high circulating levels (Colditz 2004, Althuis 2004, Lahmann 2004, Porter 2006). Obesity increases risk even further for women undergoing HRT or those with a family history of breast cancer (Key 2001, Carpenter 2003). In addition to fundamental interactions between obesity and estrogen levels, obese women tend to have larger breasts, increasing mammography image quality problems and potentially hindering cancer detection.

Lifestyle risk factors include alcohol consumption and cigarette smoking. Alcohol influences estrogen levels, generates toxic metabolites, and hinders DNA repair (Colditz 2004, Longnecker 1994, Smith-Warner 1998, Feigelson 2003, Feigelson 2001, Ross 2005). There is no conclusive evidence concerning the relationship between age at initiation of drinking habits and breast cancer risk (Okasha 2003). Heavy and prolonged smoking, as well as initiation of smoking habits during adolescence when breasts are developing, both result in increased breast cancer risk (Reynolds 2004, Key 2001, Colditz 2004, Okasha 2003). It is interesting to note that current smoking by women with a family history of breast cancer does not further increase risk, whereas current smokers without such a family history have increased breast cancer risk (Reynolds 2004). Passive

second-hand smoke exposure does not appear to increase breast cancer risk (Reynolds 2004, Okasha 2003).

Additional lifestyle risk factors include physical fitness and diet. Although lifetime exercise has the greatest breast cancer preventative effect, high levels of activity later in life is the greatest contributor to risk reduction, particularly for women without a family history of breast cancer (Friedenreich 2001, Friedenreich 2004, Carpenter 2003). The mechanism by which exercise reduces breast cancer risk is thought to be related to reduced obesity as well as alterations in hormone levels caused by regular exercise (Bernstein 1992). Recent research has explored the possible breast cancer protection and promotion effects of various nutrients. Current evidence shows that there are subgroups of women for which diet has a more pronounced effect on breast cancer risk, suggesting variable diet-gene interactions (Rock 2000). According to some researchers, calcium, vitamin E, and fiber are suspected to have age-specific protective roles against the development of breast cancer (Rock 2000, Okasha 2003). Moreover, there is a protective effect of an overall restricted caloric intake (Okasha 2003).

Adolescents who begin menstruation before 12 years of age have a 30% increased breast cancer risk than those beginning after the age of 15 (Kelsey 1993, Ma 2006, Althuis 2004, Bernstein 1987). Each full-term pregnancy poses a short-term increased cancer risk due to increased hormone levels, yet the long term effect is protective (Ma 2006, Rosner 1996, Althuis 2004). Younger age at first childbirth and breastfeeding are protective (Ma 2006, Althuis 2004). Preeclampsia, a characteristically reduced level of estradiol during later stages of pregnancy, has a protective effect against breast cancer for a female baby, while evidence suggests fraternal twins, high birth weight, and severe

nausea during pregnancy increase risk for a female baby (Potischman 1999, Okasha 2003).

Low-dose radiation, such as that delivered in medical imaging applications, exhibits a linear dose-response with no threshold below which the probability of biologic effects is zero (Bushberg 2002, Upton 2003). This is due to cross-linking of DNA proteins, DNA backbone breakage, DNA nucleotide base damage, free radical generation, or any combination of such effects, summarized in Figure 2.4 (Upton 2003). When such damage is survivable and occurs in the presence of compromised DNA repair mechanisms, the daughter cells inherit aberrant genetic information, leading to cellular disregulation and a linear increase in frequency of cancer precursors and certain types of cancers (Upton 2003).

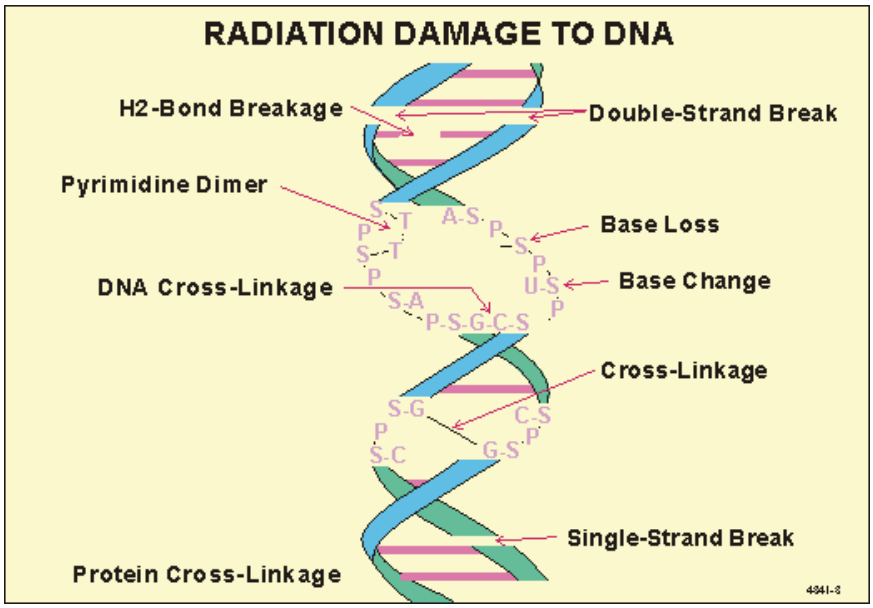

FIGURE 2.4: Radiation Damage to DNA. Radiation exposure can induce direct and indirect damage to DNA, such as backbone breakage, bond and crosslink disruption, incorrect crosslinking, base loss, and base change. Reprinted with kind permission from Scott BR, www.radiation-scott.org/radsource/3-0.htm, 2006.

A study by Berrington de Gonzalez and Darby suggested that the use of diagnostic x-rays in all medical applications increased total cancer risk by approximately

0.9% (2004). For women aged 50 to 69, the ratio of induced to prevented cancers due to conventional mammographic screening is approximated to be 1:242, but for women aged 40 to 49, this ratio is estimated to fall to 1:8 (Beemsterboer 1998). Thus, it is important to decrease the amount of radiation dose a patient receives when obtaining mammographic images in order to optimize the risk-benefit ratio.

2.7 Breast Cancer Prevention

Reducing breast cancer risk factors and regular screening have traditionally been the only breast cancer preventive measures. However, chemopreventive drugs and breast cancer vaccines are under development, potentially offering primary breast cancer prevention. The goals of both are to prevent or delay invasive breast cancer development without excessive undesirable side effects. Even though many laboratory trials have shown early promise, extensive breast cancer chemoprevention or vaccination trials in healthy women with normal risk of breast cancer have not yet been performed due to concerns over safety. Further, only women with high risk of breast cancer or with a current cancer diagnosis have been included in trials, limiting the generalization of the results. (Senn 2008)

Antiestrogen pharmaceuticals have been widely used to treat breast cancer, and recent clinical trials demonstrated their potential as chemopreventive agents. The National Surgical Adjuvant Breast and Bowel Project (NSABP) P-1 Study accrued over 13,000 women at increased risk of breast cancer development and administered tamoxifen (TAM) over the course of five years, demonstrating a 50% reduction in both invasive and DCIS cancers over the placebo control. Even in the face of serious side effects, including increased risk for thromboembolic events and endometrial cancer, the

data suggests that TAM chemoprevention might benefit certain subsets of women, including women under the age of 50, women with a history of DCIS or other atypical lesions, and women with BRCA1/BRCA2 mutations. (Fisher 1998, Fisher 2000, Fisher 2005)

Raloxifene (RAL), which has similar pharmacokinetics as TAM, was compared to TAM as a chemopreventive agent in the NSABP P-2 Study of Tamoxifen and Raloxifene. Interestingly, RAL only demonstrated a reduction in invasive cancer development, but has the advantage of being slightly less chemotoxic. Although the Food and Drug Administration (FDA) has approved both TAM and RAL for use as chemopreventive agents, neither is widely prescribed. (Vogel 2006)

Aromatase inhibitors (AIs) have also been used to treat breast cancer, with a clinical trial including 6,000 postmenopausal women underway to test the ability for this type of drug to act as a chemopreventive (Cuzick 2005). AIs do not carry the same risk of thromboembolytic events or endometrial cancer, but do have deleterious effects on bones without concurrent bone-health restorative therapy (Cuzick 2005). Another pharmaceutical category evaluated as a chemopreventive agents are statins. Although statins demonstrated promise as chemopreventatives in both *in vitro* and *in vivo* laboratory trials, meta-analysis of several clinical trials did not find an effect for reducing mortality from breast cancer in general (Seeger 2003, Alonso 1998, Bonovas 2005).

With growing understanding of the carcinogenic process, some researchers are evaluating the feasibility of breast cancer vaccines. Theoretically, these vaccines would allow the body to recognize and destroy cancerous cells. Most vaccines currently under development use antigens to prime the immune system, but have very low success rates

due to limited antigen expression in the tumor, antigen expression in regions protected from vaccine exposure, heterogenous tumor antigen exposure throughout tumor volume and throughout tumor development, and limited ability of the tumor microenvironment to mount an immune response. (Mittendorf 2007)

Prophylactic vaccines can sometimes be engineered against an infectious agent that causes disease, such as the recent clinical implementation of routine HPV vaccinations in young women that prevent certain types of cervical cancers. However, no infectious agent has definitively been associated with breast cancer development. Instead, antigens that have been considered for breast cancer vaccine include HER-2/*neu*, MUC-1, carcinoembryonic antigen, hTERT, p53, mammaglobin A, and cancer-testis antigens. No breast cancer vaccines have been studied in large, robust clinical trials within a generalizable population. (Mittendorf 2007)

Women at very high risk for breast cancer development would likely benefit the greatest from such forms of breast cancer prevention since the only other primary preventive measure is a prophylactic bilateral mastectomy. Because most chemoprevention and breast cancer vaccines are still under development, and others available in the clinic are not routinely implemented, the threshold risk level to balance the side effects has not yet been established. Much more research is required in the field of primary breast cancer prevention.

2.8 Summary

Although molecular approaches to breast cancer detection and treatment are rapidly progressing, too much remains unknown about breast cancer carcinogenesis for primary prevention. Conventional mammographic screening depends on the detection of

structural changes through images based on x-ray interaction with matter. However, it is clear that there are measurable molecular changes indicative of cancerous disease processes well before structural abnormalities become radiographically apparent. The future of breast imaging might harness these biomarkers to detect and treat only those precancerous and malignant lesions which pose a threat.

CHAPTER 3: X-RAY INTERACTION WITH MATTER

3.1 Overview

A general understanding of x-ray physics and how x-rays interact with matter facilitates understanding the differences between x-ray absorption and x-ray refraction as it pertains to medical imaging. Clinical x-ray imaging is almost exclusively based on x-ray absorption. The following discussion reviews atomic structure, photon characteristics, x-ray transmission, the photoelectric effect and x-ray absorption, x-ray scatter, x-ray refraction, and several distinct types of radiation production. Together these provide a foundation for understanding diffraction-enhanced imaging, which implements refraction-based image contrast.

Electromagnetic radiation includes radio waves, x-rays, light, and gamma rays, shown in Figure 3.1. Radiation can be non-ionizing, directly ionizing, or indirectly ionizing. Diagnostic imaging uses indirectly ionizing x-rays where an electron is released in the object, then this released electron transfers energy into the object (Podgoršak 2006). Ionizing radiation exposure to human tissue components is dangerous because tissues have low ionization energies ranging from 5 eV to 20 eV, disrupting the covalent bonds of many organic materials (Sprawls 1993).

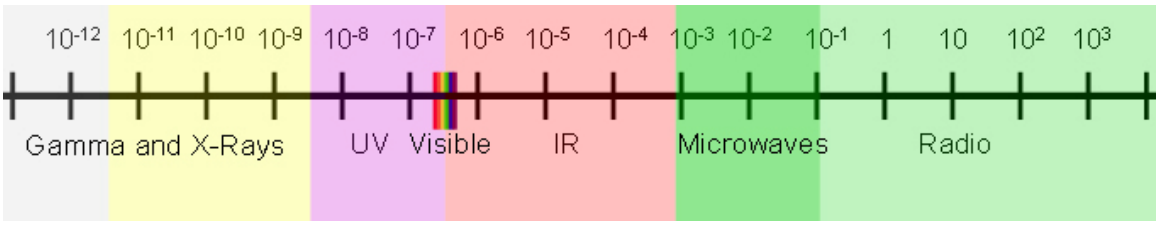

FIGURE 3.1: Electromagnetic Radiation Spectrum. The electromagnetic spectrum is composed of gamma rays, x-rays, ultraviolet (UV)-rays, visible light, infrared radiation (IR), microwaves, and radio waves. It is measured in wavelength, with units of meters.[2]

There are three categories of x-ray interaction with matter: transmission without interaction, complete absorption, and scatter. Together, absorption and scatter are said to attenuate an x-ray beam. Scatter includes a wide variety of interactions including reflection, refraction, elastic scatter (without energy transfer), and inelastic scatter (with some degree of energy transfer). All such interactions must satisfy the physical laws of conservation of energy, momentum, and electric charge.

3.2 Atomic Structure

The Bohr atomic model describes atomic structure, with protons and neutrons contained within the nucleus, while electrons circle the nucleus in designated orbits, referred to as shells. Each element has a unique atomic number (Z) equal to the number of protons in the atom. For a neutral atom, Z also equals the number of electrons. For inhomogeneous materials, effective atomic numbers (Z_{eff}) can be calculated, with several Z_{eff} values relevant to medical imaging shown in Table 3.1. Electron shells contain a maximum number of electrons, given by $2n^2$, where n is the quantum number of the shell. For example, the maximum number of electrons in the K-shell is two, eight in the L-shell, 18 in the M-shell, and 32 in the N-shell. (Bushberg 2002)

2. This figure was compiled using the following sources: Sprawls 1993, Podgoršak 2006, Ikeda 2004, Bushberg 2002.

Material	Z_{eff}	Density
Air	7.64	0.00
Water	7.42	1.00
Fat	5.92	0.91
Muscle	7.46	1.00
Bone	11.6	1.65

TABLE 3.1: Physical Properties of Biological Materials. Values listed for water and fat are representative of those obtained with soft tissue imaging. Physical density (measured in g/cm^3) and effective atomic number (Z_{eff}) values do not vary greatly for components of soft tissue, posing challenges for medical imaging.

Electron binding energies increase with distance from the nucleus. Electrons can move to higher or lower energy shells with addition or release of energy, respectively. K-shell electrons of intermediate and high Z materials have binding energies within the range of diagnostic imaging, giving rise to the phenomenon of K-edges when a photon interacts with an atom at an energy just above its shell-specific binding energy and ionizes the atom. Such absorption edges can occur with all electron shells, and are referred to as L-edges, M-edges, etc. This creates a large but transient increase in the attenuation coefficient at this energy, causing a temporary increase in photoelectric absorption. (Bushberg 2002)

3.3 The Photon

A photon, the smallest unit of electromagnetic radiation, is defined as an individual particle of no mass, with energy (E, measured in units of eV), wavelength (λ, measured in units of m), and frequency (v, measured in units of s^{-1}):

$$E = hc / \lambda \quad (1)$$
$$\lambda = c / v \quad (2)$$
$$v = E / h \quad (3)$$

where h is Planck's constant (4.13566733 x 10^{-15} eV·s) and c is the speed of light in a vacuum (2.99792458x10^8 m·s^{-1}). Photon radiation can be characterized by either the

particle model or the wave model, which are complementary to each other at this size range. Radiation wave characteristics are amplitude, wavelength, frequency, and period. Radiation particle characteristics consider individual photon quanta with a specific energy. For example, the Compton effect is explained by the particle model and x-ray diffraction is characterized by the wave model. (Bushberg 2002, Podgoršak 2006)

X-rays, composed of many photons, are characterized by their average energy as either hard (high energy) or soft (low energy). Medical imaging primarily utilizes hard x-rays between 20 and 70 keV because they are soft enough to allow absorption, while a sufficient number of photons can still effectively penetrate the body to create image contrast. X-rays become harder as they travel through a medium because lower energy x-rays are absorbed, resulting in a lower-intensity x-ray beam with higher average photon energy. Hardness is quantified by half-value layer (HVL), describing the amount of material an x-ray penetrates before half the photon's energy has been absorbed:

$$\mathrm{HVL} = 0.693 / \mu \tag{4}$$

where μ is the linear attenuation coefficient. HVL is derived from the Beer-Lambert attenuation equation:

$$I = I_0 \, e^{-\mu x} \tag{5}$$

where I is the resulting intensity, I_0 represents initial intensity, and x is the specific half-value layer to be calculated. (Bushberg 2002)

3.4 X-Ray Transmission

There must exist sufficient differential attenuation such that photons interact with the object and are transmitted to expose the detector to create image contrast. The

probability that a photon traverses an object without interaction is described by the following equation:

$$e^{-\mu x} = (e^{-\omega x})(e^{-\tau x})(e^{-\sigma x})(e^{-\kappa x})(e^{-\pi x}) \quad (6)$$

where the linear coefficients are as follows: ω is coherent scatter, τ is photoelectric absorption, σ is Compton scatter, κ is pair production, π is photodisintegration, and x is path length within the sample. For soft tissue imaging energies, the effects of coherent scatter, photodisintegration, and pair production do not contribute substantially to x-ray interactions with matter. (Hendee 2002)

Thus, the total linear attenuation coefficient (μ) is the sum of τ and σ, depending on *hv*, *Z*, and physical density (ρ), and can be calculated by the following formula:

$$\mu = (1 / \Delta x) \log [(N_0 - n) / N_0] \quad (7)$$

where n is the number of photons removed from the incident beam, N_0 is the number of incident photons, and Δx represents object thickness. The change in μ is not linear as object thickness increases. The mean path length an x-ray travels within an object, referred to as relaxation length, is described by μ^{-1}. A related value is the mass attenuation coefficient, which is equal to μ / ρ. Beam hardening with polychromatic x-rays affects the estimation of μ, requiring calculation of an effective linear attenuation coefficient (Bushberg 2002, Hendee 2002):

$$\mu_{eff} = \ln 2 / HVL \quad (8)$$

3.5 The Photoelectric Effect and X-Ray Absorption

With the photoelectric effect, a tightly-bound electron completely absorbs a photon, ejecting the electron (now referred to as a photoelectron) and ionizing the atom. The ejected photoelectron possesses kinetic energy (E_K) described as follows:

$$E_K = h\nu - E_B(K) \quad (9)$$

where $E_B(K)$ is the binding energy of the K-shell electron and $h\nu$ is the energy of the incident photon. A cascade of electrons from outer energy shells fills the vacancy created by the ejection of the photoelectron, emitting energy in the form of either characteristic radiation or an Auger electron, with an energy equal to the difference in binding energies between the shells. (Podgoršak 2006, Bushberg 2002, Hendee 2002)

The photoelectric effect, summarized in Figure 3.2, increases with increasing Z and decreasing photon energy. Photoelectric absorption still occurs at high x-ray energies where absorption edges exist, decreasing from absorption edges proportionally as:

$$1 / (h\nu)^3 \quad (10)$$

where $h\nu$ is the photon energy. However, for the primary elements in human tissue (hydrogen, carbon, nitrogen, and oxygen), the K-shell absorption edges all occur below 1 keV. (Sprawls 1993, Podgoršak 2006, Bushberg 2002, Hendee 2002)

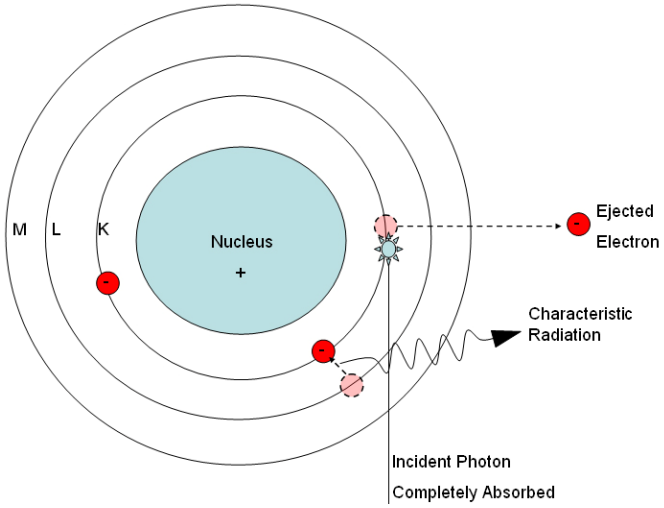

FIGURE 3.2: The Photoelectric Effect. An incident photon is completely absorbed by an electron, ejecting the electron at approximately 90°. An electron from a shell further from the nucleus moves to the closer shell to fill the vacancy, releasing either characteristic radiation or an Auger electron. This electron cascade continues until the vacancy is located in the outermost shell.[3]

3. This figure was compiled using the following sources: Sprawls 1993, Podgoršak 2006, Bushberg 2002.

3.6 X-Ray Scatter

Scatter occurs due to interatomic spacing, deflecting a photon from an atom with (inelastic) or without (elastic) energy transfer. Porod's Law states that scattering intensity increases with sample non-uniformity and that multiple scatter events increase with Z and sample thickness. Scatter relevant to x-ray imaging is nonresonant, varying smoothly with photon energy. Several categories of scatter include ultra-small angle scatter (USAXS) occurring with structure sizes on the scale of 100's of nanometers to several microns, small angle scatter (SAXS) occurring with supramolecular structures ranging from 10 to 100 nm in size, and wide angle scatter (WAXS) occurring with interatomic distances of several nanometers. While these categories depend on scattering particle size, Rayleigh, Compton, and Thomson are specific types of x-ray scatter with unique physics. Each has a distinctive role in specific applications of medical imaging.[4] (Kidane 1999, Fernández 2002, Fernández 2005, Bushberg 2002, Hendee 2002, Podgoršak 2006)

Rayleigh scatter is an elastic scattering process in which a low energy incident photon scatters in a random direction from an orbital electron without inducing a change in its wavelength, energy, or frequency and without ionizing the atom. Rayleigh scatter occurs when the scattering particle is small in comparison to the x-ray wavelength. On the other hand, Compton scatter is an inelastic scattering process that occurs when a photon scatters from a loosely bound outer-shell electron, imparting some of its energy to eject the electron, now referred to as a Compton or recoil electron, before continuing on an altered path with decreased energy. The recoil electron is absorbed near the site of interaction, whereas the scattered photon does not necessarily interact again at a nearby

4. For an exhaustive mathematical treatment of scattering, please refer to van de Hulst 1981.

site. Rayleigh and Compton scatter are diagramed in Figure 3.3. (Bushberg 2002, Hendee 2002, Podgoršak 2006, Sprawls 1993)

Compton scatter is the dominant contribution to x-ray attenuation at energies between 30 keV and 30 MeV. Because Compton scatter does not decrease as rapidly as the photoelectric effect with increasing photon energy and atomic number, Compton scatter predominates for low Z materials, such as soft tissue, when imaged at high x-ray energies. For example, Compton scatter and photoelectric interactions occur with about the same rate at 30keV. (Bushberg 2002, Hendee 2002, Podgoršak 2006, Sprawls 1993).

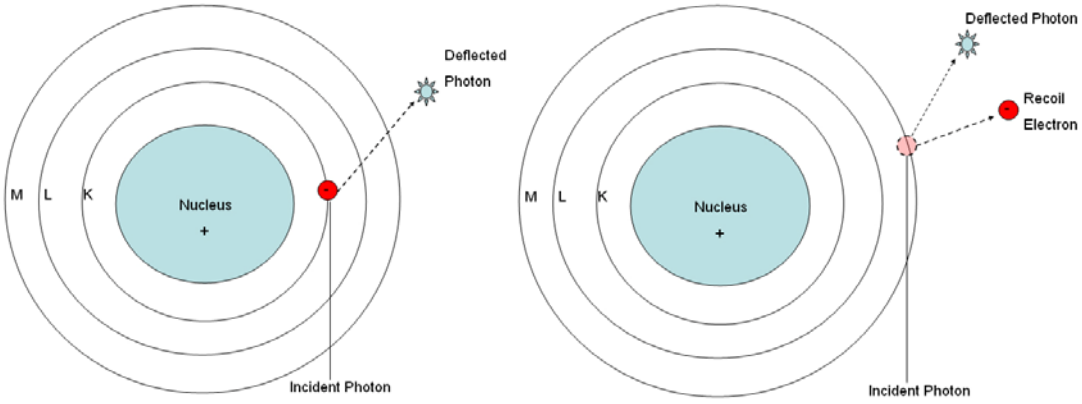

FIGURE 3.3: Rayleigh and Compton Scatter. On the left, Rayleigh scatter is produced when a low-energy incident photon is deflected from a tightly-bound electron yet does not change energy, wavelength, or frequency. The orbital electron is not dislodged from its shell. On the right, Compton scatter occurs when an incident photon strikes an outer-shell electron, deflecting the photon and ejecting the electron. The deflected photon has a reduced energy, equal to the binding energy that was required to eject the electron. The deflection angle of the photon after a Compton scattering event is related to photon energy.[5]

Thomson scatter, or forward scatter, is an elastic process and dominates as the scattering particle size increases and with high x-ray energies far from absorption edges,

5. This figure was compiled using the following sources: Sprawls 1993, Podgoršak 2006, Bushberg 2002.

scattering photons at approximately 0°. The intensity of forward-scattered photons decreases as:

$$I = I_0 \exp(-x / \lambda_S) \quad (11)$$

where x is the x-ray path length and λ_S is the scattering mean free path (Michna 2005, Authier 2001). Forward scatter forms the basis of x-ray diffraction. Diffraction from the atoms of perfect crystals allows x-ray refraction effects to be separated from attenuation for analyzer-based phase contrast imaging (discussed thoroughly in section 6.10 and chapter 8). (Hendee 2002, Podgoršak 2006)

3.7 X-Ray Refraction

Refraction occurs due to differences in density and thickness, with the greatest intensity at interfaces between tissues with different molecular structures, as shown in Figure 3.4. The refractive index is given by the following:

$$n = 1 - \delta + i\beta \quad (12)$$

where β represents x-ray absorption and δ is the phase shift due to scattering. This phase shift is described by:

$$\delta = (N \lambda^2 r_e) / 2\pi \quad (13)$$

where r_e is the classical electron radius, $2.8179402894 \times 10^{-15}$ m, and N is the number of electrons per unit volume. The formula for calculating the electrons per unit volume is:

$$N = (N_A \rho) / A \quad (14)$$

where N_A is Avogadro's Number ($6.02214179 \times 10^{23}$ atoms/mole), ρ is physical density (measured in kg/m^3), and A is the atomic mass (measured in kg/mole). The x-ray refractive index is always approximately unity, and deviations are usually very small, on the order of microradians. (Suortti 2003, Kiss 2003, Hasnah 2005)

Snell's law, depicted in Figure 3.4, describes x-ray refraction at interfaces:

$$n_1 \sin\theta_1 = n_2 \sin\theta_2 \qquad (15)$$

where n_1 is the refractive index of the medium, n_2 is the refractive index of the sample, θ_1 is the incident angle, and θ_2 is the refraction angle. The specific refraction angle at a linear interface is calculated by:

$$\Delta\theta_z \approx \Delta\delta \tan\theta_1 \approx \partial/\partial x \int_L n(x,y,z)dz \qquad (16)$$

where $\Delta\delta = n_1 - n_2$ (difference in refractive indices), L is the approximately straight path traversed by the beam, (x,y) are the spatial coordinates of the image domain, and (z) is the spatial coordinate along x-ray propagation. This derivative creates an edge-enhancement effect without the quantum noise sensitivity that plagues post-processing filtering or sharpening algorithms that provide computerized edge-enhancement. (Suortti 2003, Kiss 2003, Hasnah 2005)

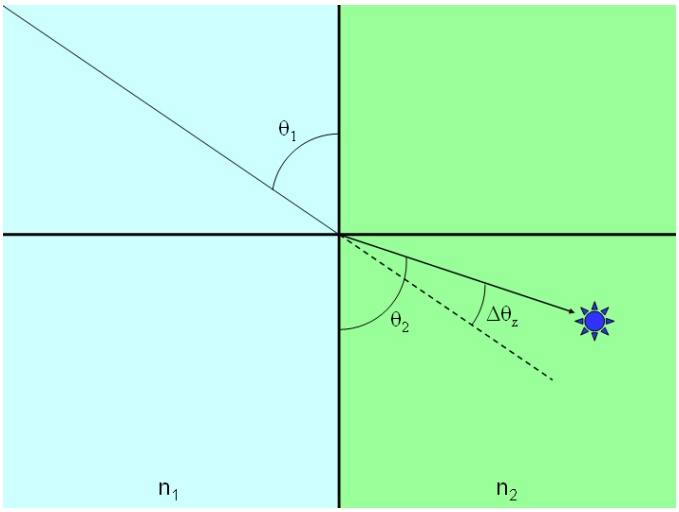

FIGURE 3.4: X-Ray Refraction. As an incident photon travels from a medium with a refractive index n_1 to a material of a different refractive index n_2, the direction of propagation will be slightly altered due to a change in photon wavelength, referred to as refraction. θ_1 is the incident angle, θ_2 is the refraction angle, and $\Delta\theta_z$ is the deflection angle. X-rays refract directionally above or below the plane of the incident x-ray beam.[6]

6. This figure was compiled using the following sources: Sprawls 1993, Podgoršak 2006, Bushberg 2002.

3.8 Generation of X-Rays

Similar to photon interactions with atoms, electrons can interact with atoms to produce electromagnetic radiation by bremsstrahlung, characteristic, or synchrotron processes. X-ray tube sources generate bremsstrahlung and characteristic radiation while synchrotron sources generate a broad range of radiation through synchrotron radiation (SR). The generated radiation diverges to cover a larger area with reduced intensity away from its source according to the inverse-square law. This law states that the intensity decreases proportionally with the inverse of the square of the distance from the source. Intensity (photon flux, φ) is defined as the number of photons delivered to a specific area (photon fluence, Φ) within a specific time (measured in watts/cm^2):

$$\varphi = \Phi/t = N/(A\ t) \qquad (17)$$

where t represents time, N is the number of photons, and A is the exposed area. Exposure is proportional to fluence at a specific x-ray energy and is measured in Roentgen (R) or Coulomb/kg (C/kg). (Sprawls 1993, Bushberg 2002)

Bremsstrahlung radiation, also referred to as white radiation, is generated by Coulomb interactions when negatively charged electrons are deflected by orbital electrons or positively charged atomic nuclei, shown in Figure 3.5. When an electron is deflected, part of the kinetic energy is released as electromagnetic radiation. The energy of the emitted radiation depends on the energy of the incident electron and the distance between the orbital electron and the nucleus. (Bushberg 2002, Podgoršak 2006)

Bremsstrahlung radiation is intrinsically a continuous polychromatic spectrum with maximum photon energy equal to the energy of the incident electron. Such polychromatic radiation sources have an effective beam energy of approximately 30% of

the peak energy. This variability leads to a bell-shaped curve describing photon fluence. Production of bremsstrahlung radiation is more efficient at higher electron energies. (Bushberg 2002, Podgoršak 2006)

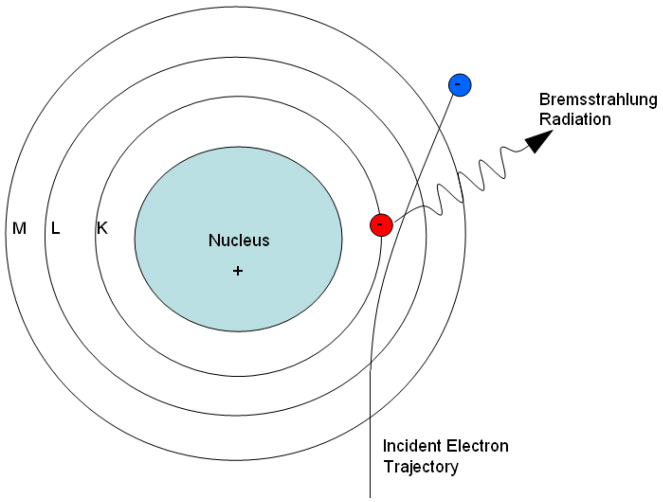

FIGURE 3.5: Bremsstrahlung Radiation. Bremsstrahlung radiation can be emitted when an incident electron trajectory is bent by either the repulsive force of an orbital electron or the attractive force of the nucleus. The energy of the emitted radiation depends on the incident electron energy as well as the orbital electron binding energy.[5]

Characteristic radiation, depicted in Figure 3.6, is also referred to as fluorescent radiation. Characteristic radiation emission occurs when electrons move between atomic shells to fill vacancies created when an electron collides with an atom with enough energy to overcome the binding energy of one of the atom's electrons, removing it from the atom. (Bushberg 2002, Podgoršak 2006)

Electrons rearrange between atomic shells to return to a lower energy ground state, emitting either Auger electrons or characteristic radiation in spikes of intensity equal to the difference in binding energies of the shells involved in the cascade. Radiation emitted from electrons cascading from the next closest shell to a vacancy in the K-shell is referred to as K_α and radiation emitted from electrons from the second closest shell is referred to as K_β, and so forth. Auger electron production competes with characteristic x-ray generation, especially for elements of low Z. Fluorescent yield describes the

probability that an electron cascade will result in characteristic radiation emission. (Bushberg 2002, Podgoršak 2006)

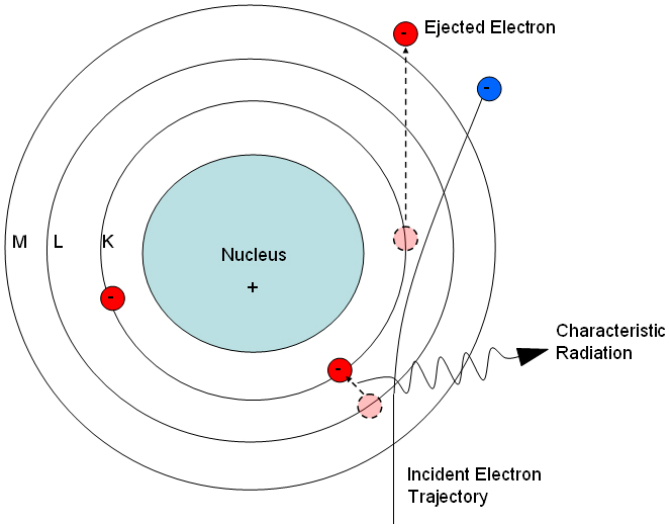

FIGURE 3.6: Characteristic Radiation. An incident electron ejects an orbital electron, releasing energy as either characteristic radiation or an Auger electron. An electron cascade fills the vacancy created by the ejected electron.[5]

Synchrotron radiation (SR) is created when an electron is accelerated to nearly the speed of light and forced to traverse a circular orbit within a magnetic field, depicted in Figure 3.7. The magnetic field causes acceleration by the Lorentz force and subsequent photon emission. The Lorentz force is described by the following equation:

$$F = q\,[E + (v \times B)] \qquad (18)$$

where F is the force in Newtons, E is the electric field in volts/meter, v is the magnetic field in teslas, q is the electric charge in coulombs, and x is the mathematical operator representing the cross product. SR is polychromatic and contains radiation throughout the entire electromagnetic spectrum, with the peak emitted wavelength linearly proportional to the radius of the accelerating particle's path. SR radiation is intense, spatially coherent, and highly collimated throughout the entire spectrum. (Margaritondo 1988, Podgoršak 2006, Arfelli 2000, Suortti 2003, Meuli 2004, Margaritondo 2003)

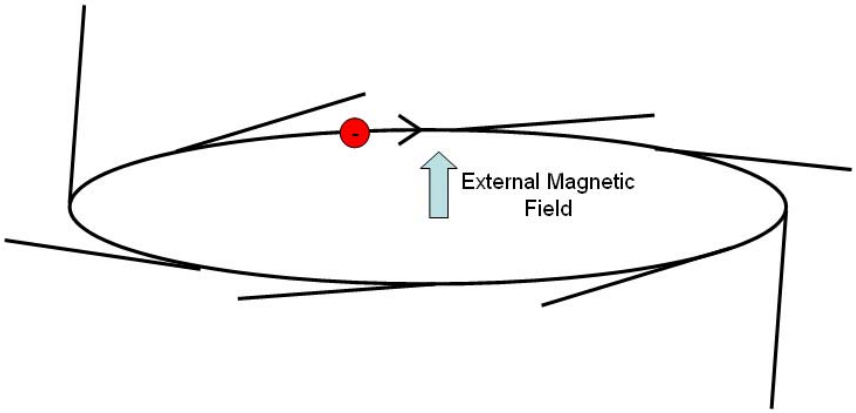

FIGURE 3.7: Synchrotron Radiation. A bending magnet synchrotron x-ray source as shown above generates a highly coherent fan beam over a broad range of wavelengths. Electrons orbit a circular storage ring in the (x,y) plane at nearly the speed of light. These orbiting electrons are exposed to a magnetic field in the (z) plane, causing radiation emission due to the Lorentz force. The emitted radiation can be accessed at many points along the orbit, referred to as beamlines, as shown by the lines radiating from the storage ring.[7]

3.9 Summary

X-rays can interact with matter in a variety of ways, leading to unique image quality considerations for different x-ray imaging modalities. There is always a noise-resolution tradeoff in medical x-ray imaging systems, which depends on the fundamentals of x-ray interactions with matter discussed in this chapter.

7. This figure was compiled using the following sources: Bushberg 2002, Margaritondo 1988.

CHAPTER 4: IMAGE QUALITY

4.1 Overview

Image quality describes how accurately a radiographic image reflects physical object features (distortion) without introducing image features not representative of a true object feature (artifacts). It is often considered and measured within a relevant clinical imaging task. Image quality factors must be balanced with important clinical parameters such as radiation dose and image acquisition time. Contrast, blur, magnification, resolution, noise, and dose are several factors influencing image quality, and are affected by imaging parameters such as intensity, exposure, and detector characteristics.

4.2 Factors Influencing Image Quality

Object or subject contrast is derived from inherent properties of the object or subject being imaged, such as gradients in ρ, Z, or thickness that alter the transmission of x-rays. X-rays detected and displayed as image contrast depend on intrinsic object contrast as well as imaging parameters such as radiation penetration, scatter, and detector characteristics. Image contrast is the visible difference in exposure between one pixel and its neighboring pixels. It is useful to consider both area contrast generated by a large feature and boundary contrast generated at an interface between features. Contrast response, described by the contrast transfer function (CTF), illustrates the ability of an imaging modality to resolve objects of increasing size. (Sprawls 1993, Bushberg 2002)

Blur, or unsharpness, quantifies the amount a defined point in an object is spread out within the image. Blur occurs due to the physical characteristics of the object, object

motion, imaging system design characteristics, and detector characteristics.

Magnification (M):

$$M = \frac{\text{image size}}{\text{object size}} = \frac{\text{source-to-detector distance}}{\text{source-to-object distance}} \quad (19)$$

may increase visibility, particularly for small regions of interest, by increasing the size of the region of interest while decreasing the field of view. However, magnification does not increase intrinsic resolution and can increase blur. (Sprawls 1993, Bushberg 2002)

Spatial resolution describes the separation of fine details and can be measured using a test object of parallel lines with increasing spatial frequency. Detector pixel size, x-ray focal spot size, source-to-sample distance, and source-to-detector distance all influence the spatial resolution. Spatial resolution is quantified by the Modulation Transfer Function (MTF), Point Spread Function (PSF), Line Spread Function (LSF), and Edge Spread Function (ESF). The Signal-to-Noise Ratio (SNR) allows comparison of true image information and noise:

$$SNR = (I - I_{min}) / \sigma \approx \sqrt{(N_{det})} \quad (21)$$

where I is the intensity, I_{min} is the minimum intensity, σ is noise, and N_{det} is the number of photons detected within a specific pixel. The detective quantum efficiency (DQE) has emerged as a valuable representation of how the imaging system affects the SNR, and quantifies the ability to detect small, low-contrast objects:

$$DQE = (SNR_{out} / SNR_{in})^2 \quad (20)$$

where SNR_{out} is the SNR output by the imaging system and SNR_{in} is the SNR received by the imaging system. (Hendee 2002, Sprawls 1993, Bushberg 2002)

Most noise in x-ray imaging is quantum noise but there is also noise associated with the structure of the object being imaged and with specific components of a particular

imaging system. Quantum noise occurs because a limited number of photons emitted from an x-ray tube with statistical Poisson distribution become incident to the detector with a random distribution. An example of structure noise is the image information due to x-ray attenuation by normal breast parenchyma such as fat and connective tissue, contributing unimportant information to the image and consequently decreasing contrast of desired features. Certain noise sources are universal to all x-ray imaging modalities, but compensatory design features introduce differences in how the noise influences image quality for particular clinical tasks. (Sprawls 1993, Bushberg 2002)

Another useful comparison quantifying the effect of noise on image quality is the signal-difference-to-noise ratio (SDNR):

$$SDNR = \frac{N_{ROI} - N_{back}}{\sigma_{ROI} - \sigma_{back}} \qquad (22)$$

where N_{ROI} is the signal within a region of interest, N_{back} is the signal within a background region, σ_{ROI} is the noise within a region of interest, and σ_{back} is the noise within a background region (Pisano 2004). Although noise is a major image quality issue, it typically only notably reduces visibility of low contrast objects. Rose's criterion states that in order to reliably identify an object in an image, the SNR or SDNR must be greater than or equal to five (Bushberg 2002). Many digital processing techniques exist to reduce the visibility of noise, including blurring, integration over time, and averaging. (Sprawls 1993)

All current clinical x-ray imaging requires differential attenuation of x-rays to create image contrast, typically through absorption. This fundamentally implies delivery of a radiation dose to the object being imaged. Greater exposure on the detector means

greater SNR, but also greater radiation dose. Absorbed radiation dose is measured in grays (Gy) or rads and can be calculated with the following formula:

$$\text{Dose} = E / m \tag{23}$$

where E is absorbed energy (measured in Joules) and m is mass (measured in kg). Mean glandular dose (MGD) quantifies the amount of ionizing radiation received by glandular tissue. Absorbed dose equivalent, a weighted estimate of actual damage caused by radiation exposure, is measured in Sieverts (Sv) or rem. The dose equivalent is found by multiplying dose by a quality factor that depends on the radiation's linear energy transfer (LET) function and weighting factors specific to various tissue radiation damage sensitivities. (Bushberg 2002, Podgoršak 2006, Hendee 2002)

4.3 Summary

Excellent image quality facilitates an observer's ability to detect features important for a clinical diagnosis. Accurate portrayal of object structure or function without artifacts and noise allows excellent contrast and resolution. All imaging systems optimize imaging protocols to maximize image quality, but for some imaging modalities, such as conventional and digital mammography, this often comes with a cost of increased subject radiation dose.

CHAPTER 5: SCREEN-FILM AND DIGITAL MAMMOGRAPHY

5.1 Overview

Fewer than 20 years after Wilhelm Roentgen discovered x-rays in 1895, rudimentary mammographic imaging was performed by Albert Salomon. The American College of Radiology was founded in 1923. Mammography as a subspecialty emerged in the 1960's but routine screening mammography was not implemented in the clinic until the 1970's, after the Breast Cancer Detection Demonstration Project generated widespread interest among women and recommendation from physicians. This chapter first presents the development of mammography and the fundamental principles of mammography before discussing mammographic system components. This is followed by a discussion of several novel developments, such as monochromatic mammography, computer-aided diagnosis, and contrast-enhanced mammography. (Lerner 2001, Law 2006)

5.2 Mammography Fundamentals

Mammographic imaging equipment and image interpretation were standardized through the Mammography Quality Standards Act and the Breast Imaging Reporting and Data System (BI-RADS), respectively. This standardization, along with dramatic improvements in detector technologies, has allowed mammography to remain the dominant breast imaging modality even among the development of many cutting-edge breast imaging technologies. (Lerner 2001)

The majority of evidence suggests a benefit from mammographic screening for women with normal breast cancer risk between the ages of 50 and 69 (Kopans 2007). Mammography is relatively insensitive for cancer detection in younger women with dense breasts, and detection of breast cancers within women over the age of 70 does not significantly extend life expectancy (Ostbye 2003). The sensitivity of mammography has been reported to range from 54 to 94%, with breast density strongly affecting sensitivity (Kopans 1992). Mammography is intended to accurately detect and diagnose breast abnormalities and cancers.

Screen-film mammography (SFM) and digital mammography (DM) image contrast is based on photoelectric absorption, depending on differing photon flux through the object. Photons are attenuated due to variations in stromal and epithelial breast components, giving rise to the radiographic appearance of the normal and abnormal breast. Compton scatter is significantly produced at mammographic imaging energies, leading to image degradation without compensatory design features such as collimators and anti-scatter grids which subsequently decrease detector exposure and increase dose requirements.

Both SFM and DM perform better at lower x-ray energies because decreasing x-ray energy increases photoelectric absorption and decreases the contribution of scatter. However, low-energy x-rays are more readily absorbed, requiring greater flux for sufficient x-ray detection and consequently greater patient radiation dose. A typical mammographic image delivers between 1 and 3 mGy MGD per view. In the United States, a patient typically receives at least two views per breast through an annual screening protocol. Additional views are sometimes recommended for women with large

breasts, or when image artifacts or structural noise either create or appear to obscure a region of interest, or when potential abnormalities are detected. (Hendee 2002, Ikeda 2004, Brenner 2002, Young 2000)

Much of the DM system setup is the same as SFM except for fundamentally distinct x-ray detection and display technologies. A general mammography system diagram is shown on the left in Figure 5.1 with contrasting features of SFM and DM shown on the right. SFM implements a cassette and screen-film combination to convert x-rays to light with an intensifying screen and expose film. DM uses digital detector technology to detect individual photons directly or to convert x-rays into light with detection of the light produced.

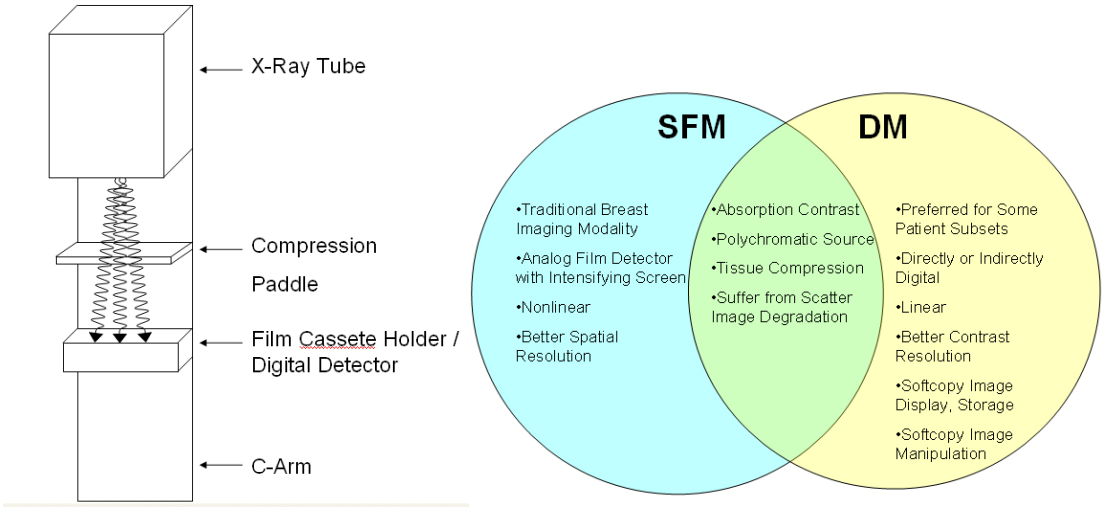

FIGURE 5.1: Mammography Unit Diagram and Comparison of SFM and DM. On the left, the system diagram shows the main components of both the SFM and DM modalities. The fundamental difference between SFM and DM is the image receptor and display system where for SFM, photons are detected using a screen-film combination and for DM, photons are captured using a digital detector. SFM images are displayed on x-ray film, whereas DM images are inherently digital and are typically viewed on a softcopy review workstation, but can also be printed to x-ray film. Both modalities traditionally use polychromatic x-ray sources to acquire absorption-based image contrast. Both also require breast compression to reduce scatter and improve image quality. While SFM is the conventional breast imaging system and has better spatial resolution, DM has recently been validated through clinical trials and is now preferred for many patient subsets.

DM has many advantages, such as improved contrast resolution, immediate image acquisition and review, versatile storage options, fewer materials required, and the opportunity to manipulate the images to change image feature saliency, but the spatial resolution is slightly less than that of SFM. A large multicenter, national clinical trial, Digital Mammographic Imaging Screening Trial (DMIST), was sponsored by the National Cancer Institute and was coordinated by the American College of Radiology Imaging Network. Approximately 50,000 asymptomatic women obtained mammograms using both standard SFM and one of five DM systems. For the entire study population, there was no significant difference in diagnostic accuracy between SFM and DM, as measured by area under the receiver operator characteristic (ROC) curves. However, DM outperformed SFM for three subgroups: women under the age of 50, pre- and peri-menopausal women, and women with heterogeneously or extremely dense breasts. (Pisano 2004, Pisano 2005a, Pisano 2005b, Pisano 2008, Hendrick 2008)

5.3 The Traditional X-Ray Tube

Conventional mammography utilizes x-ray tubes to generate polychromatic x-rays via a spectrum of superimposed bremsstrahlung and characteristic radiation. The energy spectrum of the radiation produced is conditioned by filtration but is ultimately influenced by cathode (filament) material, anode (target) material, and the voltage applied to the filament. Common high Z cathode and anode materials include molybdenum (Mo), rhodium (Rh), tungsten (W), and aluminum (Al), with material properties listed in Table 5.1.

A cathode filament is a metal wire heated with a current of electrons to a temperature that overpowers electrostatic forces to release electrons, a process called

thermionic emission. Thermionic emission increases with increasing temperature until a saturation point is reached. The voltage supplied to the filament, or filament current, dictates the energy of the freed electrons. The electron current and the electrons released from the filament give the cathode a negative charge. By placing the filament inside a negatively charged cup, electrostatic repulsion directs the freed electrons toward the target. The flow of electrons originating at the cathode and ending at the anode is called the tube current. (Hendee 2002, Sprawls 1993, Bushberg 2002)

Material	Z	Melting Point	Characteristic keV
Aluminum (Al)	13	660ºC	1.6 , -
Molybdenum (Mo)	42	2623ºC	17.5 , 19.6
Rhodium (Rh)	45	1964ºC	20.3 , 22.7
Tungsten (W)	74	3370ºC	59.3 , 67.2

TABLE 5.1: Properties of Common X-Ray Target Materials. Mammography units most commonly use x-ray tubes with some combination of Mo and Rh. It is critical to choose a cathode/anode combination of materials with physical properties amenable to the type of imaging desired. Imaging that requires extended or repeated scan times with little or no cool-down requires materials with high melting points to avoid damage from heat loading. It is also important to choose materials with characteristic emission lines that will either contribute to the desired energy flux or do not create an increased demand for filtration.

Passing a high voltage through the target creates an electrical potential energy, imparting a positive charge to the anode, and accelerates the electrons freed from the filament toward the target. This potential energy is fully converted into kinetic energy, with a velocity dependent on the voltage applied to the target. When electrons impinge on the target, they produce characteristic radiation, bremsstrahlung radiation, and heat. The tube current and filament current must be appropriately balanced to avoid electron cloud formation at the cathode that suppresses thermionic emission or an electron cloud

forming at the anode, potentially reversing the flow of electrons and destroying the x-ray tube. (Hendee 2002, Sprawls 1993, Bushberg 2002)

The x-ray tube focal spot refers to the size of the field of electron impact and x-ray production on the target. While decreasing focal spot size increases spatial resolution, the tradeoff involves increased anode heat loading and a reduced field of view. Focal spot size is modulated by tube current, voltage, filament size, filament positioning within the cathode, and anode angle. Steep anode angles decrease the apparent focal spot size but create the heel effect, where there is a notable intensity drop from the cathode to anode side of the x-ray beam, demonstrated in Figure 5.2. Some x-ray tube designs rotate the anode for greater distribution of heat loading. (Hendee 2002, Sprawls 1993, Bushberg 2002)

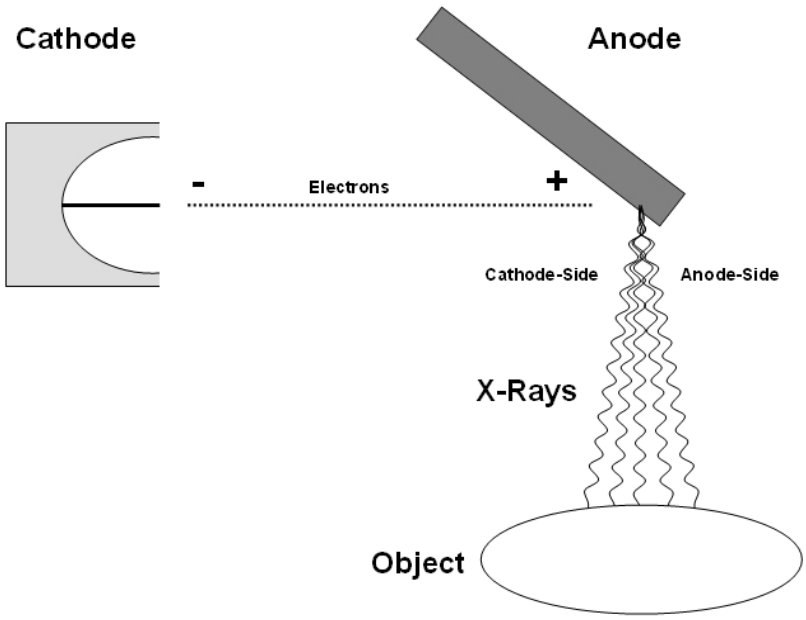

FIGURE 5.2: The Heel Effect. Electrons impinging on the anode generate x-rays. These x-rays must escape the anode without being absorbed. X-rays produced on the anode-side have less material to escape before being exiting the x-ray tube. The x-rays generated on the cathode-side of the anode are attenuated slightly more, creating an x-ray beam that increases in intensity from the cathode-side to the anode-side.

There is a particular voltage at which x-ray production is most efficient, specific to the cathode and anode materials. Power deposited to the x-ray tube (P_D), efficiency, and power radiated from the x-ray tube (P_R) are described by the following equations:

$$P_D = V * I \quad (24)$$
$$P_R = (0.9 \times 10^{-9}) * Z * V^2 * I \quad (25)$$
$$\text{Efficiency} = P_R / P_D \quad (26)$$

where V is the voltage (in volts) and I is the current (in amperes). Only a small percentage of energy supplied to the x-ray tube is actually converted into x-rays, with the remainder emitted as heat. An x-ray tube with either a high Z cathode/anode combination or a large filament current will produce higher energy photons more efficiently through bremsstrahlung emission. (Hendee 2002, Sprawls 1993, Bushberg 2002)

Characteristic radiation production will only occur when the energy provided to the x-ray tube overcomes the binding energy threshold of an electron shell specific to the filament material. When the tube current is above the shell-specific binding energy of the anode, the quantity of characteristic x-rays produced increases proportionally with the difference between the tube current and the binding energy. A polychromatic x-ray spectrum is characterized by the homogeneity coefficient, which is the ratio of the first HVL to the second HVL. The effective energy of a polychromatic x-ray beam is approximately one-third to one-half the maximal energy predicted by energy input. (Hendee 2002, Sprawls 1993, Bushberg 2002)

5.4 Additional System Components

The cathode and anode are housed in an insulating vacuum container which prevents air molecules from interfering with the tube current. The x-ray tube power supply converts power grid energy into the appropriate waveform and selects output

energy, exposure time, kV and mA. Radiopaque collimators restrict x-rays into a useful beam by absorbing all x-rays not traveling in a particular direction, parallel for fan-beam collimators or within a particular range of angles for cone-beam collimators. Alternating strips of radiopaque and radiolucent materials arranged into grids reduce scatter radiation. These grids are arranged either parallel or crossed in a focused grid. A radiolucent compression paddle immobilizes and compresses the breast. (Kopans 2007, Sprawls 1993)

5.5 X-ray Film

Conventional SFM records images onto a film with a thin transparent base, with one side coated in a silver halide emulsion and a radiolucent protective coating. Photon absorption by silver halide granules ejects an electron which is drawn into a sensitivity center. As the electrons collect, the negative charge attracts and neutralizes the positively charged silver ions, depositing the black metallic silver permanently into the emulsion. This process can repeat many times, creating a large dark deposit of metallic silver. Unaffected granules are washed away by a fixing solution, leaving an unexposed light area on the film. The gray scale in SFM image is determined by the number of silver halide granules per unit area in the film. These granules are too small to be viewed with the naked eye, giving the resulting image the appearance of continuous gray scale. (Kopans 2007, Sprawls 1993)

Films are often combined with intensifying screens and antiscatter grids. Intensifying screens are made of materials that fluoresce when an x-ray is absorbed. Film highly sensitive to the characteristic fluorescent wavelength captures the image. This reduces the required exposure because film is not very sensitive to x-ray exposure directly. Intensifying screens introduce blur, noise, and potentially artifacts. Intensifying

screens help reduce the amount of exposure required to generate a useful image, and antiscatter grids preserve image contrast by preventing scattered radiation from contributing to image formation. However, they also block some unscattered x-rays, reducing the intensity at the detector and thus increasing the exposure required. The grids move during imaging to blur gridlines from the image. (Kopans 2007, Sprawls 1993)

X-ray film contrast is nonlinear with respect to x-ray intensity, and is characterized by an Hunter and Driffield (H and D) curve showing the relationship between film density and exposure, with the slope representing contrast produced by a specific exposure. While SFM image quality depends on many factors unique to each system, resolution is typically about 0.03 mm and DQE is approximately 45% (Ikeda 2004, Bushberg 2002, Pisano 2004). SFM-specific noise sources include halide distribution in the film emulsion, anti-scatter grids, intensifying screens, and artifacts imposed by film processing, such as fingerprints and roller marks from the processor. (Kopans 2007)

5.6 Digital Detector

There are two categories of digital detectors- directly digital and indirectly digital. Indirectly digital detectors convert absorbed x-rays into light which is then detected and measured by a digital device. Directly digital detectors capture and quantize x-rays without an intermediate conversion step. Screens in indirectly digital systems use total internal reflection to channel light produced upon x-ray exposure to preserve resolution. These must be thick enough to provide sufficient conversion efficiency, but thin enough to prevent excessive lateral light spread that introduces image blur and resolution loss. Directly digital detectors avoid this intermediate conversion step by immediately

generating an electron signal in response to x-ray exposure. This provides higher resolution and relaxes thickness limitations because electrons can travel within the detector medium with limited lateral spread. (Bushberg 2002)

Spatial resolution, ranging from 0.05 to 0.1 mm, depends on detector element (del) size and arrangement, picture element (pixel) size, signal spread, and bit depth. Larger dels capture more photons, but fewer fit in the same detector matrix, decreasing resolution. Del spacing and geometrical arrangement within the matrix influence how many photons incident on the detector will actually contribute to image formation. DM gray scale is determined by many pixels, small squares of solid colors representing a single value, or shade of gray. Increased bit depth provides a digital detector with the ability to display a wide dynamic range (many shades of gray), allowing for increased contrast resolution. (Pisano 2004, Sprawls 1993)

Digital detectors offer an important advantage over film image receptors in that they can be linear with respect to intensity, and are compared with nonlinear H and D curves in Figure 5.3. To provide optimal SFM contrast, the exposure must be adjusted such that images are acquired on the steep part of the slope, instead of at the toe of the curve where highly attenuating object contrast is located, or on the heel of the curve where weakly attenuating object contrast resides. DM does not have this particular exposure level limitation since it is most often a linear system.

However, digital detectors still have DQE less than unity, meaning that not all x-rays incident on the detector contribute to image formation. Not all detector materials produce signal equally with the same amount of incident radiation. The energy-dependent quantum efficiency (η) of a digital detector is described by:

$$\eta = 1 - e^{-\mu d} \tag{27}$$

where μ is the linear attenuation coefficient for the detector material and d is the detector thickness. The following formula calculates the actual number of electron-hole pairs produced, and thus the signal generated:

$$\text{Signal} = \frac{E\,\eta}{\omega} \tag{28}$$

where E is x-ray energy (measured in eV) and ω is the amount of energy required to produce an element of signal. (Pisano 2004)

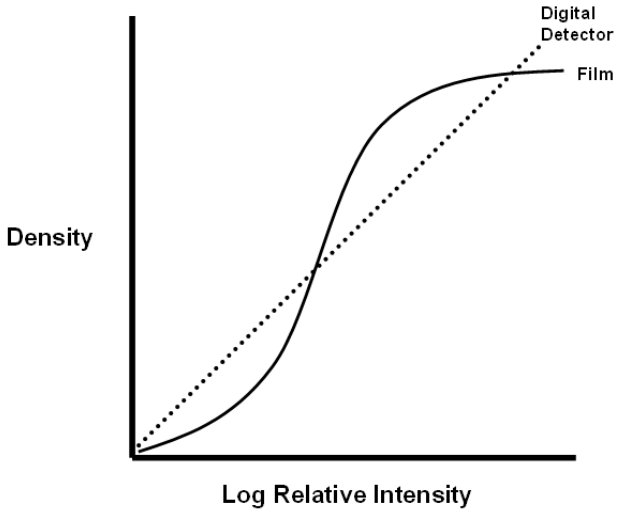

FIGURE 5.3: Screen-Film versus Digital Detector Exposure. The graph relates detector exposure to the amount of density recorded in the image.[8]

Some digital detectors uniquely possess energy resolution, the ability to distinguish between different photon energies. However, they also possess a time resolution limitation, the length of time necessary between two photon interactions with the detector in order for them to be perceived as two separate events. While scattered radiation and the heel effect are noise sources for both SFM and DM, DM-specific noise sources depend on detector material, detector geometry, digital sampling procedures,

8. The values used to create this graph are only for illustration and are not representative of an actual comparison between a specific SFM and DM system.

electronic noise, fixed-pattern detector structural noise (for example, due to dead pixels), and pixel size. Electronic noise is particularly a problem for extended imaging times because it increases with time and temperature. (Pisano 2004)

Just as SFM images can be digitized, DM images can be printed to film instead of viewed on a specialized softcopy review workstation, but this is an additional step with associated image degradation sources. When displayed using soft-copy systems, images can be manipulated for optimized feature visibility by tuning the window and level, magnification, zoom, by applying specialized image processing, and through the use of many other features. Windowing allows the user to manipulate the range of pixels that will be converted into the gray scale, with pixels containing values outside of this range being represented by either pure white or pure black. Decreasing the window width increases displayed image contrast. (Pisano 2004)

5.7 Monochromatic Mammography

Although not yet implemented clinically, the use of quasi-monochromatic x-rays could produce excellent mammographic image contrast by reducing beam hardening and allowing K-edge imaging. A polychromatic x-ray beam possesses a spectrum of energies, with lower-energy x-rays that are more readily absorbed, leading to beam hardening and contributing to radiation dose. A monochromatic x-ray beam thus reduces beam hardening that requires increased flux in polychromatic systems in order to obtain the same number of photons on the detector. Additionally, fewer photons at low energies would be absorbed that don't contribute beneficially to image formation, reducing radiation dose and increasing image quality. The heterogeneous nature of breast tissue composition implies that different monochromatic energies would be optimal for

different breast compositions or to visualize precise features within a specific type of breast. Generally, McKinley *et al* determined that for a 50% dense breast, the optimal imaging energy (for attenuation contrast) is between 30 and 40keV (2006). (Johns 1987, Carroll 1994, Boone 1999, Kimme-Smith 1999)

Monochromatic, or nearly monochromatic, x-rays might allow the detection of minute differences in tissue linear attenuation coefficients. These values are very similar between normal and cancerous tissues, but are energy-dependent. If a tissue was exposed to two different monochromatic energies, these differences might become apparent. The drawback is that this would require at least two exposures. Another way to harness K-edge imaging is to utilize contrast agents with a K-edge near the monochromatic imaging energy, taking advantage of increased x-ray absorption, and thus contrast.

Because monochromatic x-ray tube sources capable of generating sufficient flux for mammography are not currently available for use in the clinic, there are several approaches for conditioning the polychromatic x-ray beam before interaction with the subject. By using thick filters with a K-edge at the optimal imaging energy and an x-ray tube operating at the appropriate voltage, a quasi-monochromatic x-ray beam can be produced (Crotty 2007, McKinley 2004a, McKinley 2004b, McKinley 2006). Another approach is to monochromate a polychromatic x-ray beam by using perfect crystal optics (Chapman 1996, Chapman 1997, Chapman 2006) or using mosaic crystals (Gambaccini 1995, Gambaccini 1996, Gambaccini 2001, Baldelli 2004, Baldelli 2005, Lawaczeck 2005). Each type of crystal monochromator has specific advantages and disadvantages, such as diffraction efficiency, width of the angular acceptance window, ease of alignment,

and so forth. Both the thick filter and crystal monochromator approaches generate quasi-monochromatic x-rays, but in fundamentally different ways.

The use of a thick filter will stop low-energy photons from a polychromatic source. Using a filter material with a K-edge near the optimal imaging energy will cause a reduction in photons above the K-edge due to photoelectric absorption. Thus, a quasi-chromatic x-ray beam is formed surrounding the K-edge of the filter material. The energy of the photons incident on the filter must not be significantly higher than the K-edge of the filter, or a bimodal distribution of photon energies will develop. This is because an increasing portion of the photons have sufficient energy to penetrate the filter.

When a polychromatic beam strikes a perfect crystal, the beam is diffracted based on the d-spacing of the crystal. By changing the angle of the crystal, energy can be selected based on Bragg diffraction, discussed thoroughly in Chapter 8.3. Because crystals are never absolutely perfect, the number of angles that satisfy the Bragg condition occurs over a small range instead of a discrete angle. Thus, a beam diffracted from a monochromator crystal is inherently quasi-monochromatic. Different crystal materials will have different angular acceptance window widths, so in this manner, the level of monochromaticity could be selected.

An advantage of the thick filter approach is that, assuming an incident area beam, the beam emerging from the filter will still be an area beam. This allows for exposure of a larger volume of tissue, whereas perfect crystals diffract fan beams, requiring the object to be scanned through the beam. The thick filter design could potentially be implemented with existing clinical x-ray sources with little expertise required by the radiation technicians. However, the thick filter design has several major drawbacks. For example,

it is not very tunable. In order to change energy spectrum, a different filter would have to be used. The filter and tube spectrum would need to be closely matched.

A crystal monochromator system allows energy tuning by simply changing the angle of the crystal. However, the ability to tune the crystal system also presents a technical challenge not encountered with the thick filter design. Crystals are exceptionally sensitive to changes in direction, vibration, and thermal fluctuations. Alignment of the crystals might be problematic, particularly in a clinical setting.

Both the thick filter and crystal designs are subject to unwanted energies in the spectrum. For a thick filter system, unwanted energies can occur in two ways. First, for a continuous spectrum, a source that produces high energy photons (e.g. operating at high tube voltage) could create a bimodal spectrum, with some photons having enough energy to traverse the filter. Recall that photoelectric absorption is a probability distribution, and not all photons will undergo a complete absorption event, even at the K-edge. Second, the thick filter design requires secondary filtering because as the filter stops the photons just above its K-edge, characteristic x-rays will be produced. A crystal system can produce a spectrum containing unwanted energies because diffraction can occur on multiple planes of reflectivity. These additional energies would need to be removed through filtering.

Inducing monochromaticity through both of these approaches significantly decreases photon flux. Further compounding the problem, x-ray tube sources generate the majority of x-rays near the K-edge of the anode material, and unless the x-ray tube contains multiple anodes, production of x-rays away from this spectrum is inefficient. So even though the crystal system allows energy tunability, the efficiency of a conventional x-ray tube source is prohibitive. Because synchrotron sources are not clinically useful,

one might consider alternative tabletop monochromatic x-ray source designs instead, such as the terawatt laser inverse Compton scatter x-ray source (Carroll 1990, Carroll 2002) or parametric x-radiation production when an electron beam interacts with a crystal (Piestrup 2001, Sones 2007).

5.8 Computer Aided Detection

Approximately 67% of cancers are visible in retrospect, and only 15 to 30% of biopsies performed actually possess malignancy. This implies that sufficient information was contained in the image to lead to such a diagnosis. Digital image formats and the rapid evolution of sophisticated computing systems have allowed the development of computer aided diagnosis (CAD). Algorithms process mammographic images in an attempt to identify and classify regions of potential concern, with several systems commercially available (Yang 2007a, Kim 2006, Morton 2006, Gur 2004). A digital image format (through either primary digital acquisition or digitization of SFM image) allows the application of sophisticated computer algorithms to decipher information contained within an image that could be overlooked by humans, or made ambiguous by noise or artifacts. (Costaridou 2005, Bazzocchi 2007, Castellino 2005)

While CAD is highly sensitive for some cancer features, nonspecific lesion features and large overlap of cancerous and benign features reduce CAD specificity. CAD systems generally perform better for calcification detection and classification algorithms than for mass detection and classification algorithms (Freixenet 2008, Sakka 2006, Brem 2005). Algorithms generally perform well at detecting potential abnormalities, but training the programs to classify subtle image features indicative of clinical findings is more difficult. Therefore, such programs have been developed as a

second-reader function that allows review of images after initial radiologist interpretation, alerting radiologists to areas which require additional review (Gromet 2008, Taylor 2008, Georgian-Smith 2007, Taplin 2006). One study showed that implementing CAD as a second opinion reduced biopsy recommendation for benign lesions while increasing biopsy recommendation for malignant lesions. (Costaridou 2005)

Essential algorithm steps include preprocessing to enhance SNR, segmentation to extract desired signals, and rule-based distinction between true and false signals. It is important that the images used with CAD are of excellent quality or the software will not be effective. Although most current algorithms only utilize one view, research is underway to allow registration between different views such that asymmetry can be evaluated between the left and right breast, and to monitor changes between current and prior mammograms (Pu 2008, Kim 2006, van Engeland 2007, Qian 2007, Zheng 2006). (Costaridou 2005)

5.9 Contrast-Enhanced Mammography

Fast image acquisition possible with DM facilitates contrast-enhanced mammography (Dromain 2006, Jong 2003, Diekmann 2003, Lewin 2003). Recent studies have shown that contrast-enhanced mammography may be able to differentiate between benign and cancerous lesions as well as expose multifocality and multicentricity (Dromain 2006, Jong 2003, Diekmann 2003, Diekmann 2005, Diekmann 2007, Lewin 2003, Lawaczeck 2003, Baldelli 2006). Contrast enhancement is not currently used for typical screening mammography but is sometimes recommended to facilitate suspicious lesion characterization or to determine the extent of disease. Although minimal compression is needed in order to decrease motion artifacts for contrast-enhanced

imaging protocols, strong compression should be avoided with this technique because it interferes with tissue perfusion.

Contrast-enhanced mammography typically utilizes iodine-based contrast agents due to their relative safety and excellent attenuation at mammography imaging energies. The iodine K-edge is 33.2 keV, so traditional x-ray tubes of Mo or Rh are typically filtered to increase the effective beam energy and take advantage of the large increase in photoelectric absorption above the K-edge. This filtration decreases the flux and so increases the required imaging time. Moreover, the increased energy decreases absorption contrast of tissue structures, particularly for microcalcifications. This is suboptimal for simultaneously detecting anatomical features, but allows better visualization of contrast enhancement with less obscuration from structural noise. Several molecular contrast agents are undergoing evaluation for mammography-specific contrast enhancement such as bismuth and gadolinium (Diekmann 2007, Lawaczeck 2003). Recently, Diekmann *et al* demonstrated that bismuth might outperform iodine for contrast-enhanced mammography (2007). An optimal mammography contrast agent should be selected to best match the energy spectrum used, with attention to patient safety.

There are two main techniques for contrast-enhanced mammography- temporal subtraction and dual-energy. Temporal subtraction imaging protocols for DM were adapted from MRI enhancement protocols. An image acquired prior to injection of the contrast agent bolus is subtracted from a second image acquired post-injection. With dual-energy mammography, images are acquired at two energies surrounding the K-edge of the contrast material. This is currently achieved by acquiring two images post-injection of a contrast agent bolus. However, sophisticated digital detectors with excellent energy

resolution can acquire each image simultaneously using a bimodal x-ray spectrum. (Diekmann 2003, Diekmann 2005, Diekmann 2007, Jong 2003, Lewin 2003)

5.10 Summary

Although mammography is the dominant breast cancer screening modality, there are many areas where adjunctive breast imaging systems might provide increased diagnostic accuracy. Planar mammography is obscured by superimposed structures, and only acquires images based on structure as visualized by x-ray attenuation. Images based on the interaction of other signals such as sound, light, or magnetic relaxation with breast tissue can provide increased insight into normal and disease processes. Some systems can even harness physiologic processes present in breast cancers to generate images based on functional molecular processes. Thus, a battery of breast imaging technologies are available in the clinic, but have specific clinical indications to supplement the traditional mammographic imaging procedure. Recently, researchers and manufacturers alike have recognized the value in developing multimodal imaging platforms which might provide an increase in diagnostic capabilities to outweigh increased cost and imaging time.

CHAPTER 6: ADJUNCT CLINICAL AND PRECLINICAL BREAST IMAGING TECHNOLOGIES

6.1 Overview

The sensitivity of planar mammography is often excellent, especially for breasts with high fat content. However, the radiographic appearances of benign and malignant processes are sometimes ambiguous, especially when obscured by structural noise due to overlying tissues and dense breast parenchyma. For example, the mammographic sensitivity when imaging women over the age of 65 varies between 81 and 94%. For younger women, under the age of 40, with typically radiographically dense breasts, the sensitivity of mammography is lower, between 54 and 58%.[9] Moreover, low mammographic specificity leads to a high false-positive rate, with between six and eight benign lesions sampled for every 10 recommended biopsies (Meyer 1990). Additionally, an estimated 10 to 15% of breast cancers are mammographically occult (Meyer 1990). (Kopans 1992)

Conventional mammography requires compression and the use of lower energy x-rays in order to generate sufficient soft tissue contrast, at the cost of increased radiation dose by more damaging ionizing radiation. Although mammography is the dominant imaging technology used for the detection and diagnosis of breast cancer, the many shortcomings of conventional mammography allow room for improvement through adjunctive imaging technologies. These technologies might offer improved detection of

9. Thus, the National Institutes of Health Consensus Development Panel does not recommend routine mammography for women aged 40 to 49 (1997).

small or occult lesions, increased diagnostic performance for certain lesion types or within dense breast tissue, enhanced evaluation of the extent of disease, or monitoring of the course of treatment. Moreover, these systems might offer benefits such as reduced radiation dose, increased patient comfort, or decreased cost.

A wide variety of imaging methods have been successfully applied to breast imaging. While planar x-ray mammography is the current clinical standard of care for both screening and diagnostic breast imaging, there are many other modalities used clinically as adjunct or complementary procedures, and many more undergoing research and development. This chapter discusses system capabilities, components and applications of several prominent breast imaging technologies that are commercially available or are undergoing evaluation for potential clinical utility in breast cancer imaging. These include ultrasound, magnetic resonance imaging, computed tomography, tomosynthesis, nuclear imaging, optical imaging, thermography, electrical impedance tomography, and various phase-sensitive modalities.

6.2 Ultrasound

The technology necessary for ultrasound (US) imaging was developed incrementally, and was initially used for therapeutic applications. US technology was first applied to diagnostic medical imaging by George Ludwig in the late 1940's. John Julian Wild and John Reid generated real-time images of breast tumors in 1953. Today, US imaging is a widely available and inexpensive medical imaging technology with limited side effects. (Woo 2008)

A transducer composed of an array of piezoelectric crystals generates sound waves that cause movement of molecules due to mechanical pressure waves. The US

wave can be reflected, absorbed, scattered, or refracted. These interactions create an increase or decrease in echogenicity or acoustic shadowing, detected as a change in singal amplitude. US can also quantify flow as a change in scatterer position, which induces shifts in signal frequency and phase. An ultrasound wave will travel through a material with characteristic velocities and impedances based on intermolecular bonds and object density, respectively. Table 6.1 lists the velocity and impedance properties of materials important to US breast imaging. (Prince 2006, Zagzebski 1996)

Material	Velocity	Impedance
Water	1480	1.48
Blood	1570	1.61
Fat	1450	1.38
Soft Tissue	1540	1.63
Muscle	1575-1585	1.65-1.74
Bone	4080	3.75-7.38

TABLE 6.1: Measures of Ultrasound Transmission. The velocity (measured in m/s) and impedance (measured in $kg/m^2/s$) of US propagation through various tissues varies greatly based on intermolecular spacing and density. While water and fat produce similar US signals, bone essentially blocks the ultrasound signal, creating shadowing. Because calcifications are typically composed of calcium and phosphorous, US can easily detect many calcifications within its resolution limitations. US propagation through muscle tissue varies depending on muscle type and orientation of muscle fibers. (Topp 2000, Prince 2006)

Interaction between an US wave and an object depends on object density, size, and ultrasound wavelength. If a smooth object is large in comparison to the wavelength, the wave will reflect from the object largely unchanged, except for direction of propagation. Reflection strength, or echo, depends on the difference in acoustic impedance between materials at the interface, and the angle at which the ultrasound wave

becomes incident with the structure.[10] An exceedingly steep angle of incidence causes refraction of the wave instead of reflection. Refracted waves are not detected by the transducer and cause defocusing. If the object is small or comparable in size to the wavelength, the sound wave will be scattered nonuniformly, referred to as specular scatter. (Prince 2006, Zagzebski 1996)

US spatial resolution is described in axial, lateral, and elevation terms. Each is influenced by distinct imaging parameters and system design features. While typical systems operate at 5 to 10 MHz with resolution on the scale of millimeters, new high-frequency US imaging systems, operating at 20 MHz or higher, have the potential for submicron resolution and are beginning to be tested in the clinic (Chao 2007b, Wratten 2007, Teh 2000). However, two drawbacks to US for breast imaging are: suboptimal detection of microcalcifications due to resolution limitations, and excessive image noise. US noise is due to system design factors such as detector element size and spacing, noise from tissue structure, and speckle that is directly related to system resolution. Moreover, US image quality is heavily dependent on the operator, although automated breast US systems are under development (Richter 1997, Shipley 2005, Sinha 2007, Kotsianos-Hermle 2009). (Bushberg 2002, Prince 2006, Zagzebski 1996)

US is particularly useful in evaluating lesion shape, delineating lesion edge characteristics, and determining whether a lesion is solid or fluid-filled. US imaging can also be used for real-time functional studies, such as blood flow analysis. US can image dense breast tissue, and it does not use ionizing radiation, and so it is safe for repeated imaging and for use in the breasts of young women. Breast US CAD systems are under

10. The formula for US reflection: $R = [(z_2 / z_1) - \sqrt{(1 - [n - 1] \tan^2 \alpha_i)}] / [(z_2 / z_1) + \sqrt{(1 - [n - 1] \tan^2 \alpha_i)}]$, where z is the acoustic impedance in the medium, $n = (c_2 / c_1)^2$, c is the speed of sound in the medium, and α_i is the angle of incidence.

development (Drukker 2009, Yap 2008, Gruszauskas 2008, Wu 2008), with one system commercially available (Junlai 2009). Three-dimensional US imaging techniques have been developed and implemented in the clinic, potentially overcoming the limitation of operator-dependent image quality (von Ramm 1990, Duric 2007). However, even with three-dimensional imaging, US remains depth-limited, and its low spatial resolution often precludes the detection of microcalcifications, an important early indicator of breast cancer. (Bushberg 2002, Prince 2006, Zagzebski 1996)

Contrast-enhanced breast imaging might be valuable due to increased contrast agent at tumor sites due to the Enhanced Permeability and Retention (EPR) effect. US contrast agents are only recently becoming widely available. In order to manipulate the US wave, contrast agents must induce alterations in acoustic velocity or impedance. Most US contrast agents are microbubbles that change acoustic impedance via low-density insoluble perfluorocarbon gas-filled biocompatible shells. These bubbles vibrate and reflect the incident US wave, but are typically unstable for extended imaging periods. Liposomes, which are lipid bilayers containing an aqueous solution, can also manipulate US echogenicity. Nanoparticles are also being explored for contrast-enhanced US imaging (Liu 2007b, Yang 2008a). Novel nonlinear US imaging protocols such as harmonic, subharmonic, and pulse-inversion can be used in conjunction with contrast enhanced US imaging, potentially allowing for increased contrast enhancement (Forsberg 2007). Functionalization of targeted contrast-enhanced ultrasound imaging is also being developed (Behm 2006, Lanza 2003, Rapoport 2007, Gao 2008, Liu 2007b). (Dawson 1999, Dayton 2002, Cosgrove 2006, Quaia 2007, Morawski 2005)

While US is commonly used as an adjunctive breast imaging modality, it is not currently recommended for screening the general population due to limited spatial resolution and low specificity that prevents detection of small lesions without unacceptably high false-positive rates (Berg 2008). However, US does have many clinical indications. US is routinely used to classify mammographic abnormalities. For dense breast tissue containing invasive cancer, US has increased sensitivity over conventional mammography (Berg 2004, Kolb 2002). US has also demonstrated moderate diagnostic performance in screening for axillary lymph node metastases (Alvarez 2006).

Several novel US-based imaging techniques are being developed. These techniques include US elastography, photoacoustic imaging, and thermoacoustic imaging. None of these techniques have yet demonstrated clear clinical utility for breast imaging and gained clinical implementation. US elastography is a real-time, semi-quantitative technique that measures tissue stiffness. Several clinical trials have demonstrated the potential utility of breast US elastography to differentiate nonpalpable benign and malignant lesions (Cho 2008, Itoh 2006). A recent study which enrolled 235 patients that had been referred for core-needle biopsy showed that US elastography was useful for fibroadenoma classification (Fleury 2009). Additional clinical trials demonstrated that breast lesion characterization was improved with the addition of tissue stiffness parameters (Qiu 2008, Zhi 2008).

Despite these initial promising results, differences in elasticity between normal and abnormal tissues are not fully characterized, limiting the clinical application of this technique. In fact, one trial with 100 patients with nonpalpable breast masses found that

US elastography diagnostic performance was roughly equivalent to conventional US (Cho 2008). Another clinical trial of 111 patients with lesions between 5 mm and 30 mm found roughly equivalent diagnostic accuracy of US elastography as compared to conventional mammography (Itoh 2006). These results suggest that, for some patient populations, this new technique might not offer any improvement in lesion characterization over existing clinical imaging techniques. Moreover, US elastography requires compression similar to mammography, and compression affects elasticity quantification.

Photoacoustic tomography (PAT) imaging generates image contrast based on measurement of emitted wideband US after laser absorption by tissue. The absorbed laser energy generates heat, and thus thermoelastic expansion, with the magnitude of the emitted US signal based on the absorption properties of the tissue. Although some have speculated that this technology might be useful for breast imaging, most studies are restricted to phantom studies, laboratory *in vivo* studies, or pilot clinical trials. Several groups have evaluated contrast-enhanced PAT with both commercially available and novel contrast agents using phantom (Rajian 2009, Kim 2008a, Kim 2007d, Ku 2005), *in vitro* (Bhattacharyya 2008), and rat models (Song 2009, Song 2008). PAT might also be useful for evaluating the development of tumor vasculature (Lao 2008) or blood flow (Hoelen 1998). One group has constructed a prototype PAT breast imaging system, with a small pilot clinical demonstration (Manohar 2005, Vaartjes 2007, Manohar 2007, Manohar 2004). Large clinical trials with PAT technology have not yet been undertaken.

Similarly, thermoacoustic tomography (TAT) imaging generates image contrast based on measurement of emitted US after radio-frequency (rf) absorption by tissues. The

heat generated by rf absorption causes thermoelastic expansion and US emission based on the rf absorption properties of the tissue. TAT laboratory trials have been performed with tissue phantoms (Ku 2005), and breast tissue specimens (Nie 2008). One study imaged five patients with TAT to demonstrate the feasibility of breast tumor contrast enhancement (Kruger 2000). Another group has evaluated microbubbles for contrast-enhanced TAT (Mashal 2009). Others have suggested the combination of PAT and TAT into a single multi-modality imaging platform (Pramanik 2008). However, substantially more laboratory studies are needed to establish the performance of this system, and until rigorous clinical trials in patients have been undertaken, the potential applications of TAT are tentative.

6.3 Magnetic Resonance Imaging

Nuclear magnetic resonance was developed by Felix Bloch and Edward Purcell in 1946, but did not enter the clinic until the 1980's, after development into a medical imaging system by Paul Lauterbur and Peter Mansfield. MRI provides information that can not be obtained from other clinical breast imaging modalities such as mammography and ultrasound. Recent advances in imaging sequences have allowed MRI to provide images based on either anatomy or physiology. (Hornak 2007)

MRI depends on the nuclear magnetic resonance (NMR) properties of atomic nuclei. Only nuclei with odd atomic number or mass number have angular momentum (spin) and can thus generate an NMR signal. Most MRI imaging is of hydrogen, which is abundant in the human body and strongly NMR active. In general, the micromagnetic fields of nuclei are randomly oriented, resulting in a net magnetization of zero. When these nuclei are exposed to a gradient magnetic field, the spins align. Protons absorb

radiofrequency (rf) pulses at resonant frequencies, which causes a change in dipole alignment. The rf energy is re-emitted, with specialized coils detecting the frequency and phase in order to spatially encode the signal for tomographic reconstruction, while Faraday induction generates an MRI signal. (Prince 2006)

MRI signal is determined by tissue relaxation properties (T1, T2, proton density) and scanner imaging protocols (pulse sequences). T1, or spin-lattice, relaxation refers to the recovery of magnetization after an rf excitation pulse. T2, or spin-spin, relaxation refers to the decay in emitted rf signal due to free induction decay, with dephasing of the rf signal from local microenvironment inconsistencies. There are a wide variety of pulse sequences allowing weighting or suppression of different signals based on tissue-specific relaxation and composition properties. MRI acquires a series of planar images that can be reconstructed into three-dimensional tomographic images, eliminating obscuration by overlying or dense breast tissue, thus also eliminating the need for breast compression. (Prince 2006)

Typical MRI spatial resolution ranges from 25 to 100 μm. MRI spatial resolution is influenced by filtration, number of volume elements (voxels) used, the gradient applied, and the type of phase encoding used (Bushberg 2002, Prince 2006, Ikeda 2004). Sources of MRI noise include rf emission from the patient's body, thermal vibrational noise within the patient's body, as well as system noise such as additive electronic noise (Bushberg 2002, Prince 2006, Ikeda 2004). The reported sensitivity of MRI ranges from 71 to 100%, while specificity typically only ranges from 50 to 79%, depending on patient population, tumor type, and imaging sequence (Bluemke 2004, DeMartini 2008, Boné 1996, Heywang-Köbrunner 1997). This low specificity rate prevents its use as a routine

screening modality and does not allow MRI to contribute to biopsy rate reduction (van Goethem 2006).

Improved MRI systems are being developed with stronger magnetic fields and high-sensitivity dedicated breast coils. CAD for MRI is also under development, with several commercially available systems (Behrens 2007, Penn 2006, Lehman 2006, Kurz 2009). Although MRI offers exceptional three-dimensional structural and functional images, there are several disadvantages to this system. Scanners typically can not accommodate large patients or those with claustrophobia. The high magnetic fields exclude patients with certain implants, such as pacemakers. Additionally, if the MRI system is used as a multimodal or interventional platform, non-magnetic tools and equipment are required. An MRI imaging sequence requires sizeable data storage capacity as well as interpretation time. In general, the high cost, longer scan time, and lower availability hinder widespread clinical implementation of MRI.

There are a wide variety of MRI imaging sequences that have been adapted with unique potential applications in breast imaging, including magnetic resonance spectroscopy (MRS), magnetic resonance angiography (MRA), diffusion-weighted MRI (DW-MRI), and magnetic resonance elastography (MRE). MRS can detect biochemical information about proton-containing metabolites often associated with processes active within cancers, i.e. proliferation (choline) and metabolism (creatine, inositol, glucose, alanine, lactate) (Sinha 2009, Partridge 2008). The lipid and fat content of the breast creates difficulties in MRS data analysis, which might be overcome with two-dimensional MRS imaging sequences (Thomas 2005, Thomas 2001). Some have suggested that MRS might allow highly specific evaluation of *ex-vivo* fine needle

aspiration biopsy specimens as well as *in vivo* breast cancer diagnosis, with the potential to predict LN involvement and vascular invasion (Mountford 2004, Mountford 2009).

Multiple clinical trials have evaluated the potential for MRS to increase sensitivity and specificity when this data is combined with conventional MRI (Bartella 2006, Meisamy 2005, Katz-Brull 2002, Tse 2003, Huang 2004, Stanwell 2005, Kim 2003). However, these trials have also raised questions about the utility of the MRS technology for small lesions (Tse 2003), with concern for false-negatives (Yeung 2002, Stanwell 2005). Preliminary data has shown the potential of MRS for *ex vivo* axillary LN evaluation for the presence of metastases, with results complementary to histopathologic sectioning (Yeung 2002, Sharma 2004, Seenu 2005). MRS has also demonstrated the potential for *in vivo* monitoring of therapeutic response by locally advanced breast cancers (Jagannathan 2001, Meisamy 2004, Kumar 2006).

MRA is a form of contrast-enhanced MRI imaging that can be used to generate vascular maps and detect tumor-associated angiogenesis. Injected paramagnetic or superparamagnetic contrast agents are commonly used to improve tissue differentiation and breast cancer detection (Sinha 2009, Heywang-Köbrunner 1996, Kacl 1998, Kelcz 1996). Common MRI contrast agents are gadolinium chelate and iron oxide, which possess magnetic properties that induce a net change in the local magnetic field and affect longitudinal (paramagnetic) or transverse (superparamagnetic) relaxation (Morawski 2005). Although some gadolinium-based MRI contrast agents have caused adverse events such as kidney dysfunction (Ersoy 2007, Ledneva 2009), the agents currently used in the clinic are relatively safe (Bleicher 2008).

While both molecular and nanoparticle MRI contrast agents are used clinically, novel contrast agents such as quantum dots and core-shell nanoparticle composites have also been proposed (Santra 2005, Su 2007). Recent research has evaluated the potential for breast cancer targeted contrast-enhanced MRI using HER-2/*neu*, folate, and glucose (Artemov 2003, Ito 2004, Ito 2005, Wuang 2007, Wuang 2008, Sakamoto 2005, Swanson 2008, Alric 2008, Luciani 2004). Because MRI has low sensitivity, multiple contrast medium molecules must be bound to each targeting agent in order to create a detectable increased contrast agent density at the targeted location (Morawski 2005).

Contrast-enhanced MR imaging of the breast has gained some clinical implementation, but suffers from several limitations. For example, contrast agents can sometimes induce nephrotoxicity or an allergic reaction, the contrast-enhanced imaging protocol increases the imaging time (and subsequently the cost), and the complex data resulting from a contrast-enhanced MR imaging protocol sometimes lead to imprecise sizing and localization of the region of interest. Further, although contrast-enhancement demonstrates excellent sensitivity, the specificity varies, and contrast-enhanced MR imaging protocols have not been fully standardized in the clinic. (Sardanelli 2005, Sardanelli 2007, Macura 2006, Helbich 2000)

The DW-MRI imaging sequence forms images of tissue structure based on translational motion of water and can be used to detect early cellular changes associated with cancer, such as alterations in membrane permeability, cell swelling, and cell lysis (Sinha 2002). Several clinical trials have demonstrated the potential for DW-MRI to provide high sensitivity and facilitate differentiation between benign and malignant breast lesions (Marini 2007, Guo 2002, Lo 2009, Park 2007b). The performance of DW-MRI

has been compared with conventional MRI, contrast-enhanced MRI, conventional mammography, and positron emission tomography (Park 2007b, Yoshikawa 2007, Komori 2007).

MRE measures the MR signal after application of a mechanical pressure wave to the breast tissue, generating an image based on tissue elasticity or viscosity. Although this might help differentiate benign and malignant lesions, this technique yields low specificity since many benign processes also cause increased fibrosis and changes in tissue viscoelastic properties. The MRE technique has been tested *in vivo*, but all studies to date included fewer than five patients. Thus, the potential of this technique must be rigorously established through larger clinical trials before it can begin to find a potential indication for clinical use. (Xydeas 2005, Sinkus 2005, Manduca 2001, Plewes 2000)

Conventional MRI is clinically indicated for breast cancer staging, screening for residual or recurrent tumor (particularly in the presence of scar tissue), therapy monitoring, localizing occult breast disease when distant breast cancer metastases have been found, and screening women at high risk for breast cancer development (Sardanelli 2003). Some practitioners also utilize MRI for diagnostic workup to evaluate indeterminate mammographic or clinical findings (Patani 2008, van Goethem 2006). MRI may be particularly useful for detecting breast cancer in women with radiographically dense breasts (van Goethem 2006). As breast density increases, MRI tends to outperform conventional mammography (Lee 1997, Berg 2004). However, the routine use of MRI for staging of breast cancer might warrant further clinical studies, considering the rates of local recurrence after breast cancer therapy, the resolution limitations of MRI, and the risk of over- and under-estimation of tumor size (Morrow 2009). (Zakhireh 2008)

Conventional MRI is not currently used to screen the general population for breast cancer, but recent research indicates it might be useful for screening high risk women (Patani 2008, Port 2007, Saslow 2007, van Goethem 2006, Warner 2008, Lehman 2005b). When breast cancer has been detected, MRI not only gives an excellent indication of extent of disease in the affected breast, it also has demonstrated utility in detecting occult disease in the contralateral breast (Fischer 1999, Slanetz 2002, Liberman 2003, Lee 2003, Viehweg 2004, Berg 2004, Lehman 2005a, Pediconi 2007). While the many novel MRI imaging techniques have demonstrated promise for improved breast cancer detection and diagnosis, these techniques must undergo many more trials with larger populations to best identify their appropriate applications in the clinic.

6.4 Computed Tomography

Computed tomography (CT) creates a three-dimensional image from a series of planar x-ray images. Although this technique was theoretically realized in the early 1900's, it could not be practically implemented until x-ray detector technology dramatically improved. Godfrey Hounsfield and Allan McLeod Cormack pioneered CT research and development, with commercial availability of these systems in the early 1970's. Initial clinical studies using whole-body and dedicated contrast-enhanced breast CT failed due to excessive dose, low specificity, and high cost. Major improvements in imaging protocols, hardware design, and image processing algorithms might facilitate breast CT imaging applications. (Boone 2001, Boone 2006a, Boone 2006b, Glick 2007)

Images are based on the spatial distribution of attenuation without obscuration due to overlying tissue structures by reconstructing many individual planar images acquired throughout 360 degrees. Each voxel displays the averaged sum of all intensity

attenuation along the path within the object, and is represented in a pixel of the two-dimensional digital matrix. Conventional CT uses a polychromatic source, which means that beam hardening and the energy-dependence of μ must be taken into consideration. (Bushberg 2002, Podgoršak 2006, Kalendar 2005)

Quantitative CT numbers, calculated in Hounsfield units (HU), are relative to water and can be calculated by the following equation:

$$\text{CT number} = (\mu - \mu_{water})/ \mu_{water} * 1000 \text{ HU} \quad (30)$$

where μ is the linear attenuation coefficient for the object being imaged and μ_{water} is the linear attenuation coefficient for water. CT values typically range from -1,000 to +3,000 HU, with soft tissue CT numbers typically between -300 and -100 HU. High CT values represent high ρ and high Z, which translates to high x-ray contrast. (Bushberg 2002, Kalendar 2005)

For an inhomogeneous object, the distribution of μ along the x-ray's path by a single projection image is unknown, but by applying Radon's theory, μ can be approximated. Radon's theory states that if infinite line integrals are known, you can exactly calculate the two-dimensional distribution of an object. Each projection's attenuation profile is calculated by:

$$\ln(I_0/I) \quad (29)$$

where I_0 is the initial intensity and I is the attenuation after interaction with the object. A set of these attenuation profiles is referred to as a Radon transform. Image reconstruction implements convolution-backprojection, Fourier, algebraic reconstruction, or iterative reconstruction techniques. Convolution-backprojection, also called filtered back projection, is the most common reconstruction technique, smearing μ along the path of

each ray of the x-ray beam. Filtration reduces characteristic blurring and can be used to improve image feature visibility through reduced noise or increased edge enhancement. (Kalendar 2005, Bushberg 2002)

CT spatial resolution is approximately 0.5 mm. CT offers excellent contrast resolution of 0.5%, whereas conventional SFM only offers approximately 5%. CT spatial and contrast resolution are influenced by a variety of factors, summarized in Table 6.2. CT experiences similar noise and artifact sources as DM, with unique noise and artifacts introduced by beam hardening, cupping, partial volume effect, photon starvation, and inaccurate image reconstruction. A typical CT scan currently delivers a radiation dose between 10 and 40 mGy. Because images are acquired over 360 degrees, there is a higher external dose at the perimeter of the object being imaged, with a lower core dose. (Kalendar 2005, Bushberg 2002)

Because CT is an absorption-based imaging system, it most often uses the same iodine-based small molecule contrast agents as DM. However, because CT uses higher x-ray energies than DM, iodinated contrast agents are not ideal. Novel nanoparticle (Hainfeld 2006, Cai 2007, Kim 2007c, Rabin 2006, Alric 2008), quantum dot (Santra 2005, Daneshvar 2008), and molecular (Simon 2005a, Fu 2006) contrast agents have been proposed as blood-pool x-ray contrast agents, some with multimodal capabilities that might simultaneously provide magnetic or optical properties amenable to MRI or optical imaging, respectively. (Bushberg 2002, Kalendar 2005, Ikeda 2004)

Whole-body CT systems can be used to image breasts at the cost of higher dose, but several groups are currently developing dedicated low-dose breast CT systems (Shaw 2005, Lindfors 2008, Yang 2007b, Boone 2001, Brzymialkiewicz 2005). Although low-

dose dedicated breast CT systems have demonstrated excellent sensitivity, both low specificity and high dose issues remain.

Spatial Resolution	Contrast Resolution
Detector Pitch	X-Ray Tube Current
Aperture Size	Dose per Scan
Number of Views	Field of View
Number of Rays	Pixel Size
Focal Spot Size	Slice Thickness
Field of View	Patient Size
Pixel Size	Reconstruction Algorithm
Magnification	
Slice Thickness	
Reconstruction Algorithm	

TABLE 6.2: Factors Influencing CT Spatial and Contrast Resolution.

Breast CT is not currently recommended for breast cancer screening, but potential clinical indications include diagnostic follow-up to characterize ambiguous lesions, detection of suspected occult lesions, or determination of the extent of disease (Glick 2007, Taira 2008). Breast CT does not require compression, which can improve patient comfort during image acquisition. Studies have shown that contrast-enhanced breast CT and MRI have roughly equivalent diagnostic accuracy for assessing the extent of intraductal spread of cancer (Nakahara 2002, Shimauchi 2006). Further research is needed to determine where dedicated breast CT fits into the spectrum of medical imaging systems. Limited-angle tomography, referred to as tomosynthesis, might compete for this role, or each of these systems might have unique applications.

6.5 Tomosynthesis

Tomosynthesis is similar to computed tomography in that it generates a three-dimensional image through reconstruction of multiple planar images, reducing structural noise due to overlying tissue layers. Although tomography was described in the 1930's,

limited-angle tomography, termed tomosynthesis, was not described until the 1970's when image processing techniques were developed to appropriately interpolate and reconstruct the images. Several initial studies demonstrated promising results and potential applications of the technology. (Maravilla 1984, deVries 1985, Sone 1991, Niklason 1997)

A polychromatic x-ray source is rotated through an arc over the object and detector, acquiring a series of images with multiple low-dose exposures. The object and detector can remain stationary or translate horizontally to increase the field of view by reducing x-ray loss on the detector at increasingly oblique angles. Post-processing shifts planar images to realign and reinforce shifted shadows of objects in each planar image.

Because data is acquired over an incomplete three-dimensions, the necessary interpolation means that tomosynthesis images have lower resolution than those acquired over a full three-dimensions, as with CT. Specifically, the depth resolution suffers. Tomosynthesis resolution was measured to be 2.41 mm in the x and y plane, with a resolution of 3.02 mm in the z plane (Flynn 2007). Image quality is further deteriorated by scatter radiation, which can not be eliminated using an anti-scatter grid because the angle of x-ray source changes while the detector remains stationary (Diekmann 2007).

Traditional iodine-based contrast agents have been evaluated for contrast-enhanced breast tomosynthesis (Smith 2005, Park 2007a, Niklason 1997, Dobbins 2003, Chen 2007). Because tomosynthesis uses x-ray absorption to generate image contrast, commercially available and newly developed contrast agents used with DM and CT might also perform well with tomosynthesis.

Recent phantom, *ex vivo*, and two small *in vivo* clinical trials have demonstrated that tomosynthesis generates images with excellent cancer visibility which might allow increased sensitivity (Niklason 1997, Suryanarayanan 2000, Stevens 2003, Poplack 2007a, Andersson 2008). Although comparisons between tomosynthesis, SFM, and DM suggest that tomosynthesis might improve breast cancer detection and characterization, the clinical trials to date have selected study populations of women with an abnormal mammogram (Poplack 2007a, Andersson 2008). Larger studies with different populations should be conducted. Using 30 selected cases, one group found that image interpretation time increased for tomosynthesis as compared to DM, which must be weighed against the incompletely characterized ability to detect and diagnose (Good 2008). Many issues remain unresolved, such as determination of the optimal scanning arc, dose per image, and number of projection images.

The potential benefits of tomosynthesis include improved lesion detection, characterization, lesion localization, tumor volume estimation, more effective determination of extent of disease, and reduced breast compression. Several groups are developing tomosynthesis CAD algorithms that might further enhance the detection and characterization of breast lesions (Chan 2005, Chan 2008, Singh 2008). Because tomosynthesis may deliver less radiation dose than CT imaging yet generates three-dimensional images with versatile imaging parameters, it is potentially a valuable multi-modality imaging platform. Sinha *et al* recently developed a multimodal tomosynthesis system that incorporates US (2007). Another group demonstrated improved image quality when high resolution tomosynthesis images were fused with low-resolution CT images (Zeng 2007). (Park 2007a)

6.6 Nuclear Medicine

Nuclear medicine involves the detection of radiation emitted from the decay of chemical or radioactive contrast agents injected into the patient. The first radiotracers were developed and used in 1923 by Georg Von Hevesy. Nuclear imaging became clinically available in 1958 when Hal Anger developed the gamma camera. Planar scintimammography (SM), and three-dimensional single photon emission computed tomography (SPECT) and positron emission tomography (PET) are three nuclear imaging techniques that have demonstrated possible utility for breast imaging applications. PET is referred to as positron emission mammography (PEM) when applied to breast imaging. (Nuclear Medicine 2003)

These systems acquire images based on organ physiology, metabolism, perfusion, or other functional processes associated with radiotracer biodistribution. Radiotracers can either emit γ-rays at a variety of different energies through radioactive decay, or can undergo positron decay. The positrons travel a short distance before annihilating with a free electron, generating two 511 keV γ-rays that travel in opposite directions. Breast imaging with nuclear medicine began with planar scintimammography (SM) using ^{99m}Tc-labeled lipophilic cations. SPECT generates three-dimensional images through the decay of radionuclides such as ^{99m}Tc, ^{131}I, ^{123}I, ^{133}Xe, ^{201}Tl, ^{67}Ga and ^{111}In. Common PET isotopes include ^{18}F, ^{15}O, ^{13}N, and ^{11}C. High resolution SM has demonstrated up to 1 mm spatial resolution (Vincentis 2006) while SPECT has a spatial resolution of 1 to 7 cm. (Bushberg 2002, Ross 2005, Buck 2008)

PET using fluorodeoxyglucose (FDG-PET) is the most commonly used PET application because many cancers are strongly avid for glucose, and the FDG glucose

derivative is taken up readily by cells but is not easily metabolized. FDG-PET imaging is confounded by false-positive radiotracer uptake by muscle, inflammation, bowel and the urinary tract, as well as tumor-type-dependent metabolic variation and complex metabolic interactions. PET spatial resolution is typically between 6 and 8 mm, with sensitivity and specificity of PET ranging between 80 and 100% for tumors larger than 1 cm (Adler 1993, Avril 2000). FDG-PET might be better for some subsets of breast cancer imaging than SM or SPECT (Buchmann 2007, Palmedo 1997).

Photon attenuation negatively influences image quality, which can be corrected by acquisition of a planar or CT transmission image. Transmission images fused with the nuclear imaging dataset provide attenuation correction and add anatomical information to the functional data. Due to the benefit in diagnostic accuracy for metastatic disease in breast cancer with these multimodal platforms, newly produced nuclear imaging systems are nearly exclusively available coupled with CT. (Bushberg 2002, Ross 2005, Buck 2008)

Nuclear imaging sensitivity dramatically falls for lesions smaller than 1 cm, preventing these technologies from excluding the presence of cancer, and precluding their use as screening modalities (Avril 2000, Rosé 2002). However, nuclear imaging modalities might be useful as adjunct breast imaging techniques. Attachment of targeting ligands to the radiotracer hold promise for targeted imaging based on hormone and cell-membrane receptor expression densities. Potential benefits of these techniques must be weighed against the risk associated with the use of the injected radiotracers.

Some clinicians utilize nuclear imaging techniques to characterize ambiguous mammographic findings, detect suspected occult breast lesions, or for women with dense

breasts that leads to poor mammographic image quality (Brem 2007, Brem 2008, Danielsson 2000, Buscombe 2001), but the clinical data supporting these methods is limited. These techniques may also be used for determining the extent of disease, such as identifying multifocality and multicentricity, regional metastases in axillary LNs, or even distant metastatic or recurrent lesions using whole-body PET (Avril 2000, Schirrmeister 2001, Danielsson 1999, Rosé 2002, Cwikla 2000). Nuclear imaging techniques, such as SM, might be clinically indicated and cost-effective for screening young women with known breast cancer risk factors (Allen 1999). All of these applications require more clinical trial data before they are adopted widely.

Initial clinical trials have suggested that PET has high diagnostic accuracy for a variety of breast lesion types (Berg 2006, Levine 2003, Murthy 2000). Although PET does not offer an advantage in sensitivity over mammography, it may be useful to assess therapy response because cancer metabolic rates give an early indication of which patients are responding to treatment (Avril 2000, Wahl 1993, Smith 2000). While PET currently has greater spatial resolution than SM or SPECT, the fundamental resolution limitation due to positron range will not allow improved detection technologies to translate to improved resolution. So, although SPECT systems research is lagging behind PET, the tide might turn in the future as detector technologies meet and exceed fundamental PET resolutions. (Bénard 2005, Buscombe 2004)

6.7 Optical Imaging

The concept of using light to visualize breast cancers has been realized since the late 1920's, when transillumination was used to observe internal breast structures (Cutler 1929, Sickles 1984). Optical systems can measure the absorption, scatter, and even phase

differences of light. Optical imaging light wavelengths can range from UV through visible, near-infrared, and the infrared region to generate planar or three-dimensional images. Near infra-red (NIR) is most commonly used as it has the greatest penetrance through soft tissue. Technological developments and new imaging techniques such as Raman spectroscopy (RS), optical coherence tomography (OCT), and diffuse optical tomography (DOT) have only recently begun to provide sufficient data on sensitivity and specificity to support clinical applications. (Ntziachristos 2001)

Raman spectroscopy gives specific information about the biochemical composition of breast tissue based on distinctive energy shifts in elastically scattered light (can use ultraviolet through infrared), but lacks structural and morphologic information. With carcinogenic progression, cells acquire increasingly abnormal biochemical profiles in addition to micro- and macro-scopic morphologic changes. For example, malignant cells tend to have abnormal extracellular matrices with increased collagen and elastin proteins; proliferative and metabolic activity results in changes in proteins such as NADH, FADH2, ATP, phosphocholine, phosphocreatine; and proteoglycans are released when malignant cells break through the basement membrane. These unique Raman spectra have allowed distinction between tumor and background for several *ex vivo* studies (Patil 2008, Haka 2005, Bitar 2006, Chowdary 2006). One study has evaluated RS *in vivo* with 9 patients undergoing partial mastectomy, demonstrating a potential decrease in positive surgical margins when using RS (Haka 2006). Furthermore, RS can distinguish between the two main types of calcifications: calcium oxalate dehydrate mainly associated with benign conditions and calcium hydroxyapatite commonly found in proliferative lesions (Stone 2008, Haka 2002). (Hanlon 2000)

Optical coherence tomography uses reflection of NIR pulses and interferometric image formation to visualize the structure of breast lesions at resolutions substantially greater than any currently available clinical system (Hsiung 2007). OCT is limited to extremely shallow imaging depths of 2 to 3 mm, but has submillimeter resolution within these depths (Hsiung 2007). While one group has combined the RS and OCT technologies into a multimodal platform and performed *ex vivo* imaging of human breast tissue (Patil 2008), this technique will require considerably more laboratory and clinical trials before its potential utility in the detection and diagnosis of breast cancer can be established.

Diffuse optical tomography, or diffuse optical spectroscopy for two-dimensional imaging, uses transmission of NIR light to provide functional information about breast tissue, such as tissue oxygen saturation and hemoglobin concentration (Konecky 2008, Durduran 2005, Ntziachristos 2001). Because changes in local vasculature and metabolism exist before structural changes become apparent, it is possible that such systems might allow earlier detection of breast cancers, and might also determine the benign or malignant nature of a lesion that is indeterminate on mammography, or might even predict response to breast cancer therapy (Xu 2007, Leff 2008, Cerussi 2007, Tromberg 2005, Fournier 2009).

A recent review of the clinical studies involving over 2000 women imaged with DOT concluded that 85% of breast lesions were visible using DOT (Leff 2008). One study suggested DOT performed comparably with MRI for monitoring tumor response to chemotherapy (Choe 2005). However, the DOT system does not provide accurate lesion localization, and more clinical trials must be undertaken before its use as a breast imaging

modality can be established. Several groups are merging the DOT technology with other breast imaging platforms such as PET, MRI, and tomosynthesis (Konecky 2008, Shah 2005, Carpenter 2007, Unlu 2008, Boverman 2007).

All of the optical imaging techniques discussed above employ endogenous contrast, but could also be used with fluorescent or bioluminescent injected contrast agents such as indocyanine green, Nile Red, and others (Ntziachristos 2000, Licha 2000, Qian 2008, Weissleder 1999, Pham 2005). Fluorescent molecular contrast agents are stimulated by incident light, resulting in fluorescence at a different wavelength. This requires consideration both for how the incident light goes into tissue, but also how the emitted light escapes the tissue. Use of nanoparticle contrast agents such as gold or iron oxide that strongly absorb NIR light might facilitate breast lesion detection, especially at increased tissue depths (Jin 2007, Hleb 2008, Lim 2008, Rayavarapu 2007). Optical contrast agents can also be functionalized or targeted toward cancer (Achilefu 2000, Chen 2003, Qian 2008, van Tilborg 2006, Medarova 2006). Because optical imaging techniques can be relatively easily integrated with conventional breast imaging systems, multimodal contrast agents are under development (for example, contrast agents with both optical and magnetic properties for use with MRI). (Jin 2008, Lai 2008, Mulder 2006, Ntziachristos 2000, Lim 2008, Bridot 2007, van Tilborg 2006, Medarova 2006, Bertorelle 2006).

A potential advantage of optical imaging is its specificity even within mammographically dense breasts, with some systems providing exceptionally fine resolution, and others generating images with information about physiological processes and even biochemical composition. Additional advantages include the use of nonionizing

radiation, real-time image acquisition, and potentially less expensive systems. However, the performance of breast optical imaging with respect to skin pigmentation has not been evaluated. One of the major disadvantages of optical imaging is the severely limited tissue penetration of light in this region of the electromagnetic spectrum due to strong attenuation (Hawrysz 2000, Demos 2006, Hsiung 2007). This results in limited field of view and often requires breast compression. More accurate models of light interaction with tissue and better biochemical and morphological models of breast tissue are needed. Additionally, clinical diagnostic parameters for optical imaging have yet to be defined. Although there are several preclinical and clinical optical imaging systems, none are presently recommended for clinical breast imaging. (Hanlon 2000)

6.8 Thermography

All objects with a temperature above absolute zero emit infrared radiation (IR). Rudimentary thermography was used to diagnose diseases by Hippocrates in 480 B.C. Modern clinical breast thermography was implemented in 1952 when breast cancers were found to have higher temperatures than the surrounding healthy tissue. Although thermography was approved for use by the FDA in 1982, recent advances in infrared scanners have only recently allowed this technology to demonstrate potential utility as a breast imaging system. (Amalu 2003, Kennedy 2009)

The temperature signatures from normal, benign, and cancerous tissues often differ by 1 to 2 degrees (Celsius) due to physiological differences in metabolism, cellular proliferation, and angiogenesis. Emitted IR can be converted into temperature by the Stefan-Boltzmann Law (Gore 2003). Camera technology currently allows resolution of temperature differences as small as 0.08ºC. Advantages of thermographic imaging

include no ionizing radiation exposure, no breast compression required, and breast density does not affect image quality. The thermographic signature may also indicate tumor aggressiveness (Head 1993). (Kennedy 2009)

Contrast-enhanced breast thermography has not been explored, but a recent report suggests that iron oxide nanoparticles, used clinically as MRI contrast agents, absorb laser light, causing an increase in temperature (Kim 2008b). Thus, contrast-enhanced breast thermography might be possible with a multimodal contrast agent for MRI or optical imaging.

Recent research has suggested that breast thermography might offer an imaging tool for young women and as an adjunct to clinical exam and mammography. Although breast thermography has been performed on thousands of women, many of these older studies suffered from a lack of standardization and limited IR camera technology. More recent studies involving patients with suspicious mammograms and/or clinical exams suggest that breast thermography may provide support for its use as an adjunct clinical breast imaging modality, with excellent sensitivity but very low specificity reported (Parisky 2003, Keyserlingk 2000, Arora 2008, Head 2000).

The diagnostic accuracy of breast thermography is compromised by normal cyclical cellular proliferation, pregnancy, benign proliferative conditions (e.g. fibrocystic breast disease), infection, and inflammation. Breast thermography does not provide any anatomic information, and does not allow accurate lesion localization, with depth-dependent resolution on the order of centimeters (González 2007). Although microcalcifications are an important early indicator of breast cancer, they are not detected reliably with thermography. Moreover, tumors with low metabolic rates or without

abnormal angiogenesis can not be detected using breast thermography. Because angiogenesis often occurs as tumors exceed their diffusion-limited size to meet increased metabolic demand, breast thermography might have reduced sensitivity for small, early cancers. (Arora 2008, Yahara 2003, Kennedy 2009)

6.9 Electrical Impedance Tomography

Electrical impedance tomography (EIT), also called electrical impedance mammography when applied to breast imaging, generates unique images based on the spatial distribution of tissue electrical properties. The first clinical electrical impedance imaging system was developed in 1978 for thoracic imaging (Henderson 1978). A known current is injected into the body surface. Ions in cells act as charge carriers, and the voltage is measured across multiple electrodes distributed across the skin surface. Breast cancer cells conduct electricity better than normal cells due to changes in cellular water content, amount of extracellular fluid, membrane properties, cellular orientation (e.g. randomly oriented cells versus sheets), and cell density (Martín 2002, Malich 2001, Malich 2003b). (Barber 1984, Brown 2003, Hope 2004)

This three-dimensional imaging technique has many advantages since it is noninvasive, does not involve exposure to ionizing radiation, and is inexpensive. Image quality is not limited by dense breast tissue and long-term monitoring is possible. However, EIT images do not provide sharp anatomical information, particularly for large lesions (Malich 2003a). Resolution is depth-limited and measurements are dependent on frequency and the location of the region of interest (Zhenyu 2005, Malich 2003a, Merwa 2007). Dual- and multi-frequency systems increase the ability for tissue characterization (Trokhanova 2008, Halter 2008, Liu 2007c, Oh 2007, Soni 2004). Electrode design and

placement affects image quality, but magnetic impedance tomography is a variant of EIT that does not require electrode placement on skin (Merwa 2007). (Hope 2004, Brown 2003, Prasad 2008, Cherepenin 2001).

Several prospective trials have evaluated EIT for breast cancer detection and diagnosis, demonstrating significant differences between abnormal and normal breast tissue with high sensitivity, but low specificity (Poplack 2007b, Stojadinovic 2006, Kerner 2002, Soni 2004, Malich 2001). One study demonstrated EIT results to be supplemental to US and MRI, facilitating classification of equivocal mammography-detected lesions (Malich 2001). Recently, EIT has been combined with other medical imaging systems such as ultrasound (Steiner 2008), mammography (Kao 2007a), and tomosynthesis (Kim 2007a). This technology may identify women at risk for breast cancer development (Stojadinovic 2006). Although there are commercially available units, EIT is not widely used in the clinic, as further system and methodological improvements are warranted. (Hope 2004, Brown 2003)

6.10 Phase-Sensitive X-Ray Imaging Methods

There are three well-established categories of phase-sensitive x-ray imaging modalities: free-space propagation, interferometry, and analyzer-based imaging. There is also a developing method of phase contrast imaging that uses coded apertures to capture phase information. Phase contrast imaging has a specific advantage in its ability to acquire excellent images at a range of x-ray energies. Because refraction contrast does not decrease nearly as rapidly as absorption with increasing x-ray energy, we expect phase contrast imaging to remain efficient even at high energies. In fact, Donnelly and Price demonstrated that the edge enhancement effect due to phase contrast only

minimally deteriorated with increasing energy (2002). While each has specific advantages and limitations, the drawback to many phase contrast imaging systems is the requirement for coherent, high flux x-ray sources (Wu 2005). However, recent advances in x-ray tube and detector technologies have allowed development of multiple preclinical and clinical phase contrast imaging systems which are being evaluated for a range of medical imaging applications. (Kotre 1999, Fitzgerald 2000, Lewis 2004)

X-rays that refract from an object due to phase variations will cause interference effects, but these systems require some distance of travel before these intensity modulations can be detected. Techniques that obtain phase contrast by free-space propagation in order to discern interference effects go by several names, including in-line holography, refraction-enhanced imaging, and propagation-based phase contrast imaging. We will refer here to this technique as the latter. Propagation-based phase contrast imaging has been described using Fresnel (near-field diffraction) effects by placing the detector relatively close to the sample, as well as Fraunhofer (far-field diffraction) effects where the detector is placed a large distance from the source. While Fraunhofer diffraction systems can truly record refraction contrast, Fresnel diffraction-based systems record images with contrast based on both absorption and refraction, essentially increasing image quality through edge enhancement. Unlike interferometry and analyzer-based phase contrast imaging, propagation-based methods can use either monochromatic or polychromatic x-ray sources, and is possible using a divergent x-ray source. Planar and three-dimensional propagation-based phase contrast systems have been described. (Authier 2001, Arfelli 1998, Arfelli 2000, Snigirev 1995, Cloetens 1999, Pagot 2005, Peele 2005, Matsuo 2005, Gundogdu 2007, Olivo 2009)

Because the free-space propagation method is the simplest and most stable, these types of systems, particularly those based on Fresnel diffraction, are the furthest along toward clinical translation. Several researchers have implemented propagation-based phase contrast imaging systems using conventional x-ray tubes, microfocus x-ray tubes, and synchrotrons (Snigirev 1995, Wilkins 1996, Suzuki 2002, Dreossi 2008, Zhang 2008a, Zhang 2008c, Honda 2008, Olivo 2009). In 2005, Konica Minolta released the first clinical phase contrast x-ray tube mammography system based on free-space propagation detection of near-field diffraction ("Phase Contrast Technology" 2008, Tanaka 2005). This system is undergoing FDA approval trials in the U.S. at present.

Even though x-ray tubes can generate phase contrast imaging, coherent sources with exceptionally small focal spot sizes provide the best phase contrast images. This type of source is available at a synchrotron, and in 2006, Italy's Elettra Synchrotron Light Laboratory's Synchrotron Radiation for Medical Physics (SYRMEP) beamline established a phase contrast mammography project imaging live patients using free-space propagation phase contrast (Dreossi 2008). Although both the Konica Minolta and SYRMEP prototype systems are promising, they are still limited by the technical challenges imposed by these geometries which require specific source dimensions and pixel sizes in order to generate sufficient image quality (Olivo 2006).

Interferometry uses interference effects of x-rays to create an image based on phase variations induced in an incident x-ray wave by an object. After a monochromator, three perfect, matching crystals are aligned. The first crystal splits the incident beam. An object is placed in one of these two beams. A second crystal reflects both of these beams onto the third crystal which recombines the beam, creating image contrast based on the

interference effects induced by phase shifts. Several planar and three-dimensional x-ray interferometric imaging systems have been described in the literature (Momose 1996, Beckmann 1997, Weitkamp 2005, Weitkamp 2008, Pfeiffer 2006, Pfeiffer 2007, Momose 1995). (Hart 1969)

The grating interferometer can be used with coherent synchrotron sources or even incoherent commercially available x-ray tubes (Pfeiffer 2006, Pfeiffer 2007), but requires at least quasi-monochromatic x-rays and has limitations with divergent sources (Olivo 2006). Grating interferometry requires precise crystal alignment and stability, yet crystals are inherently sensitive to vibration and thermal variation. This technique is sensitive to very small phase gradients, but large phase gradients are problematic. The small field of view with grating interferometry is currently a significant limitation for medical imaging applications of this technology.

The grating interferometer phase contrast imaging system has been used for x-ray dark-field imaging (XDFI), where an image is formed based on the exclusion of unscattered photons (Pfeiffer 2008). Some XDFI imaging systems use Laue crystal optics to allow only the refracted component to contribute to image formation (Ando 2002, Ando 2005, Shimao 2006, Shimao 2007, Kunisada 2008), while others use multilayer reflector analyzers (Protopopov 2005). These XDFI systems generate images based on scatter contrast similar to the multiple image radiography image processing discussed in Section 8.5.

Planar and three-dimensional analyzer-based phase contrast imaging uses perfect crystals to manipulate an x-ray beam, extracting phase information (Ingal and Beliaevskaya 1995, Ingal 1998, Davis 1995, Chapman 1996, Chapman 1996, Briedis

2005, Dilmanian 2000). A variable number of crystals can be used to monochromate the x-ray beam before interacting with an analyzer crystal. The analyzer crystal diffracts the x-rays emerging from the object, only reflecting x-rays traveling at a very narrow range of angles satisfying the Bragg condition, rejecting the rest. This reflectivity profile is referred to as the rocking curve (described in depth in Section 8.3). As mentioned above, crystal optics can present limitations for clinical implementation due to vibration and thermal sensitivity. Optimal analyzer-based imaging requires a monochromatic, parallel-beam source.

If the analyzer is aligned with the monochromator, then x-rays that fall within the narrow acceptance window will contribute to image formation while the rest, including scatter, are excluded. If the analyzer is angled slightly with respect to the monochromator, then x-rays that fall within the acceptance window will be reflected onto the detector with increased or decreased intensity, depending on the rocking curve characteristics. The rocking curve width defines whether a phase contrast or refractometric imaging is obtained (Gureyev 1997). Manipulation of the analyzer crystal angle allows recovery of refraction, absorption and scatter effects. X-ray dark-field breast imaging uses asymmetric diffraction to generate an image with contrast based on scatter (Ando 2008).

Recently, a coded-aperture approach to capture phase contrast has been described. This uses a sample mask to create an array of individual x-ray beams that do not interfere with each other (thus this is not an interferometric technique), that interact with the sample, then become incident to the detector. A separate detector mask defines sensitive and insensitive regions along detector pixel columns or row. By only allowing x-rays to illuminate the edge of the pixel, photons that would not normally be allowed to contribute

to image formation can be deviated by the sample into the active region, increasing signal intensity. Similarly, photons that would normally interact with the active region of the pixel can be deviated outside of the active region and reduce the signal intensity. This creates positive and negative intensity peaks similar to those obtained with DEI. These masks can be designed to facilitate the use of a divergent polychromatic conventional x-ray tube. (Olivo 2006, Olivo 2007a, Olivo 2007b, Olivo 2007c, Olivo 2008a, Olivo 2008b)

The coded aperture system can be sensitive to deviations in the vertical or horizontal plane, depending on the orientation of the masks along the detector rows or columns, respectively. A system simultaneously sensitive to deviations in both planes is feasible. This system has the advantage of using an area detector without the requirement for sample scanning. Because crystals are not used, there are not vibrational or thermal stability issues, but the masks must be very precisely aligned with little margin of error. (Olivo 2006, Olivo 2007a, Olivo 2007b, Olivo 2007c, Olivo 2008a, Olivo 2008b)

Olivo *et al* suggest that the coded aperture approach does not substantially filter the x-ray beam, and only requires approximately two times increased imaging time over a conventional system to achieve the same detector statistics. Because much of the beam is blocked, this system will have increased Poisson noise and decreased detection efficiency. The coded aperture system places restrictions on the detector pixel size. This system has issues with aliasing, and has only begun to be evaluated in the laboratory. Current studies implemented phantom imaging and one biological sample, a wasp head, imaged at only 15 keV. When imaging objects with clinically relevant thickness, the increased level of

scatter and increased proportion of multiple scatter events might rapidly deteriorate edge contrast. (Olivo 2006, Olivo 2007a, Olivo 2007b, Olivo 2007c, Olivo 2008a, Olivo 2008b)

Traditional absorption-based contrast agents should also provide absorption contrast for phase contrast imaging that can acquire images with contrast contribution from absorption events. However, novel phase contrast imaging agents are not well-researched. Zhang *et al* used saline perfusion to image mouse blood vasculature (2008). Another group used phase contrast imaging before and during displacement through high intensity ultrasound, calling this method an acoustic phase contrast agent (Hamilton 2004). Furthermore, even though multimodal phase contrast imaging systems have not yet been developed, one group has suggested blending the propagation-based and analyzer-based phase contrast imaging modalities to capitalize on each systems advantages (Coan 2005).

Several groups are developing interferometric and propagation-based phase contrast imaging systems that implement incoherent x-ray tube sources (Pfeiffer 2006, Pfeiffer 2007, Tanaka 2005, Wilkins 1996, Gundogdu 2007, Honda 2008, Kotre 1999, Zhang 2008a, Zhang 2008c). Similarly, groups are developing incoherent-source analyzer-based phase contrast imaging devices, each with limited success. Several groups have used asymmetric crystals and were limited to imaging very thin objects at low x-ray energies (Davis 1995, Ingal 1995), while another group used asymmetric crystals and a commercially available x-ray tube operating at 30 keV to measure plastic phantom thicknesses (Vine 2007). Keyriläinen *et al* performed photon counting studies with phantoms using a single-crystal monochromator DEI setup with an x-ray tube source (Keyriläinen 2002). Wang developed a prototype DEI system using a laboratory-built

tungsten x-ray tube and successfully acquired phantom images, but was restricted to a very small field of view (Wang 2006).

6.11 Summary

The low resolution of US raises questions about its use for breast cancer screening, although it is used extensively as an adjunct to mammography. MRI is expensive, but has been proven useful in the screening of high risk women and in determining extent of disease. The properties of the US and MRI breast imaging systems, which are used routinely in the clinic, are summarized in Table 6.3.

	US	MRI
Signal	Absorption, Reflection of Sound	Magnetic Relaxation
Resolution	0.3 by 0.3 by 0.1 mm	25 to 100 μm^2
Advantages	No Ionizing Radiation Inexpensive	No Ionizing Radiation, Many Imaging Protocols
Disadvantages	Poor Resolution, Requires Skilled Operator	Expensive and Large Data Set, Contraindicated for Certain Implants, Requires Nonmetallic Equipment
Compression	Some	No
Contrast Source	Anatomy	Anatomy, Physiology

TABLE 6.3: Adjunct Breast Imaging Systems with Routine Clinical Implementation.

The current high radiation dose of CT prevents clinical use, but researchers are working to implement this as a low-dose imaging modality. Nuclear medicine may be useful as an adjunct system to detect occult or metastatic lesions, but limited clinical trial data, minimal anatomical detail, and the requirement for radioisotope injection prevent its use as a screening system. Properties of imaging systems that are available but not routinely implemented for breast imaging are summarized in Table 6.4.

	SM	SPECT	PET	CT
Signal	Emission of γ-rays	Emission of γ-rays	Emission of γ-rays	Absorption of x-rays
Resolution	1 mm^2	1 – 7 cm^2	2 – 8 mm^2	0.5 mm^2
Advantages	Find Occult Cancers and Metastases, Inexpensive	Tomographic, Find Occult Cancers and Metastases, Multi-Isotope Imaging, Inexpensive	Tomographic, Find Occult Cancers and Metastases, Sensitive	Excellent Spatial Resolution, Excellent Lesion Localization
Disadvantages	Requires Injection of Contrast Agent, Limited Resolution and Specificity, Radiation Dose	Requires Injection of Contrast Agent, Depth-Dependent Attenuation, Long Imaging Time, Radiation Dose	Requires Injection of Contrast Agent Radiation Dose	High Dose, Complex Scanning Geometries, Inconsistent Data
Compression	No	No	No	No
Contrast Source	Physiology	Physiology	Physiology	Anatomy

TABLE 6.4: Adjunct Breast Imaging Systems with Limited Clinical Implementation.

Tomosynthesis delivers lower radiation dose than CT, but has lower spatial resolution. Optical, thermographic, and electrical impedance imaging systems are not currently used clinically, but show promise. Preclinical breast imaging systems, which are only beginning to establish utility as breast imaging modalities are listed in Table 6.5,

	Tomosynthesis	Optical	Thermography	EIT	Phase Contrast
Signal	X-Ray Absorption	Absorption, Reflection Refraction, Emission of Light	Emission of IR	Electrical Impedance, Permittivity	X-Ray Refraction
Resolution	2.41x2.41x3.02 mm^2	0.5 mm^2	0.08°C	Variable	50 μm^2
Advantages	Excellent Spatial Resolution, Excellent Localization	Inexpensive, No Ioinizing Radiation, High Resolution, Multimodal Platform	Inexpensive, No Ionizing Radiation	Inexpensive, Sensitive, Multimodal Platform	Unique Contrast Mechanism, Potentially Low Dose
Disadvantages	Ionizing Radiation Dose, Lower Resolution than CT	Limited Depth Resolution and Field of View, Better Models Needed	Depth-Dependent Resolution	Low Specificity	Limited Clinical Research, Needs High-Flux X-Ray Source
Compression	Some	Yes	No	No	Some
Contrast Source	Anatomy	Anatomy, Physiology	Physiology	Physiology	Anatomy

TABLE 6.5: Preclinical Breast Imaging Systems.

The adjunct and preclinical breast imaging modalities presented in this chapter have all undergone some level of evaluation as breast imaging systems, but widespread implementation in the clinic has not yet been achieved. These systems must find a niche in which they offer advantages over existing breast imaging technologies. The process of demonstrating these advantages will now be covered in Chapter 7, discussing the clinical translation of medical imaging technologies.

CHAPTER 7: TRANSLATING EMERGING TECHNOLOGIES INTO THE CLINIC

7.1 Overview

Clinical trial design is an important factor in translating emerging breast imaging technologies into the clinic. These trials help establish for which women a system provides safe, accurate, and cost-effective breast cancer imaging. The following chapter reviews clinical utility, diagnostic accuracy, several methods for comparing medical imaging systems, and clinical trial design.

The climate of dramatically advancing technologic capabilities drives the improvement of existing medical imaging systems and allows novel concepts to be realized and developed. Even though many different imaging technologies have been evaluated for potential breast imaging applications, very few are actually available clinically, and even fewer are routinely used for the detection and diagnosis of breast disease. Mammography has been the staple of breast imaging clinical protocols for decades. Ultrasound has achieved routine use as an adjunct imaging technique. Although MRI has many benefits and has clearly demonstrated clinical utility, it is still not routinely used except within specific subsets of women. All other imaging modalities have not yet been subjected to sufficient study to provide appropriate evidence to justify clinical implementation. The fact that a system can acquire images of breast cancer does not necessarily mean that it will be clinically useful.

7.2 Diagnostic Accuracy

Accuracy, as it applies to breast cancer screening, describes the clinical utility of a modality and its freedom from error, both false positives and false negatives. Both quantitative accuracy and diagnostic accuracy are important. Quantitative accuracy describes error due to bias and imprecision. Diagnostic accuracy refers to the fraction of patients that are diagnosed correctly using a particular imaging system, given the errors and biases that are present in the system. Diagnostic accuracy of a qualitative diagnostic imaging system can be expressed by sensitivity/specificity, overall accuracy, likelihood ratio, predictive values, diagnostic odds ratios, or area under the receiver-operator characteristic (ROC) curve. Only the sensitivity and specificity are directly measured, using a contingency table as shown in Table 7.1. Other diagnostic accuracy parameters can be calculated from sensitivity and specificity data.

		Disease	
		+	-
Test	+	A	B
	-	C	D

TABLE 7.1: Contingency Table. The contingency table values are based on the number of cases within the population set that meet the criteria in each column and row. The (+) disease column represents the presence of the disease, in this case breast cancer. The (-) disease column are cases within the population that do not have breast cancer. The (+) test row represents cases where the test system detected an abnormality, while the (-) test row represents cases in which the test system did not detect an abnormality. So A represents the true positive tests (TP), B represents the false positive tests (FP), C represents the false negative tests (FN) and D represents the true negative tests (TN).

Sensitivity refers to the true-positive fraction of patients who have breast cancer and are diagnosed with breast cancer by screening mammography. Referring to the

contingency table above, sensitivity is defined as A / (A + C), or (TP) / (TP + FN). Specificity represents the ability of the screening modality to indicate a patient as normal when breast cancer is not present. Specificity is calculated as D / (B + D), or (TN) / (TN + FP). Diagnostic accuracy is maximized by maximizing sensitivity and specificity, and is calculated by the formula (A + D) / (A + B + C + D), or (TP + TN) / (entire population).

In the real world, imaging features of normal and diseased conditions overlap, so test thresholds must be established that balance the sensitivity and specificity of a system for specific tasks. This threshold depends partially on the cost-benefit ratio. For example, identifying more regions of interest as suspicious increases the sensitivity such that more cancers will be detected, but decreases specificity, at the cost of potentially invasive follow-up procedures. This also increases the emotional and financial burden to the patient. When determining this threshold, both prevalence and overall health risk (short- and long-term) of such a lesion should be taken into consideration. Prevalence is an estimate of the frequency of a disease state within a specific population over a finite period of time, which is given by (A + C) / (A + B + C + D), or (TP + FN) / (entire population).

Positive predictive value (PPV) and negative predictive value (NPV) can also indicate system performance. For breast cancer screening, PPV represents the fraction of patients that a screening test identified as having breast cancer that actually have breast cancer. This is calculated by: A / (A + B), or (TP) / (TP + FP). The NPV, which is calculated by D / (C + D), or (TN) / (FN + TN), is the fraction of patients whose

screening mammography was negative for the presence of breast cancer that are actually disease free. Both PPV and NPV depend on the actual prevalence of breast cancer.

The diagnostic likelihood ratios (DLRs) are not dependent upon breast cancer prevalence. The positive DLR represents the probability that a suspicious finding on screening mammography will be found when screening patients with breast cancer, compared to the probability that a suspicious finding will occur for patients without breast cancer. This can be calculated as: [sensitivity / (1 – specificity)]. Conversely, the negative DLR represents the probability that a negative screening mammogram is obtained when imaging patients that have breast cancer, compared to the probability that a negative screening mammogram will be obtained for patients that have breast cancer. This is calculated as: [(1 – sensitivity) / specificity].

7.3 Receiver-Operator Characteristic Curve and Likert Analysis

Calculation of the area under the ROC curve (AUC) is the standard method of comparing medical imaging systems, and is based on the determination of true-positives and false-positives and includes the role of reader preference in such determinations. An image of a cancer that was ranked as suspicious or highly suspicious of cancer is typically considered a true positive. False negatives are more difficult to accurately determine. For example, an image that received a ranking of probably benign or lower but proved malignant at biopsy represents a false negative. However, false negatives are also accrued when the lesion is not seen at all on the test or reference images, but is later seen in retrospect or on follow-up imaging. This type of false negative is the most difficult to quantify.

The ROC curve is a plot of the false-positives on the x-axis and the true positives on the y-axis. Similarly, a relative operating characteristic curve is constructed using the true positive and false positive *rates*. The relative ROC curve is particularly useful because it is insensitive to both uneven prevalence distribution and unequal error costs, which are common, particularly in screening studies (Fawcett 2006). Instead, it represents a relative measure of the tradeoff between the benefit of identifying a cancer as such and the cost of incorrectly identifying normal tissue as suspicious or cancerous. The ROC curve is generally calculated for each reader. Correlation values and inter-reader variability must be considered in the calculation of an averaged AUC.

The Likert scale uses gradations along a confidence scale to provide information on a range of image features. For example, readers might be asked to evaluate image quality of calcifications, general image quality or confidence of malignancy, ranking their findings on a scale which typically ranges from 5 to 7 gradations. This might allow an estimation of how far from truth the test system provides information to informed readers. Confidence rankings on a Likert scale can be compared to the reference standard to determine the TP and FP ratios. These values can then be plotted on an ROC curve. Multiple readers can rank images based on a Likert scale, which is particularly useful when analyzing systems that are unfamiliar to readers, as a significant amount of inter-reader variability might exist.

Likert scale comparison allows more flexibility for comparison of dissimilar systems than ROC analysis, which requires the same model and precludes comparison between fundamentally distinct imaging systems. Furthermore, Likert scale analysis can be more general and does not necessarily require a known truth state. ROC analysis

requires a binary truth state (either the disease is present or it is not) determined independently of the test imaging system, but truth is indeterminate for some analyses. Additionally, the Likert scale can also be used to assess reader preferences or patient perceptions, when diagnostic accuracy might not necessarily be relevant (Rampaul 2004). Likert scale analysis is a more statistically powerful method, meaning it requires fewer cases and readers to demonstrate significant differences.

7.4 Clinical Trial Design

A new technology must be rigorously evaluated in laboratory and clinical trials before being adopted for use in the clinic. Images must be acquired on the test system as well as on a reference system that is the clinical standard and/or identifies truth. Phantom imaging allows quantitative system characterization and optimization of imaging parameters with designed truth parameters. The typical next step is to image breast tissue specimens, where truth is determined through histopathologic sectioning. Imaging tissue specimens allows initial measurements of sensitivity and specificity with control over population parameters. Together, phantom and specimen imaging allows the collection of preliminary safety data.

When a system has exhibited sufficient image quality and safety in laboratory studies, a clinical trial must be designed. Potential imaging applications of the technology (screening, diagnostic imaging, assessment of extent of disease, monitoring therapy response) will influence study design. Trial procedures include patient eligibility criteria (e.g. age, race/ethnicity, mammographic density, family history, breast size, prior cancer, prior surgery, implant), imaging parameters (e.g. subject radiation dose, contrast enhancement, reference imaging system), study endpoint, associated laboratory testing

(e.g. biopsy, genetic testing), and criteria for data inclusion (e.g. image quality). Statistical procedures include study design (e.g. prospective, retrospective, blinded), study hypotheses, sample size estimation, randomization protocol, as well as data and statistical monitoring for interim and final analyses.

As of 2006, the FDA has promoted adaptive trial design, such that modification of trial and/or statistical procedures based on interim data analysis can occur while a trial is ongoing in order to increase the likelihood of achievement of study endpoints without compromising the validity of the original trial (Chow 2008, Mehta 2009). Initial pilot clinical trials often start with small targeted patient populations, which provide information on efficacy and system performance. The next step may be to compare the new technology to the gold standard in a head-to-head comparison by way of a randomized or double-blind randomized, controlled trial controlling for and possibly matching as many variables as possible. Expert radiologists analyze the images, ranking their suspicion of malignancy on a confidence scale (as used for Likert or ROC). Head-to-head studies with competing breast imaging systems supply data for cost and diagnostic accuracy, and may demonstrate further where a system might fit within the slope of breast imaging technologies.

7.5 Summary

In order to be clinically valuable, a system must demonstrate an improvement over the current gold standard. Ideally, an improvement would represent an increased ability to detect and/or diagnose breast cancer at an earlier stage, as this may lead to reduced morbidity and mortality. However, a system might also demonstrate improvement over the gold standard with respect to the risk-benefit or cost effectiveness

ratio, or in terms of patient quality of life. For example, while an imaging system might detect certain lesions with high sensitivity and specificity, it might also expose the patient to excessive ionizing radiation, or be insensitive to other types of lesions. Such demonstrations of clinical utility must be performed for every application of the imaging technology, such as for breast cancer screening, diagnostic and/or adjunct breast imaging, detection of multifocality or metastases, or tumor size quantification.

One must consider the population for which the system demonstrates clinical utility, and whether the results with this population can be generalized. Additional factors that should be considered in the evaluation of any new technology include the risk to operator health, effect on workflow capability, cost to patients (e.g. insurance reimbursement), requirement for a skilled operator, and cost to operate and maintain equipment. Every imaging system is faced with fundamental tradeoffs with respect to image quality, diagnostic accuracy, and cost. Diffraction-enhanced imaging is a novel x-ray imaging system that has undergone laboratory studies to evaluate lesion visibility and explore potential clinical applications. The DEI system and the results of previous studies evaluating DEI for breast imaging applications will be discussed in the following chapter.

CHAPTER 8: DIFFRACTION-ENHANCED IMAGING

8.1 Overview

Synchrotron radiation applied to mammography has demonstrated improved contrast and resolution due to intense, smooth, and highly collimated synchrotron x-rays (Burattini 1992, Burattini 1995, Johnston 1996, Margaritondo 1988). In 1980, Förster proposed the Schlieren method of diffractometry using synchrotron radiation, a single-crystal collimator, and a one- or two-crystal analyzer (1980). The Schlieren method was modified by Chapman in 1996, renamed diffraction-enhanced imaging (DEI), and investigated as a breast imaging modality. DEI has traditionally utilized synchrotron radiation, and is capable of producing images based on the independent contrast mechanisms of refraction, absorption, and extinction due to unique properties of x-ray diffraction in perfect crystals (Davis 1995, Ingal 1995, Chapman 1997, Hasnah 2002b).

The following chapter presents general DEI concepts and DEI system design features. This is followed by a review of how the DEI system converts x-ray refraction into image contrast using Bragg diffraction from perfect crystals. The discussion of DEI image processing techniques presents the removal of analyzer-based artifacts, as well as post-processing techniques that generate images unique to medical imaging. This is followed by presentation of three-dimensional DEI using CT image acquisition and processing techniques.

8.2 Fundamentals of Diffraction-Enhanced Imaging

The application of DEI to breast imaging has consistently provided superior contrast and signal-to-noise ratio (SNR) when compared to conventional radiographic images (Pisano 2000, Kiss 2003, Kiss 2004, Chapman 1996, Chapman 1997, Chapman 1998, Hasnah 2002b, Fiedler 2004, Liu 2007a, Fernández 2005, Lewis 2003). DEI has also demonstrated better performance than other phase contrast imaging techniques (Pagot 2005, Kitchen 2005).

The DEI system utilizes a series of two perfect crystals to make the x-ray beam monochromatic before interaction with the object. The beam emerging from the object then diffracts from a third perfect crystal, referred to as the analyzer, which directs refracted x-rays onto the detector. The analyzer separates the transmitted beam into individual images based on Bragg's law of diffraction, rejecting all wavelengths except the narrow range (approximately 1 microradian) of wavelengths at its Bragg reflection (θ_B), characterized by a rocking curve.

The narrow width and steep sides of the rocking curve convert extremely small differences in refractive indices into large changes in x-ray intensity reflected onto the detector. Rejection of scattered x-rays traveling at angles outside the narrow acceptance window of the rocking curve occurs at angles appreciably smaller than those rejected by antiscatter grids used in conventional mammography. Although monochromaticity offers distinct advantages, the contrast mechanisms of refraction and extinction uniquely provided by diffraction from the analyzer crystal allow for increased fine detail visibility. (Chapman 1996, Chapman 1997, Pisano 2000, Zhong 2000, Dilmanian 2000)

Soft tissue imaging is difficult because the physical and electron density of normal and abnormal tissues often does not vary greatly. DEI may facilitate breast tumor detection, classification, and characterization of growth patterns because of its extreme sensitivity to even exceptionally small differences in refractive indices, particularly at the interface between healthy tissue and the aberrant structure of cancerous lesions. Photons at interfaces are strongly deviated, creating a region of edge enhancement due to interference effects or rejection by the analyzer. These inherent edge enhancement effects due to interference occur without an associated increase in noise as occurs with computerized edge-enhancement algorithms. Thus, structures that are too small to produce attenuation contrast, such as thin collagen strands or thin spiculations of cancers, potentially produce refraction contrast with edge enhancement (Fiedler 2004).

At x-ray energies between 14 and 30 keV, the linear attenuation coefficient of breast cancers is often greater than that of the surrounding normal tissue (Johns 1987, Carroll 1994). Conventional mammography is restricted to low x-ray energies in order to obtain sufficient image contrast due to the rapid decrease in photoelectric absorption as x-ray energy increases. These low energy x-rays are readily absorbed, contributing to increased dose and decreased exposure on the detector which increases the noise content in the images.

DEI imaging parameters and image quality are still under investigation. We previously estimated that 60 keV is likely the optimal imaging energy for DEI, whereas conventional mammography is limited to an energy range of between 20 and 30 keV (Parham 2006). Refraction events decrease much more slowly with increasing energy, indicating that DEI can implement higher x-ray energies where radiation dose is low, and

the x-rays have greater penetrance. Because refraction imaging is not restricted to low-energy imaging, this allows a more tunable energy window.

Because ionizing radiation exposure carries stochastic risks of radiation-related diseases, exposures should remain as low as possible. Conventional attenuation contrast images require radiation absorption by the patient to create differential attenuation patterns. The typical delivered dose represents a balance between the dose required to visualize structures with sufficiently low Poisson noise while minimizing the risk of stochastic radiation damage. While the optimal dose for DEI breast imaging has yet to be defined, DEI inherently offers low-dose, high-contrast images. DEI resolution depends on which contrast mechanisms are implemented. For refraction contrast, resolution can reach 0.1 mm, while some have found resolution in the range of tens of nanometers with extinction contrast (Fernández 2005).

8.3 DEI System Setup

DEI has traditionally implemented a collimated, polychromatic 130 mm by 2 mm fan beam diverted to an imaging hutch from the bending-magnet SR source, shown in Figure 8.1. The x-ray beam first passes through a beryllium window, then an aluminum filter to reduce ozone-producing low-energy x-rays. A series of two 10 mm thick perfect float-zone silicon crystals were mounted on independently tunable stages allowing adjustment of the Bragg and azimuthal angles with 0.03 μm angular resolution. The crystals and stages were positioned in a continuously Helium-flushed steel tank with Kapton windows. This setup transforms the polychromatic SR beam into a monochromatic beam, with energy selection based on Bragg angle manipulation of the monochromator crystals. The monochromator system is on a granite block supported by

steel beams with vibration-reducing feet. The crystal optics are extremely sensitive to temperature fluctuations, which requires a warm-up period in order to reach thermal equilibrium. (Chapman 1996, Zhong 2000)

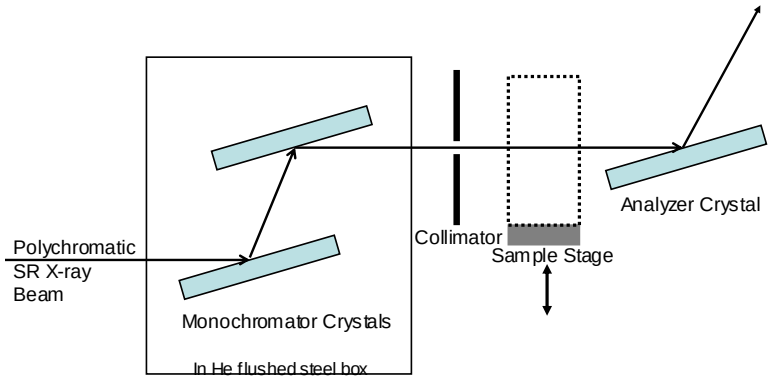

FIGURE 8.1: Synchrotron-based DEI System Configuration. An intense, collimated polychromatic synchrotron x-ray beam is made monochromatic by a parallel series of two perfect crystals, referred to as the monochromator. Manipulating the monochromator angle allows energy selection of the subsequent monochromatic x-ray beam. This monochromatic beam interacts with the object before becoming incident onto the third perfect crystal, referred to as the analyzer crystal. Manipulating the angle of the analyzer crystal allows image contrast based on either absorption or refraction, both with almost no scatter due to the highly efficient filtering by the analyzer (extinction).

The shutter and stage are isolated on an arm attached to a frame that is secured to the floor to prevent vibration. The object being imaged is then scanned through the collimated monochromatic x-ray beam by vertical translation of a sample stage. X-rays interact with the object before diffraction by the analyzer crystal. The analyzer crystal is identical to the monochromator crystals and aligned with matching reflectivity. The analyzer crystal angle can be adjusted with 0.1 μm angular resolution. The detector is positioned at twice the Bragg angle.

Both SR sources and conventional x-ray tube sources have limited capability to produce high energy x-rays at high flux. X-Ray tubes are limited by heat production when generating high flux, high energy x-rays. The DEI system can use either indirectly digital photostimulable phosphor image plates or a directly digital flat-panel detector. Although many imaging systems are transitioning to digital detectors, this is not always a practical choice for low-flux systems. For low-flux applications, the use of directly digital detectors leads to high electronic noise, compromising image quality. In this case, image plates can be used, but suffer from latent image degradation as a function of time and light contamination. Both digital detector types must have high stopping power in order to efficiently detect high energy x-rays, representing a fundamental tradeoff between resolution and noise.

8.4 Bragg Diffraction from Perfect Crystals and the Rocking Curve

Perfect crystals are made up of many planes of atoms, which form three-dimensional unit cells. These unit cells can take on many shapes. The spacing between the atoms in the unit cell is referred to as the d-spacing. Each plane of atoms in the crystal will reflect a portion of the incident beam, so the intensity drops off with increasing depths within the crystal. Diffraction from perfect crystals is described by the dynamical theory of diffraction. Bragg's Law explains the diffraction of x-rays from the surface of perfect crystals as follows:

$$n\lambda = 2d\sin(\theta) \tag{31}$$

where n is an integer representing the order of reflection (for the [111] reflectivity, n=1; for the [333] reflectivity, n=3), λ is the photon wavelength, θ is the angle measured from the crystal plane, and *d* refers to the "d-spacing" of the lattice points within the crystal.

Crystal defects or strains placed on the crystal structure will influence diffraction patterns. (Cullity 1978, Authier 2001)

The many photons constituting a polychromatic incident x-ray beam can be approximated as the superimposition of multiple scalar plane waves which might experience interference effects. This allows the application of the transport intensity equation to obtain phase information from detected intensity differences. When the plane wave is diffracted from atoms in a perfect crystal as depicted in Figure 8.2, differences in path length are introduced. This leads to phase shifts equal to the difference in path length, and thus a change in amplitude due to constructive and destructive interference. The plane-spacing equation,

$$\text{Plane Spacing} = 1 / d^2 \qquad (32)$$

combined with the Bragg formula (Eqn. 31) allows prediction of every potential angle at which diffraction might occur. However, some predicted Bragg angles are forbidden and result in zero diffracted beam intensity. (Cullity 1978, Authier 2001, Briedis 2005).

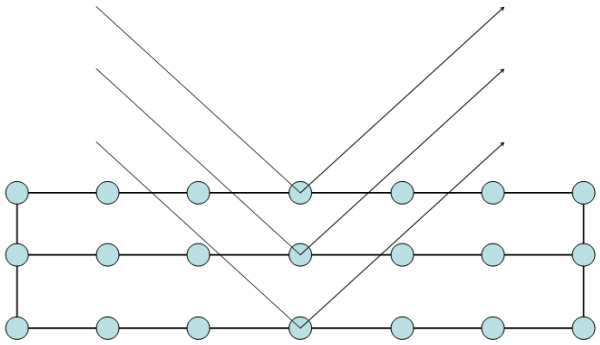

FIGURE 8.2: Perfect Crystal Diffraction. The angle of diffraction is determined by the size and shape of the crystal's unit cell, characterized by d-spacing. Incident x-rays will diffract at the same angle when they interact with an atom in a crystal, but travel different distances within the crystal before such interaction. This leads to alterations in path length and phase with subsequent interference and the reflection of only a specific narrow range of wavelengths.[11]

11. The figure adapted from the following sources: Authier 2001, Cullity 1978

The diffracted beam is not a single energy for several reasons. First, dynamical theory of diffraction predicts a narrow range of angles that satisfy the Bragg diffraction criteria. Moreover, crystal imperfections smear the permitted Bragg angles into a narrow range of angles diffracted. Lastly, crystal diffraction for a particular x-ray wavelength will also occur at $\lambda / 2$ for the second order reflection, $\lambda / 3$ for the third order reflection, and so on. (Cullity 1978)

The analyzer rocking curve, shown in Figure 8.3, represents the reflectivity profile from the analyzer crystal. The peak position represents near complete reflection, and the slopes allow small changes in refraction angles to be converted into intensity changes reflected onto the detector. The rocking curve has been modeled systematically by Oltulu *et al,* and approximated as a Taylor series by Chapman *et al*:

$$R(\theta_0 + \Delta\theta_z) = R(\theta_0) + dR/d\theta\ (\theta_0)\ \Delta\theta_z \qquad (33)$$

where $R(\theta_0)$ is the rocking curve at the ½ W_D position and $\Delta\theta_z$ is the vertical diffraction component (Oltulu 2003, Chapman 1997). The degree of intensity fluctuation due to refraction depends on the slope of the rocking curve, with steep rocking curve slopes generating the greatest refraction contrast. Factors that broaden a rocking curve and decrease slope include increasing x-ray wavelength, beam divergence, polychromaticity, non-rejected scatter radiation, and crystal reflectivity.

Analyzer tuning refers to manipulation of the analyzer crystal angle relative to the monochromator crystals. The zero rocking curve tuning angle is obtained when the crystals are positioned in parallel, and is called the Bragg angle, θ_B. The intensity diffracted from the analyzer I_R at the low angle side (I_L, -½ W_D) or high angle side (I_H, +½ W_D) is as follows:

$$I_R = (dR/d\theta)\,\Delta\theta_z \tag{34}$$

where $(dR/d\theta)$ is the gradient of the rocking curve at the respective angle and $\Delta\theta_z$ is the deflection angle, calculated as follows:

$$\Delta\theta_z \approx 2\Delta\delta\tan\theta_1 \tag{35}$$

where $\Delta\delta = n_1 - n_2$. The values of n_1 and n_2 represent the refractive indices of two materials at an interface. (Chapman 1997)

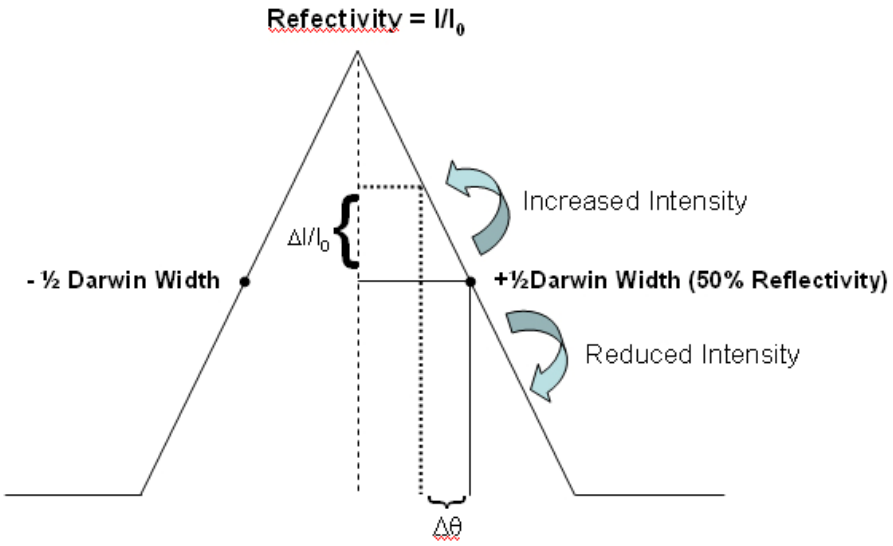

FIGURE 8.3: DEI Rocking Curve.[12] Reflectivity is equal to the intensity at the detector (I) divided by the intensity delivered to the object (I_0). For perfect silicon crystals, the rocking curve width is typically between 1 and 10 μrads. When positioned at the ±½ W_D, 50% of incident x-rays are diffracted onto the detector. Refraction above or below the plane of the incident x-ray beam will cause an increase or decrease in x-ray intensity at the detector. Maximal reflectivity occurs at the peak of the rocking curve where image contrast is due to a mixture of absorption, refraction, and scatter rejection. Excellent scatter rejection occurs at the peak and refraction of x-rays will decrease intensity regardless of the direction of refraction, creating an image that appears similar to an absorption-based image.

Rocking curve position greatly influences the relative contribution of each contrast mechanism to overall image contrast. With the analyzer tuned to the peak of the rocking curve (W_D), the incident beam is completely reflected and image contrast is

12. This figure adapted from the following source: Zhong 2000.

based predominantly on x-ray absorption. Any change in x-ray propagation direction through refraction or scatter results in decreased intensity. Benefits of imaging at the peak include maximal reflectivity and optimal scatter rejection (Fiedler 2004). For soft tissue, peak images are sharper, and possess more contrast with a wider dynamic range and reduced noise when compared to conventional radiographs (Lewis 2003, Kiss 2003).

Maximal refraction contrast is obtained at ±½ W_D, approximately the full width at half maximum of the rocking curve, where 50% of the incident beam is reflected. Refraction above or below the axis of the incident x-ray beam will cause an increase or decrease in x-ray intensity at the detector. When positioned on the slope of the rocking curve, image contrast is based predominantly on refraction, but without processing will also include contribution from absorption and USAXS. Several different methods have been developed that might allow simultaneous acquisition of absorption and refraction DEI images, facilitating dynamic DEI imaging (Siu 2005, Hasnah 2002b). (Briedis 2005, Oltulu 2003, Authier 2001)

8.5 DEI Image Processing

Crystal optics inevitably contain flaws that cause slight variations in diffracted image intensity, causing a vertical striping artifact in DEI images. Because these stripes represent differing photon counts across the image, the Poisson noise also varies across the image. These stripes are removed by an in-house image processing algorithm referred to as Dean flattening. This technique normalizes the beam intensity across the image but slightly decreases the image resolution. Because noise is a random process, it is not wholly normalized by the flattening.

8.6 Post-Processing DEI Images

Post-processing can be applied to sets of DEI images acquired in exactly the same manner except for rocking curve position, obtaining unique images such as pure refraction, apparent absorption, mass density, and extinction. However, these combinations of images suffer from increased noise since the random Poisson noise does not cancel out. Subtraction of the +½ W_D and -½ W_D images, with a normalization factor, provides a pure refraction image. Apparent absorption contrast images can be obtained by processing applied to a pair of refraction images acquired at the +½ W_D and –½ W_D with an appropriate normalization factor, calculated pixel by pixel with the following formula:

$$I_R = \frac{I_L(dR/d\theta)(\theta_H) - I_H R(\theta_L)}{R(\theta_L)(dR/d\theta)(\theta_H) - R(\theta_H)(dR/d\theta)(\theta_L)} \quad (37)$$

(Chapman 1997, Lewis 2003, Dilmanian 2000). Apparent absorption images and images acquired at the peak of the rocking curve appear almost identical (Lewis 2003).

Another post-processing technique transforms the information contained in the DEI refraction image into an energy-independent mass density image, which appears very similar to absorption images and contains much of the same information. (Hasnah 2005, Wernick 2006). A compositional image can be formed using the mass density image and the refraction image. This compositional image has direct relation to the absorption per electron of the object being imaged and might allow highly specific identification of tissue components (Hasnah 2007).

Considerable scattering occurs at diagnostic x-ray energies, becoming the dominant interaction as energy increases due to a rapid decrease in photoelectric absorption. Scatter rejection is the dominant contrast mechanism for extremely small objects approaching pixel-size because at this level, refraction averages out over the

object (Kiss 2003). Scatter images convey tissue information on a molecular level, allowing the interpretation of intensity changes to infer size, shape, and electron density of the objects imaged with the potential for excellent contrast and SNR (Johns 2002, Wernick 2002, Wernick 2003, Khelashvili 2006, Muehleman 2006a, Chou 2007). Some scatter signatures are unique to tissue type and disease state (Evans 1991, Kidane 1999, Fernández 2005, Falzon 2006, Fernández 2008).

The multiple image radiography (MIR) post-processing technique uniquely generates images with contrast depending solely on scatter due to extinction-based intensity modulations, as well as producing absorption and refraction images. Similar post-processing techniques are referred to as generalized DEI, or extended DEI, requiring image acquisition at three rocking curve positions in order to generate images with contrast based uniquely on absorption, refraction, or scatter (Rigon 2008). (Wernick 2002, Wernick 2003, Khelashvili 2006, Muehleman 2006a, Chou 2007, Pagot 2003)

8.7 DEI Computed Tomography

Although refraction contrast images are not as severely limited by tissue thickness as attenuation contrast images, overlying tissues might still decrease image quality (Gang 2005). Post-processing applied to a series of planar DEI images acquired through 360º allows tomographic refraction imaging, termed DEI-CT. The DEI-CT technique provides excellent contrast and fine detail visibility allowing lesion visibility and localization (Fiedler 2004, Dilmanian 2000, Hashimoto 2006, Wang 2006a, Yuasa 2006, Yuasa 2007, Yuasa 2008, Huang 2007, Sun 2007, Bravin 2007, Majumdar 2004, Gao 2006). DEI-CT has been applied to imaging of the breast, liver, lung, eye, bone, and cartilage (Bravin 2007, Hashimoto 2006, Majumdar 2004, Gao 2006).

Fiedler *et al* demonstrated that DEI-CT images acquired at the +½ W_D had very high contrast, and images acquired at the peak of the rocking curve that exhibited increased fine detail visibility when compared to standard clinical CT (2004). In fact, when the analyzer crystal was removed to obtain a synchrotron-CT image using the synchrotron x-rays and monochromator crystals, the image produced was still improved over standard CT images, but the previous fine details could not be resolved (Fiedler 2004). This reinforces the fact that although there is a substantial benefit to image quality by using monochromatic x-rays, the unique contrast mechanisms of refraction and extinction that are possible with DEI allow for increased visibility of fine details.

The main difference between the planar DEI and DEI-CT system configuration is that the sample stage can rotate for DEI-CT in addition to the standard vertical translation used for planar DEI. Because of the nature of computed tomography, DEI-CT requires the use of a digital detector. Otherwise, the acquisition system is the same. So far, DEI-CT has only been achieved with a SR source, but recent advances in x-ray tube technology might make DEI-CT using an x-ray tube source feasible in the future. Both planar DEI and DEI-CT suffer from flux limitations, a large technical challenge to the construction of a practical DEI-CT prototype. Several other limitations of the DEI-CT technology include limited field of view and excessive radiation dose. While field of view is not a substantial problem with planar DEI, limited field of view is much more important for DEI-CT, and might pose problems for imaging large regions of interest, such as the breast. Radiation dose delivered during DEI-CT imaging is higher than clinically acceptable, but dose can be significantly decreased by optimizing the detector, increasing the x-ray energy and decreasing the dose per slice.

DEI utilizes the refractive index gradient vector, but conventional CT algorithms require scalar data. Refraction angles, $\Delta\theta_z$, are calculated using Equation 35, then used to create a refraction-angle sinogram. The line integration of angular deviations are shown:

$$\Delta\theta_z = \int(\partial n/\partial z)(l)\mathrm{d}l \qquad (38)$$

Because it is similar to standard CT line integrals, standard filtered back-projection (FBP) algorithms can then be applied to produce refraction contrast CT images. Although less than ideal, such direct application will preserve refraction contrast. CT has also been applied to the MIR technique (Rigon 2008, Brankov 2006). (Wang 2006a, Dilmanian 2000, Fiedler 2004, Yuasa 2007, Sun 2007, Huang 2007, Yuasa 2006)

8.8 Summary

Although DEI and DEI-CT have shown initial promise, much more remains to be evaluated before potential clinical utility can be evaluated. These systems have the major advantage of being able to acquire both conventional and novel images with the potential for radiation dose reduction. Studies should evaluate these systems in clinically relevant tasks evaluating such parameters as lesion detection and characterization, recall rate, and so on. Initially, DEI might find clinical applications for problem cases or for presurgical evaluation of extent of disease. The excellent contrast and fine detail visibility possible with the DEI refraction contrast images might allow multiple clinical applications. Furthermore, DEI's many potential medical imaging applications and versatile image contrast mechanisms make it a potentially excellent multimodal imaging platform. However, identifying the appropriate clinical applications of DEI will be challenging. In order to supersede a system currently used clinically, DEI must prove to be less invasive, safer, more effective, and less expensive.

CHAPTER 9: DIFFRACTION-ENHANCED IMAGING APPLICATIONS

9.1 Overview

Phase contrast imaging techniques utilize x-ray refraction, with several advantages over absorption-based imaging, such as sensitivity to exceptionally small changes in the refractive index, as well as the ability to image at higher x-ray energies where dose is low (Donnelly 2002). Several preclinical and clinical free-space propagation, interferometric, and analyzer-based phase contrast imaging systems are under development (Kotre 1999, Fitzgerald 2000, Lewis 2004, Snigirev 1995, Wilkins 1996, Suzuki 2002, Dreossi 2008, Zhang 2008a, Honda 2008, Tanaka 2005). The DEI system generates excellent contrast over a sufficiently large field of view while delivering a low radiation dose. DEI has also been explored for imaging a variety of tissue types, such as breast, cartilage, lung, heart, liver, kidney, brain, thyroid, eye, uterus, and bone.

9.2 Breast

Breast cancer is the second most common cancer among women in the United States, behind skin cancer (U.S. Cancer Statistics Working Group 2007). It is also the second most common cause of cancer death among American women, behind lung cancer (SEER Program 2007). Earlier cancer detection generally leads to better prognosis, which has motivated a variety of medical imaging systems for breast cancer screening. Planar x-ray mammography is currently the gold standard for breast cancer detection and diagnosis. However, many other clinically available imaging systems such as ultrasound, MRI, nuclear imaging techniques, and breast CT are sometimes recommended for

adjunct breast imaging. Furthermore, many novel breast imaging systems are under development, such as techniques that harness tissue interaction with light or electricity. Clinical translation of these novel breast imaging systems is typically a long process. Breast imaging systems are reviewed in Chapters 5 and 6.

Considerable DEI research has been conducted on breast tissue. Research has consistently demonstrated increased contrast and fine detail visibility over conventional absorption-based imaging systems, as well as other phase contrast imaging systems. Work has also shown that refraction contrast images correlate well with pathology. DEI breast imaging has been performed using planar and three-dimensional platforms. (Pisano 2000, Hasnah 2002b, Hasnah 2005, Kiss 2004, Arfelli 2000, Lewis 2003, Bravin 2002, Bravin 2007, Fernández 2005, Fernández 2008, Liu 2007a, Keyriläinen 2005, Fiedler 2004, Yuasa 2008, Pagot 2005, Kiss 2004, Kao 2009)

9.3 Cartilage

Noninvasive cartilage imaging is an important way to assess cartilage damage due to injury or degenerative diseases, such as osteoarthritis. Cartilage does not possess blood vessels, so it can not rapidly or efficiently repair after damage or degradation. It may be important to identify early signs of damage or disease and intervene to prevent further injury.

Conventional x-ray imaging performs exceptionally poorly for cartilage imaging. With conventional x-ray imaging, cartilage is essentially invisible, so assessing damage or wear can only be inferred due to changes in joint spacing or processes that sometimes occur simultaneously in the underlying bone. Instead, US or MRI is often recommended to directly evaluate cartilage damage or wear (Möller 2008, Tarhan 2003). US is limited

by difficulty in resolving cartilage around joint heads (Tarhan 2003). MRI has the advantage of measuring cartilage volume as well as assessing important biochemical concentrations (Majumdar 2006, van Breuseghem 2004). Nevertheless, the diagnostic accuracy, widespread availability, and low cost of US indicate it as an initial cartilage screening modality over x-ray and MRI.

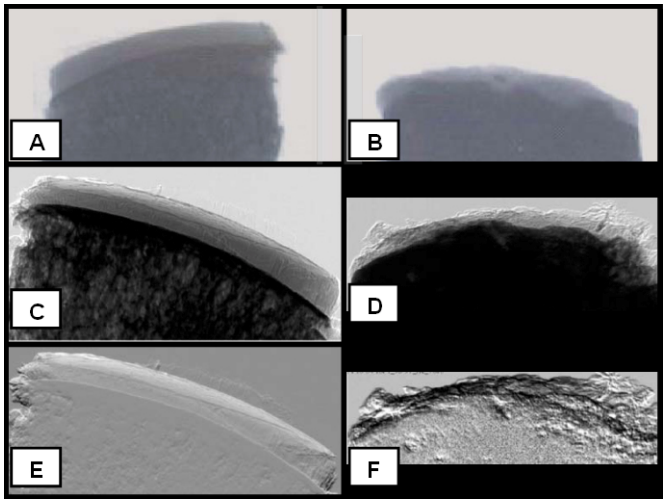

FIGURE 9.1: Cartilage Imaging. Images in the first column are of a bone with healthy overlying cartilage. Another sample with degenerated cartilage and underlying bone are shown in column 2. Panels A and B were acquired with a conventional planar x-ray system. Panels C and D are DEI absorption images. Panels E and F are refraction-contrast DEI images. Reprinted with kind permission from Springer Science+Business Media: European Radiology, 14(8), 2004, 1440-1448, Majumdar S, Issever AS, Burghardt A, Lotz J, Arfelli F, Rigon L, Heitner G, Menk RK.

Tissue Type	Refractive Index
Cartilage	1.492
Bone	1.556
Soft Tissue	1.37 – 1.4

TABLE 9.1: Refractive Indices Relevant to Cartilage Imaging. (Biwas 2002)

DEI refraction images have repeatedly demonstrated excellent cartilage soft tissue contrast, with fine detail visibility (Mollenhauer 2002, Muehleman 2003, Muehleman 2004b, Muehleman 2004c, Muehleman 2006b, Li 2005, Hashimoto 2006, Majumdar

2004, Wagner 2005). Refractive indices relevant to cartilage imaging are shown in Table 9.1. Majumdar *et al* demonstrated that both cartilage damage and changes in the underlying bone were visible simultaneously with DEI when imaging femoral osteoarthritis, shown above in Figure 9.1 (2004). Cartilage is visible using DEI because there is a measurable change in refractive indices between the cartilage, bony hard tissue, and soft tissue (Biwas 2002). Thus, DEI might provide high quality cartilage images at a lower cost than MRI without the resolution limitations of US.

9.4 Lung

Diagnostic lung imaging is important for the assessment of many disease states such as infections or cancers. Lung cancer is a leading cause of cancer death among both men and women in the United States, yet is rarely detected at an early stage of disease (CDC 2007a). Lung cancer screening programs do not currently exist, as no diagnostic imaging modalities have demonstrated a clear benefit in mortality reduction (Field 2008). A comprehensive lung imaging system should be able to evaluate the anatomical features of the lung, quantify lung volume, detect nodules or lesions, measure perfusion and ventilation, and visualize excessive fluid in or around the lungs (pleural effusion). A technical challenge associated with lung imaging remains the necessity for rapid image acquisition (or gated imaging techniques) in order to avoid motion blur from breathing.

Diagnostic lung imaging is most often performed using x-ray CT imaging, providing information on structure, perfusion, and ventilation (Field 2008, Hoffman 2004, Evans 2004). Novel techniques have been developed that allow MRI to acquire lung images in spite of the low proton density and the air-lung tissue field inhomogeneity (Hoffman 2004). MRI does not deliver an ionizing radiation dose, and has better

volumetric imaging capability than CT (Hoffman 2004). US is excellent for diagnosing pleural effusion and can be used to detect some lung lesions (Diacon 2005, Tsai 2003, Evans 2004). PET has been evaluated for lung cancer detection, but low resolution does not allow the exclusion of the presence of disease (Heron 2008, Evans 2004).

Initial studies of DEI lung imaging have been performed in mice and rabbits, demonstrating substantially better anatomic detail than possible with planar x-ray imaging, shown in Figure 9.2 (Lewis 2003, Yagi 1999, Kitchen 2005). Refractive indices relevant to lung imaging are listed in Table 9.2. DEI might offer excellent anatomical information of the lung, with simple detection of effusion due to the large differences in refractive indices between air-filled and fluid-filled tissues.

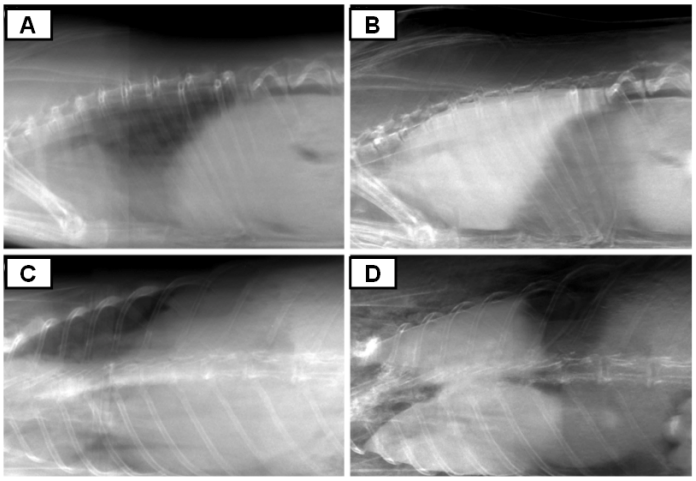

FIGURE 9.2: Lung Imaging. Panels A and C show conventional absorption-contrast image of a rabbit lung acquired along the lateral and anteroposterior views, respectively. Panels B and D depict dose-matched images of the same lung acquired using DEI at the peak of the rocking curve. Reprinted with kind permission from the Elsevier: Nucl Instr Meth Sec A, *in press*, Connor D, Zhong Z, Dilmanian A, Pisano E. Ultra low dose in vivo rabbit lung imaging using diffraction-enhanced imaging. Nucl Instr Meth Sec A *in press.*

Material	Refractive Index
Air	1.00
Water	1.33
Soft Tissue	1.37 – 1.4

TABLE 9.2: Refractive Indices Relevant to Lung Imaging. (Biwas 2002)

9.5 Heart

Heart disease is the leading cause of death in America (CDC 2008). There are a wide range of structural and functional defects from congenital or acquired disease processes. In order to diagnose heart conditions, it is often important to visualize both anatomy and perfusion. Earlier detection of the signs of heart disease in asymptomatic patients may save lives and reduce morbidity. Heart imaging is technically challenging due to tissue movement. Time gating during image acquisition can reduce motion blur, but irregular heartbeats or palpitations can still cause artifacts.

A simple planar chest x-ray is often used as a rapid, inexpensive method of screening for heart problems. Angiography using planar fluoroscopic x-ray imaging is another common clinical heart imaging procedure. However, angiography is an invasive procedure requiring the placement of a catheter to inject contrast agents. CT can acquire cardiac images with high sensitivity and specificity while quantifying coronary calcifications and evaluating plaque morphology. SPECT can be used for cardiac imaging (Buck 2008, Henneman 2007). PET imaging has also demonstrated utility in identifying areas of damaged heart tissue (Gropler 2004, Di Carli 2007). These nuclear imaging systems are highly sensitive, but not very specific. When interfaced with CT, the combination of anatomic and functional information leads to excellent diagnostic accuracy. (Petretta 2008, Chen 1997)

Echocardiography uses US to offer an inexpensive real-time cardiac imaging system. US can assess the velocity of blood flow and cardiac tissue using Doppler imaging, and can also determine perfusion using contrast agents (Villanueva 2008). Cardiac MRI has been evaluated, but many technical challenges restrict its widespread use in the clinic (Jerosch-Herold 2008, Carlsson 2008). The timing and pattern of the heart's electrical impulses are routinely measured through cardiac electrophysiology (Fogoros 2006). These systems typically output a graph instead of a traditional image, but important information about heart automaticity, conduction velocity, and refractory periods can be determined. (Petretta 2008, Chen 1997)

DEI images of an *ex-vivo* mouse heart, shown in Figure 9.3, demonstrated increased contrast and sharpness over a comparable conventional image (Lewis 2003). However, technical limitations of DEI do not currently allow image acquisition at a high enough rate of speed to avoid motion blur due to heart movements. If these time limitations could be overcome, the excellent anatomical information provided by DEI might be accentuated by valuable information about calcification and atherosclerotic plaque morphology and stability.

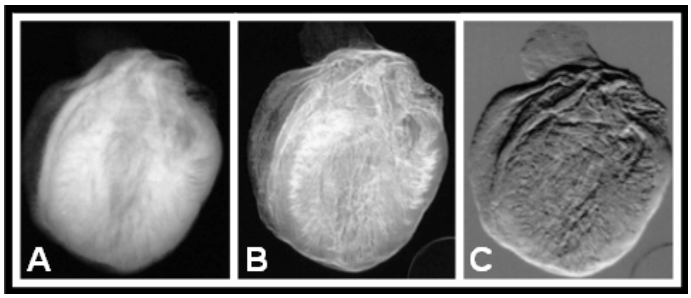

FIGURE 9.3: Heart Imaging. Panel A shows a conventional radiographic imaging of an ex-vivo mouse heart. Panels B and C depict DEI images with contrast based on absorption and refraction, respectively. Reprinted with kind permission from the British Institute of Radiology: Br J Radiol, 76(95), 2003, 301-308, Lewis RA, Hall CJ, Hufton AP, Evans S, Menk RH, Arfelli F, Rigon L, Tromba G, Dance DR, Ellis IO, Evans A, Jacobs E, Pinder SE, Rogers KD.

Material	Refractive Index
Air	1.50
Water	1.431
Soft Tissue	1.37 – 1.4

TABLE 9.3: Refractive Indices Relevant to Heart Imaging. (Biwas 2002)

9.6 Liver

The liver is a vital organ that provides filtration and plays a large role in metabolism. Chronic liver disease is the 12th leading cause of death among Americans (Kung 2008). Liver imaging predominantly looks for evidence of injury or disease processes, such as cirrhosis or cancer.

US imaging of abdominal organs is an inexpensive way to assess liver disease, but has limited spatial resolution. Contrast-enhanced liver US is the most common first method of liver imaging. MRI can generate excellent liver images, with better contrast resolution than US (van den Bos 2008, Cantwell 2008, Taouli 2004). However, use of contrast agents might be dangerous for patients with compromised liver function. Liver elastography is a unique imaging technique that can be used with both US and MRI, which might facilitate the diagnosis of fibrosis (Nguyen-Kac 2006, Castera 2008, Huwart 2008a, Huwart 2008b, Venkatesh 2008). CT can rapidly provide excellent anatomical information. Nuclear imaging has shown utility for detecting liver cancers, but suffers from low resolution (Cantwell 2008).

Refraction contrast might provide excellent detection of liver injury or disease. Fatty or fibrotic liver tissue might appear very different due to differences in refractive index. Moreover, many diseases cause retention of materials, such as iron or copper, in the liver. These might provide a natural contrast agent that would influence the refractive

indices of the liver. Initial DEI liver imaging showed increased structural detail over conventional imaging, shown in Figure 9.4. Refractive indices relevant to cardiac imaging are listed in Table 9.4.

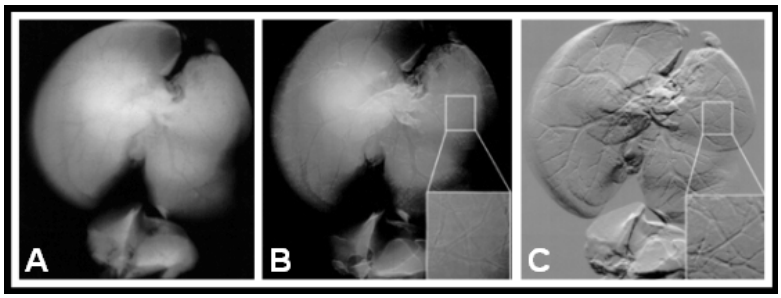

FIGURE 9.4: Liver Imaging. Panel A shows a conventional absorption-contrast image of an ex-vivo mouse liver. Panel B and C represent DEI absorption and refraction contrast images, respectively. Reprinted with kind permission from the British Institute of Radiology: Br J Radiol, 76(95), 2003, 301-308, Lewis RA, Hall CJ, Hufton AP, Evans S, Menk RH, Arfelli F, Rigon L, Tromba G, Dance DR, Ellis IO, Evans A, Jacobs E, Pinder SE, Rogers KD.

Material	Refractive Index
Air	1.45
Soft Tissue	1.37 – 1.4

TABLE 9.4: Refractive Indices Relevant to Liver Imaging. (Biwas 2002)

9.7 Kidney

The kidney does not regenerate rapidly, so damage or loss of function may lead to morbidity or death. Recent estimates found that 7.69% of the adult United States population suffer from chronic kidney disease (Coresh 2007). Kidney imaging attempts to detect damage due to trauma or disease processes such as kidney stones or cancer (Herts 2003).

Planar and CT x-ray imaging are commonly used to evaluate the liver, sometimes with the use of contrast agents. The gold standard for kidney cancer imaging is CT. Abdominal ultrasound is an inexpensive, rapid method of evaluating the kidney without a

radiation dose. MRI is also free from ionizing radiation exposure, and provides excellent soft tissue visualization, but is expensive. X-ray and MR angiography can demonstrate renal vasculature. FDG-PET only has modest affinity for kidney cancers. (Guermazi 2006)

Only one published set of DEI kidney images was found, and extensive imaging of the kidneys using refraction contrast has not yet been performed (Gang 2005). The refractive index of kidney is approximately 1.4 (Biwas 2002). Because of limited research, the utility of DEI for kidney imaging is yet to be determined.

9.8 Brain

The brain is an integral organ essential for the normal function of every other organ and system in the body. Injury and disease can be devastating or deadly. Approximately 1.4 million people in the United States suffer traumatic brain injury annually (CDC 2007b). It is important for a brain imaging system to be able to detect minute changes in both structure and function.

MRI provides superb soft tissue contrast of the brain and can provide excellent insight into functional performance of the brain soft tissue, but has many contraindications due to the strong magnetic field, lower spatial resolution, and less sensitivity for calcifications. CT has excellent spatial resolution and performs well for calcification detection. CT does not have clinical contraindications like MRI, but does suffer from bony artifacts that might interfere with image interpretation. A full CT scan can be acquired much faster than MRI, which reduces motion artifacts. PET and SPECT have demonstrated excellent brain physiologic and functional imaging. When interfaced with CT, image registration allows simultaneous analysis of fine anatomical detail, as

well as functional information. Electroencephalography measures oscillations in electric potentials in the brain in order to assess brain function, but is nonspecific and should only be used to confirm diagnoses obtained through independent clinical tests (Nunez 2006). (Fowler 2003, Mazziotta 1992)

Recently, several groups have used DEI to evaluate brain tissue (Hönnicke 2005, Mannan 2005, Connor 2008, Connor 2009). Because gray matter and white matter have different refractive indices (1.395 and 1.467, respectively), DEI might provide good anatomical images of the brain (Biwas 2002). Connor *et al* explored the utility of DEI for imaging Alzheimer's plaques (2008). However, because of limited research, the utility of DEI for brain imaging is not yet clear.

9.9 Thyroid

The thyroid is an endocrine gland important for the maintenance of metabolism and many bodily functions. Improper thyroid function can negatively influence cardiovascular health. Although thyroid disease prevalence is difficult to quantify, a recent study found that 9.5% of the studied population had abnormal thyroid hormone levels (Canaris 2000). Due to location in the anterior aspect of the neck, the thyroid is relatively simple to image with a variety of imaging modalities.

US offers a rapid and inexpensive method to screen for thyroid disease (Desser 2008). Nuclear imaging uses iodine-based radiopharmaceuticals to provide a simple method of thyroid imaging due to rapid uptake of iodine by the thyroid (Griggs 2008, Nanni 2006). While nuclear medicine has proven useful in identifying certain types of diseases, its performance as a thyroid cancer diagnostic tool is limited due to a high rate of false positives (Lansford 2006). Tomographic imaging techniques, such as CT and

MRI, are typically only indicated when part of the thyroid is situated below the sternum where ultrasound evaluation is not possible, or when cancer is highly suspected (Loevner 2008, Lansford 2006).

One report exists in the literature detailing DEI of *ex-vivo* thinly sliced thyroid glandular tissue, demonstrating excellent nodular morphology visualization (Rocha 2005). Although no published report of the refractive index of thyroid tissue was found, it is likely very similar to the general refractive index of soft tissue. Nodules of abnormal tissue might be readily visible against the normal tissue background. Despite the promising initial images, conclusions on the utility of DEI for thyroid imaging must be conservative due to the limited research to date.

9.10 Eye

Diagnostic eye imaging is performed to assess a variety of diseases of the eye, including cataracts, glaucoma and choroidal tumors. Ophthalmology has a wide range of medical imaging tools with which to assess eye structure and function. Many imaging systems have demonstrated utility in the diagnosis of injury and disease, including CT, MRI, US, various microscopy techniques, OCT, and infrared thermography (Lee 2004, Conneely 2008, Purslow 2005, Galassi 2007, Hoh 2000, Mazziotta 1992, Masters 1990).

Ex vivo DEI imaging has demonstrated excellent visualization of eye anatomy, shown in Figure 9.5. It is difficult to postulate where DEI would offer a clear advantage in diagnostic accuracy within a field with such advanced and accurate techniques, especially given the limited research conducted entirely *ex vivo* (Kelly 2007, Yin 2005, Gao 2006).

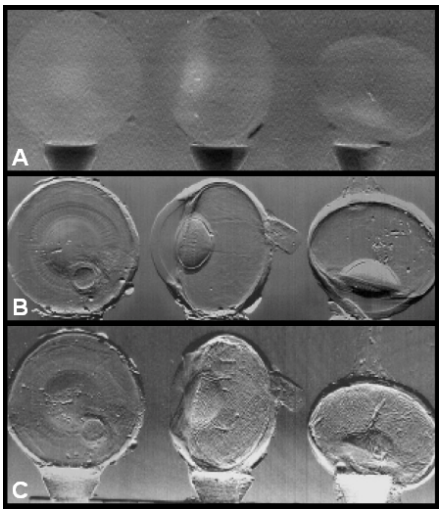

FIGURE 9.5: Eye Imaging. Conventional x-ray imaging of a pig eye is shown in Panel A. Panel B and C show DEI absorption and refraction images, respectively. Reprinted with kind permission from the Canadian Opthalmological Society: Can J Ophthalmol, 42(5), 2007, 731-733, Kelly ME, Coupal DJ, Beavis RC, Schultke E, Romanchuk K, Juurlink BH, Zhong Z, Chapman LD.

9.11 Uterus

The uterus is an essential organ in the female reproductive system. It is generally held that ionizing radiation exposure to human reproductive organs should be minimized as much as possible. Therefore, high-dose imaging systems such as CT are not clinically indicated (Ueda 1999, Hricak 2007). US does not deliver an ionizing radiation dose, is inexpensive, and does not require contrast agents, and so is the most common screening tool for uterine lesions (Ueda 1999, Hricak 2007). While MRI can provide excellent images, it is typically only used for cancer staging due to high cost and limited availability (Ueda 1999, Hricak 2007). One group demonstrated that DEI might allow improved detection of uterine lesions (Liu 2005). Further research is required before the utility of DEI as a uterine imaging modality can be evaluated. However, because DEI delivers a radiation dose, albeit small, it is unlikely that DEI would be clinically indicated when non-ionizing systems are readily available and offer sufficient diagnostic accuracy.

9.12 Bone

Bone imaging is often performed to evaluate injury, infection, and to assess bone microstructure for the diagnosis of degenerative diseases, treatment monitoring, and screening for the presence of cancer. Fracture is the most common result of bone disease, with 1.5 million Americans suffering from bone disease-related fracture annually (U.S. Department of Health and Human Services 2004).

Planar x-ray imaging is the most commonly used system to evaluate bone injury. Dual-energy x-ray absorptiometry is the clinical standard for assessment of bone density. Bone is highly attenuating, producing beam hardening artifacts, and is difficult to optimize for imaging other tissue types simultaneously. Although these hardening effects are incorrectable and quite pronounced using CT, a substantial amount of research is dedicated to evaluation of microCT for imaging bone microstructures (Genant 2008, Kalpakcioglu 2008, Kinney 1995, Laib 1999, Patel 2003, Boutroy 2005). MRI can also be used to view bone structure (Majumdar 1998). Nuclear imaging techniques can use radiopharmaceuticals targeted to bone to evaluate the presence of infection, trauma, or cancers (Grant 2008, Nadel 2007, Bridges 2007, Horger 2006, Prandini 2006).

DEI of bone has demonstrated detailed structure of bone, and has been shown to be particularly useful in evaluating the integrity and stability of metal implants, with excellent visualization of bone-implant interfaces (Wernick 2003, Muehleman 2004a, Muehleman 2006b, Kelly 2006, Connor 2005b, Connor 2006, Wagner 2006, Lewis 2003). Fine detail visible in the DEI images acquired of a rat spinal column demonstrates potential utility for evaluating degenerative bone conditions or post-treatment follow-up for procedures such as spinal fusion surgery (Kelly 2006).

9.13 Summary

As demonstrated by the growing body of research on biomedical applications of DEI, it is clear that there might be a place for this technology among the barrage of medical imaging systems currently used for clinical diagnosis. Furthermore, DEI might have applications in biology and ecology, as it has demonstrated excellent images of plants (Kao 2007b, Young 2007). As the technology develops, it is likely that some of these applications will not demonstrate sufficient diagnostic accuracy and performance to displace other currently available systems. Nonetheless, the excellent fine structure visibility afforded by DEI could mean that DEI might offer substantial benefits for specific applications of medical imaging. Clinical applications of DEI are explored in the following chapters, presenting the results from original experiements.

CHAPTER 10: FEASIBILITY OF CONTRAST-ENHANCED DIFFRACTION-ENHANCED IMAGING

10.1 Overview

This chapter discusses the feasibility of a contrast-enhanced DEI imaging protocol. First, we provide the motivation for the project and discuss potential contrast agents for DEI. Then, the hypothesis and goals of the project are discussed before a thorough description of the research methods and results for each contrast agent tested. Materials were prepared or used according to manufacturer instructions unless otherwise indicated. All experiments were performed with institutional approval as necessary. Finally, considerations for future studies are discussed, such as the mechanism for identifying an optimal DEI contrast agent.

10.2 Motivation for Exploring Contrast-Enhanced DEI

Due to the diffusion limit of oxygen in tissue, tumor growth beyond 1-2 mm is often associated with the development of a new blood vessel network to supply the tumor (Folkman 1971). This process, called angiogenesis, often results in a network of tortuous, abnormal tumor-associated vasculature, which is often related to tumor growth and metastatic potential (Schneider 2005). However, angiogenesis is not exclusive to cancer. Benign proliferative lesions can also demonstrate hypervascularity due to increased metabolic demands, with increased vascularity proportional to the pathologic severity of the lesion (Heffelfinger 1996). Methods to image the microvasculature and blood perfusion associated with suspect lesions have demonstrated significant diagnostic

potential with modalities such as ultrasound, computed tomography, and magnetic resonance imaging (Charnley 2009).

Contrast media with a particle size below approximately 400 nm undergo passive targeting in the presence of a tumor due to the Enhanced Permeation and Retention (EPR) effect. Extravasation normally depends on vessel surface area, pressure gradients, the metabolic microenvironment, and active transport (Jain 2001). This process is highly restricted in normal vasculature, but aberrant tumor vasculature lacks smooth muscle and possesses intermittent basement membrane structure with large inter-endothelial junctions, leading to "leaky" blood vessels (Jain 2001, Greish 2007, Jain 2007). Due to restrictions by normal venous vasculature, contrast agents do not re-enter circulation easily, and so are not cleared efficiently from the tumor site (Greish 2007). Together, these factors allow accumulation of contrast media at the tumor site.

However, only limited reports of Contrast-Enhanced DEI (CE-DEI) have been reported in the literature to date. One group attempted to use gold nanoparticles to enhance contrast when imaging mouse brain tissue, but were unsuccessful (Mannan 2005). Another group reported a preliminary study using microbubbles (Arfelli 2003). Materials with high electron density (i.e. atomic number) and physical density might generate refraction and absorption contrast when interfaced with low electron density and low density materials, such as fat or soft tissue. Contrast agents that cause x-ray scattering might generate extinction contrast.

10.3 Potential DEI Contrast Agents

The body is composed mostly of water, and the differences in density and atomic number do not vary greatly between types of soft tissue. The electron density (i.e. atomic

number) influences refraction contrast, while physical density is the source of absorption contrast. K-edge values represent the x-ray energy, measured in keV, at which absorption contrast (and to a lesser extent refraction contrast) experience brief spikes due to electron binding energies in a particular shell.

Iodine (Diekmann 2003, Dromain 2006, Jong 2003, Lewin 2003), ferric oxide (Yang 2008a, Yang 2009, Chen 2009, Harada 2007, Duquet 2006, Artemov 2003), and gadolinium (Strunk 2004, Thomsen 2002, Rieger 2002) are clinically used intravenous contrast agents. The most prevalent x-ray contrast agents are iodine-based, and are primarily used in the blood pool. However, contrast agents of many other materials are used clinically, with many more under investigation for clinical implementation. The properties of potential DEI contrast agents are listed in Table 10.1.

	Atomic Number (Z_{eff})	**Density (g/ml)**	**electrons/volume**	**K-edge**
Iodine	53	4.93	2.34×10^{28}	33.17
Iron	26	7.86	8.48×10^{28}	7.11
Gadolinium	64	7.90	3.03×10^{28}	50.24
Bismuth	83	9.78	2.82×10^{28}	90.53
Gold	79	19.30	5.90×10^{28}	80.72
Silver	47	10.49	5.86×10^{28}	25.51
Platinum	78	21.45	6.62×10^{28}	78.39
Tungsten	74	19.25	6.31×10^{28}	69.53

TABLE 10.1: Physical Properties of Potential X-Ray Contrast Agents.

The iodine K-edge is close to typical mammographic imaging energies, allowing an increase in image contrast due to the photoelectric effect. Iron oxide nanoparticles are used clinically as MRI contrast agents. The use of iron oxide nanoparticles as a breast imaging contrast agent has not been reported, possibly because the K-edge of iron is well below typical mammographic imaging energies.

Gadolinium chelate-based contrast agents are used clinically for MRI contrast enhancement. Recent studies have suggested that gadolinium contrast agents might have applications in x-ray imaging (Strunk 2004, Thomsen 2002, Rieger 2002, Albrecht 2000, Sandborg 1995). Gadolinium chelate does not have regulatory approval for non-MRI contrast enhancement, and has only demonstrated diagnostic-quality radiographic imaging for arterial enhancement (Strunk 2004). Abdominal organ contrast was not diagnostic quality, and no studies of gadolinium-enhanced breast x-ray imaging have been reported in the literature (Strunk 2004).

Iodine-, iron-, and gadolinium-based contrast agents are used clinically. Additional contrast agents such as bismuth, gold, silver, platinum, and tungsten have been suggested as x-ray contrast agents. Bismuth, once used regularly as an x-ray contrast agent, is now being revisited (Rabin 2006, Yu 1999, Sandborg 1995). Gold has demonstrated promise in initial laboratory-based phantom and *in vivo* studies, suggesting potential utility as an x-ray contrast agent, even though the toxicity issues associated with gold nanoparticle injection still require substantially more investigation (Hainfeld 2006, Cai 2007, Kim 2007c, Jackson 2009, Park 2007c, Geso 2007, Park 2006, Kattumuri 2007). While colloidal silver and silver salts have been studied as x-ray contrast agents, issues with cytotoxicity currently prevent their use in the clinic (Yu 1999). Platinum (Figuerola 2008, Breskin 2004) and tungsten (Yu 1999) have also been suggested as potential x-ray contrast agents, but limited data exists on their safety and efficacy.

Gases have been used as contrast agents for x-ray through CO_2 injection (Heye 2006, Chao 2007a, Shaw 2006), and for contrast-enhanced ultrasound through microbubble injection (Kedar 1996, Albrecht 1998, Reinikainen 2002, Alamo 2001,

Cassano 2006, Jiang 2007, van Esser 2007, Liu 2008, Balleyguier 2009). Initial clinical contrast-enhanced ultrasound studies of the breast were disappointing (Kedar 1996, Albrecht 1998). Improved ultrasound hardware and software technology, more advanced microbubble formulations, and optimized scanning sequences suggest that contrast-enhanced ultrasound may become an important breast imaging tool, although some results are still mixed (Reinikainen 2002, Alamo 2001, Cassano 2006, Jiang 2007, van Esser 2007, Liu 2008, Balleyguier 2009).

Microbubble contrast agents used for ultrasound imaging are stabilized gas bubbles, typically filled with a high-molecular weight gas, such as a perfluorocarbon, which has low blood solubility. The stabilizing shell consists of either a lipid or a protein for currently FDA-approved agents Definity (Lantheus Medical Imaging) or Optison (GE), respectively. Because of their size, approximately 1 to 5 microns in diameter, microbubble contrast agents are limited to the vascular space and do not readily extravasate. Although microbubble toxicity is generally considered to be lower than the toxicity of other clinically used contrast agents, potential adverse effects, such as cardiac disturbances, loss of consciousness, and respiratory distress, suggest contraindications in some patients (Main 2007, Hayat 2005, Barnett 2007).

10.4 Hypothesis and Goals

This project will focus on the evaluation of DEI contrast by commercially available contrast agents. It is our hypothesis that iodine-, iron-, and gadolinium-based commercially available contrast agents can generate DEI absorption, and possibly refraction contrast, within clinically relevant concentrations. Moreover, microbubble contrast agents might generate attenuation and extinction contrast. To this end, we

imaged phantoms containing a range of concentrations of iodine (Omnipaque^{TM}), ferric oxide (Feridex^{TM}), gadolinium (Magnevist^{TM}). We also imaged phantoms containing microbubbles of several sizes.

10.5 Predicting Absorption and Refraction Contrast.

The following calculations are adapted from Kiss *et al* to determine the refraction contrast and absorption contrast for various contrast agents at a range of x-ray energies relevant to mammographic imaging, considering the models shown in Figure 10.1 (2003).

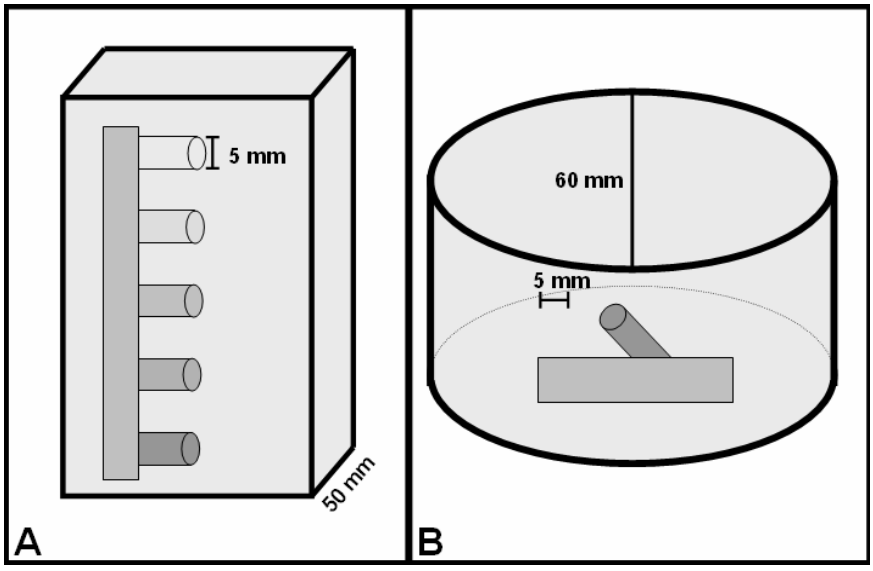

FIGURE 10.1: Model for Contrast Calculations. The model used to predict absorption and refraction contrast is a 5 mm cylinder submerged in 5 cm deep rectangular water bath for planar imaging and a 6 cm cylindrical water bath for three-dimensional imaging.

Frequency (f) and wavelength (λ) were calculated using the following formulas:

$$f = E / h \quad (39)$$
$$\lambda = c / f \quad (40)$$

where E is the x-ray energy (in eV), h is Planck's constant (6.626×10^{-34} J s), and c is the speed of light in a vacuum (299,792,458 ms^{-1}). Table 10.2 displays these values.

Energy (keV)	*f*	λ
20	4.83×10^{18}	6.21×10^{-11}
30	7.24×10^{18}	4.14×10^{-11}
40	9.66×10^{18}	3.10×10^{-11}
50	1.21×10^{19}	2.48×10^{-11}
60	1.45×10^{19}	2.07×10^{-11}

TABLE 10.2: Frequency and Wavelength at Diagnostic X-Ray Energies. The frequency (*f*) is measured in Hz; the wavelength (λ) is measured in meters.

Because refraction occurs at interfaces, a change in cylinder thickness influences x-ray absorption more than refraction. Snell's law describes x-ray refraction, stating that

$$n_1 \sin\theta_1 = n_2 \sin\theta_2 \tag{41}$$

where n_1 is the refractive index of the phantom container (acrylic), n_2 is the refractive index of the aqueous solution containing the contrast agent, θ_1 is the incident angle, and θ_2 is the refraction angle. The real portion of the refractive index is:

$$n = 1 - \delta \tag{42}$$

where

$$\delta = (N \lambda^2 r_e) / 2\pi \tag{43}$$

and where r_e is the classical electron radius ($2.8179402894 \times 10^{-15}$ m), and N is the number of electrons per unit volume, represented by:

$$N = (N_A \rho) / A \tag{44}$$

where N_A is Avogadro's Number ($6.02214179 \times 10^{23}$ atoms/mole), ρ is density (in kg/m^3), and A is the atomic mass (in kg/mole). Rewriting the equation for δ in terms of x-ray energy instead of in terms of wavelength demonstrates that the δ, and thus the angular deflection of x-rays, has a $1 / E^2$ dependency. Therefore, doubling the x-ray energy reduces angular deflection by a factor of four.

The deflection angle caused by x-ray refraction from a cylinder is calculated by:

$$\Delta\theta_z \approx 2\Delta\delta\tan\theta_1 \quad (45)$$

where $\Delta\delta = n_1 - n_2$, and $\sin\theta_1 = y / R$, with y representing the vertical position relative to the horizontal diameter of the cylinder, and R representing the radius of the cylinder. Higher up on the circle has greater the refraction contrast. For the purposes of these calculations, we chose the representative value of $y = (5 / 6) R$; thus, θ_1 was 0.985111. The amount of refraction contrast generated by a specific deflection angle depends on the slope of the rocking curve, which changes with x-ray energy. Steep rocking curve slopes generate the greatest refraction contrast. Rocking curve slopes for the given x-ray energies are shown in Table 10.3.

Energy (keV)	FWHM	Peak Reflectivity	Slope
20	3.2390	0.929394	0.286924
30	2.1035	0.949327	0.451308
40	1.5635	0.954559	0.610542
50	1.2461	0.957948	0.768739
60	1.0489	0.960566	0.915794

TABLE 10.3: Rocking Curve Slopes. The characteristics of the rocking curve at several x-ray energies relevant to mammographic imaging are listed above, where FWHM is the full width at half maximum, measured in microradians.

The change in intensity due to refraction, ΔI_{ref}, generated by a certain deflection angle is calculated by:

$$\Delta I_{ref} = (\text{Rocking Curve Slope})\ (\Delta\theta_z) \quad (46)$$

The intensity after absorption, I_{abs} can be predicted with the following formula:

$$I_{abs} = I_0 \exp(-\mu z_2) \quad (47)$$

where I_0 is the initial intensity, μ is the linear attenuation coefficient, and z_2 approximates the path length of an x-ray inside the cylinder.

$$z_2 = 2\sqrt{(R^2 + y^2)} \quad (48)$$

For a diameter of 1 mm, z_2 is 1.94365 mm; for a diameter of 10 mm, z_2 is 10.1379 mm. Absorption contrast is calculated by the following formula:

$$\text{Contrast} = (I_{medium} - I_m I_{medium}) / I_{medium} \quad (49)$$

where I_m is the intensity transmitted through the material of interest and I_{medium} is the intensity transmitted through the medium.

When considering contrast in an apparent absorption DEI-CT image, the Hounsfield units are calculated by the following formula:

$$\text{CT number} = [(\mu - \mu_{medium}) / \mu_{medium}] (1000) \quad (50)$$

where μ is the linear attenuation coefficient through the material of interest and μ_{medium} is the linear attenuation coefficient through the medium. The CT number for human soft tissue typically ranges from -300 to -100. However, highly absorbing materials, such as contrast media, will cause increased x-ray absorption, and thus an increased CT number.

The contrast generated by microbubbles can be predicted using methods previously described (Connor 2005a). These calculations are beyond the scope of the current study and have not been performed with respect to the current DEI microbubble contrast agent phantom.

10.6 Methods

Diffraction-Enhanced Imaging. DEI was performed at the National Synchrotron Light Source X15A beamline at Brookhaven National Laboratory in Upton, New York. The DEI setup is shown in Figure 10.2, as described previously (Zhong 2000). The linear collimated beam was 130 mm by 2 mm using a Bragg [333] crystal reflection. The double-crystal monochromator (Shaw Monochromators, Riverton, KS) was comprised of

a series of two perfect silicon crystals mounted on independently tunable stages in a continuously helium-flushed steel tank. The collimated monochromatic x-ray beam then interacted with the object being imaged before diffraction by the analyzer crystal. Refraction contrast images were acquired at the ±½ W_D of the rocking curve; absorption contrast images were acquired at the peak of the rocking curve.

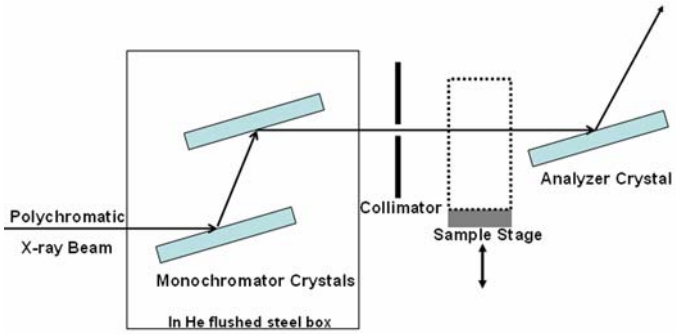

FIGURE 10.2: DEI System Setup. An intense, collimated polychromatic synchrotron x-ray beam is made monochromatic by a series of two perfect silicon crystals referred to as the monochromator. The monochromatic beam interacts with the object before becoming incident to the third perfect crystal, referred to as the analyzer crystal. The analyzer crystal diffracts the x-ray based on its rocking curve, only reflecting x-rays that fall within a narrow acceptance window. Manipulating the angle of the analyzer crystal allows the selection of image contrast based on either absorption or refraction.

The flux of the post-monochromator beam was measured using an ion chamber. Photons were detected using a 30 micron pixel size digital detector with a 120 mm by 80 mm imaging area (Photonic Science Limited, UK). For planar imaging, the sample stage scanned the phantom vertically through the x-ray beam. For DEI-CT imaging, the phantoms were placed on a Huber (Blake Industries, Scotch Plains, NJ) rotational stage. For each DEI-CT image, 1000 projections were acquired with a sample rotation step size of 0.36 degrees, and with an acquisition time of 1 second per image. The average surface dose for planar images was 0.18 mGy while the average DEI-CT surface dose was 0.114 mGy.

Planar DEI images were processed using the background subtraction tool in ImagePro Express 5.1 (Media Cybernetics, Bethesda, MD). DEI-CT images were reconstructed using filtered backprojection using IDL (ITT Visual Information Systems, Boulder, CO). Pure refraction contrast images were calculated using IDL from a series of planar images, as described previously (Chapman 1997).

Full-Field Digital Mammography. The iodine phantoms were also imaged on the General Electric (GE) Senographe 2000D (Waukesha, WI) at UNC Hospitals, with an average x-ray energy of 26 kVp. The SNR of the GE Senographe 2000D was measured to be 83.49 at 25 mm, 71.65 at 40 mm and 56.51 at 60 mm. The half-value layer was calculated to be 0.374, as measured using the ACR phantom, which simulates calcifications, fibrous calcifications in ducts, and tumor masses. The average phantom surface dose was 17.19 mGy. Images were saved in softcopy DICOM format with GE preprocessing applied.

Calculating Image Contrast. The percent absorption contrast was calculated in each image at each energy level by Equation 49; a line profile was drawn across the sample tube to measure the intensity. These values were then normalized by subtracting the percent contrast measured for the water control tube from the percent contrast measured for each sample tubes. The percent refraction contrast was calculated by drawing a line profile across the sample tube, measuring the difference in intensity between the water-sample tube interface and the sample tube-contrast agent interface.

10.7 Iodine as a Potential DEI Contrast Agent

Iodine: Expected Performance as a DEI Contrast Agent. The LD_{50} for iodine is 24.2 g/kg of body weight. Considering the standard range of iodine-based contrast agent

doses and an average human blood volume of 5 L, the typical diluted concentration of iodine in the blood *in vivo* ranges from 3 mg/ml to 11.5 mg/ml. Figure 10.3 graphs the predicted absorption and refraction contrast of iodine. Because contrast below approximately 5% is not accurately detected, an iodine-based x-ray contrast agent is expected to generate sufficient absorption contrast with a concentration of 5 to 10 mg/ml at 20 keV and at 40 keV. However, iodine is predicted to generate poor refraction contrast at clinically relevant concentrations and x-ray energies. Figure 10.4 displays the predicted CT numbers generated by an iodine contrast agent.

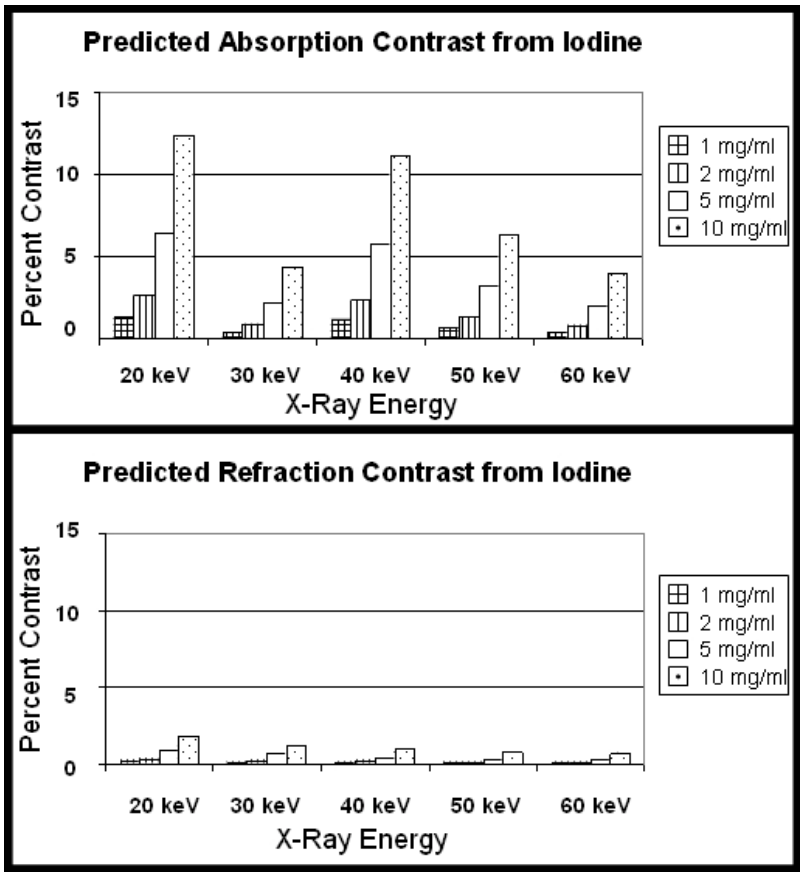

FIGURE 10.3: Predicted Absorption (*top*) and Refraction (*bottom*) Contrast from Iodine.

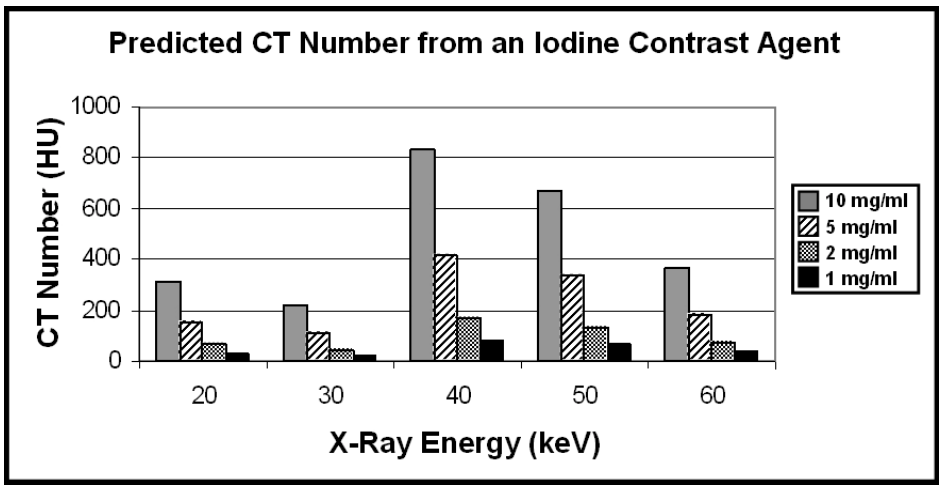

FIGURE 10.4: Predicted CT Number Generated by Iodine.

Iodine Phantom. Plastic capillary tubes (5 mm internal diameter) were filled with 10 mg/ml, 5 mg/ml, 2 mg/ml, or 1 mg/ml of Omnipaque™300 (GE Healthcare, Princeton, NJ). Each concentration was prepared by dilution in deionized water. A control capillary tube was filled with deionized water. For planar imaging, the phantom tubes were linearly arranged perpendicular to the x-ray beam. For DEI-CT imaging, the phantoms were arranged circularly, tilted at approximately 45 degrees. The tubes were sealed and submerged in a 5 cm rectangular water bath for planar imaging, or in a 6 cm cylindrical water bath for DEI-CT imaging. DEI, DEI-CT, and full-field digital mammography was performed as described in Section 10.5. Image contrast was calculated as described in Section 10.5.

Iodine: Results. The DEI absorption images generated by the iodine contrast agent phantom at a range of x-ray energies, including near the K-edge of iodine (33.117 keV), are shown in Figure 10.5. The measured absorption contrast values, graphed in Figure 10.6, are slightly less than those predicted, likely due to monochromator or analyzer drift.

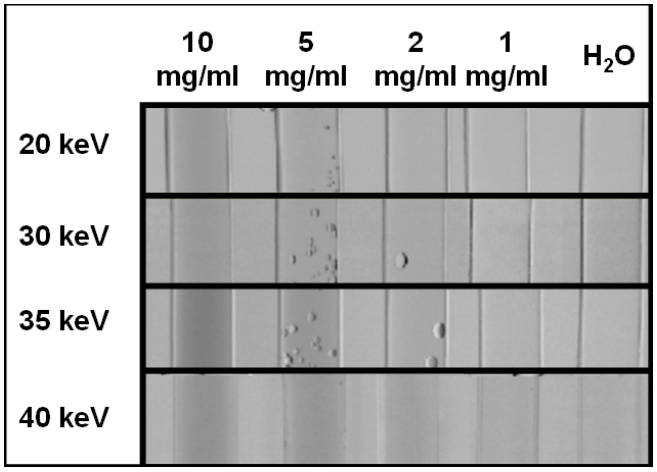

FIGURE 10.5: DEI Absorption Contrast from an Iodine Phantom. A 5 mm plastic capillary tube was filled with a range of iodine (Omnipaque™) concentrations and imaged at several x-ray energies while submerged in a 50 mm water bath. DEI images were acquired at the peak of the rocking curve. Water bubble artifacts can be seen in some regions. An increase in image contrast is noted between the images acquired at 30 keV and 35 keV, as the x-ray energy has risen above the iodine K-edge.

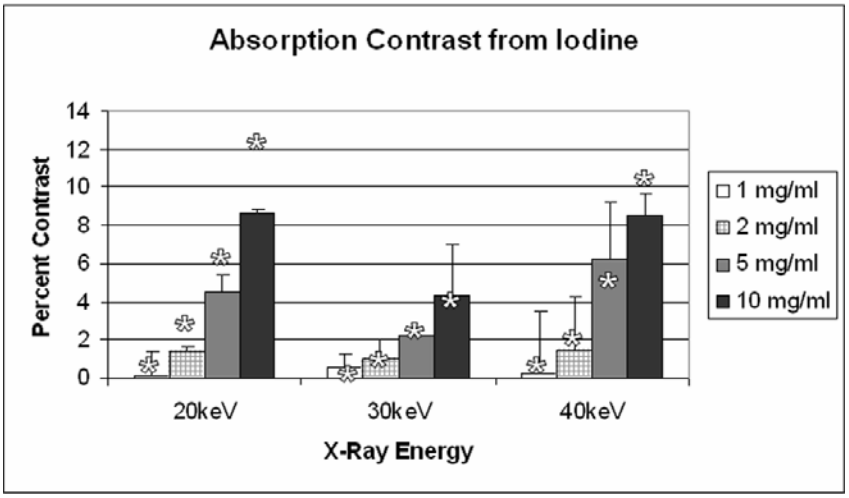

FIGURE 10.6: Measured Iodine Absorption Contrast. Percent contrast for each concentration of iodine was calculated for each x-ray energy and plotted. The (*) denotes the predicted percent contrast at that concentration and energy, as determined using the model in Figure 10.1.

The refraction contrast was measured from images acquired on the slope of the rocking curve, but the measurements were not in agreement with the predicted refraction contrast values. Because single DEI images contain a mixture of contrast mechanisms, pure refraction images were calculated. The measured refraction contrast values from the

pure refraction images are listed in Table 10.4. The measured values are now in better agreement with the predicted values.

	10 mg/ml	5 mg/ml	2 mg/ml	1 mg/ml
20 keV	3.7935 (*1.9*)	1.8949 (*1.0*)	1.1576 (*0.4*)	0.2477 (*0.2*)
30 keV	1.9090 (*1.3*)	0.7438 (*0.7*)	0.7821 (*0.3*)	0.1030 (*0.1*)
40 keV	1.4280 (*1.0*)	0.5703 (*0.5*)	0.4257 (*0.2*)	0.1796 (*0.0*)

TABLE 10.4: Percent Contrast Measured from Pure Refraction Images of Iodine. Pure refraction images were calculated as described previously (Chapman 1997), and contrast was measured using Equation 47. The predicted percent contrast for each concentration and energy are shown in parentheses.

DEI-CT images of the iodine contrast agent are shown in Figure 10.7. For apparent absorption processing (Row A), the 1 mg/ml, 5 mg/ml, 10 mg/ml, and 30 mg/ml iodine phantoms generated percent contrasts of 4.15%, 22.30%, 26.44%, and 141.07%, respectively. Similarly, the measured percent contrast in the refraction images (Row B) for 1 mg/ml, 5 mg/ml, 10 mg/ml, and 30 mg/ml iodine was -6.0167%, 5.9850%, 9.4616%, and 44.7971%.

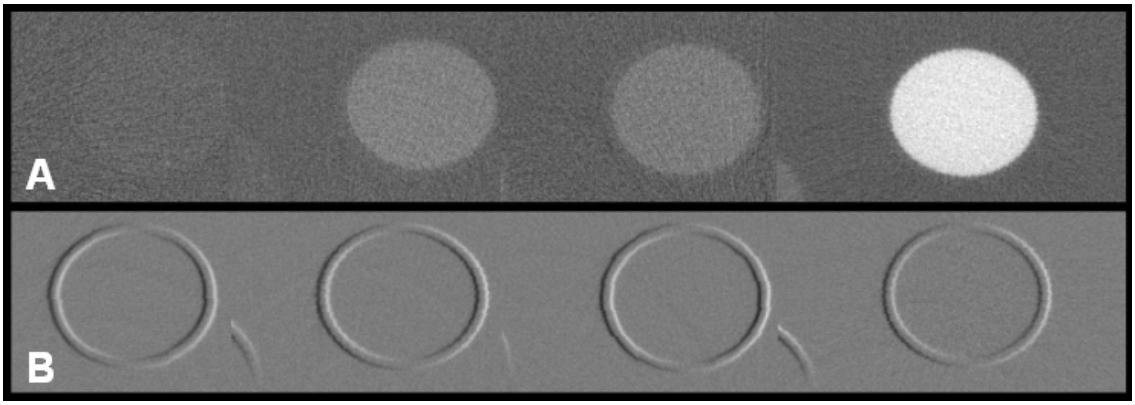

FIGURE 10.7: DEI-CT Imaging of Iodine Phantom. DEI-CT imaging was performed at 40 keV. Single representative DEI-CT slices are shown from left to right, representing 1 mg/ml, 5 mg/ml, 10 mg/ml, and 30 mg/ml iodine. Row A displays apparent absorption images; Row B shows refraction contrast images.

The iodine phantom was also imaged on a clinical digital mammography system at 26 kVp, as shown in Figure 10.8. This is a polychromatic source, so the actual average

x-ray energy is lower. The measured absorption contrast generated by 1 mg/ml, 2 mg/ml, 5 mg/ml, and 10 mg/ml iodine was 1.63%, 3.58%, 13.02%, and 22.83%, respectively.

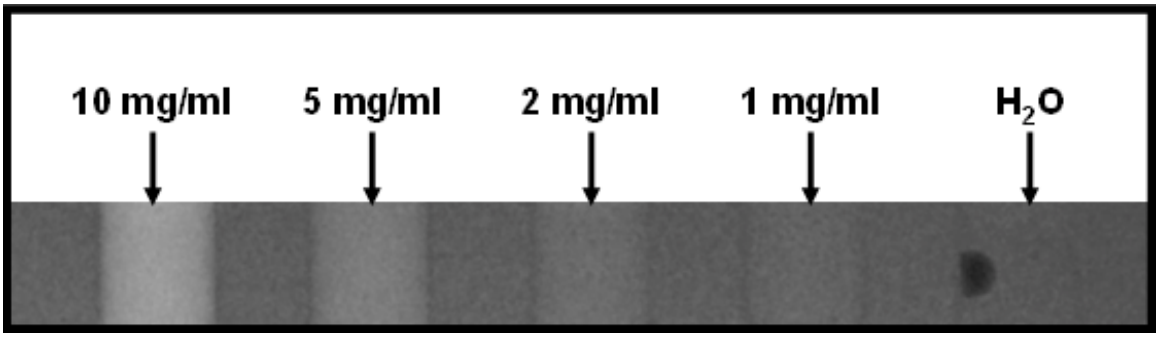

FIGURE 10.8: Digital Mammography of Iodine Phantom. Digital mammography was performed at 26 kVp of an iodine contrast agent phantom with 10 mg/ml, 5 mg/ml, 2 mg/ml, and 1 mg/ml iodine and a deionized water control.

10.8 Iron as a Potential DEI Contrast Agent

Iron: Expected Performance as a DEI Contrast Agent. The K-edge of iron is at 7.1 keV, indicating that as x-ray energy increases, absorption contrast rapidly decreases. The typical dose of iron oxide nanoparticles is 0.56 mg/kg of body weight. When diluted in the human blood volume, the concentration becomes 0.008 mg/ml of blood. While the concentrations shown in Figure 10.9 are well above the typical concentrations used clinically, even at high concentrations, an LD_{50} for Feridex^{TM} has not been reported. Thus, increased iron oxide nanoparticle concentrations might be used with limited increase in toxicity. However, iron is only predicted to generate clinically detectable absorption contrast enhancement at 5 mg/ml and 10 mg/ml at 20 keV; both of these concentrations are substantially greater than the typical clinical dose for MRI. Refraction contrast is not predicted to be sufficient at the concentrations and x-ray energies included in the current study. Figure 10.10 displays the predicted CT numbers generated by an iron contrast agent.

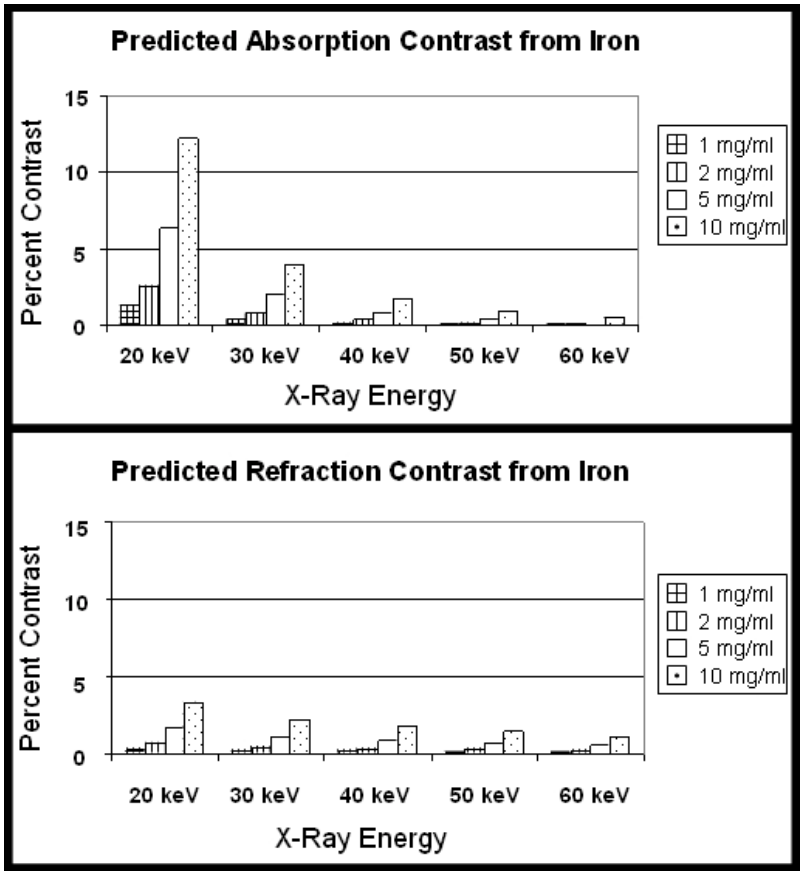

FIGURE 10.9: Predicted Absorption (*top*) and Refraction (*bottom*) Contrast from Iron.

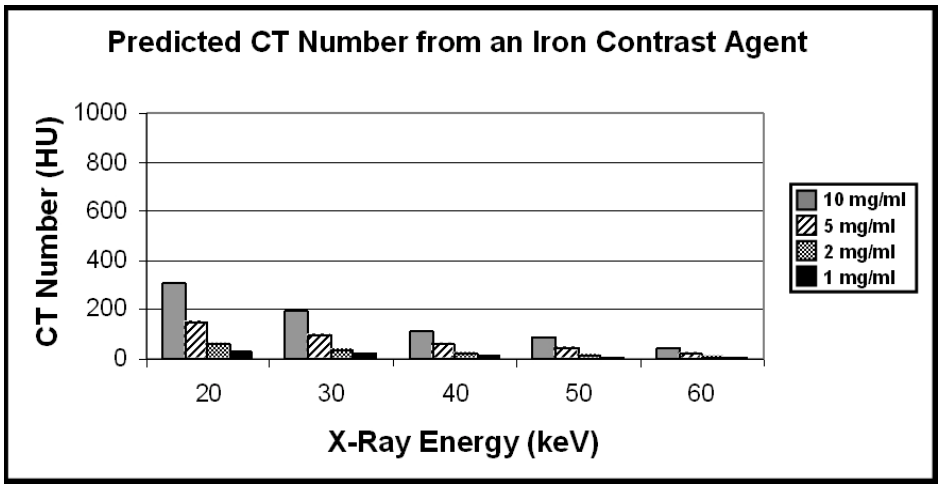

FIGURE 10.10: Predicted CT Number Generated by Iron.

Iron Phantom. Plastic capillary tubes (5 mm internal diameter) were filled with 10 mg/ml, 5 mg/ml, 2 mg/ml, or 1 mg/ml of Feridex™ (Bayer Healthcare, Leverkusen, Germany). Each concentration was prepared by dilution in deionized water. A control capillary tube

was filled with deionized water. Phantom tubes were linearly arranged perpendicular to the x-ray beam. The tubes were sealed and submerged in a 5 cm rectangular water bath. DEI and full-field digital mammography was performed as described in Section 10.5. DEI-CT was not performed for the iron phantoms. Image contrast was calculated as described in Section 10.5.

Iron: Results. DEI images generated by the iron contrast agent phantom at 20 keV and acquired at the ±½ W_D and peak rocking curve positions are shown in Figure 10.11. Only the 20 keV data is shown because, due to the low K-edge of iron (7.11 keV), absorption and refraction contrast rapidly decline with increasing x-ray energy. The measured absorption contrast values at a range of x-ray energies are graphed in Figure 10.12.

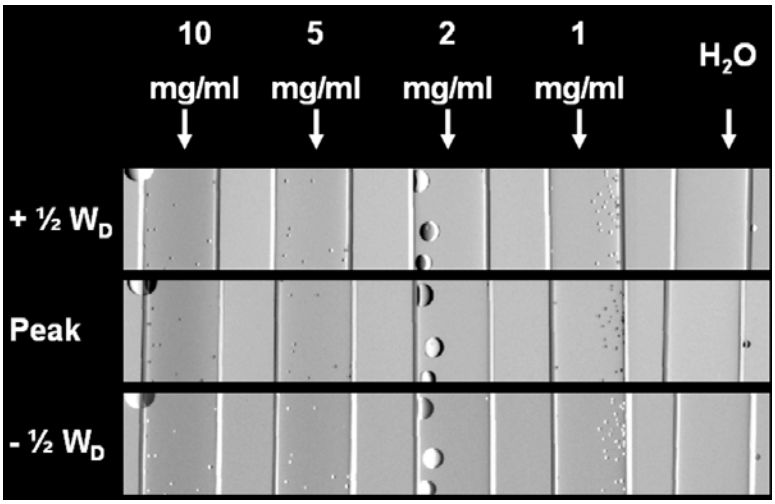

FIGURE 10.11: DEI Absorption Contrast from an Iron Phantom. A 5 mm plastic capillary tube was filled with a range of iron oxide nanoparticle (Feridex™) concentrations and imaged at 20 keV while submerged in a 50 mm water bath. DEI images were acquired at the ±½ W_D and peak rocking curve positions. Water bubble artifacts can be seen in some regions.

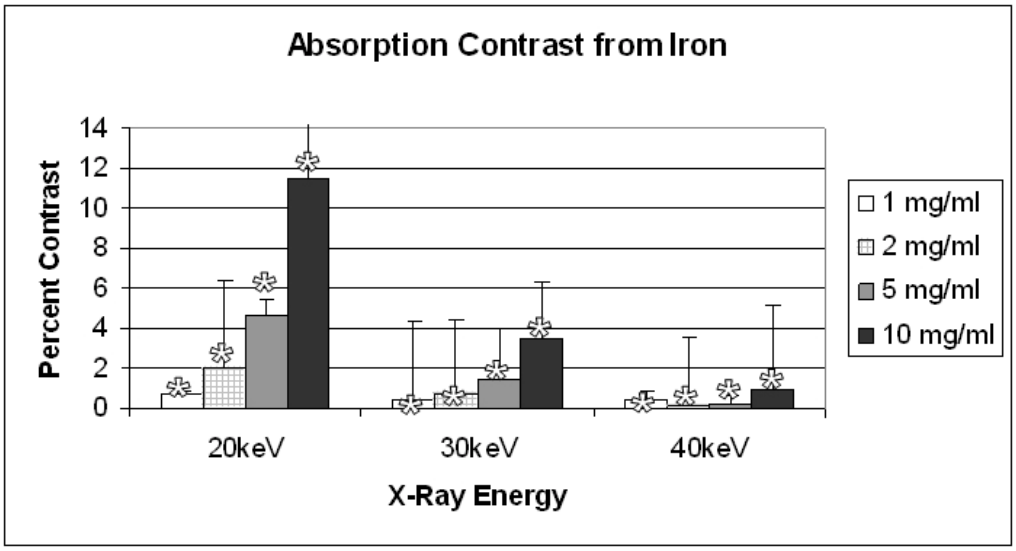

FIGURE 10.12: Measured Iron Absorption Contrast. Percent contrast for each concentration of iron was calculated for each x-ray energy and plotted. The (*) denotes the predicted percent contrast at that concentration and energy, as determined using the model in Figure 10.1.

The refraction contrast was measured from images acquired on the slope of the rocking curve, but the measurements were not in agreement with the predicted refraction contrast values. Because single DEI images contain a mixture of contrast mechanisms, pure refraction images should be calculated. However, for this dataset, the images were not acquired symmetrically on the rocking curve, likely due to monochromator or analyzer drift, preventing an accurate pure refraction contrast image. The images that were produced by this inaccurate reconstruction (data not shown) did not demonstrate any measurable refraction contrast.

The iron phantom was also imaged on a clinical digital mammography system at 26 kVp, as shown in Figure 10.13. The measured absorption contrast generated by 1 mg/ml, 2 mg/ml, 5 mg/ml, and 10 mg/ml iron was 2.27%, 12.72%, 23.67%, and 52.40%, respectively.

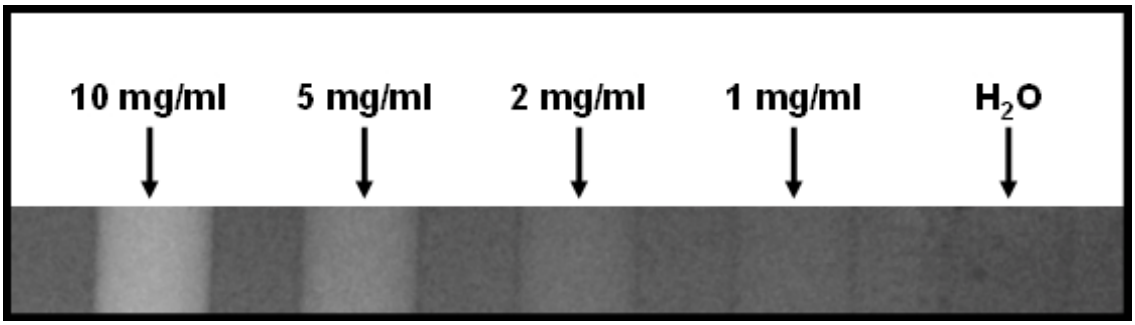

FIGURE 10.13: Digital Mammography of Iron Phantom. Digital mammography was performed at 26 kVp of an iodine contrast agent phantom with 10 mg/ml, 5 mg/ml, 2 mg/ml, and 1 mg/ml iron oxide nanoparticles and a deionized water control.

10.9 Gadolinium as a Potential DEI Contrast Agent

Gadolinium: Expected Performance as a DEI Contrast Agent. The LD_{50} for Magnevist™, a gadolinium chelate, is 1.1 g/kg of body weight. The typical dose of gadolinium-chelate contrast agent is 93.8 mg/kg of body weight. Once diluted in the average human blood volume, the concentration is approximately 1.3 mg/ml of blood. The predicted absorption and refraction contrast for gadolinium, shown in Figure 10.14, suggest that absorption contrast might be sufficient at 5 to 10 mg/ml concentrations when imaged at 20 to 30 keV. The 10 mg/ml concentration might also generate sufficient absorption contrast at 60 keV due to the photoelectric effect. However, refraction contrast is predicted to be poor at all x-ray energies evaluated. Figure 10.15 displays the predicted CT numbers generated by a gadolinium contrast agent.

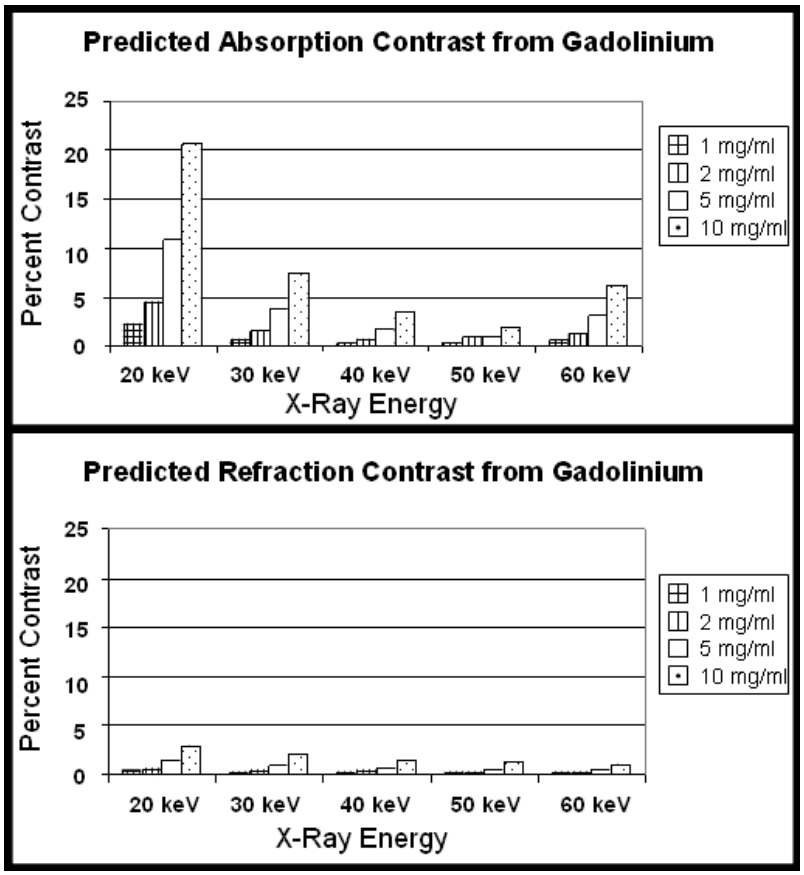

FIGURE 10.14: Predicted Absorption (*top*) and Refraction (*bottom*) Contrast from Gadolinium.

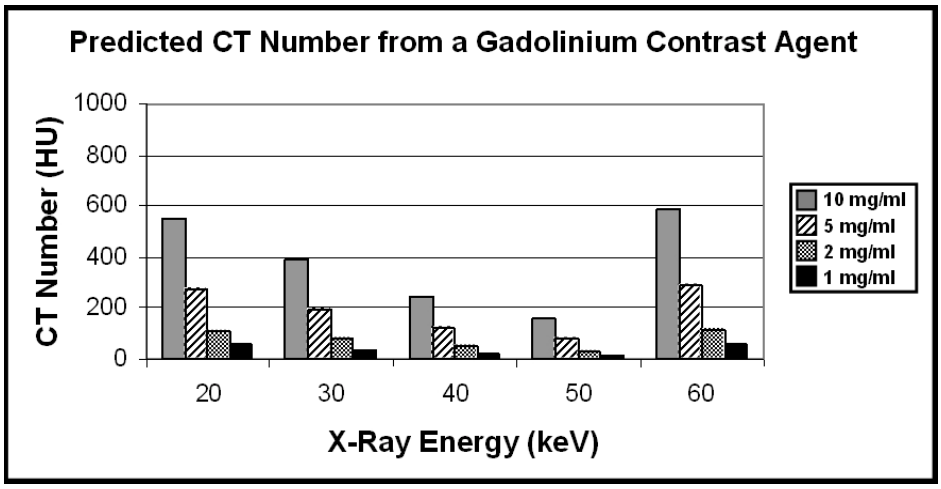

FIGURE 10.15: Predicted CT Number Generated by Gadolinium.

Gadolinium Phantom. Plastic capillary tubes (5 mm internal diameter) were filled with 10 mg/ml, 5 mg/ml, 2 mg/ml, or 1 mg/ml of Magnevist™ (Bayer Healthcare, Leverkusen, Germany). Each concentration was prepared by dilution in deionized water.

A control capillary tube was filled with deionized water. For planar imaging, the phantom tubes were linearly arranged perpendicular to the x-ray beam. For DEI-CT imaging, the phantoms were arranged circularly, tilted at approximately 45 degrees. The tubes were sealed and submerged in a 5 cm rectangular water bath for planar imaging, or in a 6 cm cylindrical water bath for DEI-CT imaging. DEI, DEI-CT, and full-field digital mammography was performed as described in Section 10.5. Image contrast was calculated as described in Section 10.5.

Gadolinium: Results. Gadolinium should theoretically generate greater absorption contrast than iodine, but gadolinium-based contrast agents have one gadolinium atom per molecule while iodine-based contrast agents have three iodine atoms per molecule of contrast agent.[13] Thus, gadolinium contrast agents for x-ray applications require increased dosages (Thomsen 2002, Nyman 2002). The DEI images generated by the gadolinium contrast agent phantom at 20 keV and acquired at the ±½ W_D and peak rocking curve positions are shown in Figure 10.16. Only the 20 keV data is shown because, due to the location of the K-edge of gadolinium (50.24 keV), absorption and refraction contrasts are declining in the range of x-ray energies used in this study.

13. Magnevist formula: $C_{28}H_{54}GdN_5O_{20}$; Omnipaque formula: $C_{19}H_{26}I_3N_3O_9$

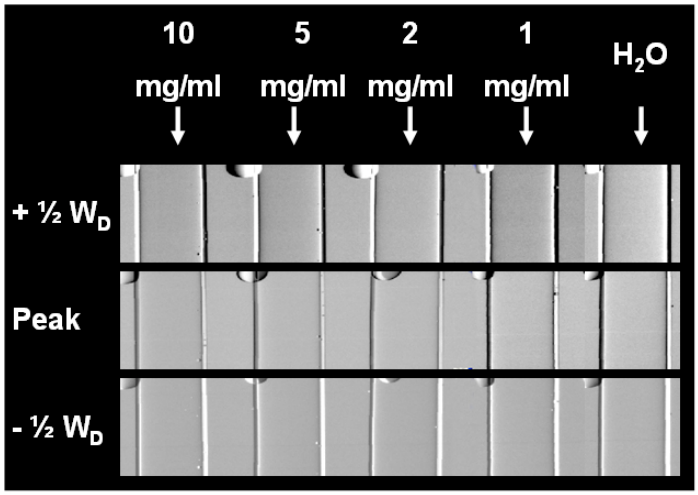

FIGURE 10.16: DEI Absorption Contrast from a Gadolinium Phantom. A 5 mm plastic capillary tube was filled with a range of gadolinium (Magnevist™) concentrations and imaged at 20 keV while submerged in a 50 mm water bath. DEI images were acquired at the ±½ W_D and peak rocking curve positions. Water bubble artifacts can be seen in some regions.

The measured absorption contrast values at 20 keV and 30 keV are graphed in Figures 10.17. The gadolinium phantom images at 40 keV contained artifacts that precluded accurate contrast measurements. As seen previously, the refraction contrast measured from a single image on the slope of the rocking curve contained a mixture of absorption and refraction contrast. A pure refraction image could only be generated from the 30 keV dataset, because the gadolinium phantom images at 20 keV were not acquired symmetrically on the rocking curve, likely due to monochromator or analyzer drift. When pure refraction processing was applied to images acquired at 30 keV, refraction contrast was not detectable (data not shown).

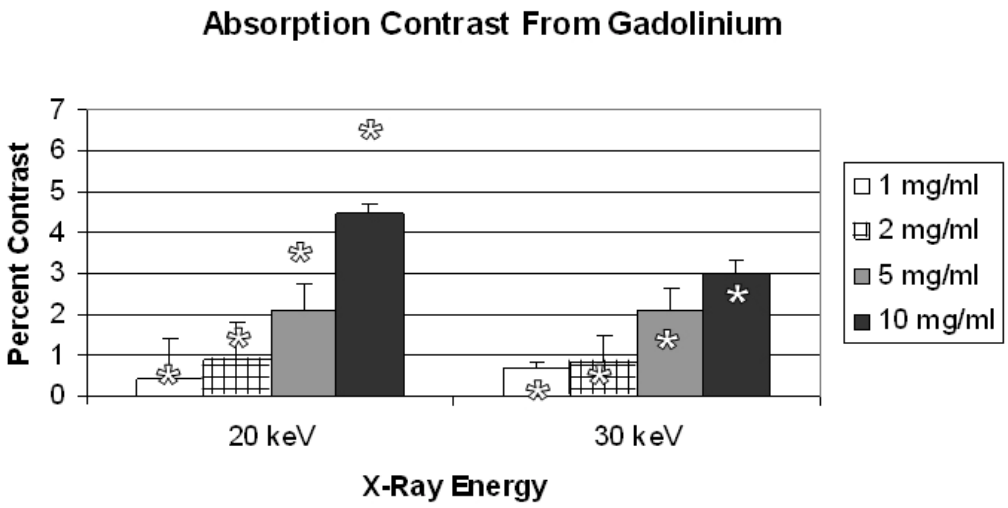

FIGURE 10.17: Measured Gadolinium Absorption Contrast. Percent contrast for each concentration of gadolinium was calculated for each x-ray energy and plotted. The (*) denotes the predicted percent contrast at that concentration and energy, as determined using the model in Figure 10.1.

DEI-CT images of the gadolinium contrast agent are shown in Figure 10.18. For apparent absorption processing (Row A), the 1 mg/ml, 5 mg/ml, 10 mg/ml, and 30 mg/ml gadolinium phantoms generated percent contrasts of 3.37%, 10.11%, 24.40%, and 53.64%, respectively. Similarly, the measured percent contrast in the refraction images (Row B) for 1 mg/ml, 5 mg/ml, 10 mg/ml, and 30 mg/ml gadolinium was -0.98%, 0.78%, 0.37%, and 0.25%.

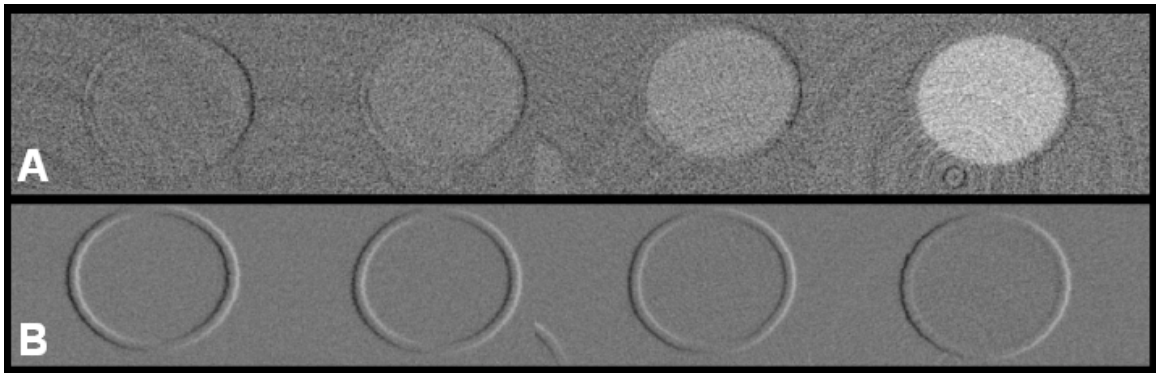

FIGURE 10.18: DEI-CT Imaging of Gadolinium Phantom. DEI-CT imaging was performed at 40 keV. Single representative DEI-CT slices are shown from left to right, representing 1 mg/ml, 5 mg/ml, 10 mg/ml, and 30 mg/ml gadolinium. Row A displays apparent absorption images; Row B shows refraction contrast images.

The gadolinium phantom was also imaged on a clinical digital mammography system at 26 kVp, as shown in Figure 10.19. The measured absorption contrast generated by 1 mg/ml, 2 mg/ml, 5 mg/ml, and 10 mg/ml gadolinium was 0.03%, 0.40%, 4.69%, and 7.36%, respectively.

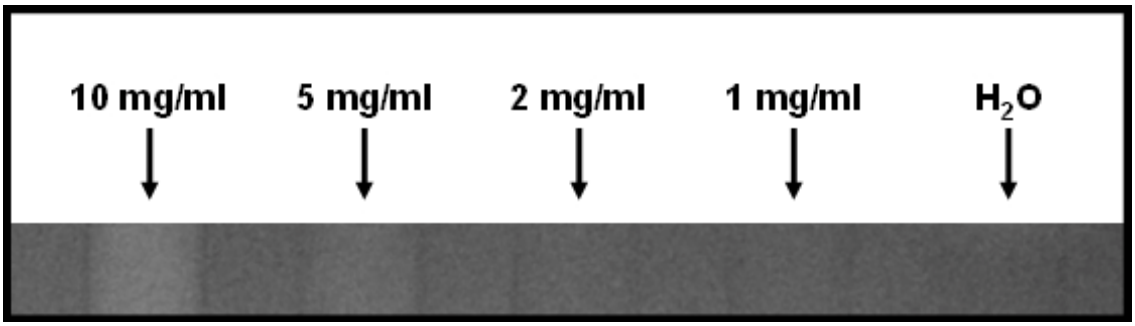

FIGURE 10.19: Digital Mammography of Gadolinium Phantom. Digital mammography was performed at 26 kVp of a gadolinium contrast agent phantom with 10 mg/ml, 5 mg/ml, 2 mg/ml, and 1 mg/ml gadolinium and a deionized water control.

10.10 Microbubbles as Potential DEI Contrast Agents

Microbubbles: Expected Performance as a DEI Contrast Agent. Contrast-enhanced ultrasound using microbubble injection has been evaluated for liver (Lencioni 2007, Rettenbacher 2007, Konopke 2007), breast (Kedar 1996, Albrecht 1998, Reinikainen 2002, Alamo 2001, Cassano 2006, Jiang 2007, van Esser 2007, Liu 2008, Balleyguier 2009), kidney (Mitterberger 2007, Correas 2006), pancreas (D'Onofrio 2007), spleen (Görg 2007, Catalano 2005), prostate (Mitterberger 2007, Heijmink 2007, Wink 2007), lymphatic mapping (Wang 2009a, Wang 2009b, Goldberg 2005), and vascular (Granada 2008, Coli 2008, Hennerici 2004) imaging applications. A previous study suggested that microbubbles might also be useful as contrast agents in DEI, since x-rays readily scatter from a gas-liquid interface (Arfelli 2003). For microbubble structures on the scale of microns, we expect x-rays to undergo ultra small angle scattering and be rejected by the analyzer crystal. In prior studies, gases have been used as a contrast agent

for x-ray through CO_2 injection for vascular imaging applications (Heye 2006, Chao 2007a, Shaw 2006).

Microbubble Phantoms: Lipid-encapsulated microbubbles were prepared as previously described (Zhao 2004).[14] Size distribution and concentration were measured using an optical particle sizer (Accusizer 780, Particle Sizing System, Santa Barbara, CA) immediately after microbubble synthesis. Microbubbles were maintained in sealed 1.5 mL vials under perfluorobutane gas for 24 hours during transport to the imaging facility. Prior to imaging, microbubble solutions were transferred into 10 mm by 10 mm (internal dimension) plastic cuvettes. A magnetic stir bar was placed in each sample tube and stirred at a rate of 120 rotations per minute, and then sealed with a plastic stopper to reduce microbubble decay during imaging. A control capillary tube was filled with phosphate buffered saline

Diffraction-Enhanced Imaging. DEI was performed as described in section 10.5, with the following modifications. Photons were detected using a 9 micron pixel size digital detector with a 36 mm by 24 mm imaging area (Photonic Science Limited, UK). DEI images were acquired at 30 keV. The full-width-at-half-maximum of the rocking curve is 2.10350 microradians. A series of images were acquired at the peak of the rocking curve. The average dose for these images was 0.26 ± 0.01 mGy.

We also acquired a series of images at analyzer crystal positions ranging from -5 microradians to +5 microradians in step sizes of 0.2 microradians. Each image was acquired with a dose of 0.04 ± 0.01 mGy, for a total of 2.08 mGy dose for the entire image set. This image series was used to calculate the change in the rocking curve width induced by the microbubble contrast agents, evaluating the FWHM, Full-Width-at-1/10th-

[14] Prepared in the laboratory of Dr. Paul Dayton at the University of North Carolina at Chapel Hill

Maximum (FW-1/10th-M), and the Full-Width-at-1/20th-maximum (FW-1/20th-M). These values were determined by separately selecting regions from the PBS control and the microbubble images, calculating the median intensity of each image.

The data for each image is an array of two sets of 50 points each, each corresponding to the 50 points acquired along the rocking curve. This was extrapolated to 5000 data points, creating a corresponding array of angles corresponding to the rocking curve positions. The maximum value of the data was measured, along with the location in the data set where the value was half, 1/10th or 1/20th of the peak value on both sides of the rocking curve, corresponding to the +/- FWHM/2, +/- FWHM/10, and +/- FWHM/20 points, thus finding the corresponding angle on the rocking curve. The FWHM is the difference in the values of those two points. Because the FWHM for the PBS control should be the same for all the control data sets, the standard deviation in the FWHM of the control was considered to be the standard deviation for both the control and microbubble data sets (+/- 0.03 microradians).

Microbubbles: Results. Microbubble size distribution and concentration for each sample (as measured immediately after microbubble synthesis) are listed in Table 10.5. When each sample is imaged at the peak of the rocking curve, the DEI attenuation contrast increases with increasing microbubble size, as shown in Figure 10.20. The peak position of the DEI rocking curve provides the greatest absorption contrast, with optimal scatter rejection by the analyzer crystal. Within this size range, we expected larger microbubbles to generate greater DEI contrast. For Sample A (1.1 μm), the measured attenuation contrast was 4.6 ± 0.9%. For Sample B (1.4 μm), the measured contrast was 15.0 ± 1.0%. For Sample C (2.9 μm), the measured contrast was 46.4 ± 1.0%.

	Mean	Standard Deviation	Median	Initial Concentration
Sample A	1.1 μm	0.4 μm	1.0 μm	$2.5x10^{10}$ microbubbles/ml
Sample B	1.4 μm	0.7 μm	1.4 μm	$1.7x10^{10}$ microbubbles/ml
Sample C	2.9 μm	1.5 μm	2.9 μm	$2.6x10^{9}$ microbubbles/ml

TABLE 10.5. Microbubble Characterization. Measurements were acquired immediately after microbubble synthesis.

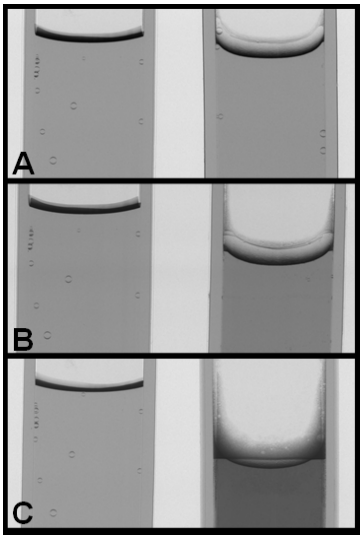

FIGURE 10.20: Effect of Microbubble Size. DEI images were acquired at 30 keV at the peak of the rocking curve. The phosphate buffered saline control is shown on the left, with each microbubble sample shown on the right. Panel A shows Sample A, approximately 1.1 μm; Panel B shows Sample B, approximately 1.4 μm; Panel C shows Sample C, approximately 2.9 μm.

We acquired a series of images across the DEI rocking curve. Figure 4 compares an image acquired at the peak (0 microradians) of the rocking curve (Panel A) to an image acquired in the tail (+5 microradians) of the rocking curve (Panel B). Increased contrast is seen at the peak, due to x-ray attenuation, a combination of x-ray absorption and scatter rejection. The images acquired at the tail of the rocking curve demonstrated an increase in scattered x-rays over the PBS control.

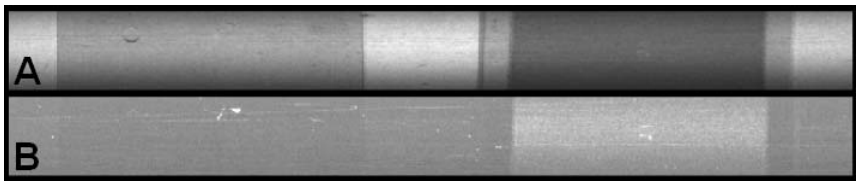

FIGURE 10.21: Extinction Contrast by Microbubbles. DEI images of Sample C (5 μm) were acquired at 30 keV at the peak and tail of the rocking curve. The phosphate buffered saline control is shown on the left, with each microbubble sample shown on the right. Panel A shows an image acquired along the rocking curve at the peak position. Panel B depicts an image acquired along the rocking curve on the tail of the rocking curve.

This series of images acquired along the rocking curve was used to calculate the FWHM, FW-1/10th-M, and the FW-1/20th-M of the microbubble phantom, with results listed in Table 10.6. When evaluating the FWHM, we did not detect substantial broadening of the rocking curve. This might be because the amount of broadening of the rocking curve is on the scale of the resolution for detecting angular change. However, when evaluating the FW-1/10th-M, where the ability to resolve differences in the rocking curve width is improved, there is a measurable increase in rocking curve width as microbubble size increased. At the FW-1/20th-M, we found a dramatic broadening of the rocking curve as microbubble size increased. However, these values are qualitative, and need to be confirmed in a quantitative study. The uncertainty in measuring the percent difference for the FWHM, FW-1/10th-M, and FW-1/20th-M was 0.04 μradians, 0.06 μradians, and 0.13 μradians, respectively.

		FWHM	FW-1/10th-M	FW-1/20th-M
Sample A	PBS	1.812	3.468	4.300
	Microbubble	1.808	3.526	4.526
	% Difference	**-0.22**	**1.7**	**5.3**
Sample B	PBS	1.742	3.462	4.306
	Microbubble	1.736	3.716	5.318
	% Difference	**-0.34**	**7.0**	**23.5**
Sample C	PBS	1.744	3.390	4.114
	Microbubble	1.772	4.270	6.640
	% Difference	**1.61**	**26.0**	**61.4**

TABLE 10.6: Rocking Curve Measurements. The Full-Width-at-Half-Maximum (FWHM), Full-Width-at-1/10th-Maximum (FW-1/10th-M), and the Full-Width-at-1/20th-Maximum (FW-1/20th-M) were calculated for the PBS control and the microbubble phantom. These values are reported in units of μradians. The percent difference in the widths between the microbubble sample and PBS control was also calculated.

10.11 Discussion

This project evaluated a variety of commercially available, clinically used contrast agents, performing DEI at a range of x-ray energies. Although we expected conventional molecular contrast agents or novel nanoparticle contrast agents to generate absorption contrast, we did not expect these types of contrast agents to generate substantial refraction or extinction contrast. However, we expected contrast agents with unique structures, such as microbubbles, would generate sufficient x-ray scattering, causing these x-rays to be rejected by the analyzer crystal and generating extinction contrast. It is possible that other unique contrast agent structures, on the scale of microns, might also generate scatter to take advantage of the unique DEI extinction contrast mechanism.

For iodine, iron, and gadolinium, the absorption and refraction contrasts measured from the contrast agent phantoms were generally in agreement with the predicted values. As expected, iodine generated good DEI absorption contrast, with detectable absorption contrast generated by 10 mg/ml Omnipaque^{TM} at 20 keV and by 5 through 10 mg/ml Omnipaque^{TM} at 40 keV. However, refraction contrast was poor. Iron oxide nanoparticles generated detectable absorption contrast by 10 mg/ml Feridex^{TM} at 20 keV. Pure refraction images could not be calculated for this dataset, but we expect that the true refraction contrast generated by this phantom is poor and below the clinical detection threshold. Moreover, the concentrations evaluated in this study were substantially greater than that used clinically for MRI contrast enhancement. Gadolinium chelate (Magnevist^{TM}) generated poor absorption and refraction contrast at the concentrations and energies used in this study. This was likely because the gadolinium contrast agent molecule has only one atom of gadolinium, while an iodine contrast agent contains three atoms of iodine per contrast agent molecule.

Microbubbles generated attenuation and extinction contrast, with increasing contrast as the microbubble size increased. The microbubbles caused increased x-ray scattering, which was rejected by the analyzer crystal, increasing the attenuation contrast when images were acquired at the peak of the rocking curve. We detected a widening of the rocking curve and increased intensity on the tail of the rocking curve, both confirming that the microbubbles indeed caused x-ray scattering which induced increased attenuation contrast.

In summary, molecular contrast agents might influence DEI contrast by affecting the physical density and effective electron density of the material. However, these

contrast agents only substantially influenced DEI absorption contrast. This contrast mechanism is not unique to DEI. Gaseous bubbles on the scale of microns created DEI attenuation and extinction contrast, with contrast dependant upon microbubble size. The extinction contrast mechanism is unique to DEI, and thus microbubbles might be an important DEI contrast agent. However, further analysis is needed to assess the potential of microbubbles as DEI contrast agents more completely.

10.12 Future Directions

The unique microbubble shape generates substantial DEI extinction contrast (for 5 μm microbubbles). There might be other contrast agent materials, shapes, or sizes that also allow increased contrast enhancement. Other materials not tested in the current study have been considered as x-ray contrast agents, including gold, silver, bismuth, platinum, tungsten, cesium, thorium, tin, zirconium, tantalum, ytterbium, and dysprosium (Yu 1999). Moreover, it will be important to establish the x-ray energy and concentration required to generate sufficient DEI contrast enhancement to ensure that these values are synergistic with safety and practicality.

Specific contrast-enhanced imaging protocols (e.g. digital subtraction, functionalization of contrast agents) or multimodal imaging techniques might further improve CE-DEI, while *in vivo* experiments will be necessary to determine if CE-DEI might be viable outside of laboratory studies. Digital subtraction of images acquired above and below the K-edge allows visualization of contrast agent biodistribution within the field of view, with minimized obscuration by surrounding or overlying tissue. A recent study demonstrated image enhancement using an iodine contrast agent by performing digital subtraction of images acquired above and below the iodine K-edge

using a bent Laue monochromator and x-ray tube source (Zhong 1997). A similar method might be possible using the DEI setup.

Although the amount of contrast agent at the tumor site is largely dependent on the degree of angiogenesis and the EPR effect (for contrast agents small enough to extravasate), attachment of a functional or targeting group might increase contrast enhancement, allow for extended imaging times, or provide a vehicle for delivery of diagnostic or therapeutic agents. Future studies might explore functionalized, contrast-enhanced DEI using a targeting agent such as Herceptin, a monoclonal antibody against HER-2 (erbB2/*neu*). This gene is expressed in all breast epithelial cells, and overexpressed in 10 to 34% of human breast cancers (Slamon 1989, Ross 2003, Camp 2003). A tumor overexpressing HER-2 will also demonstrate amplification in its metastatic sites (Niehans 1993).

Breast cancer targeting using Herceptin-functionalized contrast agents has been demonstrated using ferric oxide nanoparticles (Wuang 2007, Ito 2004, Wuang 2008, Sakamoto 2005), gold nanoparticles (Copland 2004), quantum dots (Tada 2007), and other novel nanoparticles (Sun 2008, Cirstoui-Hapca 2007). Herceptin is an attractive functionalization biomolecule because it is a commonly used antiproliferative, anti-angiogenic pharmaceutical agent that induces apoptosis in HER-2 expressing breast cancer cells (Nahta 2006).

The potential for contrast agents to have multimodal functionality has been recognized. For example, a magnetic contrast agent that might generate excellent x-ray absorption contrast might also be able to be used for MRI imaging. Some have suggested core-shell nanoparticle structures for multimodal contrast agents (Breskin 2004, Alric

2008, Zhang 2008b, Park 2007, de la Fuente 2006). Further, fluorescent dyes or gamma-emitting radioisotopes might also allow multimodal imaging. For example, gold nanoparticles strongly absorb electromagnetic radiation. With enough energy absorption, substantial heat can be generated, which ablates surrounding tissue, suggesting value for concurrent imaging and therapy with a single injection of contrast agent (Hainfeld 2008, Rahman 2009, von Maltzahn 2009, McMahon 2008, Lowery 2006).

In vivo CE-DEI is an important step to demonstrate that this imaging technique has value for clinical contrast-enhanced imaging. By acquiring a series of images at a single rocking curve position over minutes and hours, the initial enhancement, washout, and tumor retention might be visualized. However, this might be most appropriately assessed on a second-generation DEI system operating with faster image acquisition time because contrast agent concentration and biodistribution changes rapidly within the first hour post-injection. After imaging and euthanasia, the tumors, kidneys, liver, and spleen might be excised and frozen separately for elemental analysis by inductively coupled plasma mass spectrometry (ICP-MS) to confirm the biodistribution profile.

Contrast-enhanced DEI is just one of many potential applications of DEI, with potential applications outside of breast imaging. While the visibility of contrast agents with DEI is still only beginning to be explored, the visibility of many breast lesion characteristics has been shown to be excellent using DEI. DEI imaging parameters are still being established, and it is possible that DEI might allow improvements in these parameters over conventional mammography, such as a reduction in the compression required in order to generate a clinically useful image.

CHAPTER 11: EFFECT OF BREAST COMPRESSION ON LESION CHARACTERISTIC VISIBILITY WITH DIFFRACTION-ENHANCED IMAGING

11.1 Overview

Portions of this chapter include previously published data (Faulconer 2009b) reprinted with kind permission from Elsevier: Academic Radiology, *in press*. This chapter discusses the effect of breast tissue thickness on DEI lesion feature visibility. First, we provide an overview of the project. The hypothesis and goals of the project are discussed before a thorough description of the research methods, results, and discussion. Finally, a discussion of potential future studies is presented.

11.2 Motivation for Evaluating Lesion Visibility as a Function of Tissue Thickness

Breast cancer imparts distinct and measurable changes in breast tissue at the cellular level. Conventional mammography attempts to detect these changes by utilizing attenuation contrast based on the spatial distribution of x-ray attenuation. This contrast mechanism requires compression of the breast between radiolucent plates to decrease x-ray path length and separate overlapping breast structures, while creating more uniform thickness for even exposure levels throughout the breast, as depicted in Figure 11.1. This effectively reduces scatter, decreases subject radiation dose, and dramatically improves image quality. The American College of Radiology suggests a maximum compression force for mammography between 25 and 40 pounds (Hendrick 1999). Many women report the perception of pain associated with breast compression, potentially contributing

to noncompliance with annual screening mammography recommendations for women in the United States over the age of 40 (Keemers-Gels ME, Poulos 2003, Sapir 2003).

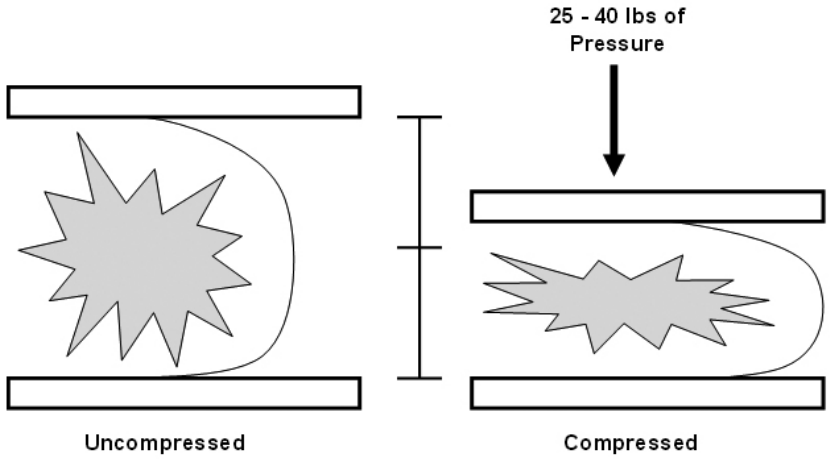

FIGURE 11.1: Breast Compression. Compression decreases structural noise by flattening and spreading out superimposed tissue layers. The decreased path length contributes to decreased absorption and subsequent dose reduction while less scattering volume improves image quality and increases the amount of x-rays transmitted onto the detector. Compression also ensures more even tissue exposure at the periphery of the breast.

It is generally accepted that increased tissue thicknesses decreases image quality for conventional mammography (Helvie 1994, Guest 2000). This is particularly true for low-energy x-rays. The percent intensity of x-ray transmission through breast soft tissue after x-ray absorption is shown in Figure 11.2. The increased tissue thickness attenuates more radiation, leading to higher Poisson noise, and also contributes to greater structural noise through superimposition of tissue structures. A recent study suggests, using Monte Carlo simulations, that the typical level of breast compression for digital mammography could be decreased by approximately 12.5% with minimal impact on image quality (Saunders 2008). Another study found that for a 9% and 23% change in tissue thickness, the contrast was reduced by 5% and 12%, respectively, while the resolution was decreased by 8% and 19%, respectively (Helvie 1994).

However, even with maximal breast compression, attenuation contrast does not always provide sufficient contrast due to minimal differences in physical and electron density between normal and cancerous tissues. Although monochromaticity alone has demonstrated the potential to decrease dose and facilitate reduced breast compression (Liu 2007a, Arfelli 2000, Boone 1999, Johnston 1996, Kimme-Smith 1999, Lawaczeck 2005), we believe that the contrast mechanisms that are unique to DEI might enable mammography with reduced breast compression. Although refraction contrast may not be as severely limited by tissue thickness, overlying structures might cause multiple refraction events that may reduce overall refraction contrast for a thick object (Gang 2005).

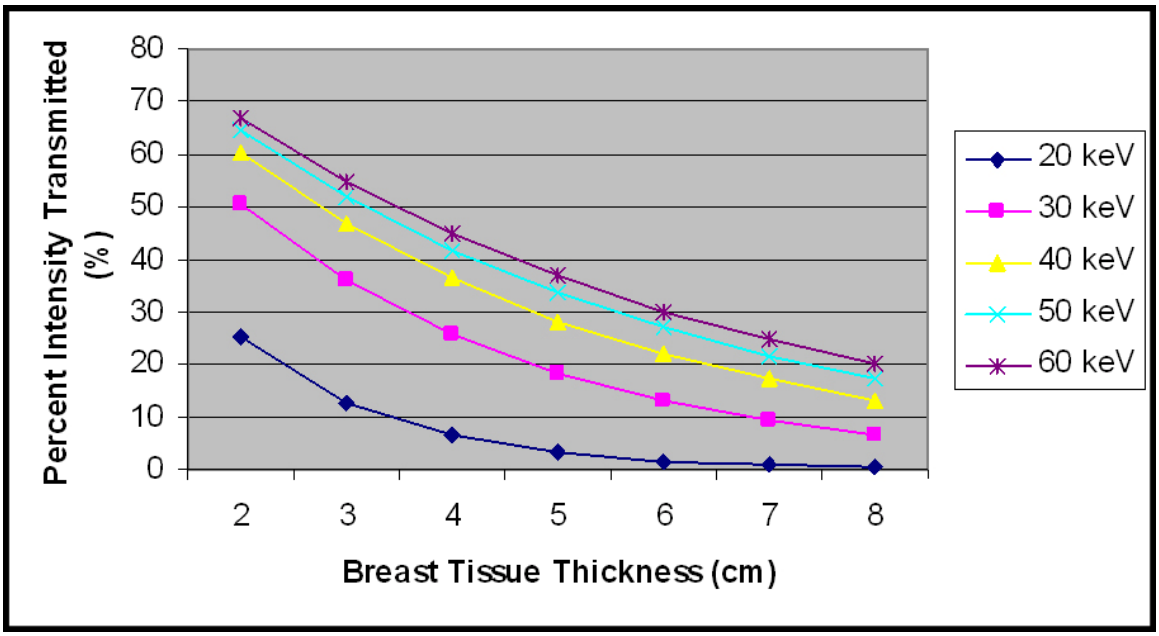

FIGURE 11.2: Decrease in X-Ray Transmission as Tissue Thickness Increases. The graph plots the percent intensity of x-ray transmission, considering decrease in x-ray intensity due to absorption effects with respect to tissue thickness. Low-energy x-rays are more readily absorbed, decreasing the x-ray intensity incident on the detector, and thus increasing Poisson noise in the resulting image. Calculations are for half-glandular half-fatty tissue composition (50% density).

11.3 Hypothesis and Goals

The current study investigates the effect of breast compression on DEI image quality and lesion characteristic visibility. It is our hypothesis that decreased breast compression might be possible with DEI without significantly altering image quality. In this paper, we present our results for the imaging of human breast tissue specimens at 30 keV, with evaluation of the effect of tissue thickness on image quality via a reader study performed by five expert radiologists. This work demonstrates a potential advantage of DEI mammography over conventional mammography for reduced compressed tissue thickness without substantially compromising image quality.

11.4 Study Design and Methods

All experiments were conducted with appropriate approvals granted by the University of North Carolina at Chapel Hill (UNC-CH) Institutional Review Board and were HIPAA-compliant.

Specimen Selection. Four mastectomy specimens were obtained from the Department of Pathology at UNC-CH without identifying patient information. As per usual clinical practice, these tissues were sliced for clinical purposes prior to acquisition for use in this study. Representative thin slices containing regions of interest (ROIs) with suspicious pathology were excised from the whole specimen. Seven full-thickness, un-sliced breast specimens were obtained by dissection from cadavers made available by the UNC-CH Department of Cell Biology and Anatomy. All specimens were fixed in 10% buffered formalin and stored at room temperature.

For thin specimen imaging, specimens were placed directly between two 5 mm Acrylic plates with compression adjustment by a series of threaded rods. Full-thickness

specimens were first placed in deionized water in plastic bags with care to eliminate air bubbles before being placed between Acrylic plates. Specimen mounting is diagrammed in Figure 11.3. After the specimens were immobilized in the compression devices, natural resting thicknesses were measured using a standard ruler. Half- and fully- compressed thicknesses were 25% ± 1% and 47% ± 5% of resting thicknesses, respectively.

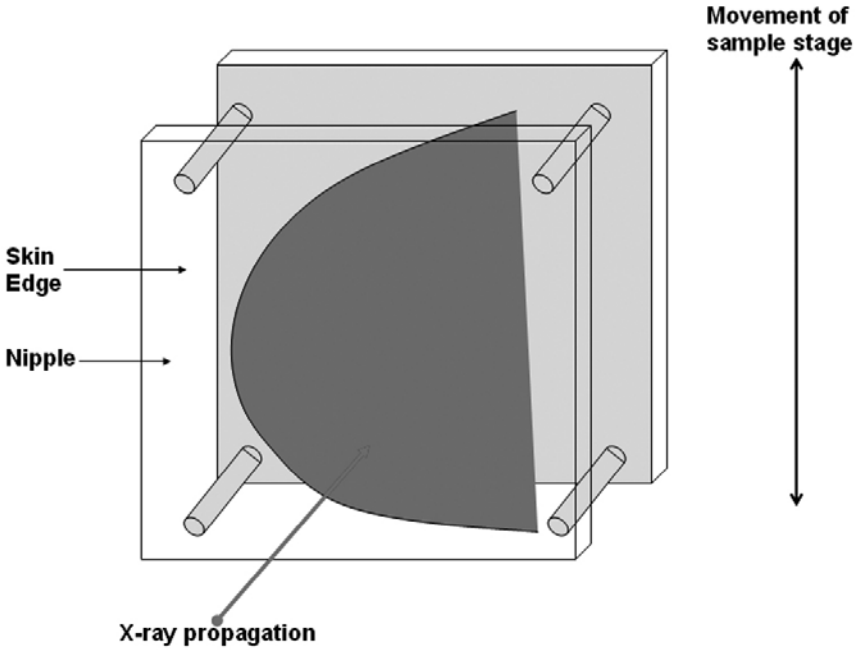

FIGURE 11.3: Diagram of Specimen Mounting in Compression Plates. Thin specimens were mounted directly between two 5 mm thick Acrylic plates. Full thickness specimens were placed in plastic bags (26.8 by 15.4 by 8.8 cm, 1.75 to 2.00 mil) filled with deionized water. Care was taken to eliminate air bubbles when mounting. Compression levels were changed by adjusting nuts on threaded bolts positioned through each corner of the Acrylic plates.

Diffraction-Enhanced Imaging. DEI was performed at the National Synchrotron Light Source X15A beamline at Brookhaven National Laboratory in Upton, New York. The DEI setup is shown in Figure 11.4, as described previously (Zhong 2000). The linear collimated beam was 130 mm by 2 mm using a Bragg [333] crystal reflection. The double-crystal monochromator (Shaw Monochromators, Riverton, KS) was comprised of a series of two perfect silicon crystals mounted on independently tunable stages in a

continuously helium-flushed steel tank. By manipulating the angle of the monochromator crystals, 30 keV x-rays were selected based on the Bragg angle. The collimated monochromatic x-ray beam then interacted with the object being imaged before diffraction by the analyzer crystal, only reflecting x-rays that fall within a narrow range of energies and angles. Manipulating the angle of the analyzer crystal allowed the selection of image contrast based on either absorption or refraction. Refraction contrast images were acquired at the ±½ Darwin width (W_D) of the rocking curve, which is equal to half of the full width at half maximum. Attenuation contrast images were acquired at the peak of the rocking curve.

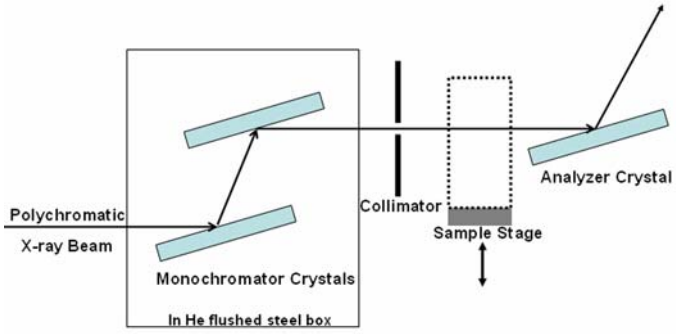

FIGURE 11.4: DEI System Setup. An intense, collimated polychromatic synchrotron x-ray beam is made monochromatic by a series of two perfect silicon crystals referred to as the monochromator. The monochromatic beam interacts with the object before becoming incident to the third perfect crystal, referred to as the analyzer crystal. The analyzer crystal diffracts the x-ray based on its rocking curve, only reflecting x-rays that fall within a narrow acceptance window. Manipulating the angle of the analyzer crystal allows the selection of image contrast based on either absorption or refraction.

The flux of the post-monochromator beam was measured using an ion chamber. Images were acquired with a stimulable phosphor Fuji ST-VI image plate (Fuji Medical Systems, Stamford, CT) and developed by laser on the Fuji BAS-2500 image plate reader (Fuji Medical Systems, Stamford, CT). The image plate was affixed perpendicular to the x-ray beam diffracted from the analyzer crystal at twice the Bragg angle. Images were acquired un-compressed (resting thickness), half-compressed (75% of resting thickness)

and fully-compressed (50% of resting thickness) at each of three rocking curve positions: -½ W_D, +½ W_D, and peak. DEI surface dose was approximately 0.33 mGy.

Vertical linear artifacts created by crystal glitches were corrected manually using an Interactive Data Language (IDL) (ITT Visual Information Systems, Boulder, CO) image processing technique that included an in-house flattening algorithm applied to the vertical axes. DEI image files were converted from tiff to DICOM format using DICOMAccess (DesAcc, Chicago IL) software for display on the Sectra IM.5X mammography softcopy review workstation (Sectra, AB., Shelton, Connecticut).

Full-Field Digital Mammography. The specimens were imaged on the General Electric (GE) Senographe 2000D (Waukesha, WI) at UNC Hospitals, with an average x-ray energy of 26 keV for thin specimens and 27.5 keV for thick specimens. The SNR of the GE Senographe 2000D was measured to be 83.49 at 25 mm, 71.65 at 40 mm, and 56.51 at 60 mm. The half-value layer was calculated to be 0.374, as measured using the ACR phantom, which simulates calcifications, fibrous calcifications in ducts, and tumor masses. The x-ray energy and tube voltage were manipulated manually by an experienced radiology technologist to achieve an optimal absorption image at each compression level. Thus, the average surface doses for un-, half- and fully-compressed breast specimen images were 20.96 mGy, 13.54 mGy and 8.52 mGy, respectively. Images were saved in softcopy DICOM format with GE preprocessing applied for review workstation display.

Specimen Assessment. While blinded to history, lesion pathology, and lesion location, a breast imaging radiologist (EDP) identified 21 regions of interest (ROIs) using DM images. Further, this reader evaluated fully-compressed DM images of each specimen, estimating the radiographic density (percent adipose and glandular tissue

composition). An expert pathologist (CAL) performed pathologic sectioning of the 21 ROIs previously identified within 10 tissue specimens.

Reader Study. A training set of six ROIs within four specimens was compiled detailing the interpretation of refraction-contrast DEI images containing both benign (fibrous tissue spiculations) and malignant (invasive lobular carcinoma, infiltrating ductal carcinoma) features. DM specimen images were provided for reference. Readers were instructed on refraction-based contrast mechanisms, guided through the use of the softcopy review workstation, and introduced to several common DEI image artifacts. Possible image manipulations included magnification, zoom, pan, and window/level adjustments. Training required approximately 30 minutes. Informed consent was obtained from participating radiologists.

All images were displayed on the calibrated softcopy workstation. Each DEI image acquired with full-compression was displayed side-by-side with a DEI image acquired either half- or un- compressed. A reference DM image acquired at full-compression was displayed on a second monitor. This image was for reference only, displaying each ROI using attenuation contrast in a familiar format. ROIs were circled and pathology was provided, with instruction to consider positioning differences between images. Five expert radiologists were asked to compare lesion characteristic visibility between each DEI image pair using a seven-point quality score scale. Readers were given a five minute break for every 50 minutes of read time with additional breaks as desired. The average read time was two hours. A research assistant was present to assist the readers with any technical difficulties.

Statistical Method. We fit a multivariate linear mixed model to investigate whether scores differed by breast compression. In the model, the responses were the scores generated by the five readers. To account for the heterogeneity among the specimens, in addition to the main effect of full-compression versus half-compression and full-compression versus no-compression, other covariates included in the regression model were the specimen thickness when un-compressed, specimen type (cadaveric versus mastectomy), rocking curve position (-½ W_D, peak or +½ W_D), lesion type (atypical, benign, *in situ* or malignant), and variables representing the five readers.

Furthermore, the interactions between breast compression and all these covariates were included in order to study possible modifying effects due to these covariates. We used 0.05 / 20 = 0.0025 as the level for statistical significance to adjust for a total of 20 comparisons, with a 95% confidence interval. Each region of interest from the specimen was treated as random effect in the linear mixed model. The model fit was carried out in SAS version 9 (SAS Institute, Cary, NC).

11.5 Effect of Tissue Compression on Lesion Visibility with DEI

Specimen Parameters. Specimen parameters that could influence image quality include specimen thickness as well as the relative glandular and adipose tissue composition. Specimens with greater glandular composition will attenuate more x-rays and might demonstrate increased structural noise. Specimen thickness and percent density is listed in Table 11.1.

The median radiographic density of the specimens included in this study was comparable to the typical radiographic density for pre- and peri-menopausal women (Kelemen 2008). For the full-thickness specimens included in this study, the average un-

compressed, half-compressed, and fully-compressed thicknesses were 6.46 cm, 4.97 cm, and 3.5 cm, respectively. Of the 21 ROIs, 13 were benign, one was atypical, and seven were malignant. The malignant lesions included ductal carcinoma *in situ* (DCIS) and invasive metaplastic carcinoma.

	Glandular (%)	Adipose (%)	Un-Compressed Thickness (cm)	Half-Compressed Thickness (cm)	Fully-Compressed Thickness (cm)
Specimen 1	10	90	3.9	2.9	2.0
Specimen 2	20	80	3.9	2.9	2.0
Specimen 3	30	70	3.9	2.9	2.0
Specimen 4	40	60	3.9	2.9	2.0
Specimen 5	90	10	6.7	6.1	3.4
Specimen 6	30	70	5.8	4.3	2.9
Specimen 7	50	50	5.1	3.8	2.5
Specimen 8	10	90	7.1	5.3	3.6
Specimen 9	40	60	6.5	4.9	4.0
Specimen 10	20	80	6.0	4.7	3.2
Specimen 11	30	70	8.0	6.7	5.5

TABLE 11.1: Measured Specimen Thicknesses and Percent Densities. Specimens were compressed an average of 24.7 ± 1.2 (%) of resting thickness at half-compression and 46.6 ± 4.6 (%) of resting thickness at full compression. The glandular / fatty composition of each specimen was assessed by an experienced radiologist.

Qualitative Assessment of Lesion Visibility as a Function of Tissue Thickness. Attenuation increases as tissue thickness increases. Images acquired at the peak of the rocking curve have a substantial proportion of image contrast due to x-ray absorption, and so image quality was expected to deteriorate with increasing tissue thickness. We expected refraction contrast images to be less affected by tissue thickness due to the properties of x-ray refraction and excellent scatter rejection by the analyzer crystal.

As can be seen qualitatively in Figures 11.5 and 11.6, DEI image quality did not vary greatly with respect to tissue thickness for either cancerous or benign pathologies,

respectively. As expected, DEI images acquired at the rocking curve peak suffered a greater loss of lesion detail visibility than those acquired at the ±½ W_D due to contrast based predominantly on attenuation contrast mechanisms. Qualitatively, structural noise increased as tissue thickness increased, even on DEI images.

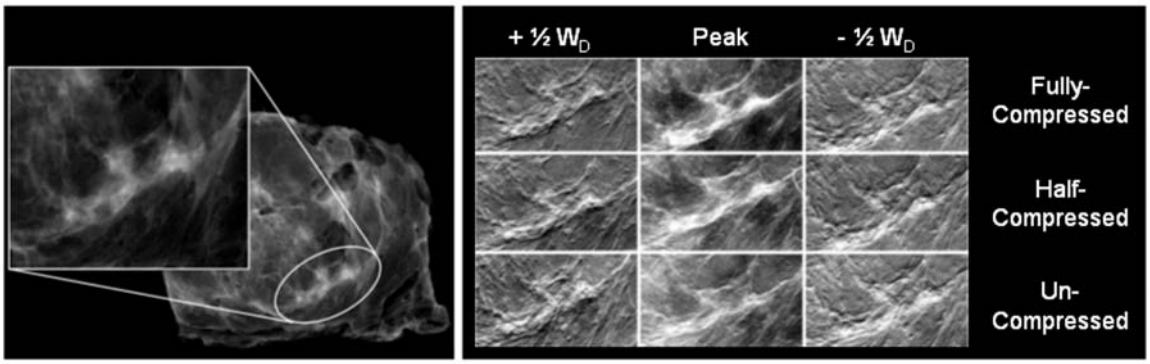

FIGURE 11.5: Effect of Tissue Thickness on Cancerous Lesion Visibility. The circled region of interest contained extensive comedo-type ductal carcinoma *in situ* of nuclear grade three with necrosis and lobule cancerization, without calcifications. The left panel depicts a digital mammogram of a mastectomy specimen. The panel on the right shows the same lesion, cropped and shown at full-, half-, and un-compression at each DEI rocking curve position.

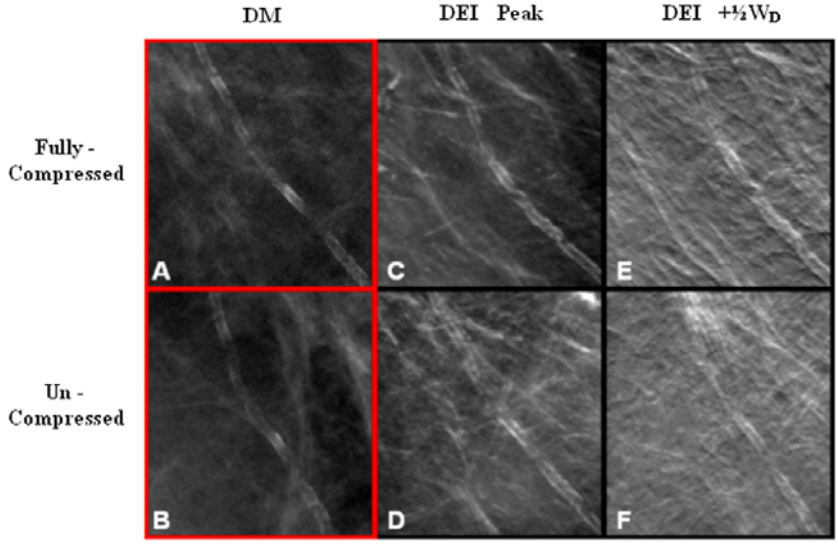

FIGURE 11.6: Effect of Tissue Thickness on Benign Feature Visibility. All images were acquired at 30 keV. This ROI represents a vascular calcification. DM images are displayed in the first column (A,B). The second column (C,D) represents images acquired at the peak of the rocking curve, and the third column (E,F) were acquired at the + ½ W_D. The fully compressed DM image (panel A) was acquired with a surface dose of 7.46 mGy while the dose required to acquire an optimal image of the uncompressed specimen (panel B) was 30.93 mGy. DEI images were acquired with relatively constant doses at all thicknesses, with an average dose of 0.30 mGy for the above images.

Reader Study Analysis. Expert radiologist perception of image quality was ascertained through a reader study where DEI images of fully-compressed specimens were compared to DEI images acquired at either half- or un-compressed thickness. The average scores recorded by the radiologists were plotted as a function of the difference in tissue thickness, shown in Figure 11.7. As the difference in tissue thicknesses increased, radiologists tended to perceive lesion features supportive of the diagnosis better in the fully-compressed images. DEI lesion feature visibility tended to decrease more rapidly with increasing thickness for images acquired at the peak of the rocking curve, where contrast is based predominantly on x-ray absorption.

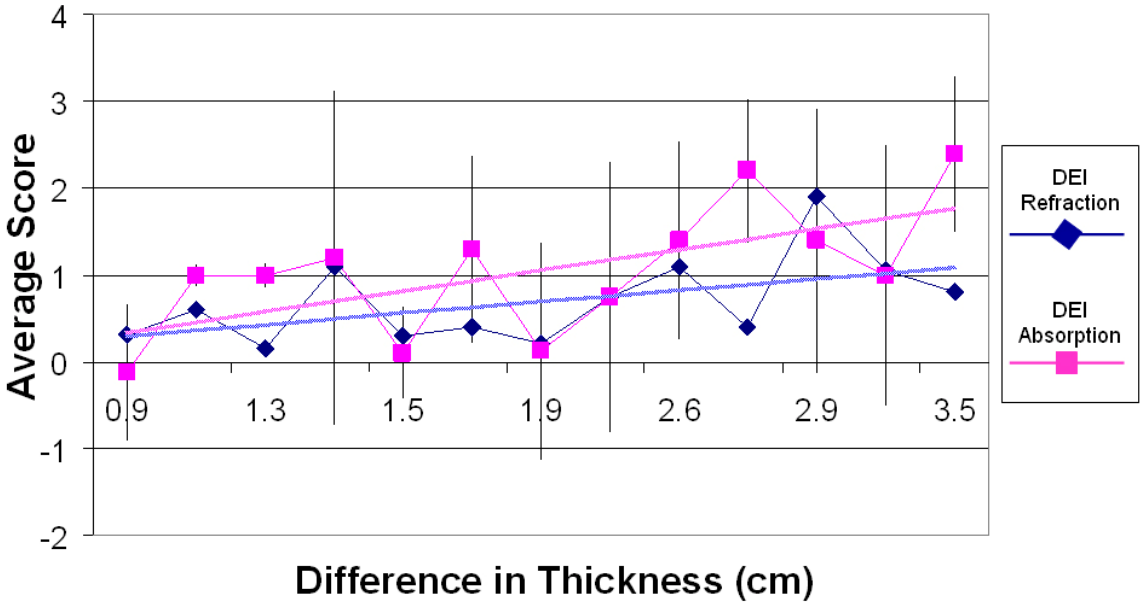

FIGURE 11.7: Trend in Lesion Perception as Tissue Thickness Increases. The average scores reported by the radiologists were plotted as a function of the difference in tissue thickness, measured in cm. The score values could range from -3 (the fully-compressed DEI image displays lesion feature visibility supportive of the diagnosis significantly *worse* than the DEI image acquired with reduced compression), to 0 (no difference between either image), to +3 (the fully-compressed DEI image displays lesion feature visibility supportive of the diagnosis significantly *better* than the DEI image acquired with reduced compression).

No evidence indicates that the scores depend on the thickness of the uncompressed breast (p-value = 0.80). From the fitted model, we predicted the mean scores for fully-compressed versus half-compressed and fully-compressed versus un-compressed across different imaging conditions or features of the specimen. Overall, there is no evidence that the scores given by radiologists for fully-compressed versus half-compressed are different from zero (p-value = 0.147). However, the mean score for fully-compressed specimens versus un-compressed specimens is significantly different from zero (p-value = 0.0004).

Because previous DEI research only included thin tissue specimens, we sought to determine if there was a difference between these thin mastectomy specimens and full-thickness breast tissues. The results shown in Table 11.2 demonstrate that DEI image quality is not significantly decreased for approximately a 25% change in tissue thickness. Overall, feature visibility was significantly different between DEI images acquired with a 50% difference in tissue thickness. When evaluated by specimen type, mastectomy thin specimens or cadaveric thick specimens, we did not detect a difference in reader perception of lesion characteristic visibility. It is noted that the findings for a 50% difference in thickness in cadaveric thick specimens approached statistical significance.

	Difference in Tissue Thickness	Mean	Standard Error	95% CI	p-value
Cadaveric	25%	0.3863	0.3357	(-0.273, 1.046)	0.2504
	50%	0.9678	0.3357	(0.308, 1.627)	**0.0041**
Mastectomy	25%	0.1019	0.2331	(-0.356, 0.560)	0.6623
	50%	0.2212	0.2331	(-0.237, 0.679)	0.3430

TABLE 11.2: Reader Study Results: Effect of Specimen Type. The p-values were calculated based on the calculated means, standard errors, and a 95% confidence interval (CI). Radiologist perception of lesion visibility for a 50% difference in tissue thickness in cadaveric specimens approached significance.

We also evaluated whether rocking curve position influenced radiologist perception of lesion visibility for differences in tissue thickness, shown in Table 11.3. We did not detect a difference in lesion visibility dependent upon rocking curve position for a 25% difference in tissue thickness. For a 50% difference in tissue thickness, we found a significant difference for the -½ W_D rocking curve position (p-value = 0.0001), and the results approached significance at the peak and +½ W_D positions.

	Difference in Tissue Thickness	Mean	Standard Error	95% CI	p-value
-½ W_D	25%	0.2631	0.2002	(-0.130, 0.656)	0.1892
	50%	0.7818	0.2002	(0.389, 1.175)	**0.0001**
Peak	25%	0.1679	0.2002	(-0.225, 0.561)	0.4020
	50%	0.5056	0.2002	(0.113, 0.899)	**0.0118**
+½ W_D	25%	0.3012	0.2002	(-0.092, 0.694)	0.1329
	50%	0.4961	0.2002	(0.103, 0.889)	**0.0135**

TABLE 11.3: Reader Study Results: Effect of Rocking Curve Position. Scores for both specimen types (i.e. cadaveric and mastectomy) were averaged at each rocking curve position and compression level. The p-values were calculated based on the calculated means, standard errors, and a 95% confidence interval (CI). For a 50% difference in tissue thickness, radiologist perception of lesion visibility was different for each rocking curve position, but we only found statistical significance at the –½ W_D position. The results approached significance at the peak and +½ W_D positions.

Moreover, we investigated whether radiologist perception of lesion visibility was influenced by the type of lesion (benign, atypical, *in situ*, or malignant). Results are displayed in Table 11.4. The only significant difference was found for benign lesions (p-value < 0.0001), when the difference in tissue thickness was approximately 50%. It is interesting to note that benign lesion visibility for a 25% difference in tissue thickness approached statistical significance. Additionally, visibility of *in situ* lesions for a 50% difference in tissue thickness approached significance (p-value 0.0087). Thus, for a 25%

difference in tissue thicknesses, radiologists tended to perceive benign lesion features worse with reduced compression. For a 50% difference in tissue thickness, the difference in radiologist perception of benign lesion features between the image pair was significantly different, and we detected a trend for decreased perception of *in situ* lesion features for this difference in tissue thickness.

	Difference in Tissue Thickness	Mean	Standard Error	95% CI	p-value
Benign	25%	0.3719	0.1454	(0.086, 0.657)	**0.0108**
	50%	0.6389	0.1454	(0.353, 0.925)	**<0.0001**
Atypical	25%	0.3052	0.4643	(-0.607, 1.217)	0.5113
	50%	0.5500	0.4643	(-0.362, 1.462)	0.2367
In Situ	25%	0.3941	0.2932	(-0.182, 0.970)	0.1794
	50%	0.7723	0.2932	(0.196, 1.348)	**0.0087**
Malignant	25%	-0.09481	0.2641	(-0.614, 0.424)	0.71975
	50%	0.4167	0.2651	(-0.102, 0.935)	0.1152

TABLE 11.4: Reader Study Results: Effect of Lesion Type. The p-values were calculated based on the calculated means, standard errors, and a 95% confidence interval (CI). Difference in the perception of benign lesion visibility approached significance for a 25% difference in tissue thickness, and achieved significance at a 50% difference in tissue thickness. *In situ* lesion visibility also approached significance for a 50% difference in tissue thickness.

Because DM images were obtained with different imaging parameters than DEI, direct comparisons are not appropriate between the effect of compression on DEI images and DM images. However, we did acquire DM images at each compression level, allowing the DM proprietary software to automatically calculate the optimal imaging parameters at each compression level. The average score reported for fully-compressed versus half-compressed DM images was 0.5 ± 1.2. However, as the tissue thickness increased, scores for fully-compressed versus un-compressed averaged 1.3 ± 1.1. This suggests that, even with optimization of imaging parameters as tissue thickness increases,

the lesion feature visibility deteriorates with increasing tissue thickness for DM. When compared to the overall average scores for DEI lesion visibility at 25% and 50% difference in tissue thickness, the DEI images tended to received an overall better score than DM images, shown in Figure 11.8, even though DM image acquisition was optimized at each compression level whereas DEI image acquisition parameters remained constant.

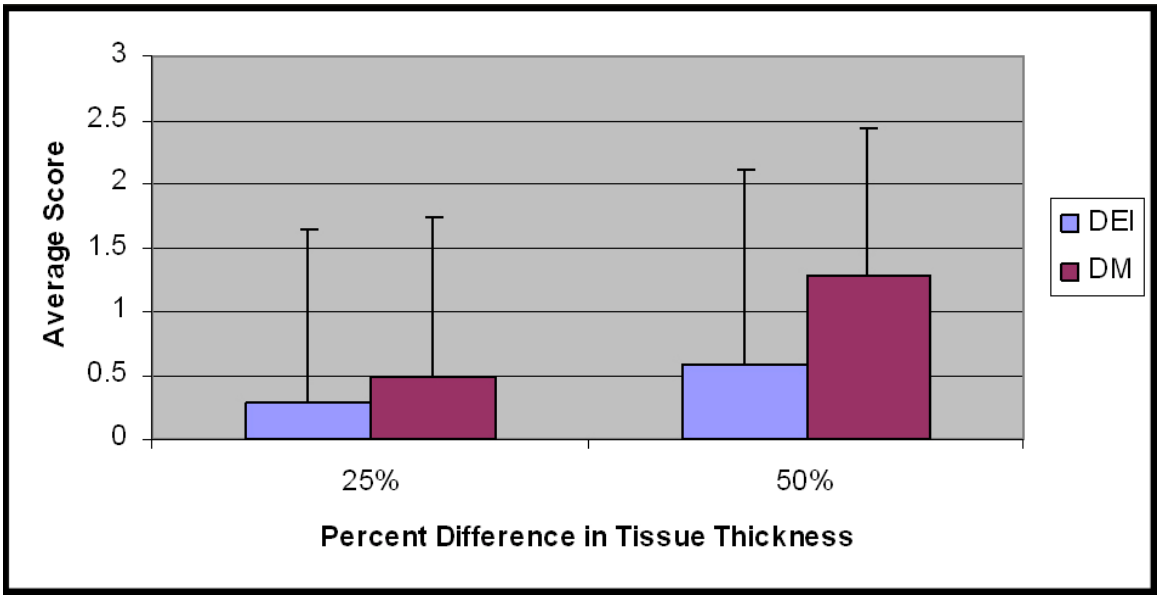

FIGURE 11.8: Overall, DEI Lesion Visibility Less Affected than DM. The score values could range from -3 (the fully-compressed DEI image displays lesion feature visibility supportive of the diagnosis significantly *worse* than the DEI image acquired with reduced compression), to 0 (no difference between either image), to +3 (the fully-compressed DEI image displays lesion feature visibility supportive of the diagnosis significantly *better* than the DEI image acquired with reduced compression). When the lesion visibility scores were averaged across all readers for DEI and Digital Mammography (DM), the reported scores for DEI tended to suggest that DEI was less affected by increasing tissue thickness than DM, although this result was not significant.

11.6 Discussion

Breast soft tissue poses many challenges due to minimal differences in the radiographic appearance of benign and cancerous tissues. Although often perceived as painful, compression is necessary for sufficient image quality in conventional

mammography. This discomfort can be mitigated through optimized imaging techniques and technologies (Dibble 2005, Dullum 2000, Markle 2004, Miller 2008, Montgomery 208), but an ideal system would not require compression. Refraction sensitivity, higher x-ray energy, scatter rejection by the analyzer crystal, use of a monochromatic beam, and all unique features available using DEI might allow reduced breast compression without compromising lesion feature visibility supportive of the pathologic diagnosis.

Our reader study suggests that radiologist perception of DEI image quality is not significantly changed for a 25% difference in tissue thickness, but as the difference in tissue thickness approaches 50%, differences in radiologist perception of lesion visibility were detected. With a 50% difference in tissue thickness, statistically significant results, indicating decreased lesion visbility, were found at the $-\frac{1}{2}$ W_D rocking curve position. Scores for the peak and $+\frac{1}{2}$ W_D rocking curve positions at a 50% difference in tissue thickness approached significance, indicating that the lesion visibility might tend to decrease at these rocking curve positions as well at greater tissue thicknesses. Although images acquired at the $\pm\frac{1}{2}$ W_D represent the same physical contrast mechanism, radiologist perception of the images or system instability might have led to the scoring differences found in the current study.

We expected the peak rocking curve position to be negatively affected by increasing tissue thickness moreso than refraction contrast images. However, the current study suggests that lesion feature visibility was decreased at all three rocking curve positions when the difference in thickness was approximately 50%, with significant difference for the $-\frac{1}{2}$ W_D position, yet no differences were detected for any rocking curve positions for a 25% difference in tissue thickness. In spite of the superior physics of DEI

image contrast, a combination of multiple refraction events and increased structural noise are likely the causes of decreased lesion visibility for 50% difference in tissue thickness. But, these results are encouraging- suggesting that some reduction in breast compression might be possible for DEI applied to clinical breast imaging.

This difference at the $-\frac{1}{2}$ W_D rocking curve position, and not also at the $+\frac{1}{2}$ W_D, might have occurred due to analyzer or monochromator drift. This difference might disappear with a larger set of specimens, or with different radiologists. Moreover, we detected a significant difference in lesion perception scores between the five radiologists. This demonstrates a strong need to develop a refraction-contrast breast feature atlas in order to thoroughly train radiologists in refraction-contrast image interpretation, with comparison to conventional radiographic features when DEI is applied clinically.

Except in our previous studies (Parham 2009, Faulconer 2009a), to the best of our knowledge, all DEI breast specimen imaging has been performed using thin specimens not representative of clinical imaging parameters. In the current study, radiologist perception of lesion visibility did not depend on uncompressed specimen thickness. Thus, mastectomy specimens and the full-thickness cadaveric specimens might not demonstrate substantially different lesion feature visibility. Therefore, conclusions drawn from prior studies using such thin specimens might be relevant to imaging full-thickness specimens. However, this implication might be biased due to the fact that the mastectomy specimens in the current dataset typically contained malignant features, while the lesions in the cadaveric specimens typically contained benign features. Although our previous work suggested that the lesion type did not influence radiologist perception of lesion features in

full-thickness breast specimens at the [333] reflectivity (Faulconer 2009a), the current data suggest that benign feature perception might be affected by tissue thickness.

The limitation to specimen imaging is an inherent constraint on the current study since formalin-fixed tissues do not compress in the same manner as living tissue. Formalin dehydrates tissues and alters the structure of collagen by decreasing the d-spacing, with more severe effects associated with longer periods of fixation (Fernández 2005). This may affect lesion radiographic appearance and the mechanics of breast compression. Inherent lesion stiffness might also affect image quality with respect to tissue thickness. As the tissue is compressed, the breast parenchymal tissue and the lesion thicknesses might not change at the same rate. This might affect the x-ray attenuation, and thus the attenuation contrast. Compression is less likely to induce a large change in the interface between these regions to affect refraction contrast with respect to lesion stiffness.

Specimens obtained from surgical pathology have been sliced throughout the entire specimen, as per usual clinical practice. Compressing a sliced specimen does not represent a realistic situation, with un-reproducible shift artifacts and unrealistic compression mechanics. Thus, our study used thin specimens with malignancies and cadaveric full-thickness, un-sliced specimens. Because of the many differences between specimen and *in vivo* imaging, this study should be repeated when a DEI system is available for clinic-based studies.

Several drawbacks to reduced compression might still exist, such as uneven exposure, motion artifacts, and the ability to image near the chest wall. Digital post-processing algorithms can adjust images acquired with uneven tissue exposure levels

allowing excellent contrast through both thick and thin regions at breast edges. Immobilization of the breast combined with breathing techniques during imaging might help minimize motion artifacts. Compression is typically used to pull tissue away from the chest wall. Patient positioning and imaging techniques might facilitate imaging near the chest wall without breast compression.

In summary, we believe that some degree of reduced compression can generate DEI images with excellent lesion feature visibility, free from scatter, and without a high radiation dose. While recent studies have shown that digital mammography image quality can be preserved with a minimal reduction in tissue thickness (Saunders 2008), DEI might allow a 25% or greater reduction in breast tissue thickness without significantly compromising lesion feature visibility. This study demonstrates the potential of DEI to acquire images of breast lesions with reduced compression without substantially compromising visibility of lesion features important for the pathologic diagnosis. This might have an important impact on patient comfort, potentially increasing compliance with annual mammographic screening recommendations.

11.7 Future Directions

Because of the several limitations that were unavoidable at the time of this study, the data should be confirmed in future clinical studies. Data should be collected using a clinical DEI system, with particular attention to women with large breasts or women with lesions located near the chest wall. A recent study suggested that tomosynthesis might allow a reduction in breast compression without compromising mass and calcification conspicuity (Saunders 2009). It would be interesting to evaluate how three-dimensional DEI, through either the existing DEI-CT system or through a limited-angle reconstruction

of a set of DEI images, might influence lesion visibility with respect to varying breast tissue thicknesses. Further, because reduced breast compression would likely increase patient comfort, a quality of life survey might evaluate whether this reduction in compression affects patient perception of pain or anxiety related to breast imaging.

CHAPTER 12: READER STUDY EVALUATION OF A DIFFRACTION-ENHANCED IMAGING PROTOTYPE

12.1 Overview

Portions of this chapter include previously published data (Faulconer 2009a) reprinted with kind permission from Elsevier: Academic Radiology, *in press*. This chapter discusses the performance evaluation of a DEI prototype in a clinically relevant task. First, we provide an overview of the project. Then hypothesis and goals of the project are discussed, before a thorough description of the research methods, results and discussion. Finally, design considerations for a second-generation DEI prototype system are presented.

12.2 Motivation for the Development of a DEI Prototype

Cancer imparts distinct and measurable changes in breast tissue at the cellular level. Contrast based on the spatial distribution of x-ray attenuation is not always sufficient to distinguish between normal and cancerous tissues. However, additional contrast can be gained from the refraction of x-rays, which is exploited by phase-contrast imaging. X-ray refraction contrast is not yet widely used in medical imaging, although several phase-contrast imaging devices are in various stages of research and development (Chapman 1997, Cloetens 1999, Ingal 1999, Pagot 2005, Peele 2005, Pfeiffer 2007, Tanaka 2005, Weitkamp 2005, Wu 2003).

Traditionally, DEI has used intense, highly collimated Synchrotron Radiation (SR) to produce images based on absorption, refraction, and extinction contrast (Chapman 1997, Chapman 1996, Hasnah 2002b). Because DEI refraction contrast decreases

proportionally with $(\text{energy})^{-1}$ whereas absorption contrast decreases proportionally with $(\text{energy})^{-3}$ (Bushberg 2002), relatively high energy x-rays (60 keV) can be used to produce soft tissue contrast with a greatly reduced subject radiation dose.

To be clinically useful, the DEI system must transition to an x-ray tube source, but x-ray tube technology has only recently been capable of generating sufficient flux to overcome the limitations imposed by the use of crystal optics. Previous efforts to translate the DEI system into an SR-independent, clinically viable imaging modality have experienced major limitations, such as restriction to low x-ray energies without the capability to image thick objects (Forster 1980, Ingal 1998, Kim 1998, Vine 2007, Wang 2006). Recently, our laboratory developed a DEI prototype (DEI-PR) utilizing a readily available tungsten x-ray tube source and traditional DEI crystal optics capable of acquiring images of phantoms and full-thickness breast tissue specimens at 60 keV with extremely promising initial results (Parham 2009).

12.3 Hypothesis and Goals

It is our hypothesis that our DEI-PR generates images with comparable image quality to those produced by the traditional synchrotron-based DEI (DEI-SR) system, while avoiding significant loss of resolution or additional noise. To this end, we performed imaging studies with full-thickness human breast specimens. This allowed us to measure radiologist perception of image quality parameters with the DEI-SR and DEI-PR systems. In this paper, we present our first results of imaging full-thickness human breast tissue specimens on a non-synchrotron-based DEI prototype system. We evaluated the performance of this system using a clinically relevant task, demonstrating its potential utility as a clinical mammography system.

12.4 Study Design and Methods

All experiments were conducted with appropriate approvals granted by the University of North Carolina at Chapel Hill (UNC-CH) Institutional Review Board. The studies were also HIPAA-compliant.

Specimen Selection. Six mastectomy specimens were obtained from the Department of Pathology at UNC-CH. Specimens were fixed in 10% buffered formalin and stored at room temperature. The specimens were mounted as shown in Figure 12.1. While blinded to history, lesion pathology, and lesion location, a breast imaging radiologist (EDP) in the UNC-CH Department of Radiology identified 14 regions of interest (ROIs) by using Digital Mammography (DM) specimen images. Radiographic features were grouped into two categories: (1) masses (which included all lesions characterized by EDP as masses, architectural distortions, focal densities, and asymmetric densities) and (2) calcifications.

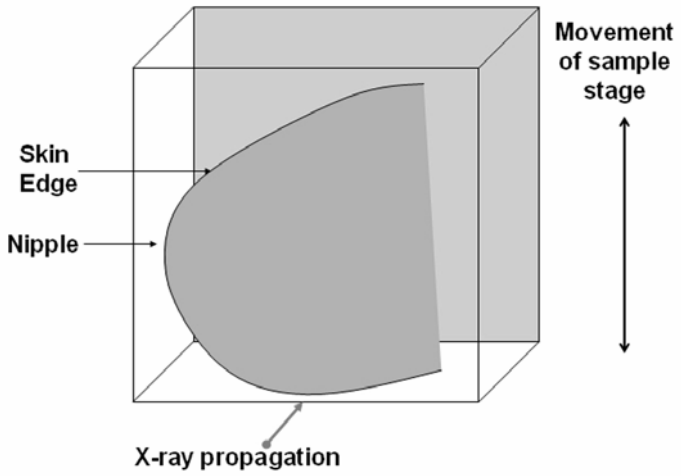

FIGURE 12.1: Specimen Mounting. The specimens were sliced as per usual clinical practice prior to inclusion in the current study. The slices were realigned and care was taken to eliminate air bubbles from the tissue layers before mounting the specimen with deionized water in the imaging container, with mild compression in order to prevent movement.

Diffraction-Enhanced Imaging. All DEI imaging was performed at the National Synchrotron Light Source X15A beamline at Brookhaven National Laboratory in Upton, New York. The DEI-SR setup is shown in Figure 12.2 Panel A as described previously (Zhong 2000). The linear collimated beam from the bending-magnet SR source was 130 mm by 2 mm using either a Bragg [333] or [111] crystal reflection. The DEI-SR source-to-detector distance was approximately 18 m.

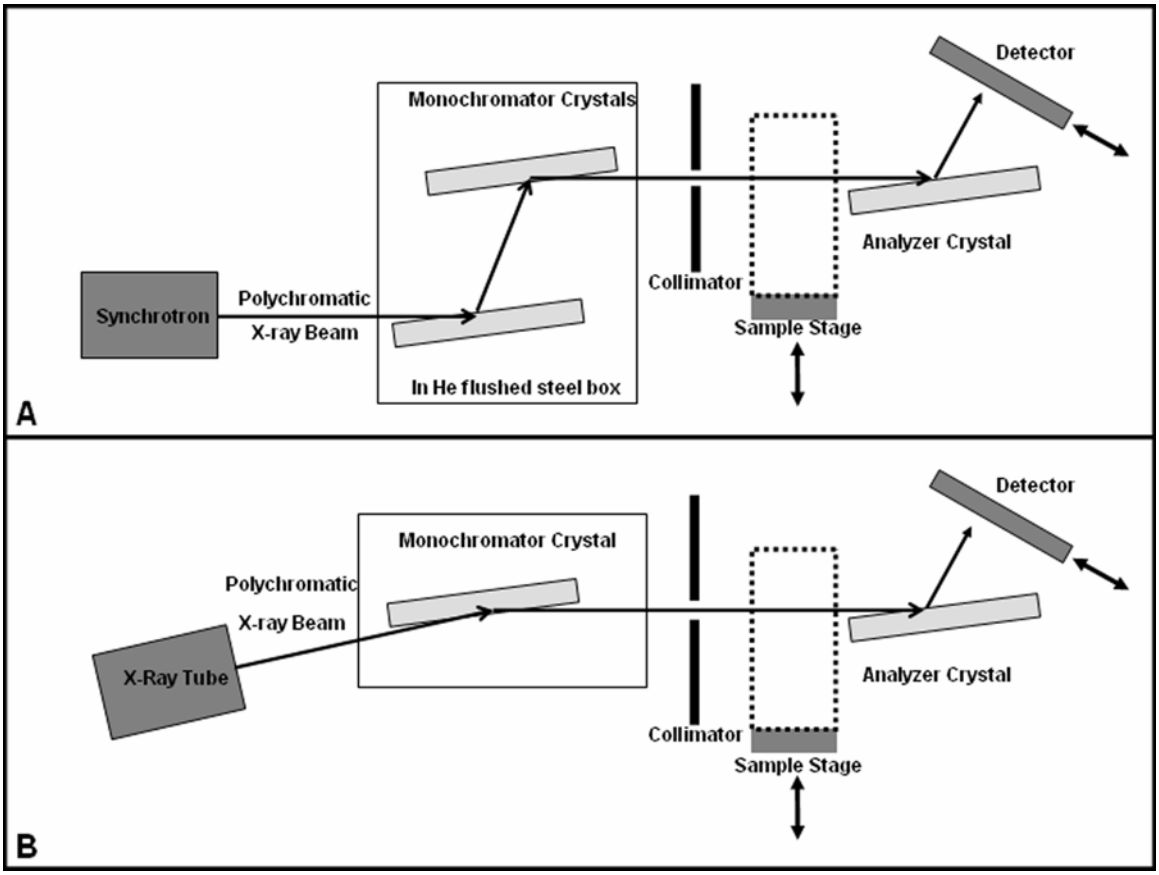

FIGURE 12.2: DEI-SR and DEI-PR Configurations. *Panel A* depicts the traditional synchrotron-based DEI configuration, which implements a synchrotron source. *Panel B* shows the prototype DEI (DEI-PR) setup, with two significant modifications from the traditional system. First, the x-ray source is a commercially available tabletop x-ray tube. Second, DEI-PR uses a single-crystal monochromator instead of the traditional double-crystal monochromator. Both systems use a fan-beam.

The double-crystal monochromator (Shaw Monochromators, Riverton, KS) was comprised of a series of two perfect silicon crystals mounted on independently tunable

stages in a continuously helium-flushed steel tank. The collimated monochromatic x-ray beam then interacts with the object being imaged before diffracting from the analyzer crystal, only reflecting x-rays that fall within a narrow range of energies and angles.

Refraction contrast images were acquired at the ±½ Darwin width (W_D) of the rocking curve, which is equal to half of the full width at half maximum. Attenuation contrast images were acquired at the peak of the rocking curve. The flux of the post-monochromator beam was measured using an ion chamber. Images were acquired with a stimulable phosphor Fuji ST-VI image plate (Fuji Medical Systems, Stamford, CT) and developed by laser on the Fujifilm BAS-2500 image plate reader (Fuji Medical Systems, Stamford, CT). The image plate was affixed perpendicular to the x-ray beam diffracted from the analyzer crystal at twice the Bragg angle.

There were two primary modifications made to the DEI-PR system, depicted in Figure 12.2 Panel B. For a complete description of the DEI-PR system, please refer to (Parham 2009). The DEI-PR utilized a stationary-anode tungsten Comet MXR-160HP/20 x-ray tube source (Comet AG, Flammatt, Switzerland) with a 0.4 mm focal spot. This was powered by the Titan 160 x-ray system (GE Inspection Technologies, Ahrensburg, Germany), with a maximum voltage of 160 kV and 1 kW total power. The single-crystal monochromator (Shaw Monochromators, Riverton, KS) passed both the 59.318 keV $K_{\alpha 1}$ and the 57.982 keV $K_{\alpha 2}$ characteristic tungsten emission lines, as well as the Bremsstrahlung within a narrow range of these energies. The source-to-detector distance was 959 mm ± 5 mm.

There were 79 DEI-SR images (37 at [333], 42 at [111] reflectivity) and 30 DEI-PR images (22 at [333], 8 at [111] reflectivity) acquired. DEI-SR and DEI-PR images

were acquired at 60 keV with a typical surface dose of 0.1 mGy. Sample and detector scanning protocols, described in depth previously (Zhong 2000), were the same for both the DEI-SR and DEI-PR systems. However, imaging time for the DEI-PR system was greater than that for the DEI-SR system by a factor of 10. Vertical linear artifacts created by crystal glitches were corrected manually using an IDL (ITT Visual Information Systems, Boulder, CO) image processing algorithm that included an in-house flattening algorithm applied to the image. DEI image files were converted from tiff to DICOM format using DICOMAccess (DesAcc, Chicago IL) software for display on the Sectra IM.5X mammography softcopy review workstation (Sectra, AB., Shelton, Connecticut).

Full-Field Digital Mammography. The specimens were imaged on the GE Senograph 2000D (Waukesha, WI) at UNC Hospitals. Exact positioning of the full-thickness breast tissue specimens was strictly maintained throughout imaging on DEI-SR, DEI-PR, and DM systems. The signal-to-noise ratio of the GE Senograph 2000D was 83.49 at 25 mm, 71.65 at 40 mm, and 56.51 at 60 mm. The half-value layer was calculated to be 0.374, as measured using the ACR phantom. The compression paddle was brought into contact with the specimen container sides, allowing the GE software to automatically calculate clinically optimal imaging parameters based on specimen thickness.

Pathology Correlation. An expert pathologist (CAL) in the UNC-CH Department of Pathology and Lab Medicine performed pathologic sectioning of the 14 ROIs previously identified. In these 14 ROIs, there were 10 benign lesions, 2 atypical lesions and 2 cancerous lesions. One cancer was ductal carcinoma *in situ* (DCIS) and one was an invasive metaplastic carcinoma.

Flux, Dose, and Signal Measured at the Detector. For DEI images, the flux, dose, and signal measured at the detector were calculated using IDL (ITT Visual Information Systems, Boulder, CO). Using the measured values from the photon-counting detector, flux in the DEI-SR and DEI-PR systems was calculated to be 1.5×10^7 ph/s/cm^2 and 3.83×10^4 ph/s/cm^2, respectively. DEI-SR flux, and subsequently the dose rate, decreases from the time of electron injection. Scan speed was modified for DEI-SR imaging to match the dose delivered to the specimens during DEI-PR imaging, delivering an average of 0.1 mGy surface dose.

MGD depends on tissue thickness and the percentages of glandular and adipose tissue present in the tissue. An expert radiologist (EDP) determined the ratio of glandular and adipose tissue by reviewing DM specimen images. Specimen thicknesses were recorded as the thickness of the imaging container. The percent density and calculated thicknesses of glandular and adipose tissues, given total tissue thicknesses, are listed in Table 12.1 and were used to calculate the MGD for each image.

DEI-SR and DEI-PR refraction-contrast images were acquired at 60 keV, where surface dose and MGD are low. The average DEI-SR surface dose and MGD were 0.09 mGy and 0.05 mGy, respectively. The average DEI-PR surface and MGD were 0.09 mGy and 0.04 mGy, respectively. DM images were acquired at 30 keV with substantially higher radiation exposure, averaging 25.63 mGy surface dose and 3.99 mGy MGD. The average measured signal at the detector was determined by averaging counts across the raw image.

	Percent Density	Glandular Thickness (cm)	Adipose Thickness (cm)
Specimen 1	20%	1.35	5.40
Specimen 2	30%	2.55	5.95
Specimen 3	20%	1.70	6.80
Specimen 4	50%	2.25	2.25
Specimen 5	30%	2.55	5.95
Specimen 6	30%	2.55	5.95

TABLE 12.1: Percent Density and Specimen Thickness. The percent density is the percent of the breast tissue composition that is glandular tissue. Considering the full resting thickness of the specimen, relative thicknesses of glandular and adipose tissue were calculated for each specimen. These tissue composition measurements were used to calculate the mean glandular dose, given additional knowledge of the x-ray energy and flux.

Reader Study. A training set of six ROIs in four specimens was compiled detailing the interpretation of refraction-contrast DEI images containing both benign (fibrous tissue spiculations) and malignant (invasive lobular carcinoma, infiltrating ductal carcinoma) pathologies. DM specimen images were provided for comparison. Readers were instructed on refraction-based contrast mechanisms, guided through use of the softcopy review workstation and introduced to several common DEI image artifacts. Possible image manipulations included magnification, zoom, pan, and window / level adjustments. Training required approximately 30 minutes. Informed consent was obtained from participating radiologists.

A panel of three expert radiologists evaluated a set of 123 images acquired on the DEI-SR, DEI-PR, or DM systems. Images were displayed one at a time with ROIs circled on a calibrated Sectra IM.5X mammography softcopy workstation (Sectra, AB., Shelton, Connecticut). A worksheet was provided with the pathologic results specific to the ROI to be evaluated in each image. Readers assessed whether general radiographic features

were present in the ROI using BI-RADS receptors (e.g. mass, calcification), then determined how easily each feature present could be seen, ranked on a scale from 1 (not easily seen) to 5 (easily seen). For each pathologic feature in the diagnosis, readers indicated how well the imaging findings provided information supportive of the pathologic diagnosis, ranked on a scale from 1 (image completely unsupportive of the diagnosis) to 5 (image completely supportive of the diagnosis). Readers were given a five minute break for every 50 minutes of read time with additional breaks as desired. The average reading time was 1.5 hours. A research assistant was present to assist the readers with any technical difficulties.

Statistical Method. We investigated if perception of radiographic features differed on the DEI-SR and DEI-PR systems with consideration for the influence of specific crystal reflectivities and rocking curve position. We used the Generalized Estimating Equations (GEE) models for each radiographic feature, adjusting for system, interaction between rocking curve position and system, and interaction between reflectivity and system. Chi-square test procedures were used for the multiple comparisons. Since we evaluated four conditions (there are two systems, DEI-SR and DEI-PR, as well as two reflectivities, [111] and [333]), we adopted $p = 0.0125$ or 0.05/4 as the significance level for the conservative Bonferroni multiple test adjustment. All analyses were performed using SAS 8.0 statistical software (SAS Institute, Cary, NC).

12.5 Evaluation of Imaging Results for the DEI-PR and DEI-SR Systems

Phantom Imaging. The objective of this study was to compare the images generated by the DEI-PR system to the traditional DEI-SR system with optimal imaging parameters applied (Parham 2006). Initial phantom imaging using the DEI-PR system

demonstrated successful refraction contrast of a test object on the scale of 100 μm, shown below in Figure 12.3 (Parham 2009). It is apparent that the DEI-PR images have reduced contrast and resolution with increased noise as compared to the DEI-SR images.

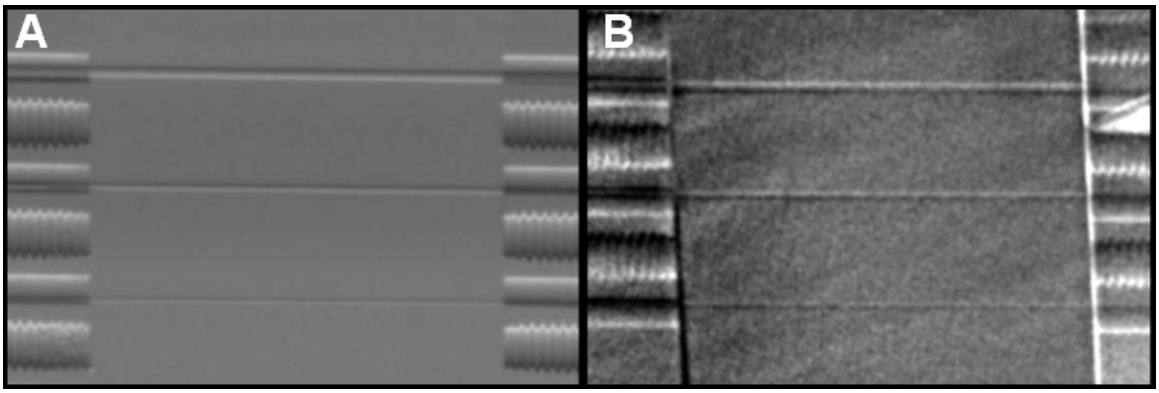

FIGURE 12.3 DEI-PR Phantom Imaging. Images were acquired on both DEI-SR (panel A) and DEI-PR (panel B) at 60 keV at the +½ W_D. The phantom was constructed of 500, 200, and 100 micron diameter nylon wires stretched across an Acrylic frame and secured with metal screws. These initial phantom images successfully demonstrated refraction contrast visibility of even the 100 micron nylon fiber. Reprinted with kind permission from Elsevier: Academic Radiology, 16(8), 2009, 911-917, Parham C, Zhong Z, Connor DM, Chapman LD, Pisano ED.

The contrast and differential SNR (SNR_{diff}) were calculated using the following formulas, and are displayed in Table 12.2:

$$SNR_{diff} = (I_{ROI} - I_{back}) / \sigma_{back} \quad (51)$$

$$Contrast = (I_{ROI} - I_{back}) / I_{back} \quad (52)$$

The DEI-SR system generated better images of each diameter nylon wire with respect to contrast and the SNR_{diff}. Using NIH Image (developed at the U.S. National Institutes of Health and available on the Internet at http://rsb.info.nih.gov/nih-image/), the number of pixels spanned by the smallest nylon wire of 100 μm was measured. For DEI-SR, the span was 4.45 pixels, while for DEI-PR, the span was 5.11 pixels. This represents a 13.03% difference, indicating a reduced ability to resolve fine details using the current DEI-PR system as compared to the traditional DEI-SR system.

	Wire Thickness (µm)	SNR_{diff}	Percent Contrast
DEI-SR	500	35.34	12.83
	200	16.40	8.93
	100	8.45	4.87
DEI-PR	500	4.76	8.90
	200	3.65	4.92
	100	1.80	2.46

TABLE 12.2: Measured Image Quality Parameters of Nylon Wire Phantom. The Differential Signal to Noise Ratio (SNR_{diff}) was calculated using Equation 38; contrast was calculated using Equation 39.

DEI-PR Measured Detector Counts Lower than DEI-SR. When comparing the average measured signal at the detector, differences in detector counts for different samples are expected due to individual object properties such as object thickness and relative glandular density. Counts in DEI-PR images were consistently lower than DEI-SR when considering the same specimen, although imaging parameters were matched as closely as possible. In general, the average measured DEI-SR counts were 136.94 ± 39.08 counts per pixel while DEI-PR averaged 46.5 ± 9.31 counts per pixel. This might be explained by the difference in image acquisition time due to time- and light-contamination of the image plate.

Qualitative Lesion Visibility on DEI-SR and DEI-PR Systems. Full-thickness breast tissue specimens were visualized well on both the DEI-SR and DEI-PR systems. The image quality and lesion feature visibility for images of benign and cancerous ROIs acquired at the ±½ W_D and [333] reflectivity were only minimally decreased in the DEI-PR images compared to the DEI-SR images, as shown in Figures 12.4 and 12.5.

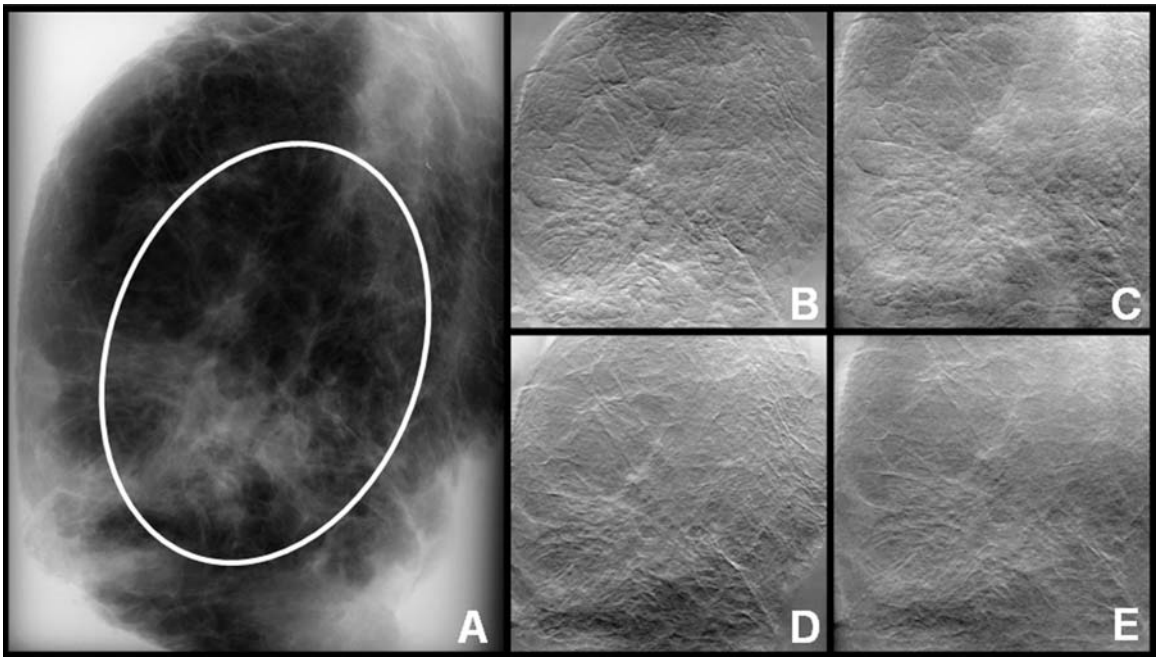

FIGURE 12.4: Comparison of Benign Lesion Characteristic Visibility. The circled region of interest represents dense stromal sclerosis, a biopsy cavity, fibrocystic change and focal atypical ductal hyperplasia with associated calcifications. Panel A displays the digital mammogram standard, acquired at 22 keV. DEI images shown in panels B-E were acquired at 60 keV using the [333] reflectivity. Synchrotron-based DEI images are displayed in the first column; prototype DEI images are shown in the second column. The top row, panels B and C, displays the +½ Darwin width (W_D) rocking curve position, the bottom row, panels D and E, displays the –½ W_D rocking curve position.

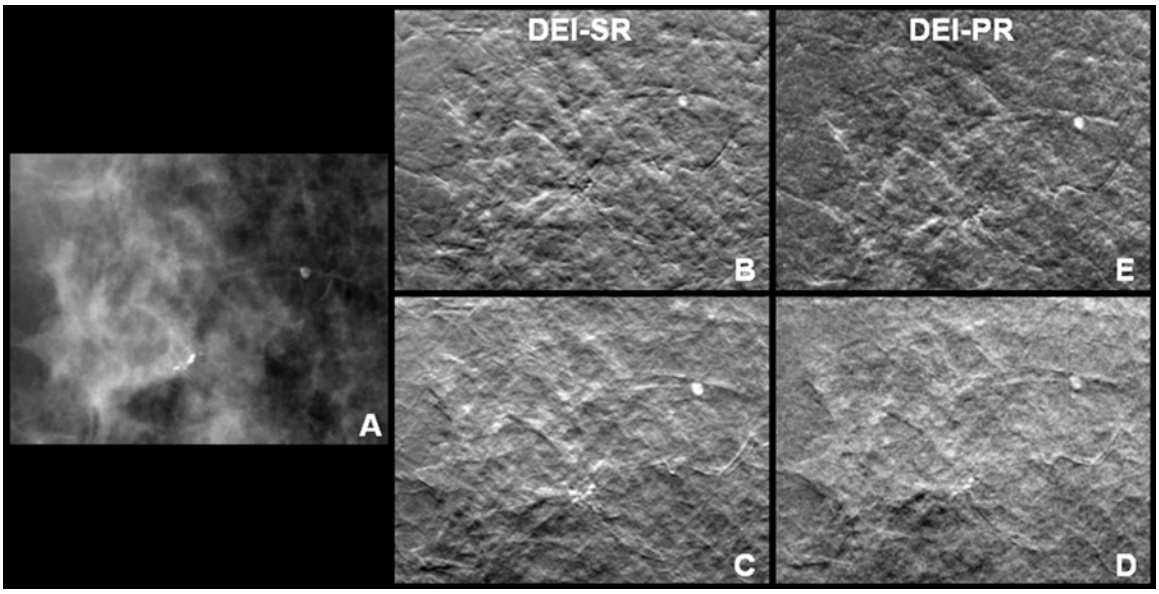

FIGURE 12.5: Comparison of Malignant Lesion Characteristic Visibility. The magnified views of this region of interest represent apocrine-type ductal carcinoma *in situ* (nuclear grade 2-3 with necrosis without associated calcifications), proliferative fibrocystic change and duct ectasia. Panel A displays the digital mammogram standard, acquired at 29 keV. DEI images shown in panels B-E were acquired at 60 keV using the [333] reflectivity. The first column (B,C) was acquired on synchrotron-based DEI and the second column (E,D) was acquired on prototype DEI. The top row, panels B and E, displays the +½ Darwin width (W_D) rocking curve position while the bottom row, panels C and D, displays the –½ W_D rocking curve position.

Qualitative Effect of Crystal Reflectivity. To evaluate whether the crystal reflectivity influenced radiologist perception of radiographic and pathologic features important for the diagnoses, we included images of full-thickness specimens acquired at each reflectivity. Figure 12.6 depicts images acquired on the DEI-SR system at both the [111] and [333]. It is clear that the ±½ W_D images acquired at the [111] reflection do not have as much edge enhancement as those acquired at the [333] reflection. The [111] images generally appear more similar to the absorption-based images acquired at the peak of the rocking curve and the DM images.

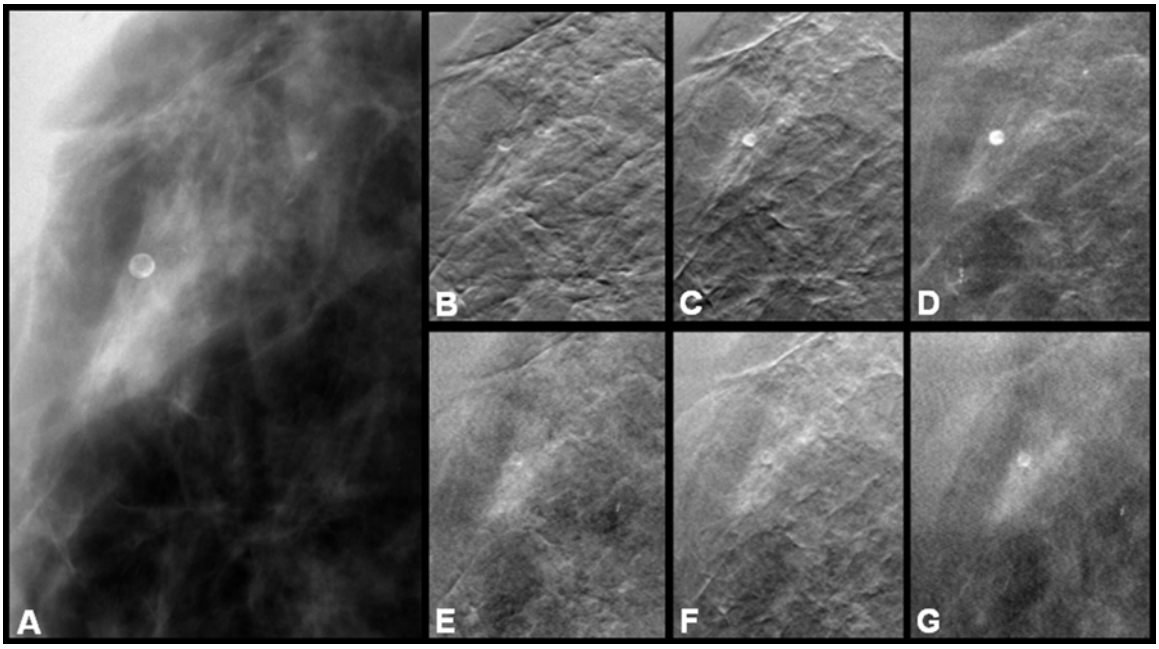

FIGURE 12.6: Effect of Crystal Reflectivity on Lesion Feature Visibility. This magnified region of interest contains duct ectasia, proliferative fibrocystic change, stromal sclerosis, and calcifications at pathologic analysis. The digital mammographic image is displayed in Panel A , acquired at 28 keV. Panels B through D show the region of interest acquired on the synchrotron-based DEI (DEI-SR) system at 60 keV, the [333] reflectivity, at the +½ Darwin width (W_D), -½ W_D and peak rocking curve positions, respectively. Panels E through G represent the same region of interest, x-ray energy and rocking curve positions acquired on the DEI-SR system at the [111] reflectivity.

Reader Study Analysis. Expert radiologists evaluated a series of images, ranking the ease of visibility of lesion features, with results shown in Figure 12.7. Based on GEE models, we did not detect a significant difference between the average radiographic feature visibility rankings for either masses or calcifications on either the DEI-SR or DEI-PR systems. Neither rocking curve position nor crystal reflectivity influenced these findings. Readers also ranked feature visibility in DM images, but comparison to DEI-SR and DEI-PR performance is limited because DM images were not dose- or energy-matched to the DEI images.

Radiographic feature perception was not significantly better on the DM system, but was slightly improved. This difference is likely because lower x-ray energies

facilitate differential attenuation contrast and the DM images were acquired with significantly greater radiation dose, decreasing the effect of Poisson noise. It is interesting to note that calcifications were perceived roughly equally across all three systems.

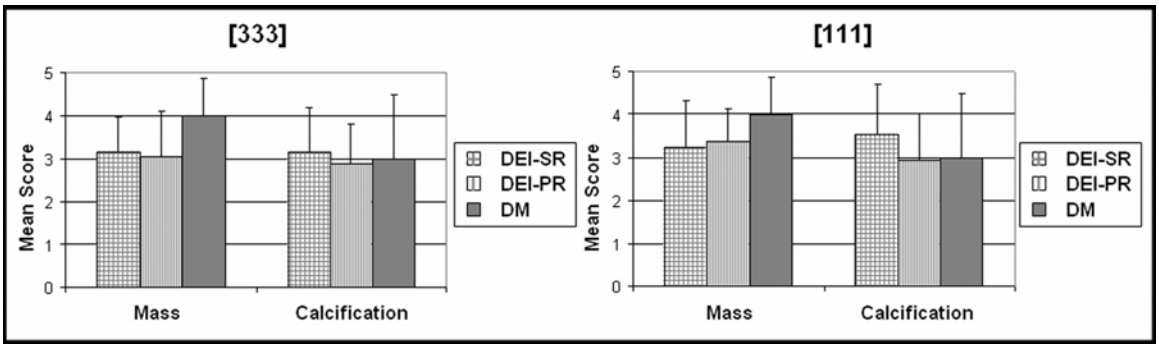

FIGURE 12.7: Reader Study Analysis of Radiographic Feature Visibility. Three expert radiologists ranked radiographic feature visibility on a scale of 1 (not easily appreciated) to 5 (easily appreciated). These scores were averaged for all mass-like and calcification regions of interest as perceived on the synchrotron-based DEI (DEI-SR), prototype DEI (DEI-PR) and digital mammography (DM) systems. The graph on the left displays average scores obtained for images acquired at the [333] reflectivity while the graph on the right shows average scores for the [111] reflectivity.

Readers also scored how well they believed images correlated with known pathologic diagnoses. The average ranking for each diagnosis at the [333] and [111] crystal reflectivities are tabulated in Table 12.3. Based on GEE models, we did not detect a significant difference between the correlation with the diagnosis for any lesion type when comparing the DEI-SR and DEI-PR systems at the [333] reflectivity. However, for the benign pathologic lesions acquired at the [111] reflectivity, readers perceived the DEI-SR system better than these same features were perceived using the DEI-PR system (p-value 0.0003). No significant differences between DEI-SR and DEI-PR were detected at [111] for the atypical or cancerous lesions. However, for comparisons made between categories with lower frequencies (N), there is uncertainty about the results and further assessment will be needed.

The dataset for [111] images acquired on the DEI-PR system was not complete, and small sample sizes might have influenced interpretation of the reader study analysis of pathologic findings. Considering the limitations of the current study, when we compared reader perception of correlation with pathologic diagnosis between the [333] and [111] datasets, we found that radiologists perceived malignant lesions significantly better (p-value <0.0001) at the [111] reflectivity as compared to the [333] reflectivity when imaging on the DEI-SR system. A similar significant difference was not detected for either benign or atypical lesions. A significant difference between [111] and [333] reflectivities was not detected for any type of pathologic diagnosis on the DEI-PR system.

		DEI-SR			**DEI-PR**			
	Pathology Feature	*N*	Mean	Standard Deviation	*N*	Mean	Standard Deviation	***p*-value**
333	Benign	17	1.84	0.35	9	1.94	0.74	**0.8294**
	Atypical	9	1.87	0.43	6	2.03	0.51	**0.4367**
	Malignant	11	1.94	0.47	7	1.88	0.48	**0.5465**
111	Benign	18	2.05	0.38	4	1.46	0.25	**0.0003**
	Atypical	6	2.06	0.69	4	2.03	0.37	**0.9061**
	Malignant	18	2.92	0.89	-	-	-	**-**

TABLE 12.3: Reader Study Analysis of DEI Image Correlation with Pathology. Three expert radiologists ranked correlation of imaging findings with pathologic diagnosis on a scale of 1 (image completely unsupportive of the diagnosis) to 5 (image completely supportive of the diagnosis). The difference between the mean scores for synchrotron-based DEI and prototype DEI (DEI-PR) were calculated using GEE models with Pearson correlations to obtain p-values. *N* represents the number of instances. Data is missing for DEI-PR images of cancerous lesions acquired at [111].

12.6 Preliminary Comparison between DEI-SR, DEI-PR and Tomosynthesis

Breast tomosynthesis (TS) prototypes are currently undergoing clinical trials and have the potential to offer three-dimensional breast imaging at approximately twice the

dose of conventional mammography, but substantially lower dose than dedicated breast CT systems. TS images have the advantage of lesion localization over planar mammography, but because TS reconstructs three-dimensional images over an incomplete dataset, the images have lower resolution than CT reconstructions.

Several groups have suggested the application of TS processing to refraction contrast images (Majidi 2007, Shimao 2007, Shimao 2008, Maksimenko 2007, Ando 2008). Majidi *et al* demonstrated that an optimal number of angular views exists for MIR TS reconstructions, with each type of image possessing a different optimal number of angles (2007). Through phantom imaging and Simultaneous Iterative Reconstruction Technique, they demonstrated that attenuation contrast image reconstructions have an optimal maximum tomographic angle above 55°, and the maximal angle for refraction contrast image reconstructions ranges between 30° and 40°, while the optimal maximum angle for USAXS images is between 50° and 60° (Majidi 2007).

Another group performed DEI-TS, imaging at 17.5 keV using the Si [220] reflectivity (Maksimenko 2007). This study only imaged a small phantom and a cylindrical (3 mm diameter) breast tissue specimen. Images were reconstructed using a shrink-shift-and-add reconstruction technique. Still another group used x-ray dark-field refraction-contrast TS with shift-and-add reconstruction to image a finger joint (Shimao 2007, Shimao 2008). Together, these studies demonstrated proof-of-principle for refraction-contrast TS through phantom and small specimen imaging. No studies have compared planar or three-dimensional DEI to either in-plane TS slices or full tomosynthesis reconstructions for full-thickness breast specimens. Further, no reader studies have been performed to allow these comparisons.

The following presents a qualitative comparson of images of full-thickness breast tissue specimens on a clinical digital mammography system, a preclinical TS prototype, and both synchrotron- and x-ray tube- based DEI. The specimens were imaged using DEI and DM as described above in Section 12.4. The specimens were also imaged on the GE Senographe DS Acquisition System (Waukesha, WI) at UNC Hospitals. Exact positioning of the full-thickness breast tissue specimens was strictly maintained. The compression paddle was brought into contact with the specimen container sides, allowing the GE software to automatically calculate clinically optimal imaging parameters based on specimen thickness. Images were acquired with 36kVp using a dual-track Mo/Rh x-ray tube with a flat panel amorphous silicon / cesium iodide directly digital detector. Both the DEI-SR and DEI-PR images were acquired at 60 keV and approximately 0.1 mGy of surface dose.

An experienced radiologist selected the in-plane TS slices most representative of each region of interest, then evaluated DEI-SR or DEI-PR images displayed beside these in-plane images. Figures 12.8 and 12.9 demonstrate comparison between images acquired of benign and malignant breast features on the DM, TS, DEI-SR and DEI-PR systems. An experienced radiologist determined that the in-plane TS images display lesion features significantly better than the two-dimensional DEI images, considering this preliminary evaluation with a limited data set and minimal controls.

Although two-dimensional DEI, using either the DEI-SR or DEI-PR systems might not demonstrate breast features better than in-plane TS slices, the comparison of DEI-CT or DEI-TS to conventional TS is an interesting potential future area of study.

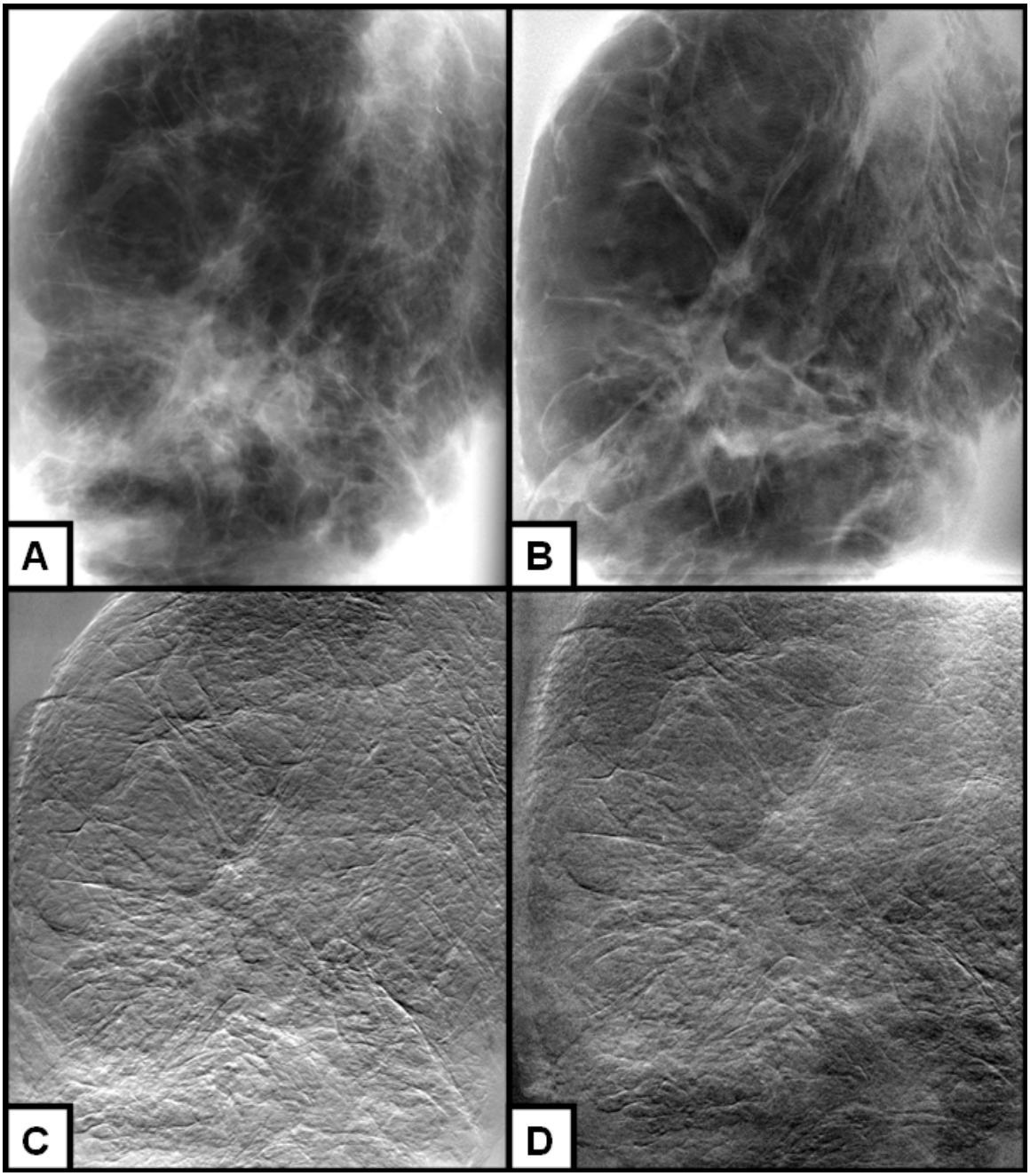

FIGURE 12.8: Comparison of DM, TS, and DEI for Benign Lesions. This specimen contained dense stromal sclerosis, a biopsy cavity, fibrocystic change, and focal atypical ductal hyperplasia with associated calcifications. Digital mammography, tomosynthesis, synchrotron-based diffraction-enhanced imaging (DEI), and x-ray tube-based DEI images are shown in Panels A through D, respectively.

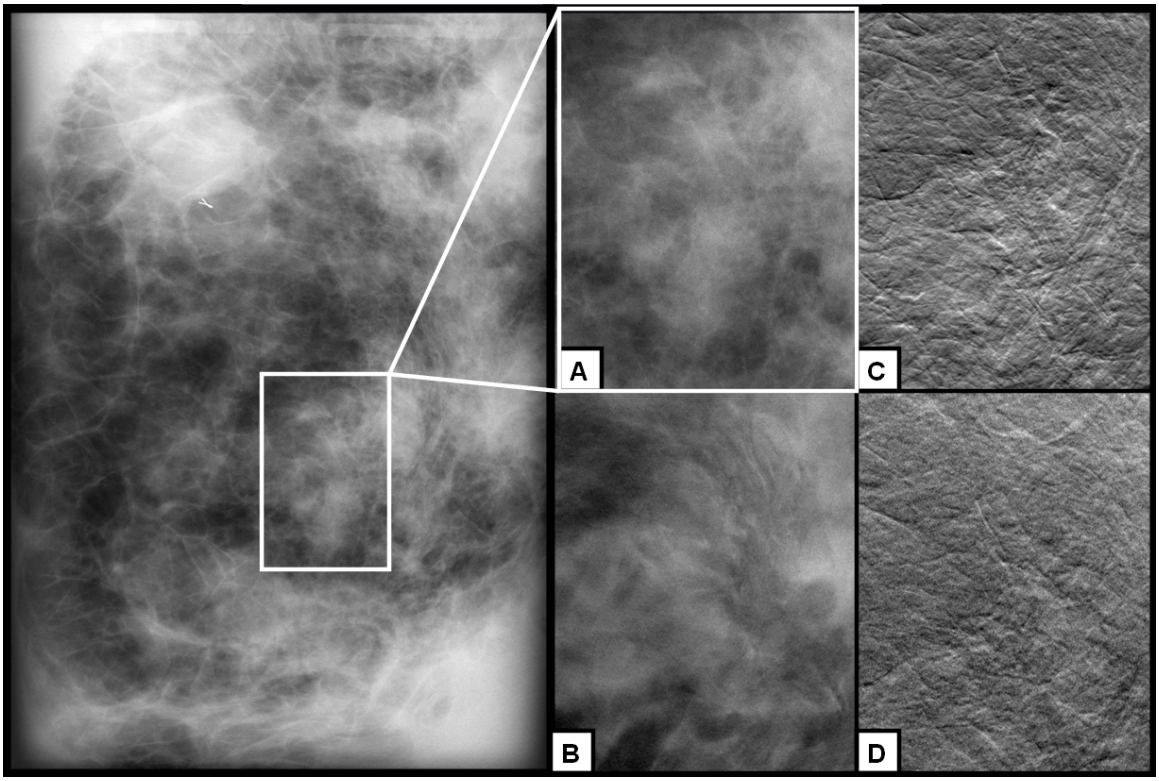

FIGURE 12.9: Comparison of DM, TS, and DEI for Malignant Lesions. This specimen contained three regions of interest (ROI). The circled ROI represented invasive metaplastic carcinoma. Digital mammography, tomosynthesis, synchrotron-based diffraction-enhanced imaging (DEI), and x-ray tube-based DEI images are shown in Panels A through D, respectively.

12.7 Discussion

In 1980, Forster proposed the Schlieren method of diffractometry using a single-crystal collimator and a one- or two-crystal analyzer (Forster 1980). This method was modified by Chapman in 1996 and renamed diffraction-enhanced imaging (Chapman 1996). DEI traditionally required the use of a synchrotron radiation source in order to achieve sufficient flux for image acquisition because perfect crystal optics severely limits x-ray beam intensity (Chapman 1996, Chapman 1997). Developing a synchrotron-independent DEI system is an integral step toward the clinical translation of this imaging modality. Our group developed a prototype DEI system using a commercially available stationary anode tungsten source and traditional DEI crystal optics (Parham 2009).

The current study demonstrates acquisition of low-dose, high-contrast images of full-thickness breast specimens with a large field of view using this DEI-PR system. DEI-PR performance was compared to the performance of the traditional DEI-SR system in clinically relevant tasks using a range of benign and malignant breast lesions.

For mammographic features (mass, calcification), no significant difference was detected between the DEI-SR and DEI-PR systems. Benign lesions were perceived as better seen by radiologists using the DEI-SR system than the DEI-PR system at the [111] reflectivity, with generalizations limited by small sample size. A similar significant difference was not detected between the DEI-PR and DEI-SR images of benign mammographic features at the [333] reflectivity. No significant difference between DEI-SR and DEI-PR was detected for any other lesion type (atypical, cancer) at either crystal reflectivity. Thus, except for benign lesion characterizations at the [111] crystal reflectivity, our DEI-PR system performance was roughly equivalent to the traditional DEI system in a clinically relevant task. Overall, this project demonstrates a significant step toward clinical translation of this modality for breast cancer applications.

While considerable synchrotron-based DEI research has assessed breast lesion characteristic visibility, no previously published studies have evaluated full-thickness human breast tissue specimens on either a synchrotron- or an x-ray-tube- based DEI system (Fernández 2005, Fiedler 2004, Kiss 2004, Liu 2007, Pisano2000, Bravin 2007, Keyriläinen 2005). The current study demonstrates that images acquired on our DEI-PR system have clinical utility for breast imaging applications at reduced radiation dose.

Although DEI-SR and DEI-PR images were acquired with the same imaging parameters (e.g. x-ray energy, radiation dose, field of view), there was a marked decrease

in counts measured at the detector for DEI-PR images. This was likely due to the extended imaging times, causing signal decay on the imaging plate. Because of the extended imaging times required to acquire an image with the same surface dose on the DEI-PR system as compared to the DEI-SR system, the comparison made in the current study is not an ideal comparison. Moreover, the measured contrast and SNR was decreased on the DEI-PR as compared to the DEI-SR. Nonetheless, reader study analysis did not detect a significant difference in the ease of radiographic feature perception between the DEI-SR and DEI-PR systems.

Previous research demonstrated that the DEI-SR images correlate well with pathology as compared to digital mammography (Pisano 2000, Keyriläinen 2005). In most cases, we failed to detect a significant difference between pathologic correlation with the DEI-SR and DEI-PR systems for the pathologic types included in our sample. This implies that our DEI-PR system can demonstrate images of pathologic features that correlate equally well with the pathologic diagnosis as images acquired on the DEI-SR system. For the instance where we did detect a significant difference between the correlation with pathology for the DEI-SR and DEI-PR systems, the sample sizes are relatively small. These differences might be due to fundamental properties of the lesion that were not displayed equally using our flux-limited DEI-PR system that suffered from lower detector exposure than the traditional DEI-SR. However, these differences might disappear with a more robust sample size and distribution.

The [111] reflectivity is more commonly utilized by DEI researchers due to high flux and increased stability, but the [333] reflectivity has steeper rocking curve slopes and generates increased refraction contrast. This study demonstrated that generally, the [333]

and [111] reflectivities do not affect radiologist perception of radiographic features or interpretation of correlation with pathologic findings. For the instance where we did detect a significant difference in reader perception of image correlation with pathologic diagnosis when comparing [333] and [111] reflectivities, we suspect that the radiologists may have been more comfortable with the visual cues provided by the [111] images, which were more similar in appearance to the familiar absorption-contrast images. Furthermore, the [111] dataset was quite small, limiting the generalization of these results without further studies. The results give insight into the need to develop an atlas of breast features to help train radiologists in how to interpret the currently unfamiliar refraction contrast images and how these compare to conventional radiographic features.

While we were able to successfully produce images on the DEI-PR system, there were several design flaws unavoidable at the time of construction due to technology limitations. Primarily, our current DEI-PR system is photon-limited, demanding imaging times well outside of those acceptable for clinical use. Conventional mammography acquires images with sub-second imaging time, with softcopy display available within seconds. In its current configuration, the DEI-SR imaging system requires several minutes for image acquisition, while the DEI-PR imaging acquisition time required hours. Even though DEI can generate images at significantly lower dose than standard mammography, the appropriate number of photons per pixel for a clinically useful DEI image has not yet been established.

Because DEI is not as thickness-limited as conventional absorption-based mammography, planar DEI images of full-thickness breast specimens might provide sufficient lesion characteristic information without the increased dose required for

limited-angle tomography. Future studies might provide a quantitative comparison between planar DEI, DEI-CT, and TS. Further, these studies might also evaluate detection and the accurate assessment of extent of disease.

Given the specimen samples and readers in the current study, our first generation DEI-PR system successfully displayed refraction contrast with roughly equivalent radiographic detail visibility and pathologic correlation to the DEI-SR system. This study demonstrates an important step toward overcoming the technical limitations that have prevented clinical translation of this technology. This is the first application of a prototype incoherent-source DEI system to a clinically relevant imaging task.

12.8 Future Directions

The focus of a second-generation preclinical DEI prototype should center on reducing imaging time while developing a system configuration amenable to clinical imaging. Considerations for a second-generation DEI prototype include crystal optics, x-ray source, system configuration, digital detector, and user interface.

Several factors must be balanced when designing the crystal optics in a second-generation DEI prototype, including temperature loading, type of crystal, crystal reflectivity, vibrational and thermal isolation, and control systems. With increasing photon flux, temperature loading on the DEI crystal optics might become a greater concern. Temperature loading causes expansion of the crystal's unit cell, and thus increases d-spacing, affecting diffraction. Diffracted intensity at the Bragg angle decreases while an increased amount of diffuse scatter at non-Bragg angles is allowed to reflect from the crystal. Thus, thermal stability of the crystal optics affects the monochromaticity of the incident beam as well as the purity of the beam diffracted from

the analyzer. Crystal elasticity plays a role in the thermal loading properties, so it might be possible that another crystal type offers improved heat loading capabilities while providing Bragg diffraction. (Cullity 1978)

While DEI crystals have traditionally been made of silicon, other common crystal materials include germanium, quartz, graphite, and mica. These materials might allow improved heat loading or flux, with consideration for energies at which each crystal operates most efficiently. Using bent, or cylindrically curved, crystals might also allow for increased photon flux by increasing the effective area for diffraction from the crystal because the Bragg angle of incident x-rays is satisfied over a larger surface area (Wittry 2001, Colonna 2001). Johan and Johansson curved crystals reduce vertical divergence and focus horizontally-divergent photons, but these crystals are not easily tunable and might not be robust enough in a clinical setting (Authier 2001, Bingölbali 2008).

If large crystals are used, parallel detection of multiple wavelengths might be possible by diffraction from different planes in different parts of the crystal (Wittry 2001). This might facilitate simultaneous K-edge imaging, with potential applications for calcification detection or contrast-enhanced imaging protocols (Lemacks 2002, Sarnelli 2006). However, there are practical difficulties in crystal alignment, there are limited types of crystals that can facilitate parallel detection, and the diffraction efficiency is reduced (Wittry 2001). One group suggested the simultaneous use of a Bragg and Laue analyzer, allowing simultaneous acquisition of all data required to generate DEI absorption and refraction contrast, minimizing the potential for motion between image acquisitions (Hasnha 2002a).

Different crystal reflectivities affect the flux of photons diffracted from the crystal, the amount of refraction contrast given a specific angular deviation, and have distinct stability properties. For example, the [111] reflection delivers significantly more flux to the detector at the cost of reduced refraction contrast, while higher order reflectivities, such as [333], are more susceptible to thermal fluctuations. The majority of DEI research has been performed at either the [333] or [111] reflectivities, although asymmetric reflections have been used. One group demonstrated that synchrotron radiation flux from perfect crystal monochromators could be increased by excitation using ultrasound waves to dynamically adjust crystal reflectivity (Polikarpov 1994).

Thermal fluctuation and mechanical vibration will both negatively impact the performance of a DEI system. The first-generation DEI system utilized a series of independently mounted arms, rubber pads, and a large granite block to dampen vibrational noise. However, shock vibration could still induce a detectable change in signal. Thermally-induced crystal fluctuations were minimized through water cooling systems and manual realignment control systems. The second-generation DEI system should implement real-time monitoring and automated correction for optimized thermal and vibrational isolation, with consideration for shock reduction.

The first generation DEI-PR utilized a 1 kW stationary anode x-ray tube. A more powerful x-ray tube capable of operating at increased tube voltages and with a rotating anode would allow higher heat-loading capacity without causing damage at continuous or near-continuous operation potential. X-ray tubes currently commercially available can operate at up to 100 kW at approximately 150 kV. Because this is polychromatic radiation composed of overlapping characteristic and bremsstrahlung spectrums, the

average photon energy is typically one-third to one-half the maximal value dictated by the peak kV, indicating an average photon energy range between 50 and 75 keV. Thus, current state of the art x-ray tubes typically used for computed tomography applications might be an optimal source for a second-generation DEI system. Several improvements in x-ray tube technology might allow for increased efficiency of these conventional x-ray sources, such as beam steering and increased anode surface area. Electron beam steering with magnetic fields increases efficiency by increasing the number of electrons that impinge on the anode (Reed 2000). Traditional anodes are disk-shaped, but other shapes, such as spherical, have been proposed that might increase heat-loading properties (Lustberg 2003).

Novel x-ray sources such as cold cathode field emission systems, microfocus systems, systems with multiple circular filaments, or laser x-ray sources might offer advantages in high-flux with extended use for DEI and DEI-CT applications. Field emission x-ray sources are receiving increased attention for their potential as medical imaging x-ray sources (Cao 2009, Yang 2008b). However, the existing prototypes have only been evaluated for small animal imaging and may not be suitable for high-flux imaging with DEI.

Microfocus x-ray tubes have been developed for use with x-ray spectroscopy and micro-CT applications. Phase contrast imaging prototype systems using a microfocus x-ray tube have already been used to image tissues (Zhang 2008c, Kashyap 2008). Although these systems can generate x-rays at a range of energies (Maeo 2009), the flux is likely not sufficient for DEI due to lower power limitations. Multifilament x-ray sources, with circular filaments arranged concentrically, might allow sufficient flux for

DEI applications. The increased surface area of circular filaments allows increased electron production over traditional line filament x-ray sources, but also requires increased active cooling (Kim 2007). Theoretical modeling suggests that this type of concentric, circular multifilament source might allow comparable flux as a synchrotron source (Kim 2007).

Several types of laser systems can generate x-rays, including free-electron lasers, x-ray lasers, and Compact Light Sources (CLS). Although free electron laser sources have excellent power and high coherence, these systems are large and thus are not ideal for a tabletop DEI system (Edwards 2005). X-ray lasers use electronic transitions in highly stripped ions to generate highly coherent, monochromatic soft x-rays, but can not generate the hard x-rays required for medical imaging applications. CLS systems use Compton scattering to generate x-rays, generating a highly coherent beam that might perform well as an x-ray source for DEI applications (Bech 2009, Carroll 1990). (Umstadter 2002)

Reconfiguring the DEI system to maximally decrease imaging distances could decrease imaging time, but is limited by magnification and detector field of view. Because the DEI optimal imaging energy was previously estimated to be 60 keV, an ideal digital detector for a second-generation DEI prototype should have sufficient efficiency and accuracy at this energy. DEI uses monochromatic x-rays, so an energy-sensitive detector might also be useful. Because breast imaging requires the detection of very fine details with limited subject contrast, the detector would need to have excellent spatial and contrast resolution with a field of view large enough to accommodate the majority of

breast sizes. A cryo-cooled electronic detector might allow extended imaging times without drastically increased electronic noise.

A clinical system requires a user-friendly interface with the ability to adjust imaging parameters as well as internal system stability monitoring and correction. The operating system should automatically and precisely adjust multiple-axis crystal alignment. Development of a user interface would facilitate imaging technologist use of the system with the ability to adjust crystals to accommodate imaging at a various rocking curve positions, a wide range of x-ray energies, and even different crystal reflectivities.

Many technical advances facilitate the construction of a preclinical second-generation DEI prototype. Construction of this system will begin in the near future. This system will enable many additional studies, potentially even clinical studies with living human patients, helping to define exactly where this technology fits within the landscape of breast imaging, as well as other tissue and organ system medical imaging technologies.

CHAPTER 13: SUMMARY AND IMPLICATIONS

13.1 Overview

Benign, atypical, and cancerous breast features can differ by structure, physiology, or molecular composition. It is important to detect cancerous and precancerous lesions, and accurately assess their potential for causing morbidity or mortality, as early as possible. Conventional mammography acquires only structural or anatomic information about the breast based on x-ray absorption. However, many additional imaging modalities use other types of signals to generate important information concerning breast structure, as well as physiology and the molecular composition of the breast tissue. The following summarizes the research presented in this dissertation and discusses how this research likely impacts the field of breast imaging.

13.2 Summary of Research

Diffraction-enhanced imaging can provide high-resolution images of many breast cancer features. This dissertation provides an important step toward the clinical translation of DEI. One specific aim was to evaluate the feasibility of a contrast-enhanced DEI imaging protocol. Through phantom imaging, we established that several commercially available contrast agents can generate DEI contrast enhancement, although conventional x-ray contrast agents appear to generate predominantly absorption contrast. Of the contrast agents tested, microbubbles performed the best, taking advantage of the unique extinction contrast mechanism. This is important because contrast-enhanced digital mammography is a potentially growing sector of the field. Further work should be performed to define an optimal DEI contrast agent. Moreover, targeted delivery systems

that might facilitate highly specific breast cancer imaging are rapidly being developed. An *in vivo* mouse model might allow evaluation of passive targeting through the EPR effect, or even demonstration of functionalized CE-DEI by using a targeting ligand such as Herceptin.

The second specific aim of this dissertation was to compare the lesion feature visibility of benign and malignant breast lesions at a range of breast tissue thicknesses. We have established an advantage of DEI in that substantially decreased breast compression might be possible with minimal loss of lesion feature visibility. However, multiple refraction events will increase as tissue thickness increases. The effect of multiple refraction events on DEI image quality should be better quantified. This means that DEI might increase patient comfort, which might increase adherence to recommended screening protocols. The effect of this potential reduced compression should be evaluated in a larger dataset to assess the effect of increasing thickness on diagnostic accuracy with DEI. Clinical studies must be performed before making this claim with greater confidence.

DEI attenuation contrast images appear similar to those obtained with screen-film and digital mammography, but how DEI attenuation contrast images affect diagnostic accuracy remains to be evaluated in a clinical setting. DEI also provides unique refraction contrast images. The effect of DEI refraction contrast images on diagnostic accuracy in a clinical setting also remains to be evaluated. Before these studies can be undertaken, a clinical prototype must be developed.

Thus, the final specific aim of this dissertation demonstrated a clinically viable prototype system using a tabletop x-ray source. This is an important step toward

transitioning from laboratory to clinical trials. At constant dose, our first generation DEI prototype that used a commercially available x-ray tube source generated images with roughly equivalent image feature visibility as the traditional synchrotron-based DEI system. Design modifications are underway in order to construct a second-generation preclinical prototype which will substantially decrease the imaging time to the order of seconds, which is comparable to the imaging time required on the synchrotron-based DEI system. This study should be repeated using the second-generation DEI prototype.

Although several recent studies have suggested that digital mammography can be performed at a reduced subject dose with a minimal decrease in diagnostic accuracy (Ruschin 2007, Samei 2007), these doses are still substantially greater than those delivered by an unoptimized DEI system. Future studies should evaluate optimal DEI sampling procedures, e.g. the number of photons needed per pixel to generate a clinically useful refraction-contrast image.

13.3 How DEI Compares to Other Breast Imaging Modalities

Although several studies have demonstrated excellent DEI contrast as compared to conventional mammography, head-to-head comparison between DEI and either conventional mammography or adjunct breast imaging technologies will be most appropriately conducted when the performance of an optimized DEI system can be evaluated clinically. Clinical studies should be designed such that the diagnostic accuracy of DEI, including the ability to detect lesions, is compared to that of clinical breast imaging technologies that acquire images based on breast structure, including US, MRI, and CT.

Performance for a specific diagnostic purpose might also be evaluated when compared to other modalities that acquire images based on breast structure that are currently undergoing clinical trails, such as tomosynthesis and additional phase sensitive x-ray imaging systems like the Konica Minolta propagation-based phase contrast imaging system. DEI performance compared to clinical systems that acquire images based on physiology might also be performed, including MRI or nuclear imaging, as well as other systems that are being evaluated for breast imaging applications such as optical imaging, thermography, and electrical impedance tomography. Although ROC analysis is generally the ideal comparison between imaging systems, refraction contrast versus the contrast mechanisms of other medical imaging modalities might not make this an appropriate analysis. Because image contrast mechanisms and interpretation of diagnostically important image features are unique for each modality, these systems might be best compared by matching imaging parameters where possible and performing Likert analysis.

The influence of DEI-detected lesions on patient treatment and survival outcomes can not be determined until a system has been constructed that can be tested in the clinic. Ultimately, receiver operating characteristic (ROC) analysis in a diagnostic and screening setting with radiologists familiar with refraction contrast image analysis should be performed to systematically evaluate a clinical DEI prototype. While the physics of x-ray refraction facilitate edge-detection and fine detail visibility, issues with refraction contrast image quality are not yet well-established.

Because of excellent fine detail visibility and spiculation visualization, it might be useful for determining local extent of disease prior to breast-conserving therapy. Also,

due to the low radiation dose and the decreased dependence on tissue thickness, the DEI system might be useful for women with large breasts, or women who do not tolerate breast compression well. The effect of refraction contrast on lesion detection and characterization within dense breast tissue has not yet been evaluated. Optimized image processing algorithms that preserve refraction contrast have not yet been developed. Moreover, the optimal methods for image display to radiologists, such as pure absorption, pure refraction, or some filtered compositional image, have not yet been studied. CAD algorithms for refraction contrast have not yet been developed.

13.4 How DEI Compares to Other Phase Contrast Imaging Techniques

Propagation-based phase contrast imaging is the furthest toward clinical translation, with a prototype currently being tested in the clinic. However, the initial image quality observed from this system was not as great as expected, likely due to the stringent technical requirements imposed on the source and detector due to this type of phase contrast information capture. Interferometric and analyzer-based phase contrast imaging systems all use crystals, which possess the disadvantage of thermal and vibrational noise. DEI allows a substantially greater field of view than current interferometric systems. DEI also readily allows the use of increased x-ray energies, and has demonstrated successful imaging of full-thickness specimens in clinically relevant tasks, neither of which has been achieved by any other phase contrast imaging modality.

Coded aperture phase contrast imaging systems appear to be a potentially strong competitor for the clinical translation of phase contrast imaging, but very few imaging studies have been published with this technique. This system depends on the pixel size of the detector, and requires a direct digital detector for optimal image quality. However,

direct digital detectors have not yet demonstrated widespread success in the clinic. Although the coded aperture approach doesn't substantially filter the x-ray beam, which is an improvement over interferometric or analyzer-based phase contrast imaging systems, this technique needs to be evaluated at a range of x-ray energies using full-thickness tissue specimens, with comparison to the clinical gold standard. Further, this system has not yet demonstrated that it is scaleable to realistic subject sizes for medical imaging and that there is not a substantial loss of subject information due to the apertures. Thus, coded aperture-based phase contrast imaging is lagging significantly behind the recent substantial developments in the DEI technology. As further research is performed on coding aperture phase contrast imaging, additional limitations may surface that inhibit its clinical translation.

13.5 Summary

Overall, the DEI technology has recently overcome several longstanding hurdles that previously limited clinical evaluation and assessment of appropriate clinical applications. This dissertation represents the successful implementation of a DEI prototype in a clinically relevant task, and explores novel applications of the DEI technology while imaging thick objects. Much work remains to be done in order to establish where DEI fits in the spectrum of breast imaging technologies. While this dissertation focuses on DEI as a potential breast imaging modality, DEI has demonstrated potential utility for imaging other tissues and organ systems, such as cartilage, lung, heart, liver, kidney, brain, thyroid, eye, uterus, and bone. Moreover, DEI might be useful for industrial inspection imaging of castings, welds, material stress and faults, tires, and composite materials. With the restriction to a synchrotron x-ray source removed, the DEI

technology might now be developed into a preclinical system that would allow comparisons between DEI and existing medical imaging technologies. This might facilitate testing for breast or other medical imaging applications, or industrial inspection and security applications.

REFERENCES

Achilefu S, Dorshow RB, Bugaj JE, Rajagopalan R. Novel receptor-targeted fluorescent contrast agents for in vivo tumor imaging. Invest Radiol **35:** 479-485 (2000).

Adler LP, Crowe JP, al-Kaisi NK, Sunshine JL. Evaluation of breast masses and axillary lymph nodes with [F-18] 2-deoxy-2-fluoro-D-glucose PET. Radiology **187:** 743-750 (1993).

Adriance MC, Inman JL, Petersen OW, Bissell MJ. Myoepithelial cells: good fences make good neighbors. Breast Cancer Res **7:** 190-197 (2005).

Alamo L, Fischer U. Contrast-enhanced color Doppler ultrasound characteristics in hypervascular breast tumors: comparison with MRI. Eur Radiol **11:** 970–977 (2001).

Albertini JJ, Lyman GH, Cox C, Yeatman T, Balducci L, Ku N, Shivers S, Berman C, Wells K, Rapaport D, Shons A, Horton J, Greenberg H, Nicosia S, Clark R, Cantor A, Reintgen DS. Lymphatic mapping and sentinel node biopsy in the patient with breast cancer. JAMA **276:** 1818-1822 (1996).

Alberts B, Johnson A, Lewis J, Raff M, Roberts K and Walter P. Molecular Biology of the Cell. 4th edition. Garland Science: New York, 2002.

Albrecht T, Dawson P. Gadolinium-DTPA as x-ray contrast medium in clinical studies. Br J Radiol **73:** 878-882 (2000).

Albrecht T, Patel N, Cosgrove DO, Jayaram V, Blomley MJ, Eckersley R. Enhancement of power Doppler signals from breast lesions with the ultrasound contrast agent EchoGen emulsion: subjective and quantitative assessment. Acad Radiol **5:** S195-S198 (1998).

Allen MW, Hendi P, Bassett L, Phelps ME, Gambhir SS. A study on the cost effectiveness of sestamibi scintimammography for screening women with dense breasts for breast cancer. Breast Cancer Res Treat **55:** 243-258 (1999).

Alonso DF, Farina HG, Skilton G, Gabri MR, De Lorenzo MS, Gomez DE. Reduction of mouse mammary tumor formation and metastasis by lovastatin, an inhibitor of the mevalonate pathway of cholesterol synthesis. Breast Cancer Res Treat **50:** 83-93 (1998).

Alric C, Taleb J, Le Duc G, Mandon C, Billotey C, Le Meur-Herland A, Brochard T, Vocanson F, Janier M, Perriat P, Roux S, Tillement O. Gadolinium chelate coated gold nanoparticles as contrast agents for both x-ray computed tomography and magnetic resonance imaging. J Am Chem Soc **130:** 5908-5915 (2008).

Althuis MD, Fergenbaum JH, Garcia-Closas M, Brinton LA, Madigan MP, Sherman ME. Etiology of hormone receptor-defined breast cancer: a systematic review of the literature. Cancer Epidemiol Biomarkers Prev **13:** 1558-1568 (2004).

Alvarez S, Añorbe E, Alcorta P, López F, Alonso I, Cortés J. Role of sonography in the diagnosis of axillary lymph node metastases in breast cancer: a systematic review. AJR Am J Roentgenol **186:** 1342-1348 (2006).

Amalu WC. "A Review of Breast Thermography." International Academy of Clinical Thermology (2003): http://www.iact-org.org/articles/articles-review-btherm.html. Accessed: 12-9-2008.

American Cancer Society. *Breast Cancer Facts & Figures 2007-2008*. Atlanta: American Cancer Society Inc (2008).

Anderson WF, Chatterjee N, Ershler WB, Brawley OW. Estrogen receptor breast cancer phenotypes in the Surveillance, Epidemiology, and End Results database. Breast Cancer Res Treat **76:** 27-36 (2002).

Andersson I, Ikeda DM, Zackrisson S, Ruschin M, Svahn T, Timberg P, Tingberg A. Breast tomosynthesis and digital mammography: a comparison of breast cancer visibility and BIRADS classification in a population of cancers with subtle mammographic findings. Eur Radiol **18:** 2817-2825 (2008).

Ando M, Bando H, Endo T, Ichihara S, Hashimoto E, Hyodo K, Kunisada T, Li G, Maksimenko A, Mori K, Shimao D, Sugiyama H, Yuasa T, Ueno E. Refraction-based 2D, 2.5D and 3D medical imaging: stepping forward to a clinical trial. Eur J Radiol **68:** S32-S36 (2008).

Ando M, Maksimenko A, Sugiyama H, Pattanasiriwisawa W, Hyodo K, Uyama C. Simple x-ray dark- and bright-field imaging using achromatic laue optics. The Rigaku Journal **20:** 21-24 (2003).

Ando M, Yamasaki K, Toyofuku F, Sugiyama H, Ohbayashi C, Lis G, Pan L, Jiang X, Pattanasiriwisawa W, Shimao D, Hashimoto E, Kimura T, Tsuneyoshi M, Ueno E, Tokumori K, Maksimenko A, Higashida Y, Hirano M. Attempt at visualizing breast cancer with x-ray dark field imaging. Jpn J Appl Phys **44:** L528-L531 (2005).

Antoniou A, Pharoah PD, Narod S, Risch HA, Eyfjord JE, Hopper JL, Loman N, Olsson H, Johannsson O, Borg A, Pasini B, Radice P, Manoukian S, Eccles DM, Tang N, Olah E, Anton-Culver H, Warner E, Lubinski J, Gronwald J, Gorski B, Tulinius H, Thorlacius S, Eerola H, Nevanlinna H, Syrjäkoski K, Kallioniemi OP, Thompson D, Evans C, Peto J, Lalloo F, Evans DG, Easton DF. Average risks of breast and ovarian cancer associated with BRCA1 or BRCA2 mutations detected in case

series unselected for family history: a combined analysis of 22 studies. Am J Hum Genet **72:** 1117-1130 (2003).

Arfelli F, Assante M, Bonvicini V, Bravin A, Cantatore G, Castelli E, Dalla Palma L, Di Michiel M, Longo R, Olivo A, Pani S, Pontoni D, Poropat P, Prest M, Rashevsky A, Tromba G, Vacchi A, Vallazza E, Zanconati F. Low-dose phase contrast x-ray medical imaging. Phys Med Biol **43:** 2845-2852 (1998).

Arfelli F, Bonvicini V, Bravin A, Cantatore G, Castelli E, Palma LD, Michiel MD, Fabrizioli M, Longo R, Menk RH, Olivo A, Pani S, Pontoni D, Poropat P, Prest M, Rashevsky A, Ratti M, Rigon L, Tromba G, Vacchi A, Vallazza E, Zanconati F. Mammography with synchrotron radiation: phase-detection techniques. Radiology **215:** 286-293 (2000).

Arfelli F, Rigon L, Menk RH, Besch JH. On the possibility of utilizing scattering-based contrast agents in combination with diffraction-enhanced imaging (2003). SPIE Physics of Medical Imaging **5030:** 274-283 (2003).

Arora N, Martins D, Ruggerio D, Tousimis E, Swistel AJ, Osborne MP, Simmons RM. Effectiveness of a noninvasive digital infrared thermal imaging system in the detection of breast cancer. Am J Surg **196:** 523-526 (2008).

Artemov D, Mori N, Okollie B, Bhujawalla ZM. MR molecular imaging of the Her-2/neu receptor in breast cancer cells using targeted iron oxide nanoparticles. Magn Reson Med **49:** 403-408 (2003).

Authier A. Dynamical Theory of X-Ray Diffraction. Oxford University Press: Great Britain (2001).

Avril N, Rosé CA, Schelling M, Dose J, Kuhn W, Bense S, Weber W, Ziegler S, Graeff H, Schwaiger M. Breast imaging with positron emission tomography and fluorine-18 fluorodeoxyglucose: use and limitations. J Clin Oncol **18:** 3495-3502 (2000).

Baldelli P, Bravin A, Di Maggio C, Gennaro G, Sarnelli A, Taibi A, Gambaccini M. Evaluation of the minimum iodine concentration for contrast-enhanced subtraction mammography. Phys Med Biol **51:** 4233-4251 (2006).

Baldelli P, Taibi A, Tuffanelli A, Gambaccini M. Dose comparison between conventional and quasi-monochromatic systems for diagnostic radiology. Phys Med Biol **49:** 4135-4146 (2004).

Baldelli P, Taibi A, Tuffanelli A, Gilardoni MC, Gambaccini M. A prototype of a quasi-monochromatic system for mammography applications. Phys med Biol **50:** 2225-2240 (2005).

Balleyguier C, Opolon P, Mathieu MC, Athanasiou A, Garbay JR, Delaloge S, Dromain C. New potential and applications of contrast-enhanced ultrasound of the breast: own investigations and review of literature. Eur J Radiol **69:** 14-23 (2009).

Barber DC, Brown BH. Applied potential tomography. J Phys E Sci Instrum **17:** 723-733 (1984).

Barnett SB, Duck F, Ziskin M. Recommendations on the safe use of ultrasound contrast agents. Ultrasound Med Biol **33:** 173-174 (2007).

Bartella L, Morris EA, Dershaw DD, Liberman L, Thakur SB, Moskowitz C, Guido J, Huang W. Proton MR spectroscopy with choline peak as malignancy marker improves positive predictive value for breast cancer diagnosis: preliminary study. Radiology **239:** 686-692 (2006).

Basham VM, Lipscombe JM, Ward JM, Gayther SA, Ponder BA, Easton DF, Pharoah PDP. BRCA1 and BRCA2 mutations in a population-based study of male breast cancer. Breast Cancer Res **4:** R2 (2002).

Baykal A, Rosen D, Zhou C, Liu J, Sahin AA. Telomerase in breast cancer: a critical evaluation. Adv Anat Pathol **11:** 262-268 (2004).

Bazzocchi M, Mazzarella F, Del Frate C, Girometti R, Zuiani C. CAD systems for mammography: a real opportunity? A review of the literature. Radiol Med (Torino) **112:** 329-353 (2007).

Bech M, Bunk O, David C, Ruth R, Rifkin J, Loewen R, Feidenhans'l R, Pfeiffer F. Hard x-ray phase-contrast imaging with the Compact Light Source based on inverse Compton x-rays. J Synchrotron Radiat **16:** 43-47 (2009).

Beckmann F, Bonse U, Busch F and Günnewig O. X-ray microtomography (microCT) using phase contrast for the investigation of organic matter. J Comput Assist Tomogr **21:** 539-553 (1997).

Beemsterboer PM, Warmerdam PG, Boer R, de Koning HJ. Radiation risk of mammography related to benefit in screening programmes: a favourable balance? J Med Screen **5:** 81-87 (1998).

Begg CB, McNeil BJ. Assessment of radiologic tests: control of bias and other design considerations. Radiol **167:** 565-569 (1988).

Behm CZ, Lindner JR. Cellular and molecular imaging with targeted contrast ultrasound. Ultrasound Q **22:** 67-72 (2006).

Behrens S, Laue H, Althaus M, Boehler T, Kuemmerlen B, Hahn HK, Peitgen HO. Computer assistance for MR based diagnosis of breast cancer: present and future challenges. Comput Med Imaging Graph **31:** 236-247 (2007).

Bénard F, Turcotte E. Imaging in breast cancer: single-photon computed tomography and positron-emission tomography. Breast cancer Res **7:** 153-162 (2005).

Berg WA, Blume JD, Cormack JB, Mendelson EB, Lehrer D, Böhm-Vélez M, Pisano ED, Jong RA, Evans WP, Morton MJ, Mahoney MC, Larsen LH, Barr RG, Farria DM, Marques HS, Boparai K; ACRIN 6666 Investigators. Combined screening with ultrasound and mammography vs mammography alone in women at elevated risk of breast cancer. JAMA **299:** 2151-2163 (2008).

Berg WA, Gutierrez L, NessAiver MS, Carter WB, Bhargavan M, Lewis RS, Ioffe OB. Diagnostic accuracy of mammography, clinical examination, US, and MR imaging in preoperative assessment of breast cancer. Radiology **233:** 830-849 (2004).

Berg WA, Weinberg IN, Narayanan D, Lobrano ME, Ross E, Amodei L, Tafra L, Adler LP, Uddo J, Stein W 3rd, Levine EA, Positron Emission Mammography Working Group. High-resolution fluorodeoxyglucose positron emission tomography with compression ("positron emission mammography") is highly accurate in depicting primary breast cancer. Breast J. **12:** 309-23 (2006).

Bernstein L. Epidemiology of endocrine-related risk factors for breast cancer. J Mammary Gland Biol Neoplasia **7:** 3-15 (2002).

Bernstein L, Ross RK, Lobo RA, Hanisch R, Krailo MD, Henderson BE. The effects of moderate physical activity on menstrual cycle patterns in adolescence: implications for breast cancer prevention. Br J Cancer **55:** 681-685 (1987).

Bernstein L, Ross RD, Henderson BE. Prospects for the primary prevention of breast cancer. Am J Epidemiol **135:** 142-152 (1992).

Berrington de Gonzalez A, Darby S. Risk of cancer from diagnostic x-rays: estimates for the UK and 14 other countries. The Lancet **363:** 345-351 (2004).

Bertorelle F, Wilhelm C, Roger J, Gazeau F, Ménager C, Cabuil V. Fluorescence-modified superparamagnetic nanoparticles: intracellular uptake and use in cellular imaging. Langmuir **22:** 5385-5391 (2006).

Bhattacharyya S, Wang S, Reinecke D, Kiser W Jr, Kruger RA, DeGrado TR. Synthesis and evaluation of near-infrared (NIR) dye-herceptin conjugates as photoacoustic computed tomography (PCT) probes for HER-2 expression in breast cancer. Bioconjug Chem **19:** 1186-1193 (2008).

Bingölbali A, MacDonald CA. Curved crystal x-ray optics for monochromatic imaging with a clinical source. Med Phys **36:** 1176-1183 (2008).

Bitar RA, Martinho Hda S, Tierra-Criollo CJ, Zambelli Ramalho LN, Netto MM, Martin AA. Biochemical analysis of human breast tissues using Fourier-transform Raman spectroscopy. J Biomed Opt **11:** 054001 (2006).

Biwas TK, Gupta AK. Retrieval of true color of the internal organ of CT images and attempt to tissue characterization by refractive index: initial experience. Indian Journal of Radiology and Imaging **12:** 169-178 (2002).

Bleicher AG, Kanal E. Assessment of adverse reaction rates to a newly approved MRI contrast agent: review of 23,553 administrations of gadobenate dimeglumine. AJR Am J Roentgenol **191:** W307-W311 (2008).

Bluemke DA, Gatsonis CA, Chen MH, DeAngelis GA, DeBruhl N, Harms S, Heywang-Köbrunner SH, Hylton N, Kuhl CK, Lehman C, Pisano ED, Causer P, Schnitt SJ, Smazal SF, Stelling CB, Weatherall PT, Schnall MD. Magnetic resonance imaging of the breast prior to biopsy. JAMA **292:** 2735-2742 (2004).

Boné B, Aspelin P, Bronge L, Isberg B, Perbeck L, Veress B. Sensitivity and specificity of MR mammography with histopathological correlation in 250 breasts. Acta Radiol **37:** 208-213 (1996).

Bonovas S, Filioussi, Tsavaris N, Sitaras NM. Use of statins and breast cancer: a meta-analysis of seven randomized clinical trials and nine observational studies. J Clin Oncol **23:** 8606-8612 (2005).

Boone JM. Glandular breast dose for monoenergetic and high-energy x-ray beams: Monte Carlo assessment. Radiology **213:** 23-37 (1999).

Boone JM, Kwan AL, Yang K, Burkett GW, Lindfors KK, Nelson TR. Computed tomography for imaging the breast. J Mammary Gland Biol Neoplasia **11:** 103-111 (2006a).

Boone JM, Lindfors KK. Breast CT: potential for breast cancer screening and diagnosis. Future Oncol **2:** 351-356 (2006b).

Boone JM, Nelson TR, Lindfors KK, Seibert JA. Dedicated breast CT: radiation dose and image quality evaluation. Radiology **221:** 657-667 (2001).

Boutroy S, Bouxsein ML, Munoz F, Delmas PD. In vivo assessment of trabecular bone microarchitecture by high resolution peripheral quantitative computed tomography. J Clin Endocrinol Metab **90:** 6508-6515 (2005).

Boverman G, Fang Q, Carp SA, Miller EL, Brooks DH, Selb J, Moore RH, Kopans DB, Boas DA. Spatio-temporal imaging of the hemoglobin in the compressed breast with diffuse optical tomography. Phys Med Biol **52:** 3619-3641 (2007).

Boyd NF, Guo H, Martin LJ, Sun L, Stone J, Fishell E, Jong RA, Hislop G, Chiarelli A, Minkin S, Yaffe MJ. Mammographic density and the risk and detection of breast cancer. N Engl J Med **356:** 227-236 (2007).

Bradbury AR, Olopade OI. Genetic susceptibility to breast cancer. Rev Endocr Metab Disord **8:** 255-267 (2007).

Brankov JG, Wernick MN, Yang Y, Li J, Muehleman C, Zhong Z, Anastasio MA. A computed tomography implementation of multiple-image radiography. Med Phys **33:** 278-289 (2006).

Bravin A, Fiedler S, Thomlinson W. Very low dose mammography: new perspectives in diffraction-enhanced imaging (DEI) mammography. SPIE **4682:** 167-173 (2002).

Bravin A, Keyriläinen J, Fernández M, Fiedler S, Nemoz C, Karjalainen-Lindsberg ML, Tenhunen M, Virkkunen P, Leidenius M, von Smitten K, Sipilä P, Suortti P. High-resolution CT by diffraction-enhanced x-ray imaging: mapping of breast tissue samples and comparison with their histo-pathology. Phys Med Biol **52:** 2197-2211 (2007).

Brem RF, Fishman M, Rapelyea JA. Detection of ductal carcinoma in situ with mammography, breast specific gamma imaging and magnetic resonance imaging: a comparative study. Acad Radiol **14:** 945-950 (2007).

Brem RF, Floerke AC, Rapelyea JA, Teal C, Kelly T, Malhur V. Breast-specific gamma imaging as an adnunct imaging modality for the diagnosis of breast cancer. Radiology **247:** 651-657 (2008).

Brem RF, Hoffmeister JW, Zisman G, DeSimio MP, Rogers SK. A computer-aided detection system for the evaluation of breast cancer by mammographic appearance and lesion size. AJR Am J Roentgenol **184:** 893-896 (2005).

Brenner DJ, Sawant SG, Hande MP, Miller RC, Elliston CD, Fu Z, Randers-Pehrson G, Marino SA. Routine screening mammography: How important is the radiation-risk side of the benefit-risk equation? Int J Radiat **78:** 1065-1067 (2002).

Breskin A, Chechik R, Paltiel Z, Schechter B, Warshawsky A, Shanzer A, Neeman M. X-ray imaging of tumors with dextran carriers of platinum compounds. U.S. Patent 6,694,171 (2004).

Bridges RL, Wiley CR, Christian JC, Strohm AP. An introduction to Na(18)F bone scintigraphy: basic principles, advanced imaging concepts, and case examples. J Nucl Med Technol **35:** 64-76 (2007).

Bridot JL, Faure AC, Laurent S, Rivière C, Billotey C, Hiba B, Janier M, Josserand V, Coll JL, Elst LV, Muller R, Roux S, Perriat P, Tillement O. Hybrid gadolinium oxide nanoparticles: multimodal contrast agents for in vivo imaging. J Am Chem Soc **129:** 5076-5084 (2007).

Briedis D, Siu KK, Paganin DM, Pavlov KM, Lewis RA. Analyzer-based mammography using single-image reconstruction. Phys Med Biol **50:** 3599-3611 (2005).

Brown BH. Electrical impedance tomography (EIT): a review. J Med Eng Technol **27:** 97-108 (2003).

Brzymialkiewicz CN, Tornai MP, McKinley RL, Bowsher JE. Evaluation of fully 3-D emission mammotomography with a compact cadmium zinc telluride detector. IEEE Trans Med Imaging **24:** 868-877 (2005).

Buchmann I, Riedmüller K, Hoffner S, Mack U, Aulmann S, Haberkorn U. Comparison of 99m technetium pertechnetate and 123iodide SPECT with FDG-PET in patients suspicious for breast cancer. Cancer Biother Radiopharm **22:** 779-789 (2007).

Buck AK, Nekolla S, Ziegler S, Beer A, Krause BJ, Herrmann K, Scheidhauer K, Wester HJ, Rummeny EJ, Schwaiger M, Drzezga A. SPECT/CT. J Nucl Med **49:** 1305-1319 (2008).

Burattini E, Gambaccini M, Marziani M, Rimondi O, Indovina PL, Pocek M, Simonetti G, Benassi M, Tirelli C, Passariello R. X-ray mammography with synchrotron radiation. Rev Sci Instrum **63:** 638-640 (1992).

Burattini E, Cossu E, Di Maggio C, Gambaccini M, Indovina PL, Marziani M, Pocek M, Simeoni S, Simonetti G. Mammography with synchrotron radiation. Radiology **195**: 239-244 (1995).

Burwinkel B, Wirtenberger M, Klaes R, Schmutzler RK, Grybowska E, Försti A, Frank B, Bermejo JL, Bugert P, Wappenschmidt B, Butkiewicz D, Pamula J, Pekala W, Zientek H, Mielzynska D, Siwinska E, Bartram CR, Hemminki K. Association of NCOA3 polymorphisms with breast cancer risk. Clin Cancer Res **11:** 2169-2174 (2005).

Buscombe JR, Cwikla JB, Holloway B, Hilson AJ. Prediction of the usefulness of combined mammography and scintimammography in suspected primary breast cancer using ROC curves. J Nucl Med **42:** 3-8 (2001).

Buscombe JR, Holloway B, Roche N, Bombardieri E. Position of nuclear medicine modalities in the diagnostic work-up of breast cancer. Q J Nucl Med Mol Imaging **48:** 109-118 (2004).

Bushberg J, Seibert A, Leidholdt M and Boone J. The Essential Physics of Medical Imaging. 2nd ed. Philadelphia: Lippincott Williams and Wilkins (2002).

Cai QY, Kim SH, Choi KS, Kim SY, Byun SJ, Kim KW, Park SH, Juhng SK, Yoon KH. Colloidal gold nanoparticles as a blood-pool contrast agent for x-ray computed tomography in mice. Invest Radiol **42:** 797-806 (2007).

Camp RL, Dolled-Filhart M, King BL, Rimm DL. Quantitative analysis of breast cancer tissue microarrays shows that both high and normal levels of HER-2 expression are associated with poor outcome. Cancer Research **63:** 1445-1448 (2003).

Canaris GJ, Manowitz NR, Mayor G, Ridgway EC. The Colorado thyroid disease prevalence study. Arch Intern Med **160:** 526-534 (2000).

Cantwell CP, Setty BN, Holalkere N, Sahani DV, Fischman AJ, Blake MA. Liver lesion detection and characterization in patients with colorectal cancer: a comparison of low radiation dose non-enhanced PET/CT, contrast-enhanced PET/CT, and liver MRI. J Comput Assist Tomogr **32:** 738-744 (2008).

Cao G, Lee YZ, Peng R, Liu Z, Rajaram R, Calderon-Colon X, An L, Wang P, Phan T, Sultana S, Lalush DS, Lu JP, Zhou O. A dynamic micro-CT scanner based on a carbon nanotube field emission x-ray source. Phys Med Biol **54:** 2323-2340 (2009).

Carey LA, Perou CM, Livasy CA, Dressler LG, Cowan D, Conway K, Karaca G, Troester MA, Tse CK, Edmiston S, Deming SL, Geradts J, Cheang MC, Nielsen TO, Moorman PG, Earp HS, Millikan RC. Race, breast cancer subtypes, and survival in the Carolina Breast Cancer Study. JAMA **295:** 2492-2502 (2006).

Carlsson M, Arheden H, Higgins CB, Saeed M. Magnetic resonance imaging as a potential gold standard for infarct quantification. J Electrocardiol **41:** 614-620 (2008).

Carpenter CL, Ross RK, Paganini-Hill A, Bernstein L. Effect of family history, obesity and exercise on breast cancer risk among postmenopausal women. Int J Cancer **106:** 96-102 (2003).

Carpenter CM, Pogue BW, Jiang S, Dehghani H, Wang X, Paulsen KD, Wells WA, Forero J, Kogel C, Weaver JB, Poplack SP, Kaufman PA. Image-guided optical spectroscopy provides molecular-specific information in vivo: MRI-guided spectroscopy of breast cancer hemoglobin, water, and scatterer size. Opt Lett **32:** 933-935 (2007).

Carroll FE. Tunable monochromatic x-rays: a new paradigm in medicine. AJR **179:** 483-490 (2002).

Carroll FE, Waters JW, Andrews WW, Price RR, Pickens DR, Willcott R, Tompkins P, Roos C, Page D, Reed G. Attenuation of monochromatic x-rays by normal and abnormal breast tissues. Invest Radiol **29:** 266-272 (1994).

Carroll FE, Waters JW, Price RR, Brau CA, Roos CF, Tolk NH, Pickens DR, Stephens WH. Near-monochromatic x-ray beams produced by the free electron laser and Compton backscatter. Invest Radiol **25:** 465-471 (1990).

Cassano E, Rizzo S, Bozzini A, Menna S, Bellomi M. Contrast enhanced ultrasound of breast cancer. Cancer Imaging **6:** 4-6 (2006).

Castellino RA. Computer aided diagnosis (CAD): an overview. Cancer Imaging **1:** 25-27 (2005).

Castera L, Forns X, Alberti A. Non-invasive evaluation of liver fibrosis using transient elastography. J Hepatol **48:** 835-847 (2008).

Catalano O, Sandomenico F, Matarazzo I, Siani A. Contrast-enhanced sonography of the spleen. AJR Am J Roentgenol **184:** 1150-1156 (2005).

CDC. "Heart Disease Facts and Statistics." http://www.cdc.gov/heartdisease/statistics.htm. Accessed: 12-2-2008 (2008).

CDC. "Statistics." http://www.cdc.gov/cancer/lung/statistics. Accessed: 12-2-2008 (2007a).

CDC. "Traumatic Brain Injury." http://www.cdc.gov/ncipc/factsheets/tbi.htm. Accessed: 12-2-2008 (2007b).

Cerussi A, Hsiang D, Shah N, Mehta R, Durkin A, Butler J, Tromberg BJ. Predicting response to breast cancer neoadjuvant chemotherapy using diffuse optical spectroscopy. Proc Natl Acad Sci USA **104:** 4014-4019 (2007).

Chan HP, Wei J, Sahiner B, Rafferty EA, Wu T, Roubidoux MA, Moore RH, Kopans DB, Hadjiiski LM, Helvie MA. Computer-aided detection system for breast masses on digital tomosynthesis mammograms: preliminary experience. Radiology **237:** 1075–1080 (2005).

Chan HP, Wei J, Zhang Y, Helvie MA, Moore RH, Sahiner B, Hadjiiski L, Kopans DB. Computer-aided detection of masses in digital tomosynthesis mammography: comparison of three approaches. Med Phys **35:** 4087-4095 (2008).

Chao A, Major K, Kumar SR, Patel K, Trujillo I, Hood DB, Rowe VL, Weaver FA. Carbon dioxide digital subtraction angiography-assisted endovascular aortic aneurysm repair in the azotemic patient. J Vasc Surg **45:** 451-458 (2007a).

Chao CY, Ashkenazi S, Huang SW, O'Donnell M, Guo LJ. High-frequency ultrasound sensors using polymer microring resonators. IEEE Trans Ultrason Ferroelectr Freq Control **54:** 957-965 (2007b).

Chapman D, Nesch I, Hasnah MO, Morrison TI. X-ray optics for emission line x-ray source diffraction enhanced systems. Nucl Instrum Methods Phys Res A **562:** 461-467 (2006).

Chapman D, Pisano E, Thomlinson W, Zhong Z, Johnston RE, Washburn D, Sayers D, Malinowska K. Medical applications of diffraction-enhanced imaging. Breast Dis **10:** 197-207 (1998).

Chapman D, Thomlinson W, Arfelli F, Gmür N, Zhong Z, Menk R, Johnston RE, Washburn D, Pisano E, Sayers D. Mammography imaging studies using a laue crystal analyzer. Rev Sci Instrum **67** (CD suppl) (1996).

Chapman D, Thomlinson W, Johnston RE, Washburn D, Pisano E, Gmür N, Zhong Z, Menk R, Arfelli F, Sayers D. Diffraction-enhanced x-ray imaging. Phys Med Biol **42:** 2015-25 (1997).

Charnley N, Donaldson S, Price P. Imaging angiogenesis. Methods Mol Biol **467:** 25-51 (2009).

Chen JTTT. Essentials of Cardiac Imaging 2nd ed. Lippincott-Raven: Philadelphia (1997).

Chen SC, Carton AK, Albert M, Conant EF, Schnall MD and Maidment AD. Initial clinical experience with contrast-enhanced digital breast tomosynthesis. Acad Radiol **14:** 229-238 (2007).

Chen TJ, Cheng TH, Chen CY, Hsu SC, Cheng TL, Liu GC, Wang YM. Targeted Herceptin-dextran iron oxide nanoparticles for noninvasive imaging of HER2/neu receptors using MRI. J Biol Inorg Chem **14:** 253-260 (2009).

Chen Y, Zheng G, Zhang ZH, Blessington D, Zhang M, Li H, Liu Q, Zhou L, Intes X, Achilefu S, Chance B. Metabolism-enhanced tumor localization by fluorescence imaging: in vivo animal studies. Opt Lett **28:** 2070-2072 (2003).

Cherepenin V, Karpov A, Korjenevsky A, Kornienko V, Mazaletskaya A, Mazourov D, Meister D. A 3-D electrical impedance tomography (EIT) system for breast cancer detection. Physiol Meas **22:** 9-18 (2001).

Choe R, Corlu A, Lee K, Durduran T, Konecky SD, Grosicka-Koptyra M, Arridge SR, Czerniecki BJ, Fraker DL, DeMichele A, Chance B, Rosen MA, Yodh AG. Diffuse optical tomography of breast cancer during neoadjuvant chemotherapy: a case study with comparison to MRI. Med Phys **32:** 1128-1139 (2005).

Cho N, Moon WK, Park JS, Cha JH, Jang M, Seong MH. Nonpalpable breast masses: evaluation by US elastography. Korean J Radiol **9:** 111-118 (2008).

Chou CY, Anastasio MA, Brankov JG, Wernick MN Brey EM, Connor DM and Zhong Z. An extended diffraction-enhanced imaging method for implementing multiple-image radiography. Phys Med Biol **52:** 1923-1945 (2007).

Chow SC. Chang M. Adaptive design methods in clinical trials – a review. Orphanet J Rare Dis **3:** 11 (2008).

Chowdary MV, Kumar KK, Kurien J, Mathew S, Krishna CM. Discrimination of normal, benign and malignant breast tissues by Raman spectroscopy. Biopolymers **83:** 556-569 (2006).

Chu KC, Anderson WF, Fritz A, Ries LA, Brawley OW. Frequency distributions of breast cancer characteristics classified by estrogen receptor and progesterone receptor status for eight racial/ethnic groups. Cancer **92:** 37-45 (2001).

Cirstoui-Hapca A, Bossy-Nobs L, Buchegger F, Gurny R, Delie F. Differential tumor cell targeting of anti-HER2 (Herceptin) and anti-CD20 (Mabthera) coupled nanoparticles. Int J Pharm **331:** 190-196 (2007).

Claus EB, Schildkraut J, Iversen ES Jr, Berry D, Parmigiani G. Effect of BRCA1 and BRCA2 on the association between breast cancer risk and family history. J Natl Cancer Inst **90:** 1824-1829 (1998).

Cloetens P, Ludwig W, Baruchel J, van Dyck D, van Landuyt J, Guigay JP, Schlenker M. Holotomography: quantitative phase tomography with micrometer resolution using hard synchrotron radiation x rays. Appl Phys Lett **75:** 2912-2914 (1999).

Coan P, Pagot E, Fiedler S, Cloetens P, Baruchel J, Bravin A. Phase-contrast x-ray imaging combining free space propagation and Bragg diffraction. J Synchrotron Radiat **12:** 241-245 (2005).

Colditz GA, Rosner BA, Chen WY, Holmes MD, Hankinson SE. Risk factors for breast cancer according to estrogen and progesterone receptor status. J Natl Cancer Inst **96:** 218-228 (2004).

Coli S, Magnoni M, Sangiorgi G, Marrocco-Trischitta MM, Melisurgo G, Mauriello A, Spagnoli L, Chiesa R, Cianflone D, Maseri A. Contrast-enhanced ultrasound

imaging of intraplaque neovascularization in carotid arteries: correlation with histology and plaque echogenicity. J Am Coll Cardiol **52:** 223-230 (2008).

Colonna S, D'Acapito F, Mobilio S, Onori S, Pugliani L, Romanzetti S, Rustichelli F. Curved optics for x-ray phase contrast imaging by synchrotron radiation. Phys Med Biol **46:** 967-974 (2001).

Conneely MF, Hacein-Bey L, Jay WM. Magnetic resonance imaging of the orbit. Semin Ophthalmol **23:** 179-189 (2008).

Connor DM. Application of diffraction enhanced imaging to bone [dissertation]. Raleigh (NC): North Carolina State University; (2005a).

Connor DM, Benveniste H, Dilmanian A, Miller L, Kritzer MF, Zhong Z. Detection of amyloid plaques by diffraction-enhanced imaging in a mouse model of Alzheimer's disease. Alzheimer's and Dementia **4:** T77 (2008).

Connor DM, Benveniste H, Dilmanian A, Kritzer MF, Miller LM, Zhong Z. Computed tomography of amyloid plaques in a mouse model of Alzheimer's disease using diffraction enhanced imaging. NeuroImage **46:** 908-914 (2009).

Connor DM, Sayers D, Sumner DR, Zhong Z. Diffraction-enhanced imaging of controlled defects within bone, including bone-metal gaps. Phys Med Biol **51:** 3283-3300 (2006).

Connor DM, Sayers D, Sumner DR, Zhong Z. Identification of fatigue damage in cortical bone by diffraction-enhanced imaging. Nucl Instrum Methods Phys Res A **548:** 234-239 (2005b).

Copland JA, Eghtedari M, Popov VL, Kotov N, Mamedova N, Motamedi M and Oraevsky AA. Bioconjugated gold nanoparticles as molecular based contrast agnet: implications for imaging of deep tumors using optoacoustic tomography. Mol Imaging Biol **6:** 341-349 (2004).

Costantino JP, Gail MH, Pee D, Anderson S, Redmond CK, Benichou J, Wieand HS. Validation studies for models projecting the risk of invasive and total breast cancer incidence. J Natl Cancer Inst **91:** 1541-1548 (1999).

Coresh J, Selvin E, Stevens LA, Manzi J, Kusek JW, Eggers P, Van Lente F, Levey AS. Prevalence of chronic kidney disease in the United States. JAMA **298:** 2038-2047 (2007).

Correas JM, Claudon M, Tranquart F, Hélénon AO. The kidney: imaging with microbubble contrast agents. Ultrasound Q **22:** 53-66 (2006).

Cosgrove D. Ultrasound contrast agents: an overview. Eur J Radiol **60:** 324-330 (2006).

Costaridou L. Medical Image Analysis Methods. Taylor & Francis Group: Boca Raton (2005).

Cox CE, Nguyen K, Gray RJ, Salud C, Ku NN, Dupont E, Hutson L, Peltz E, Whitehead G, Reintgen D, Cantor A. Importance of lymphatic mapping in ductal carcinoma in situ (DCIS): why map DCIS? Am Surg **67:** 513-519 (2001).

Crotty DJ, McKinley RL, Tornai MP. Experimental spectral measurements of heavy K-edge filtered beams for x-ray computed mammotomography. Phys Med Biol **52:** 603-616 (2007).

Cullity BD. Elements of x-ray diffraction, 2nd ed. Addison-Wesley Publishing Company, Inc: Reading, Massachusetts (1978).

Cutler M. Transillumination as an aid in the diagnosis of breast lesions. Surg Gynecol Obstet **48:** 721-729 (1929).

Cuzick J. Aromatase inhibitors for breast cancer prevention. J Clin Oncol **23:** 1636-1643 (2005).

Cwikla JB, Kolasinska A, Buscombe JR, Hilson AJ. Tc-99m MIBI in suspected recurrent breast cancer. Cancer Biother Radiopharm **15:** 367-372 (2000).

Daneshvar H, Nelms J, Muhammad O, Jackson H, Tkach J, Davros W, Peterson T, Vogelbaum MA, Bruchez MP, Toms SA. Imaging characteristics of zinc sulfide shell, cadmium telluride core quantum dots. Nanomed **3:** 21-29 (2008).

Danielsson R, Boné B, Perbeck L, Aspelin P. Evaluation of planar scintimammography with ^{99m}Tc-MIBI in the detection of axillary lymph node metastasis of breast carcinoma. Acta Radiol **40:** 491-495 (1999).

Danielsson R, Reihnér E, Grabowska A, Boné B. The role of scintimammography with ^{99m}Tc-sestamibi as a complementary diagnostic technique in the detection of breast cancer. ACTA Radiol **41:** 441-445 (2000).

Davis TJ, Gureyev TE Gao D, Stevenson AW, Wilkins SW. X-ray image contrast from a simple phase object. Phys Rev Lett **74:** 3173-3176 (1995).

Dawson P, Cosgrove DO and Grainger RG. Textbook of Contrast Media. Isis Medical Media Ltd. Oxford, UK (1999).

Dayton PA, Ferrara KW. Targeted imaging using ultrasound. J Magn Reson Imaging **16:** 362-377 (2002).

de la Fuente JM, Alcántara, Eaton P, Crespo P, Rojas TC, Fernández A, Hernando A, Penadés S. Gold and gold-iron oxide magnetic glyconanoparticles: synthesis, characterization and magnetic properties. J Phys Chem B **110:** 13021-13028 (2006).

DeMartini W, Lehman C. A review of current evidence-based clinical applications for breast magnetic resonance imaging. Top Magn Reson Imaging **19:** 143-150 (2008).

Demos SG, Vogel AJ and Gandjbakhche AH. Advances in optical spectroscopy and imaging of breast lesions. J Mammary Gland Biol Neoplasia. **11:** 165-181 (2006).

Desser TS, Kamaya A. Ultrasound of thyroid nodules. Neuroimaging Clin N Am **18:** 463-478 (2008).

deVries N, Miller FJ, Wojtowycz MM, Brown PR, Yandow DR, Nelson JA, Kruger RA. Tomographic digital subtraction angiography: initial clinical studies using tomosynthesis—work in progress. Radiology **157:** 239–241 (1985).

Diacon AH, Theron J, Bollinger CT. Transthoracic ultrasound for the pulmonologist. Curr Opin Pulm Med **11:** 307-312 (2005).

"Diane's Story of Living Life with Breast Cancer and Dying With Dignity." http://diane.ponpines.com/what_is_breast_cancer.html. Accessed: 2-6-2008.

Dibble SL, Israel J, Nussey B, Sayre JW, Brenner RJ, Sickles EA. Mammography with breast cushions. Womens Health Issues **15:** 55-63 (2005).

Di Carli MF, Dorbala S, Meserve J, El Fakhri G, Sitek A, Moore SC. Clinical myocardial perfusion PET/CT. J Nucl Med **48:** 783-793 (2007).

Diekmann F, Bick U. Tomosynthesis and contrast-enhanced digital mammography: recent advances in digital mammography. Eur Radiol **17:** 3086-3092 (2007).

Diekmann F, Diekmann S, Jeunehomme F, Muller S, Hamm B, Bick U. Digital mammography using iodine-based contrast media: initial clinical experience with dynamic contrast medium enhancement. Invest Radiol **40:** 397-404 (2005).

Diekmann F, Diekmann S, Taupitz M, Bick U, Winzer KJ, Hüttner C, Muller S, Jeunehomme F, Hamm B. Use of iodine-based contrast media in digital full-field mammography: initial experience. Rofo **175:** 342-345 (2003).

Diekmann F, Sommer A, Lawaczeck R, Diekmann S, Pietsch H, Speck U, Hamm B, Bick U. Contrast-to-noise ratios of different elements in digital mammography: evaluation of their potential as new contrast agents. Invest Radiol **42:** 319-325 (2007).

Dilmanian FA, Zhong Z, Ren B, Wu XY, Chapman LD, Orion I, Thomlinson WC. Computed tomography of x-ray index of refraction using the diffraction-enhanced imaging method. Phys Med Biol **45:** 933-946 (2000).

Dobbins JT 3rd, Godfrey DJ. Digital x-ray tomosynthesis: current state of the art and clinical potential. Phys Med Biol **48:** R65-R106 (2003).

Donnelly EF, Price RR. Quantification of the effect of kvp on edge-enhancement index in phase-contrast radiography. Med Phys **29:** 999-1002 (2002).

D'Onofrio M, Zamboni G, Faccioli N, Capelli P, Pozzi Mucelli R. Ultrasonography of the pancreas. 4. Contrast-enhanced imaging. Abdom Imaging **32:** 171-181 (2007).

Dreossi D, Abrami A, Arfelli F, Bregant P, Casarin K, Chenda V, Cova MA, Longo R, Menk RH, Quai E, Quaia E, Rigon L, Rokvic T, Sanabor D, Tonutti M, Tromba G, Vascotto A, Zanconati F, Castelli E. The mammography project at the SYRMEP beamline. Eur J Radiol **68:** S58-S62 (2008).

Dromain C, Balleyguier C, Muller S, Mathieu MC, Rochard F, Opolon P, Sigal R. Evaluation of tumor angiogenesis of breast carcinoma using contrast-enhanced digital mammography. AJR Am J Roentgenol **187:** 528-537 (2006).

Drukker K, Sennett CA, Giger ML. Automated method for improving system performance of computer-aided diagnosis in breast ultrasound. IEEE Trans Med Imaging **28:** 122-128 (2009).

Dullum JR, Lewis EC, Mayer JA. Rates and correlates of discomfort associated with mammography. Radiology **214:** 546-552 (2000).

Duquet E, Vasseur S, Momet S, Devoisselle JM. Magnetic nanoparticles and their applications in medicine. Nanomed **1:** 157-168 (2006).

Duric N, Littrup P, Poulo L, Babkin A, Pevzner R, Holsapple E, Rama O, Glide C. Detection of breast cancer with ultrasound tomography: first results with the Computed Ultrasound Risk Evaluation (CURE) prototype. Med Phys **34:** 773-785 (2007).

Durduran T, Choe R, Yu G, Zhou C, Tchou JC, Czerniecki BJ, Yodh AG. Diffuse optical measurement of blood flow in breast tumors. Opt Lett **30:** 2915-2917 (2005).

Edwards GS, Allen SJ, Haglund RF, Nemanich RJ, Redlich B, Simon JD, Yang WC. Applications of free-electron lasers in the biological and material sciences. Photochem Photobiol **81:** 711-735 (2005).

Ersoy H, Rybicki RJ. Biochemical safety profiles of gadolinium-based extracellular contrast agents and nephrogenic systemic fibrosis. J Magn Reson Imaging **26:** 1190-1197 (2007).

Evans AL, Gleeson FV. Radiology in pleural disease: state of the art. Respirology **9:** 300-312 (2004).

Evans SH, Bradley DA, Dance DR, Bateman JE and Jones CH. Measurement of small-angle photon scattering for some breast tissues and substitute materials. Phys Med Biol **36**, 7-18 (1991).

Falzon G, Pearson S, Murison R, Hall C, Siu K, Evans A, Rogers K, Lewis R. Wavelet-based feature extraction applied to small-angle x-ray scattering patterns from breast tissue: a tool for differentiating between tissue types. Phys med Biol **51:** 2765-2477 (2006).

Faulconer LS, Connor DM, Euliss L, Dilmanian FA, Zhong Z, Cole E, Pisano E. Feasibility of Contrast-Enhanced Diffraction Enhanced Imaging. *Under Review.*

Faulconer LS, Parham C, Connor DM, Koomen M, Kuzmiak C, Pavic D, Livasy CA, Eunhee K, Zeng D, Cole EB, Zhong Z, Pisano ED. Radiologist evaluation of an x-ray tube-based diffraction-enhanced imaging prototype using full-thickness breast specimens. Acad Radiol (2009a epub ahead of print).

Faulconer LS, Parham C, Connor DM, Livasy CA, Koomen M, Kuzmiak C, Cho KR, Lee Y, Rafoth J, Eunhee K, Zeng D, Cole EB, Zhong Z, Pisano ED. Effect of Breast Compression on Lesion Characteristic Visibility Using Diffraction Enhanced Imaging. Adad Radiol (2009b in press)

Fawcett T. An introduction to ROC analysis. Pattern Recognition Letters **27:** 861-874 (2006).

Feigelson HS, Calle EE, Robertson AS, Wingo PA, Thun MJ. Alcohol consumption increases the risk of fatal breast cancer (United States). Cancer Causes Control **12:** 895-902 (2001).

Feigelson HS, Jonas CR, Robertson AS, McCullough ML, Thun MJ, Calle EE. Alcohol, folate, methionine and risk of incident breast cancer in the American Cancer Society Cancer Prevention Study II nutrition cohort. Cancer Epidemiol Biomarkers Prev **12:** 161-164 (2003).

Fentiman IS, Fourquet A, Hortobagyi GN. Male Breast Cancer. Lancet **367:** 595-604 (2006).

Fernández M, Keyriläinen J, Serimaa R, Torkkeli M, Karjalainen-Lindsberg ML, Tenhunen M, Thomlinson W, Urban V, Suortti P. Small-angle x-ray scattering studies of human breast tissue specimens. Phys Med Biol **47:** 577-592 (2002).

Fernández M, Keyriläinen J, Serimaa R, Torkkeli M, Karjalainen-Lindsberg ML, Leidenius M, von Smitten K, Tenhunen M, Fiedler S, Bravin A, Weiss TM, Suortti P. Human breast cancer *in vitro*: matching histo-pathology with small-angle x-ray scattering and diffraction-enhanced x-ray imaging. Phys Med Biol **50:** 2991-3006 (2005).

Fernández M, Suhonen H, Keyriläinen J, Bravin A, Fiedler S, Karjalainen-Lindsberg ML, Leidenius M, von Smitten K, Suortti P. USAXS and SAXS from cancer-bearing breast tissue samples. Eur J Radiol **68:** S89-S94 (2008).

Fiedler S, Bravin A, Keyriläinen J, Fernández M, Suortti P, Thomlinson W, Tenhunen M, Virkkunen P, Karjalainen-Lindsberg M. Imaging lobular breast carcinoma: comparison of synchrotron radiation DEI-CT technique with clinical CT, mammography and histology. Phys Med Biol **49:** 175-188 (2004).

Field JK, Duffy SW. Lung cancer screening: the way forward. Br J Cancer **99:** 557-562 (2008).

Figuerola A, Fiore A, Di Corato R, Falqui A, Giannini C, Micotti E, Lascialfari A, Corti M, Cingolani R, Pellegrino T, Cozzoli PD, Manna L. One-pot synthesis and characterization of size-controlled bimagnetic FePt-iron oxide heterdimer nanocrystals. J Am Chem Soc **130:** 1477-1487 (2008).

Fischer U, Kopka L, Grabbe E. Breast carcinoma: effect of preoperative contrast-enhanced MR imaging on the therapeutic approach. Radiology **213:** 881-888 (1999).

Fisher B, Costantino JP, Wickerham DL, Cecchini RS, Cronin WM, Robidoux A, Bevers TB, Kavanah MT, Atkins JN, Margolese RG, Runowicz CD, James JM, Ford LG, Wolmark N. Tamoxifen for the prevention of breast cancer: current status of the National Surgical Adjuvant Breast and Bowel Project P-1 Study. J Natl Cancer Inst **97:** 1652-1662 (2005).

Fisher B, Costantino JP, Wickerham DL, Redmond CK, Kavanah M, Cronin WM, Vogel V, Robidoux A, Dimitrov N, Atkins J, Daly M, Wieand S, Tan-Chiu E, Ford L, Wolmark N. Tamoxifen for prevention of breast cancer: report of the National Surgical Adjuvant Breast and Bowel Project P-1 Study. J Natl Cancer Inst **90:** 1371-1388 (1998).

Fisher B, Powles TJ, Pritchard KJ. Tamoxifen for the prevention of breast cancer. Eur J Cancer **36:** 142-150 (2000).

Fitzgerald R. Phase-sensitive x-ray imaging. Phys Today **53:** 23-26 (2000).

Fleury EF, Rinaldi JF, Piato S, Fleury JC, Junior DR. Appearance of breast masses on sonoelastography with special focus on the diagnosis of fibroadenomas. Eur Radiol **19:** 1337-1346 (2009).

Flynn M, Ksar J, Blechinger J, McGee R. "Spatial Response of X-Ray Tomosynthesis in Relation to Computed Tomography." Session: Physics (Tomosynthesis/ Breast Tomosynthesis), RSNA (2007).

Fogoros RN. Electrophysiologic Testing 4th ed. Blackwell Publishing: Massachusetts (2006).

Folkman J. Tumor angiogenesis: therapeutic implications. New England Journal of Medicine **285,** 1182-1186 (1971).

Forsberg F, Piccoli CW, Merton DA, Palazzo JJ, Hall AL. Breast lesions: imaging with contrast-enhanced subharmonic US-- initial experience. Radiology **244:** 718-726 (2007).

Forster E, Goetz K and Zaumseil P. Double crystal diffractometry for the characterization of targets for laser fusion experiments. Krist Tech **15:** 937-945 (1980).

Fournier LS, Vanel D, Athanasiou A, Gatzemeier W, Masuykov IV, Padhani AR, Dromain C, Galetti K, Sigal R, Costa A, Balleyguier C. Dynamic optical breast imaging: a novel technique to detect and characterize tumor vessels. Eur J Radiol **69:** 43-49 (2009).

Fowler TJ, Scadding JW. Clinical Neurology. 3rd ed. Arnold: London (2003).

Freixenet J, Oliver A, Marti R, Lladó X, Pont J, Pérez E, Denton ER, Zwiggerlaar R. Eigendetection of masses considering false positive reduction and breast density information. Med Phys **35:** 1840-1853 (2008).

Friedenreich CM. Physical activity and breast cancer risk: the effect of menopausal status. Exerc Sport Sci Rev **32:** 180-184 (2004).

Friedenreich CM, Courneya KS, Bryant HE. Influence of physical activity in different age and life periods on the risk of breast cancer. Epidemiology **12:** 604-612 (2001).

Fu Y, Nitecki DE, Maltby D, Simon GH, Berejnoi K, Raatschen HJ, Yeh BM, Shames DM, Brasch RC. Dendritic iodinated contrast agents with PEG-cores for CT imaging: synthesis and preliminary characterization. Bioconjug Chem **17:** 1043-1056 (2006).

Galassi F, Giambene B, Corvi A, Falaschi G. Evaluation of ocular surface temperature and retrobulbar haemodynamics by infrared thermography and colour Doppler imaging in patients with glaucoma. Br J Ophthalmol **91:** 878-881 (2007).

Gambaccini M, Taibi A, Del Guerra A, Frontera F, Marziani M. Narrow energy band x-rays via mosaic crystal for mammography application. Nucl Instrum Methods A **365:** 248-254 (1995).

Gambaccini M, Taibi A, Del Guerra A, Frontera F. Small-field imaging properties of narrow energy band x-ray beams for mammography. IEEE Trans Nucl Sci **43:** 2049-2052 (1996).

Gambaccini M, Tuffanelli A, Taibi A, Del Guerra A. Spatial resolution measurements in quasimonochromatic x-rays with mosaic crystals for mammography applications. Med Phys **28:** 412-418 (2001).

Gang L, Chen ZH, Wu ZY, Ando M, Lin P, Wang JY, Jiang XM. Image quality dependence on thickness of sliced rat kidney taken by a simplest DEI construction. Nucl Instrum Methods Phys Res A **548:** 200-206 (2005).

Gao X, Luo S, Yin H, Liu B, Xu M, Yuan Q, Gao X, Zhu P. A micro-tomography method based on x-ray diffraction-enhanced imaging for the visualization of micro-organs and soft tissues. Comput Med Imaging Graph **30:** 339-347 (2006).

Gao Z, Kennedy AM, Christensen DA, Rapoport NY. Drug-loaded nano/Microbubbles for combining ultrasonography and targeted chemotherapy. Ultrasonics **48:** 260-270 (2008).

Gasco M, Shami S, Crook T. The p53 pathway in breast cancer. Breast Cancer Res **4:** 70-76 (2002).

Genant HK, Engelke K, Prevrhal S. Advanced CT bone imaging in osteoporosis. Rheumatology (Oxford) **47 Suppl 4:** iv9-iv16 (2008).

Georgian-Smith D, Moore RH, Halpern E, Yeh ED, Rafferty EA, D'Alessandro HA, Staffa M, Hall DA, McCarthy KA, Kopans DB. Blinded comparison of computer-aided detection with human second reading in screening mammography. AJR Am J Roentgenol **189**, 1135-1141 (2007).

Geso M. Gold nanoparticles: a new x-ray contrast agent. Br J Radiol **80:** 64-65 (2007).

Glick SJ. Breast CT. Annu Rev Biomed Eng **9:** 501-526 (2007).

González FJ. Infrared imager requirements for breast cancer detection. Conf Proc IEEE Eng Med Biol Soc **2007:** 3312-3314 (2007).

Good WF, Abrams GS, Catullo VJ, Chough DM, Ganott MA, Hakim CM, Gur D. Digital breast tomosynthesis: a pilot observer study. AJR Am J Roentgenol **190:** 865-869 (2008).

Goldberg BB, Merton DA, Liu JB, Murphy G, Forsberg F. Contrast-enhanced sonographic imaging of lymphatic channels and sentinel lymph nodes. J Ultrasound Med **24:** 953-965 (2005).

Gore JP, Xu LX. Thermal imaging for biological and medical diagnostics, Ch 17 in Biomedical Photonics Handbook, Vo-Dinh T. CRC Press p17-1 thru 17-12 (2003).

Görg C. The forgotten organ: contrast enhanced sonography of the spleen. Eur J Radiol **64:** 189-201 (2007).

Granada JF, Feinstein SB. Imaging of the vasa vasorum. Nat Clin Pract Cardiovasc Med **5 Suppl 2:** S18-S25 (2008).

Grant FD, Fahey FH, Packard AB, Davis RT, Alavi A, Treves ST. Skeletal PET with 18F-fluoride: applying new technology to an old tracer. J Nucl Med **49:** 68-78 (2008).

Greendale GA, Reboussin BA, Slone S, Wasilauskas C, Pike MC, Ursin G. Postmenopausal hormone therapy and change in mammographic density. J Natl Cancer Inst **95:** 30-37 (2003).

Greish K. Enhanced permeability and retention of macromolecular drugs in solid tumors: a royal gate for targeting anticancer nanomedicines. J Drug Target **15**: 457-464 (2007).

Griggs WS, Divgi C. Radioiodine imaging and treatment in thyroid disorders. Neuroimaging Clin N Am **18:** 505-515 (2008).

Gromet M. Comparison of computer-aided detection to double reading of screening mammograms: review of 231,221 mammograms. AJR Am J Roentgenol **190:** 854-859 (2008).

Gropler RJ, Soto P. Recent advances in cardiac positron emission tomography in the clinical management of the cardiac patient. Curr Cardiol Rep **6:** 20-26 (2004).

Gruszauskas NP, Drukker K, Giger ML, Sennett CA, Pesce LL. Performance of breast ultrasound computer-aided diagnosis: dependence on image selection. Acad Radiol **15:** 1234-1245 (2008).

Guermazi A. Imaging of Kidney Cancer. Springer: Berlin (2006).

Guest AR, Helvie MA, Chang HP, Hadjiiski LM, Bailey JE, Roubidoux MA. Adverse effects of increased body weight on quantitative measures of mammographic image quality. AJR **175:** 805-810 (2000).

Gundogdu O, Nirgianaki E, Che Ismail E, Jenneson PM, Bradley DA. Benchtop phase-contrast x-ray imaging. Appl Radiat Isot **65:** 1337-1344 (2007).

Guo Y, Cai YQ, Cai ZL, Gao YG, An NY, Ma L, Mahankali S, Gao JH. Differentiation of clinically benign and malignant breast lesions using diffusion-weighted imaging. J Magn Reson Imaging **16:** 172-178 (2002).

Gur D, Stalder JS, Hardesty LA, Zheng B, Sumkin JH, Chough DM, Shindel BE, Rockette HE. Computer-aided detection performance in mammographic examination of masses: assessment. Radiology **233:** 418-423 (2004).

Gureyev TE, Wilkins SW. Regimes of x-ray phase-contrast imaging with perfect crystals. Il Nuovo Cimento **19:** 545-552 (1997).

Hainfeld JF, Dilmanian FA, Slatkin DN, Smilowitz HM. Radiotherapy enhancement with gold nanoparticles. J Pharm Pharmacol **60:** 977-985 (2008).

Hainfeld JF, Slatkin DN, Focella TM, Smilowitz HM. Gold nanoparticles: a new x-ray contrast agent. Br J Radiol **79:** 248-253 (2006).

Haka AS, Shafer-Peltier KE, Fitzmaurice M, Crowe J, Dasari RR, Feld MS. Diagnosing breast cancer by using Raman spectroscopy. Proc Natl Acad Sci USA **102:** 12371-12376 (2005).

Haka AS, Shafer-Peltier KE, Fitzmaurice M, Crowe J, Dasari RR, Feld MS. Identifying microcalcifications in benign and malignant breast lesions by probing differences in their chemical composition using Raman spectroscopy. Cancer Res **62:** 5375-5380 (2002).

Haka AS, Volynskaya Z, Gardecki JA, Nazemi J, Lyons J, Hicks D, Fitzmaurice M, Dasari RR, Crowe JP, Feld MS. In vivo margin assessment during partial mastectomy breast surgery using raman spectroscopy. Cancer Res **66:** 3317-3322 (2006).

Hall JM, Lee MK, Newman B, Morrow JE, Anderson LA, Huey B, King MC. Linkage of early-onset familial breast cancer to chromosome 17q21. Science **250:** 1684-1689 (1990).

Halter RJ, Hartov A, Paulsen KD. A broadband high-frequency electrical impedance tomography system for breast imaging. IEEE Trans Biomed Eng **55:** 650-659 (2008).

Hamilton TJ, Bailat CJ, Rose-Petruck C, Diebold GJ. Acoustically modulated x-ray phase contrast imaging. Phys Med Biol **49:** 4985-4996 (2004).

Hanlon EB, Manoharan R, Koo TW, Shafer KE, Motz JT, Fitzmaurice M, Kramer JR, Itzkan I, Dasari RR, Feld MS. Prospects for in vivo Raman spectroscopy. Phys Med Biol **145:** R1-R59 (2000).

Harada T, Tanigawa N, Matsuki M, Nohara T, Narabayashi I. Evaluation of lymph node metastases of breast cancer using ultrasmall superparamagnetic iron oxide-enhanced magnetic resonance imaging. Eur J Radiol **63:** 401-407 (2007).

Harris JR, Hellman S, Henderson IC and Kinne DW. Breast Diseases, 2nd Edition. JB Lippincott Company, Philadelphia: 1991.

Hart M, Milne AD. X-ray Interferometry. J Phys E: Sci Instrum **2:** 646-648 (1969).

Hartmann LC, Sellers TA, Frost MH, Lingle WL, Degnim AC, Ghosh K, Vierkant RA, Maloney SD, Pankratz VS, Hillman DW, Suman VJ, Johnson J, Blake C, Tlsty T, Vachon CM, Melton JL 3rd, Visscher DW. Benign breast disease and the risk of breast cancer. N Engl J Med **353:** 229-237 (2005).

Hashimoto E, Maksimenko A, Sugiyama H, Hyodo K, Shimao D, Nishino Y, Ishikawa T, Ando M. First application of x-ray refraction-based computed tomography to a biomedical object. Zoolog Sci **23:** 809-813 (2006).

Hasnah MO, Oltulu O, Zhong Z, Chapman D. Single-exposure simultaneous diffraction-enhanced imaging. Nucl Instrum Methods Phys Res A **492:** 236-240 (2002a).

Hasnah MO, Parham C, Pisano ED, Zhong Z, Oltulu O, Chapman D. Mass density images from the diffraction-enhanced imaging technique. Med Phys **32:** 549-552 (2005).

Hasnah MO, Zhong Z, Oltulu O, Pisano E, Johnson RE, Sayers D, Thomlinson W, Chapman D. Diffraction-enhanced imaging contrast mechanisms in breast cancer specimens. Med Phys **29:** 2216-2221 (2002b).

Hasnah MO, Zhong Z, Parham C, Zhang H, Chapman D. Compositional images from the diffraction-enhanced imaging technique. Nucl Instrum and Methods Phys Res A **572:** 953-957 (2007).

Haus AG. Technologic improvements in screen-film mammography. Radiology **174:** 628-637 (1990).

Hawrysz DJ, Sevick-Muraca EM. Developments toward diagnostic breast cancer imaging using near-infrared optical measurements and fluorescent contrast agents. neoplasia **2:** 388-417 (2000).

Hayat SA, Senior R. Safety: the heart of the matter. Eur J Echocardiogr **6:** 235-237 (2005).

Head JF, Wang F, Elliott RL. Breast thermography is a noninvasive prognostic procedure that predicts tumor growth rate in breast cancer patients. Ann N Y Acad Sci **698:** 153-158 (1993).

Head JF, Wang F, Lipari CA, Elliott RL. The important role of infrared imaging in breast cancer. IEEE Eng Med Biol Mag **19:** 52-57 (2000).

Heffelfinger SC, Yassin R, Miller MA, Lower E. Vascularity of proliferative breast disease and carcinoma in situ correlates with histological features. Clin Cancer Res **2:** 1873-1878 (1996).

Heijmink SW, Barentsz JO. Contrast-enhanced versus systematic transrectal ultrasound-guided prostate cancer detection: an overview of techniques and a systematic review. Eur J Radiol **63,** 310-316 (2007).

Helbich TH. Contrast-enhanced magnetic resonance imaging of the breast. Eur J Radiol **34:** 208-219 (2000).

Helvie MA, Chan HP, Adler DD, Boyd PG. Breast thickness in routine mammograms – effect on image quality and radiation-dose. Am J Roentgenol **163:** 1371-1374 (1994).

Hendee WR and Ritenour ER. Medical Imaging Physics. Wiley: New York, New York (2002).

Henderson RP, Webster JG. An impedance camera for spatially specific measurements of the thorax. IEEE Trans Biomed Eng **25:** 250-254 (1978).

Hendrick RE, Bassett L, Botsco MA, *et al*. Patient positioning and compression. In: ACR Committee on Quality Assurance in Mammography, eds. Mammography Quality Control Manual. Reston, VA: American College of Radiology (1999).

Hendrick RE, Cole EB, Pisano ED, Acharyya S, Marques H, Cohen MA, Jong RA, Mawdsley GE, Kanal KM, D'Orsi CJ, Rebner M, Gatsonis C. Accuracy of soft-copy digital mammography versus that of screen-film mammography according to digital manufacturer: ACRIN DMIST retrospective multireader study. Radiology **247:** 38-48 (2008).

Henneman MM, van der Wall EE, Ypenburg C, Bleeker GB, van de Veire NR, Marsan NA, Chen J, Garcia EV, Westenberg JJ, Schalij MJ, Bax JJ. Nuclear imaging in cardiac resynchronization therapy. J Nucl Med **48:** 2001-2010 (2007).

Hennerici M, Baezner H, Daffertshofer M. Ultrasound and arterial wall disease. Cerebrovasc Dis **17 Suppl 1:** 19-33 (2004).

Heron DE, Andrade RS, Beriwal S, Smith RP. PET-CT in radiation oncology: the impact on diagnosis, treatment planning and assessment of treatment response. Am J Clin Oncol **31:** 352-362 (2008).

Herts BR. Imaging for renal tumors. Curr Opin Urol **13:** 181-186 (2003).

Heuts EM, van der Ent FW, von Meyenfeldt MF, Voogd AC. Internal mammary lymph drainage and sentinel node biopsy in breast cancer – a study on 1008 patients. Eur J Surg Oncol **35:** 252-257 (2009).

Heye S, Maleux G, Marchal GJ. Upper extremity venography: CO_2 versus iodinated contrast material. Radiology **241:** 291-297 (2006).

Heywang-Köbrunner SH, Beck R. Contrast enhanced MRI of the breast, 2nd ed Springer Verlag: Berlin (1996).

Heywang-Köbrunner SH, Viehweg P, Heinig A, Küchler C. Contrast-enhanced MRI of the breast: accuracy, value, controversies, solutions. Eur J Radiol **24:** 94-108 (1997).

Hleb EY, Hu Y, Drezek RA, Hafner JH, Lapotko DO. Photothermal bubbles as optical scattering probes for imaging living cells. Nanomed **3:** 797-812 (2008).

Hoelen CG, de Mul FF, Pngers R, Dekker A. Three-dimensional photoacoustic imaging of blood vessels in tissue. Opt Lett **23:** 648-650 (1998).

Hoffman EA. Clough AV, Christensen GE, Lin CL, McLennan G, Reinhardt JM, Simon BA, Sonka M, Tawhai MH, van Beek EJ, Wang G. The comprehensive imaging-based analysis of the lung: a forum for team science. Acad Radiol **11:** 1370-1380 (2004).

Hoh ST, Greenfield DS, Mistleberger A, Liebmann JM, Ishikawa H, Ritch R. Optical coherence tomography and scanning laser polarimetry in normal, ocular hypertensive, and glaucomatous eyes. Am J Ophthalmol **129:** 129-135 (2000).

Honda C, Ohara H. Advantages of magnification in digital phase-contrast mammography using a practical x-ray tube. Eur J Radiol **68:** S69-S72 (2008).

Hönnicke MG, Rigon L, Menk RH, Cusatis C. Quantitative and qualitative studies on high-contrast x-ray radiography with an asymmetrical crystal set-up at Elettra. J Synchrotron Radiat **12:** 701-706 (2005).

Hope TA, Iles SE. Technology review: the use of electrical impedance scanning in the detection of breast cancer. Breast Cancer Res **6:** 69-74 (2004).

Horger M, Bares R. The role of single-photon emission computed tomography/computed tomography in benign and malignant bone disease. Semin Nucl Med **36:** 286-294 (2006).

Hornak JP. "The Basics of MRI: Chapter 1, Introduction." Accessed: 12-1-08. http://www.cis.rit.edu/htbooks/mri/chap-1/chap-1.htm (2007).

Hricak H, Akin O, Sala E, Ascher S, Levine D, Reinhold C. Diagnostic Imaging Gynecology 1st ed. Amirsys: Canada (2007).

Hsiung PL, Phatak DR, Chen Y, Aguirre AD, Fujimoto JG, Connolly JL. Benign and malignant lesions in the human breast depicted with ultrahigh resolution and three-dimensional optical coherence tomography. Radiology **244:** 865-874 (2007).

Huang W, Fisher PR, Dulaimy K, Tudorica LA, O'Hea B, Button TM. Detection of breast malignancy: diagnostic MR protocol for improved specificity. Radiology **232:** 585-591 (2004).

Huang ZF, Kang KJ, Zhu PP, Huang WX, Yuan QX, Wang JY. Strategy of extraction methods and reconstruction algorithms in computed tomography of diffraction-enhanced imaging. Phys Med Biol **52:** 1-12 (2007).

Huwart L, Salameh N, ter Beek L, Vicaut E, Peeters F, Sinkus R, Van Beers BE. MR Elastography of liver fibrosis: preliminary results comparing spin-echo and echo-planar imaging. Eur Radiol **18:** 2535-2341 (2008a).

Huwart L, Sempoux C, Vicaut E, Salameh N, Annet L, Danse E, Peeters F, ter Beek LC, Rahier J, Sinkus R, Horsmans Y, Van Beers BE. Magnetic resonance elastography for the noninvasive staging of liver fibrosis. Gastroenterology **135:** 32-40 (2008b)

Ikeda DM. Breast Imaging: The Requisites. Elselvier: Philadelphia, Pennsylvania (2004).

Ingal VN, Beliaevskaya EA. X-ray plane-wave topography observation of the phase contrast from a non-crystalline object. J Phys D: Appl Phys **28:** 2314-2317 (1995).

Ingal VN, Beliaevskaya EA, Brianskaya AP, Merkurieva RD. Phase mammography -- a new technique for breast investigation. Phys Med Biol **43:** 2555-2567 (1998).

Ito A, Kuga Y, Honda H, Kikkawa H, Horiuchi A, Watanabe Y, Kobayashi T. Magnetite nanoparticle-loaded anti-HER-2 immunoliposomes for combination of antibody therapy with hyperthermia. Cancer Lett **212:** 167-175 (2004).

Ito A, Shinkai M, Honda H, Kobayashi T. Medical application of functionalized magnetic nanoparticles. J Biosci Bioeng **100:** 1-11 (2005).

Itoh A, Ueno E, Tohno E, Kamma H, Takahashi H, Shiina T, Yamakawa M, Matsumura T. Breast disease: clinical application of ultrasound elastography for diagnosis. Radiology **239:** 341-350 (2006).

Jackson PA, Rahman WN, Wong CJ, Ackerly T, Geso M. Potential dependent superiority of gold nanoparticles in comparison to iodinated contrast agents. Eur J Radiol (2009 epub ahead of print).

Jacobs TW, Byrne C, Colditz G, Connolly JL, Schnitt SJ. Radial scars in benign breast-biopsy specimens and the risk of breast cancer. N Engl J Med **340:** 430-436 (1999).

Jagannathan NR, Kumar M, Seenu V, Coshic O, Dwivedi SN, Julka PK, Srivastava A, Rath GK. Evaluation of total choline from in-vivo volume localized proton MR spectroscopy and its response to neoadjuvant chemotherapy in locally advanced breast cancer. Br J Cancer **84:** 1016-1022 (2001).

Jain RK. Delivery of molecular medicine to solid tumors: lessons from in vivo imaging of gene expression and function. J Control Release **74**: 7-25 (2001).

Jain PK, El-Sayed IH, El-Sayed MA. Au nanoparticles target cancer. Nanotoday **2**: 18-29 (2007).

Jakub JW, Pendas S, Reintgen DS. Current status of sentinel lymph node mapping and biopsy: facts and controversies. Oncologist **8:** 59-68 (2003).

Jemal A, Siegel R, Ward E, Muray T, Xu J, Thum M. Cancer Statistics, 2007. CA Cancer J Clin **57:** 43-66 (2007).

Jerosch-Herold M, Kwong RY. Optimal imaging strategies to assess coronary blood flow and risk for patients with coronary artery disease. Curr Opin Cardiol **23:** 599-606 (2008).

Jiang YX, Liu H, Liu JB, Zhu QL, Sun Q, Chang XY. Breast tumor size assessment: comparison of conventional ultrasound and contrast-enhanced ultrasound. Ultrasound Med Biol **33:** 1873-1881 (2007).

Jin H, Kang KA. Application of novel metal nanoparticles as optical/thermal agents in optical mammography and hyperthermic treatment for breast cancer. Adv Exp Med Biol **599:** 45-52 (2007).

Jin T, Yoshioka Y, Fujii F, Komai Y, Seki J, Seiyama A. Gd(3+)-functionalized near-infrared quantum dots for in vivo dual modal (fluorescence/magnetic resonance) imaging. Chem Commun (Camb) **44:** 5764-5766 (2008).

Johns PC, Leclair RJ, Wismayer MP. Medical x-ray imaging with scattered photons. SPIE **TD01:** 355-357 (2002).

Johns PC, Yaffe MJ. X-ray characterization of normal and neoplastic breast tissues. Phys Med Biol **32:** 675-695 (1987).

Johnston RE, Washburn D, Pisano E, Burns C, Thomlinson WC, Chapman D, Arfelli F, Gmur NF, Zhong Z, Sayers D. Mammographic phantom studies with synchrotron radiation. Radiology **200:** 659-663 (1995).

Jong RA, Yaffe MJ, Skarpathiotakis M, Shumak RS, Danjoux NM, Gunesekara A, Plewes DB. Contrast-enhanced digital mammography: initial clinical experience. Radiology **228:** 842-850 (2003).

Junlai L, DanFei S, Debin X, Junpeng G, Xuzhen Z, Jie T. The value of computer-aided detection for breast ultrasonography (B-CAD) in the diagnosis of breast cancer. 12th World Congress of the World Federation for Ultrasound in Medicine and Biology (2009).

Kacl GM, Liu P, Debatin JF, Garzoli E, Caduff RF, Krestin GP. Detection of breast cancer with conventional mammography and contrast enhanced MR imaging. Eur Radiol **8:** 194-200 (1998).

Kalendar WA. Computed Tomography: Fundamentals, System Technology, Image Quality, Applications. Publicus Corporate Publishing: Germany (2005).

Kalpakcioglu BB, Morshed S, Engelke K, Genant HK. Advanced imaging of bone macrostructure and microstructure in bone fragility and fracture repair. J Bone Joint Surg Am **90 Suppl 1:** 68-78 (2008).

Kamath VJ, Giuliano R, Dauway EL, Cantor A, Berman D, Ku NN, Cox CE, Reintgen DS. Characteristics of the sentinel lymph node in breast cancer predict further involvement of higher-echelon nodes in the axilla: a study to evaluate the need for complete axillary lymph node dissection. Arch Surg **136:** 688-692 (2001).

Kao TJ, Saulnier GJ, Xia H, Tamma C, Newell JC, Isaacson D. A compensated radiolucent electrode array for combined EIT and mammography. Physiol Meas **28:** S291-S299 (2007a).

Kao T, Connor D, Dilmanian FA, Faulconer L, Liu T, Parham C, Pisano ED, Zhong Z. Characterization of diffraction enhanced imaging contrast in breast cancer. Phys Med Biol **54:** 3247-3256 (2009).

Kao T, Liu CJ, Yu XH, Young L, Connor D, Dilmanian A, Parham C, Reaney M, Zhong Z. Characterization of diffraction-enhanced imaging contrast in plants. Nucl Instrum Methods Phys Res A **582:** 208-211 (2007b).

Kashyap YS, Yadav PS, Roy T, Sarkar PS, Shukla M, Sinha A. Laboratory-based x-ray phase-contrast imaging technique for material and medical science applications. Appl Radiat Isot **66:** 1083-1090 (2008).

Kattumuri V, Katti K, Bhaskaran S, Boote EJ, Casteel SW, Fent GM, Robertson DJ, Chandrasekhar M, Kannan R, Katti KV. Gum Arabic as a phytochemical construct for the stabilization of gold nanoparticles: in vivo pharmacokinetics and x-ray-contrast-imaging studies. Small **3:** 333-341 (2007).

Katz-Brull R, Lavin PT, Lenkinski RE. Clinical utility of proton magnetic resonance spectroscopy in characterizing breast lesions. J Natl Cancer Inst **94:** 1197-1203 (2002).

Kauppila S, Stenbäck F, Risteli J, Jukkola A, Risteli L. Aberrant type I and type III collagen gene expression in human breast cancer *in vivo*. J Pathol **186:** 262-268 (1998).

Kedar RP, Cosgrove D, McCready VR, Bamber JC, Carter ER. Microbubble contrast agent for color Doppler US: effect on breast masses. Work in progress. Radiology **198:** 679-686 (1996).

Keemers-Gels ME, Groenendijk RP, van den Heuvel JH, Boetes C, Peer PG, Wobbes TH. Pain experienced by women attending breast cancer screening. Breast Cancer Res Treat **60:** 235-240 (2000).

Kelemen LE, Pankratz VS, Sellers TA, Brandt KR, Wang A, Janney C, Fredericksen ZS, Cerhan JR, Vachon CM. Age-specific trends in mammographic density: the Minnesota Breast Cancer Family Study. Am J Epidemiol **167:** 1027-1036 (2008).

Kelly ME, Beavis RC, Fourney DR, Schültke E, Parham C, Juurlink BH, Zhong Z, Chapman LD. Diffraction-enhanced imaging of the rat spine. Can Assoc Radiol J **57:** 204-210 (2006).

Kelly ME, Coupal DJ, Beavis RC, Schultke E, Romanchuk K, Juurlink BH, Zhong Z, Chapman LD. Diffraction-enhanced imaging of a porcine eye. Can J Ophthalmol **42:** 731-733 (2007).

Kelly TA, Kim JA, Patrick R, Grundfest S, Crowe JP. Axillary lymph node metastases in patients with a final diagnosis of ductal carcinoma in situ. Am J Surg **186:** 368-370 (2003).

Kelsey JL, Gammon MD, John EM. Reproductive factors and breast cancer. Epidemiol Rev **15:** 36-47 (1993).

Kelcz F, Santyr GE, Cron GO, Mongin SJ. Application of a quantitative model to differentiate benign from malignant breast lesions detected by dynamic, gadolinium-enhanced MRI. J Magn Reson Imaging **6:** 743-752 (1996).

Kelemen LE, Pankratz VS, Sellers TA, Brandt KR, Wang A, Janney C, Fredericksen ZS, Cerhan JR, Vachon CM. Age-specific trends in mammographic density: the Minnesota Breast Cancer Family Study. Am J Epidemiol **167:** 1027-1036 (2008).

Kennedy DA, Lee T, Seely D. A comparative review of thermography as a breast cancer screening technique. Integr Cancer Ther **8:** 9-16 (2009).

Kerner TE, Paulsen KD, Hartov A, Soho SK, Poplack SP. Electrical impedance spectroscopy of the breast: clinical imaging results in 26 subjects. IEEE Trans Med Imaging **21:** 638-645 (2002).

Keyriläinen J, Fernández M, Fiedler S, Bravin A, Karjalainen-Lindsberg ML, Virkkunen P, Elo EM, Tenhunen M, Suortti P, Thomlinson W. Visualisation of calcifications and thin collagen strands in human breast tumour specimens by the diffraction-enhanced imaging technique: a comparison with conventional mammography and histology. Eur J Radiol **53:** 226-237 (2005).

Keyriläinen J, Fernández M, Suortti P. Refraction contrast in x-ray imaging. Nucl Instrum Methods Phys Res A, **480:** 419-427 (2002).

Keyserlingk JR, Ahlgren PD, Yu E, Belliveau N, Yassa M. Functional infrared imaging of the breast. IEEE Eng Med Biol Mag **19:** 30-41 (2000).

Key TJ, Verkasalo PK, Banks E. Epidemiology of breast cancer. Oncology **2:** 133-140 (2001).

Khelashvili G, Brankov JG, Chapman D, Anastasio MA, Yang Y, Zhong Z, Wernick MN. A physical model of multiple-image radiography. Phys Med Biol **51:** 221-236 (2006).

Kidane G, Speller RD, Royle GJ, Hanby AM. X-ray scatter signatures for normal and neoplastic breast tissue. Phys Med Biol **44:** 1791-1802 (1999).

Kim BS, Isaacson D, Xia H, Kao TJ, Newell JC, Saulnier GJ. A method for analyzing electrical impedance spectroscopy data from breast cancer patients. Physiol Meas **28:** S237-246 (2007a).

Kim C, Song KH, Wang LV. Sentinel lymph node detection ex vivo using ultrasound-modulated optical tomography. J Biomed Opt **13:** 020507 (2008a).

Kim CH. A study of monochromatic x-ray area beam for application in diffraction-enhanced imaging [dissertation]. Raleigh (NC): North Carolina State University; (2007b).

Kim D, Park S, Lee JH, Jeong YY, Jon S. Antibiofouling polymer-coated gold nanoparticles as a contrast agent for in vivo x-ray computed tomography imaging. J Am Chem Soc **129:** 7661-7665 (2007c).

Kim G, Huang SW, Day KC, O'Donnell M, Agayan RR, Day MA, Kopelman R, Ashkenazi S. Indocyanine-green embedded PEBBLEs as a contrast agent for photoacoustic imaging. J Biomed Opt **12:** 044020 (2007d).

Kim JK, Park SH, Lee HM, Lee YH, Sung NK, Chung DS, Kim OD. In vivo 1H-MRS evaluation of malignant and benign breast diseases. Breast **12:** 179-182 (2003).

Kim J, Oh J, Kang HW, Feldman MD, Milner TE. Photothermal response of superparamagnetic iron oxide nanoparticles. Lasers Surg Med **40:** 415-421 (2008b).

Kimme-Smith C. New digital mammography systems may require different x-ray spectra and, therefore, more general normalized glandular dose values. Radiology **213:** 7-10 (1999).

Kim SJ, Moon WK, Cho N, Cha JH, Kim SM, Im JG. Computer-aided detection in digital mammography: comparison of craniocaudal, mediolateral oblique, and mediolateral views. Radiology **241**, 695-701 (2006).

Kinney JH, Lane NE, Haupt DL. In vivo, three dimensional microscopy of trabecular bone. J Bone Miner Res **10:** 264-270 (1995).

Kiss MZ, Sayers DE, Zhong Z. Measurement of image contrast using diffraction-enhanced imaging. Phys med Biol **48:** 325-340 (2003).

Kiss MZ, Sayers DE, Zhong Z, Parham C, Pisano ED. Improved image contrast of calcifications in breast tissue specimens using diffraction-enhanced imaging. Phys Med Biol **49:** 3427-3439 (2004).

Kitchen MJ, Lewis RA, Yagi N, Uesugi K, Paganin D, Hooper SB, Adams G, Jureczek S, Singh J, Christensen CR, Hufton AP, Hall CJ, Cheung KC, Pavlov KM. Phase contrast x-ray imaging of mice and rabbit lungs: a comparative study. Br J Radiol **78:** 1018-1027 (2005).

Klijn JG, Berns PM, Schmitz PI, Foekens JA. The clinical significance of epidermal growth factor receptor (EGF-R) in human breast cancer: a review on 5232 patients. Endocr Rev **13:** 3-17 (1992).

Kolb TM, Lichy J, Newhouse JH. Comparison of the performance of screening mammography, physical examination, and breast ultrasound and evaluation of factors that influence them: an analysis of 27,825 patient evaluation. Radiology **225:** 165-175 (2002).

Komori T, Narabayashi I, Matsumura K, Matsuki M, Akagi H, Ogura Y, Aga F, Adachi I. 2-[Fluorine-18]-fluoro-2-deoxy-D-glucose positron emission tomography/computed tomography versus whole-body diffusion-weighted MRI for detection of malignant lesions: initial experience. Ann Nucl Med **21:** 209-215 (2007).

Konecky SD, Choe R, Corlu A, Lee K, Wiener R, Srinivas SM, Saffer JR, Freifelder R, Karp JS, Hajjioui N, Azar F, Yodh AG. Comparison of diffuse optical tomography of human breast with whole-body and breast-only positron emission tomography. Med Phys **35:** 446-455 (2008).

Konopke R, Bunk A, Kersting S. The role of contrast-enhanced ultrasound for focal liver lesion detection: an overview. Ultrasound Med Biol **33:** 1515-1526 (2007).

Kopans DB. Breast Imaging. 3rd ed. Lippincott Williams & Wilkins: Philadelphia (2007).

Kopans DB. The positive predictive value of mammography. Am J Roentgenol. **158:** 521-526 (1992).

Kotre CJ, Birch IP. Phase contrast enhancement of x-ray mammography: a design study. Phys Med Biol **44:** 2853-2866 (1999).

Kotsianos-Hermle D, Hiltawsky KM, Wirth S, Fischer T, Friese K, Reiser M. Analysis of 107 breast lesions with automated 3D ultrasound and comparison with mammography and manual ultrasound. Eur J Radiol **71:** 109-115 (2009).

Kruger RA, Miller KD, Reynolds HE, Kiser WL Jr, Reinecke DR, Kruger GA. Breast cancer in vivo: contrast enhancement with thermoacoustic CT at 434 MHz – feasibility study. Radiology **216:** 279-283 (2000).

Ku G, Fornage BD, Jin X, Xu M, Hunt KK, Wang LV. Thermoacoustic and photoacoustic tomography of thick biological tissues toward breast imaging. Technol Cancer Res Treat **4:** 559-566 (2005).

Kumar M, Jagannathan NR, Seenu V, Dwivedi SN, Julka PK, Rath GK. Monitoring the therapeutic response of locally advanced breast cancer patients: sequential in vivo proton MR spectroscopy study. J Magn Reson Imaging **24:** 325-332 (2006).

Kung HC, Hoyert DL, Xu J, Murphy SL. Deaths: final data for 2005. Natl Vital Stat Rep **56:** 1-120 (2008).

Kunisada T, Shimao D, Sugiyama H, Takeda K, Ozaki T, Ando M. X-ray dark field imaging of human articular cartilage: possible clinical application to orthopedic surgery. Eur J Radiol **68:** S18-S21 (2008).

Kurz KD, Steinhaus D, Klar V, Cohnen M, Wittsack HJ, Saleh A, Mödder U, Blondin D. Assessment of three different software systems in the evaluation of dynamic MRI of the breast. Eur J Radiol **69:** 300-307 (2009).

Lahmann PH, Hoffman K, Allen N, van Gils CH, Khaw KT, Tehard B, Berrino F, Tjønneland A, Bigaard J, Olsen A, Overvad K, Clavel-Chapelon F, Nagel G, Boeing H, Trichopoulos D, Economou G, Bellos G, Palli D, Tumino R, Panico S, Sacerdote C, Krough V, Peeters PH, Bueno-de-Mesquito HB, Lund E, Ardanoz E, Amiano P, Pera G, Quirós JR, Martinez C, Tormo MJ, Wirfält E, Berglund G, Hallmans G, Key TJ, Reeves G, Bingham S, Norat T, Biessey C, Kaaks R, Riboli E. Body size and breast cancer risk: findings from the European Prospective Investigation into Cancer and Nutrition (EPIC). International Journal of Cancer **111:** 762-771 (2004).

Laib A, Rüegsegger P. Calibration of trabecular bone structure measurements of in vivo three-dimensional peripheral quantitative computed tomography with 28-microm-resolution microcomputed tomography. Bone **24:** 35-39 (1999).

Lai CW, Wang YH, Lai CH, Yang MJ, Chen CY, Chou PT, Chan CS, Chi Y, Chen YC, Hsaio JK. Iridium-complex-functionalized Fe3O4/SiO2 core/shell nanoparticles: a facile three-in-one system in magnetic resonance imaging, luminescence imaging, and photodynamic therapy. Small **4:** 218-224 (2008).

Lakhani SR, Collins N, Sloane JP, Stratton MR. Loss of heterozygosity in lobular carcinoma in situ of the breast. J Clin Pathol: Mol Pathol **48:** M74-M78 (1995a).

Lakhani SR, Chaggar R, Davies S, Jones C, Collins N, Odel C, Stratton MR, O'Hare MJ. Genetic alterations in 'normal' luminal and myoepithelial cells of the breast. J Pathol **189:** 496-503 (1999).

Lakhani SR, Collins N, Stratton MR, Sloane JP. Atypical ductal hyperplasia of the breast: clonal proliferation with loss of heterozygosity on chromosomes 16q and 17p. J Clin Pathol **48:** 611-615 (1995b).

Lakhani SR, O'Hare MJ. The mammary myoepithelial cells: Cinderella or ugly sister? Breast Cancer Res **3:** 1-4 (2001).

Lakhani SR, Slack DN, Hamoudi RA, Collins N, Stratton MR, Sloane JP. Detection of allelic imbalance indicates that a proportion of mammary hyperplasia of usual type are clonal, neoplastic proliferations. Lab Invest **74:** 129-135 (1996).

Lanza GM, Wickline SA. Targeted ultrasonic contrast agents for molecular imaging and therapy. Curr Probl Cardiol **28:** 625-653 (2003).

Lalloo F, Varley J, Moran A, Ellis D, O'dair L, Pharoah P, Antoniou A, Hartley R, Shenton A, Seal S, Bulman B, Howell A, Gareth D, Evans R. BRAC1, BRCA2 and TP53 mutations in very early-onset breast cancer with associated risks to relatives. European Journal of Cancer **42:** 1143-1150 (2006).

Lansford CD, Teknos TN. Evaluation of the thyroid nodule. Cancer Control **13:** 89-98 (2006).

Lao Y, Xing D, Yang S, Xiang L. Noninvasive photoacoustic imaging of the developing vasculature during early tumor growth. Phys Med Biol **53:** 4203-4212 (2008).

Law J. The development of mammography. Phys Med Biol **51:** R155-R167 (2006).

Lawaczeck R, Arkadiev V, Diekmann F, Krumrey M. Monochromatic x-rays in digital mammography. Invest Radiol **40:** 33-39 (2005).

Lawaczeck R, Diekmann F, Diekmann S, Hamm B, Bick U, Press WR, Schirmer H, Schön K, Weinmann HJ. New contrast media designed for x-ray energy subtraction imaging in digital mammography. Invest Radiol **38:** 602-608 (2003).

Ledneva E, Karie S, Launay-Vacher V, Janus N, Deray G. Renal safety of gadolinium-based contrast media in patients with chronic renal insufficiency. Radiology **250:** 618-628 (2009).

Lee AG, Brazis PW, Garrity JA, White M. Imaging for neuro-ophthalmic and orbital disease. Am J Ophthalmol **138:** 852-862 (2004).

Lee NA, Rusinek H, Weinreb J, Chandra R, Toth H, Singer C, Newstead G. Fatty and fibroglandular tissue volumes in the breasts of women 20-83 years old: comparison of x-ray mammography and computer-assisted MR imaging. AJR Am J Roentgenol **168:** 501-506 (1997).

Lee SG, Orel SG, Woo IJ, Cruz-Jove E, Putt ME, Solin LJ, Czerniecki BJ, Schnall MD. MR imaging screening of the contralateral breast in patients with newly diagnosed breast cancer: preliminary results. Radiology **226:** 773-778 (2003).

Leff DR, Warren OJ, Enfield LC, Gibson A, Athanasiou T, Patten DK, Hebden J, Yang GZ, Darzi A. Diffuse optical imaging of the healthy and diseased breast: a systematic review. Breast cancer Res Treat **108:** 9-22 (2008).

Lehman CD, Blume JD, Thickman D, Bluemke DA, Pisano E, Kuhl C, Julian TB, Hylton N, Weatherall P, O'loughlin M, Schnitt SJ, Gatsonis C, Schnall MD. Added cancer yield of MRI in screening the contralateral breast of women recently

diagnosed with breast cancer: results from the International Breast Magnetic Resonance Consortium (IBMC) trial. J Surg Oncol **92:** 9-15 (2005a).

Lehman CD, Blume JD, Weatherall P, Thickman D, Hylton N, Warner E, Pisano E, Schnitt SJ, Gatsonis C, Schnall M, DeAngelis GA, Stomper P, Rosen EL, O'Loughlin M, Harms S, Bluemke DA; International Breast MRI Consortium Working Group. Screening women at high risk for breast cancer with mammography and magnetic resonance imaging. Cancer **103:** 1898-1905 (2005b).

Lehman CD, Gatsonis C, Kuhl CK, Hendrick RE, Pisano ED, Hanna L, Peacock S, Smazal SF, Maki DD, Julian TB, DePeri ER, Bluemke DA, Schnall MD; ACRIN Trial 6667 Investigators Group. MRI evaluation of the contralateral breast in women with recently diagnosed breast cancer. N Engl J Med **356:** 1295-1303 (2007).

Lehman CD, Peacock S, DeMartini WB, Chen X. A new automated software system to evaluate breast MR examinations: improved specificity without decreased sensitivity. AJR Am J Roentgenol **187:** 51-56 (2006).

Lemacks MR, Kappadath SC, Shaw CC, Liu X, Whitman GJ. A dual-energy subtraction technique for microcalcification imaging in digital mammography – a signal-to-noise analysis. Med Phys **29:** 1739-1751 (2002).

Lencioni R, Della Pina C, Crocetti L, Bozzi E, Cioni D. Clinical management of focal liver lesions: the key role of real-time contrast-enhanced US Eur Radiol **17 Suppl 6:** F73-F79 (2007).

Lerner BH. To see today with the eyes of tomorrow: a history of screening mammography. Background paper for the Institute of Medicine report: Mammography and Beyond: Developing technologies for the early detection of breast cancer (March 2001).

Levine EA, Freimanis RI, Perrier ND, Morton K, Lesko NM, Bergman S, Geisinger KR, Williams RC, Sharpe C, Zavarzin V, Weinberg IN, Stepanov PY, Beylin D, Lauckner K, Doss M, Lovelace J, Adler LP. Positron emission mammography: initial clinical results. Ann Surg Oncol **10:** 86-91 (2003).

Lewin JM, Isaacs PK, Vance V, Larke FJ. Dual-energy contrast-enhanced digital subtraction mammography: feasibility. Radiology **299:** 261-268 (2003).

Lewis RA, Hall CJ, Hufton AP, Evans S, Menk RH, Arfelli F, Rigon L, Tromba G, Dance DR, Ellis IO, Evans A, Jacobs E, Pinder SE, Rogers KD. X-ray refraction effects: applications to the imaging of biological tissues. Br J Radiol **76:** 301-308 (2003).

Lewis RA. Medical phase contrast x-ray imaging: current status and future prospects. Phys Med Biol **49:** 3573-3583 (2004).

Liberman L, Morris EA, Kim CM, Kaplan JB, Abramson AF, Menell JH, Van Zee KJ, Dershaw DD. MR imaging findings in the contralateral breast of women with recently diagnosed breast cancer. AJR Am J Roentgenol **180:** 333-341 (2003).

Licha K, Riefke B, Ntziachristos V, Becker A, Chance B, Semmler W. Hydrophilic cyanine dyes as contrast agents for near-infrared tumor imaging: synthesis, photophysical properties and spectroscopic in vivo characterization. Photochem Photobiol **72:** 392-398 (2000).

Li J, Williams JM, Zhong Z, Kuettner KE, Aurich M, Mollenhauer J, Muehleman C. Reliability of diffraction-enhanced imaging for assessment of cartilage lesions, ex vivo. Osteoarthritis Cartilage **13:** 187-197 (2005).

Lim YT, Cho MY, Choi BS, Lee JM, Chung BH. Paramagnetic gold nanostructures for dual modal bioimaging and phototherapy of cancer cells. Chem Commun (Camb) **40:** 4930-4932 (2008).

Lindfors KK, Boone JM, Nelson TR, Yang K, Kwan AL, Miller DF. Dedicated breast CT: initial clinical experience. Radiology **246:** 725-733 (2008).

Liu C, Yan X, Zhang X, Yang W, Peng W, Shi D, Zhu P, Huang W, Yuan Q. Evaluation of x-ray diffraction-enhanced imaging in the diagnosis of breast cancer. Phys Med Biol **52**: 419-427 (2007a).

Liu C, Zhang Y, Zhang X, Yang W, Peng W, Shi D, Zhu P, Tian Y, Huang W. X-ray diffraction-enhanced imaging of uterine leiomyomas. Med Sci Monit **11:** MT33-38 (2005).

Liu H, Jiang YX, Liu JB, Zhu QL, Sun Q. Evaluation of breast lesions with contrast-enhanced ultrasound using the microvascular imaging technique: initial observations. Breast **17:** 532-539 (2008).

Liu J, Li J, Rosol TJ, Pan X, Voorhees JL. Biodegradable nanoparticles for targeted ultrasound imaging of breast cancer cells in vitro. Phys Med Biol **52:** 4739-4747 (2007b).

Liu R, Dong X, Fu F, You F, Shi X, Ji Z, Wang K. Multi-frequency parameter mapping of electrical impedance scanning using two kinds of circuit model. Physiol Meas **28:** S85-S100 (2007c).

Loevner LA, Kaplan SL, Cunnane ME, Moonis G. Cross-sectional imaging of the thyroid gland. Neuroimaging Clin N Am **18:** 445-461 (2008).

Lo GG, Ai V, Chan JK, Li KW, Cheung PS, Wong TT, Ma M, Lee R, Chien D. Diffusion-weighted magnetic resonance imaging of breast lesions: first experiences at 3 T. J Comput Assist Tomogr **33:** 63-69 (2009).

Longnecker M. Alcoholic beverage consumption in relation to risk of breast cancer: meta-analysis and review. Cancer Causes Control **5:** 73-82 (1994).

Lowery AR, Gobin AM, Day ES, Halas NJ, West JL. Immunonanoshells for targeted photothermal ablation of tumor cells. In J Nanomedicine **1:** 149-154 (2006).

Luciani A, Olivier JC, Clement O, Siauve N, Brillet PY, Bessoud B, Gazeau F, Uchegbu IF, Kahn E, Frija G, Cuenod CA. Glucose-receptor MR imaging of tumors: study in mice with PEGylated paramagnetic niosomes. Radiology **231:** 135-142 (2004).

Lustberg H. "X-ray tube having spherical anode." Patent 6522721 (2003).

Macura KJ, Ouwerkerk R, Jacobs MA, Bluemke DA. Patterns of enhancement on breast MR imaging: interpretation and imaging pitfalls. Radiographics **26:** 1719-1734 (2006).

Maeo S, Krämer M, Taniguchi K. Development of a microfocus x-ray tube with multiple excitation sources. Rev Sci Instrum **80:** 033108 (2009).

Magnusson C. Baron JA, Correia N, Bergström R, Adami HO, Persson I. Breast-cancer risk following long-term oestrogen- and oestrogen-progestin-replacement therapy. Int J cancer **81:** 339-344 (1999).

Ma H, Bernstein L, Pike MC, Ursin G. Reproductive factors and breast cancer risk according to joint estrogen and progesterone receptor status: a meta-analysis of epidemiological studies. Breast Cancer Research **8:** R43 (2006).

Main ML, Goldman JH, Grayburn PA. Thinking outside the "box" – the ultrasound contrast controversy. J Am Coll Cardiol **50:** 2434-2437 (2007).

Majidi K, Brankov JG, Wernick MN. Tomosynthesis implementation of multiple image radiography. IEEE Xplore (2007).

Majumdar S, Issever AS, Burghardt A, Lotz J, Arfelli F, Rigon L, Heitner G, Menk RH. Diffraction-enhanced imaging of articular cartilage and comparison with micro-computed tomography of the underlying bone structure. Eur Radiol **14:** 1440-1448 (2004).

Majumdar S. Magnetic resonance imaging and spectroscopy of the intervertebral disc. NMR Biomed **19:** 894-903 (2006).

Majumdar S. A review of magnetic resonance (MR) imaging of trabecular bone micro-architecture: contribution to the prediction of biomechanical properties and fracture prevalence. Technol Health Care **6:** 321-327 (1998).

Maksimenko A, Yuasa T, Ando M, Hashimoto E. Refraction-based tomosynthesis: proof of the concept. Appl Phys Lett **91:** 234108 (2007).

Malich A, Boehm T, Facius M, Freesmeyer MG, Fleck M, Anderson R, Kaiser WA. Differentiation of mammographically suspicious lesions: evaluation of breast ultrasound, MRI mammography and electrical impedance scanning as adjunctive technologies in breast cancer detection. Clin Radiol **56:** 278-283 (2001).

Malich A, Facius M, Anderson R, Böttcher J, Sauner D, Hansch A, Marx C, Petrovitch A, Pfleiderer S, Kaiser W. Influence of size and depth on accuracy of electrical impedance scanning. Eur Radiol **13:** 2441-2446 (2003a).

Malich A, Fuchsjäger M. Electrical impedance scanning in classifying suspicious breast lesions. Invest Radiol **38:** 302-304 (2003b).

Manduca A, Oliphant TE, Dresner MA, Mahowald JL, Kruse SA, Amromin E, Felmlee JP, Greenleaf JF, Ehman RL. Magnetic resonance elastography: non-invasive mapping of tissue elasticity. Med Image Anal **5:** 237-254 (2001).

Mannan KA, Schültke E, Menk RH, Siu K, Pavlov K, Kelly M, McLoughlin G, Beveridge T, Tromba G, Juurlink BH, Chapman D, Rigon L, Griebel RW. Synchrotron supported DEI/KES of a brain tumor in an animal model: the search for a microimaging modality. Nucl Instrum Methods Phys Res A **548:** 106-110 (2005).

Manohar S, Kharine A, van Hespen JC, Steenbergen W, van Leeuwen TG. Photoacoustic mammography laboratory prototype: imaging of breast tissue phantoms. J Biomed Opt **9:** 1172-1181 (2004).

Manohar S, Kharine A, van Hespen JC, Steenbergen W, van Leeuwen TG. The Twente Photoacoustic Mammoscope: system overview and performance. Phys Med Biol **50:** 2543-2557 (2005).

Manohar S, Vaartjes SE, van Hespen JGC, Klaase JM, van den Engh FM, Thé AKH, Steenbergen W, van Leeuwen TG. Region-of-interest breast images with the Twente Photoacoustic Mammoscope (PAM). Photons Plus Ultrasound: Imaging and Sensing 2007: The Eighth Conference on Biomedical Thermoacoustics, Optoacoustics, and Acousto-Optics (2007).

Maravilla KR, Murry RC Jr, Diehl J, Suss R, Allen L, Chang K, Crawford J, McCoy R. Digital tomosynthesis: technique modifications and clinical applications for neurovascular anatomy. Radiology **152:** 719–724 (1984).

Margaritondo G. Introduction to Synchrotron Radiation. New York: Oxford University Press (1988).

Margaritondo G, Meuli R. Synchrotron radiation in radiology. Novel x-ray sources. Eur Radiol **13:** 2533-2541 (2003).

Markle L, Roux S, Sayre JW. Reduction of discomfort during mammography utilizing a radiolucent cushioning pad. Breast J **10:** 345-349 (2004).

Marini C, Iacconi C, Giannelli M, Cilotti A, Moretti M, Bartolozzi C. Quantitative diffusion-weighted MR in the differential diagnosis of breast lesion. Eur Radiol **17:** 246-255 (2007).

Markle L, Roux S, Sayre JW. Reduction of discomfort during mammography utilizing a radiolucent cushioning pad. Breast J **10:** 345-349 (2004).

Martín G, Martín R, Brieva MJ, Santamaría L. Electrical impedance scanning in breast cancer imaging: correlation with mammographic and Histologic diagnosis. Eur Radiol **12:** 1471-1478 (2002).

Mashal A, Booske JH, Hagness SC. Toward contrast-enhanced microwave-induced thermoacoustic imaging of breast cancer: an experimental study of the effects of Microbubbles on simple thermoacoustic targets. Phys Med Biol **54:** 641-650 (2009).

Masters BR. Noninvasive Diagnostic Techniques in Ophthalmology. Springer Verlag: New York (1990).

Matsuo S, Katafuchi T, Tohyama K, Morishita J, Yamada K, Fujita H. Evaluation of edge effect due to phase contrast imaging for mammography. Med Phys **32:** 2690-2697 (2005).

Mazziotta JC, Gilman S. Clinical Brain Imaging: Principles and Applications. F.A. Davis Company: Philadelphia (1992).

McKinley RL, Tornai MP, Samei E, Bradshaw ML. Development of an optimal x-ray beam for dual-mode emission and transmission mammotomography. Nucl Instrum Methods Phys Res A **527:** 102-209 (2004a).

McKinley RL, Tornai MP, Samei E, Bradshaw ML. Simulation study of a quasi-monochromatic beam for x-ray computed tomography. Med Phys **31:** 800-813 (2004b).

McKinley RL, Tornai MP. Preliminary investigation of dose for a dedicated mammotomography system. Proc SPIE: Physics of Medical Imaging **6142:** 60-70 (2006).

McMahon SJ, Mendenhall MH, Jain S, Currell F. Radiotherapy in the presence of contrast agents: a general figure of merit and its application to gold nanoparticles. Phys Med Biol **53:** 5635-5651 (2008).

Medarova Z, Pham W, Kim Y, Dai G, Moore A. In vivo imaging of tumor response to therapy using a dual-modality imaging strategy. Int J cancer **118:** 2796-2802 (2006).

Mehta C, Gao P, Bhatt DL, Harrington RA, Skerjanec S, Ware JH. Optimizing trial design: sequential, adaptive, and enrichment strategies. Circulation **119:** 597-605 (2009).

Meisamy S, Bolan PJ, Baker EH, Bliss RL, Gulbahce E, Everson LI, Nelson MT, Emory TH, Tuttle TM, Yee D, Garwood M. Neoadjuvant chemotherapy of locally advanced breast cancer: predicting response with in vivo (1)H MR Spectroscopy: a pilot study at 4T. Radiology **233:** 424-431 (2004).

Meisamy S, Bolan PJ, Baker EH, Pollema MG, Le CT, Kelcz F, Lechner MC, Luikens BA, Carlson RA, Brandt KR, Amrami KK, Nelson MT, Everson LI, Emory TH, Tuttle TM, Yee D, Garwood M. Adding in vivo quantitative ^{1}H MR spectroscopy to improve diagnostic accuracy of breast MR imaging: preliminary results of observer performance study at 4.0 T. Radiology **236:** 465-475 (2005).

Merwa R, Scharfetter H. Magnetic induction tomography: evaluation of the point spread function and analysis of resolution and image distortion. Physiol Meas **28:** S313-324 (2007).

Meuli R, Hwu Y, Je JH, Margaritondo G. Synchrotron radiation in radiology: radiology techniques based on synchrotron sources. Eur Radiol **14:**1550-1560 (2004).

Meyer JE, Eberlein TJ, Stomper PC, Sonnenfeld MR. Biopsy of occult breast lesions. Analysis of 1261 abnormalities. J Am Med Ass **263:** 2341-2343 (1990).

Michna ML. Novel imaging techniques using the transport of intensity equation [dissertation]. Melbourne: University of Melbourne; 2005.

Mihich E, Housman D. Cancer Genes: Functional Aspects. Plenum Press: New York (1996).

Milanese TR, Hartmann LC, Sellers TA, Frost MH, Vierkant RA, Maloney SD, Pankratz VS, Degnim AC, Vachon CM, Reynolds CA, Thompson RA, Melton III LJ,

Goode EL, Visscher DW. Age-related lobular involution and risk of breast cancer. J Nat lancer Inst **98:** 1600-1607 (2006).

Miller D, Livingstone V, Herbison P. Interventions for relieving the pain and discomfort of screening mammography. Cochrane Database Syst Rev **1:** CD002942 (2008).

Milstein M, Mooser CK, Hu H, Fejzo M, Slamon D, Goodglick L, Dry S, Colicelli J. RIN1 is a breast tumor suppressor gene. Cancer Res **67:** 11510-11516 (2007).

Missmer SA, Eliassen AH, Barbieri RL, Hankinson SE. Endogenous estrogen, androgen, and progesterone concentrations and breast cancer risk among postmenopausal women. J Natl Cancer Inst **96:** 1856-1865 (2004).

Mittendorf EA, Peoples GE, Singletary SE. Breast cancer vaccines: promise for the future or pipe dream? Cancer **110:** 1677-1686 (2007).

Mitterberger M, Pelzer A, Colleselli D, Bartsch G, Strasser H, Pallwein L, Aigner F, Gradl J, Frauscher F. Contrast-enhanced ultrasound for diagnosis of prostate cancer and kidney lesions. Eur J Radiol **64:** 231-238 (2007).

Mollenhauer J, Aurich ME, Zhong Z, Muehleman C, Cole AA, Hasnah M, Oltulu O, Kuettner KE, Margulis A, Chapman LD. Diffraction-enhanced x-ray imaging of articular cartilage. Osteoarthr Cartilage **10:** 163-171 (2002).

Möller I, Bong D, Naredo E, Filippucci E, Carrasco I, Moragues C, Iagnocco A. Ultrasound in the study and monitoring of osteoarthritis. Osteoarthritis Cartilage **16 Suppl 3:** S4-7 (2008).

Momose A, Fukuda J. Phase-contrast radiographs of nonstained rat cerebellar specimen. Med Phys **22:** 375-379 (1995).

Momose A, Takeda T, Itai Y, Hirano K. Phase-contrast x-ray computed tomography for observing biological soft tissues. Nat Med **2:** 473-475 (1996).

Montgomery P, Conlon M. Review: preprocedure information, breast cushions, and patient-controlled breast compression reduce mammography pain. Evid Based Nurs **11:** 111 (2008).

Morawski AM, Lanza GA, Wickline SA. Targeted contrast agents for magnetic resonance imaging and ultrasound. Curr Opin Biotechnol **16:** 89-92 (2005).

Morrow M. Should routine breast cancer staging include MRI? Nat Clin Pract Oncol **6:** 72-73 (2009).

Morton MJ, Whaley DH, Brandt KR, Amrami KK. Screening mammograms: interpretation with computer-aided detection—prospective evaluation. Radiology **239:** 375-383 (2006).

Mountford CE, Doran S, Lean CL, Russell P. Proton MRS can determine the pathology of human cancers with a high level of accuracy. Chem Rev **104:** 3677-3704 (2004).

Mountford C, Ramadan S, Stanwell P, Malycha P. Proton MRS of the breast in the clinical setting. NMR Biomed **22:** 54-64 (2009).

Muehleman C, Chapman LD, Kuettner KE, Rieff J, Mollenhauer JA, Massuda K, Zhong Z. Radiography of rabbit articular cartilage with diffraction-enhanced imaging. Anat Rec **272:** 392-397 (2003).

Muehleman C, Sumner DR, Zhong Z. Refraction effects of diffraction-enhanced radiographic imaging: a new look at bone. J Am Podiatr Med Assoc **94:** 453-455 (2004a).

Muehleman C, Li J, Wernick M, Brankov J, Kuettner K, Zhong Z. Yes, you can see cartilage with x-rays; diffraction-enhanced x-ray imaging for soft and hard tissues. J Musculoskelet Neuronal Interact **4:** 369-370 (2004b).

Muehleman C, Li J, Zhong Z, Brankov JG, Wernick MN. Multiple-image radiography for human soft tissue. J Anat **208:** 115-124 (2006a).

Muehleman C, Li J, Zhong Z. Preliminary study on diffraction-enhanced radiographic imaging for a canine model of cartilage damage. Osteoarthritis Cartilage **14:** 882-888 (2006b).

Muehleman C, Majumdar S, Issever AS, Arfelli F, Menk RH, Rigon L, Heitner G, Reime B, Metge J, Wagner A, Kuettner KE, Mollenhauer J. X-ray detection of structural orientation in human articular cartilage. Osteoarthritis Cartilage **12:** 97-105 (2004c).

Mulder WJ, Koole R, Brandwijk RJ, Storm G, Chin PT, Strijkers GJ, de Mello Donegá C, Nicolay K, Griffioen AW. Quantum dots with a paramagnetic coating as a bimodal molecular imaging probe. Nano Lett **6:** 1-6 (2006).

Murthy K, Aznar M, Thompson CJ, Loutfi A, Lisbona R, Gagnon JH. Results of preliminary clinical trials of the positron emission mammography system PEM-I: a dedicated breast imaging system producing glucose metabolic images using FDG. J Nucl Med **41:**1851-8 (2000).

Nadel HR. Bone scan update. Semin Nucl Med **37:** 332-339 (2007).

Nadler Y, Camp RL, Giltnane JM, Moeder C, Rimm DL, Kluger HM, Kluger Y. Expression patterns and prognostic value of Bag-1 and BCL-2 in breast cancer. Breast Cancer Res **10:** R35 (2008).

Nahleh Z, Girnius S. Male Breast Cancer: a gender issue. Nature Clinical Practice Oncology **3:** 428-437 (2006).

Nahta R, Esteva FJ. Herceptin: mechanisms of action and resistance. Cancer Lett **232:** 123-138 (2006).

Nakahara H, Namba K, Wakamatsu H, Watanabe R, Furusawa H, Shirouzu M, Matsu T, Tanaka C, Akiyama F, Ifuku H, Nakahara M, Tamura S. Extension of breast cancer: comparison of CT and MRI. Radiat Med **20:** 17-23 (2002).

Nanni C, Rubello D, Fanti S, Farsad M, Ambrosini V, Rampin L, Banti E, Carpi A, Muzzio P, Franchi R. Role of 18F-FDG-PET and PET/CT imaging in thyroid cancer. Biomed Pharacother **60:** 409-413 (2006).

Narod SA, Foulkes WD. BRCA1 and BRCA2: 1994 and beyond. Nat Rev Cancer **4:** 665-676 (2004).

National Institutes of Health Consensus Development Panel. National Institutes of Health consensus development conference statement: Breast cancer screening for women ages 40-49, January 21-23, 1997. J Natl Cancer Inst **89:** 1015-1026 (1997).

Nguyen-Kac E, Capron D. Noninvasive diagnosis of liver fibrosis by ultrasonic transient elastography (Fibroscan). Eur J Gastroenterol Hepatol **18:** 1321-1325 (2006).

Niehans GA, Singleton TP, Dykoski D, Kiang DT. Stability of HER-2/neu expression over time and at multiple metastatic sites. J Natl Cancer Inst **85:** 1230-1235 (1993).

Nie L, Xing D, Zhou Q, Yang D, Guo H. Microwave-induced thermoacoustic scanning CT for high-contrast noninvasive breast cancer imaging. Med Phys **35:** 4026-4032 (2008).

Niklason LT, Christian BT, Niklason LE, Kopans DB, Castleberry DE, Opsahl-Ong BH, Landberg CE, Slanetz PJ, Giardino AA, Moore R, Albagli D, DeJule MC, Fitzgerald PF, Fobare DF, Giambattista BW, Kwasnick RF, Liu J, Lubowski SJ, Possin GE, Richotte JF, Wei CY, Wirth RF. Digital tomosynthesis in breast imaging. Radiol **205:** 399-406 (1997).

Ntziachristos V, Chance B. Probing physiology and molecular function using optical imaging: applications to breast cancer. Breast Cancer Res **3:** 41-46 (2001).

Ntziachristos V, Yodh AG, Schnall M, Chance B. Concurrent MRI and diffuse optical tomography of breast after indocyanine green enhancement. Proc Natl Acad Sci USA **97:** 2767-2772 (2000).

"Nuclear Medicine." National Atomic Museum (2003). http://www.atomicmuseum.com/tour/nuclearmedicine.cfm. Accessed: 12-8-2008.

Nunez PL, Srinivasan R. Electric Fields of the Brain: The Neurophysics of EEG. Oxford University Press: Oxford (2006).

Oh TI, Lee J, Seo JK, Kim SW, Woo EJ. Feasibility of breast cancer lesion detection using a multi-frequency trans-admittance scanner (TAS) with 10Hz to 500kHz bandwidth. Physiol Meas **28:** S71-S84 (2007).

Okasha M, McCarron P, Gunnell D, Smith GD. Exposures in children, adolescence and early adulthood and breast cancer risk: a systematic review of the literature. Breast Cancer Res Treat **78:** 223-276 (2003).

Olivo A, Speller R. A coded-aperture technique allowing x-ray phase contrast imaging with laboratory sources. Appl Phys Lett **91:** 074106 (2007a).

Olivo A, Speller R. Experimental validation of a simple model capable of predicting the phase contrast imaging capabilities of any imaging system. Phys Med Biol **51:** 3015-3030 (2006).

Olivo A, Speller R. Image formation principles in coded-aperture based x-ray phase contrast imaging. Phys Med Biol **53:** 6461-6474 (2008a).

Olivo A, Speller R. Modelling of a novel x-ray phase contrast imaging technique based on coded apertures. Phys Med Biol **52:** 6555-6573 (2007b).

Olivo A, Speller R. Phase contrast imaging. International Patent WO/2008/029107 (2008b).

Olivo A, Speller R. Polychromatic phase contrast imaging as a basic step towards a widespread application of the technique. Nucl Instrum Methods A **580:** 1079-1082 (2007c).

Olivo A, Rigon L, Vinnicombe SJ, Cheung KC, Ibison M, Speller RD. Phase contrast imaging of breast tumours with synchrotron radiation. Appl Radiat Isot **67:** 1033-1041 (2009).

Oltulu O, Zhong Z, Hasnah M, Wernick MN, Chapman D. Extraction of extinction, refraction and absorption properties in diffraction-enhanced imaging. J Phy D: Appl Phys **36:** 2152-2156 (2003).

Ostbye T, Greenberg GN, Taylor DH Jr, Lee AM. Screening mammography and Pap tests among older American women 1996-2000: results from the Health and Retirement Study (HRS) and Asset and Health Dynamics Among the Oldest Old (AHEAD). Ann Fam Med **1:** 209-217 (2003).

Pagot E, Cloetens P, Fiedler S, Bravin A, Coan P, Baruchel J, Härtwig J, Thomlinson W. A method to extract quantitative information in analyzer-based x-ray phase contrast imaging. Appl Phys Lett **82:** 3421-3423 (2003).

Pagot E, Fiedler S, Cloetens P, Bravin A, Coan P, Fezzaa K, Baruchel J, Hartwig J, von Smitten K, Leidenius M, Karjalainen-Lindsberg ML, Keyriläinen J. Quantitative comparison between two phase contrast techniques: diffraction-enhanced imaging and phase propagation imaging. Phys Med Biol **50:** 709-724 (2005).

Paik S, Shak S, Tang G, Kim C, Baker J, Cronin M, Baehner FL, Walker MG, Watson D, Park T, Hiller W, Fisher ER, Wickerham DL, Bryant J, Wolmark N. A multigene assay to predict recurrence of tamoxifen-treated, node-negative breast cancer. N Engl J Med. **351**: 2817-2826 (2004).

Palmedo H, Bender H, Grünwald F, Mallmann P, Zamora P, Krebs D, Biersack HJ. Comparison of fluorine-18 fluorodeoxyglucose positron emission tomography and technetium-99m methoxyisobutylisonitrile scintimammography in the detection of breast tumors. Eur J Nucl Med **24:** 1138-1145 (1997).

Palomares MR, Machia JR, Lehman CD, Daling JR, McTiernan A. Mammographic density correlation with Gail Model breast cancer risk estimates and component risk factors. Cancer Epidemiol Biomarkers Prev **15:** 1324-1330 (2006).

Parham CA. System parameters and performance specifications for the application of diffraction-enhanced imaging and multiple image radiography to breast imaging [dissertation]. Chapel Hill (NC): University of North Carolina at Chapel Hill; 2006.

Parham C, Zhong Z, Connor DM, Chapman LD, Pisano ED. Design and implementation of a compact low-dose diffraction-enhanced medical imaging system. Acad Radiol **16:** 911-917 (2009).

Parisky YR, Sardi A, Hamm R, Hughes K, Esserman L, Rust S, Callahan K. Efficacy of computerized infrared imaging analysis to evaluate mammographically suspicious lesions. AJR Am J Roentgenol **180:** 263-269 (2003).

Park JM, Franken EA Jr, Garg M, Fajardo LL, Niklason LT. Breast tomosynthesis: present considerations and future applications. Radiographics **27:** S231-240 (2007a).

Park MJ, Cha ES, Kang BJ, Ihn YK, Baik JH. The role of diffusion-weighted imaging and the apparent diffusion coefficient (ADC) values for breast tumors. Korean J Radiol **8:** 390-396 (2007b).

Park YS, Kasuya A, Dmytruk A, yasuto N, Takedo M, Ohuchi N, Sato Y, Tohji K, Uo M, Watari F. Concentrated colloids of silica-encapsulated gold nanoparticles: colloidal stability, cytotoxicity, and x-ray absorption. J Nanosci Nanotechnol **7:** 2690-2695 (2007c).

Park YS, Liz-Marzán LM, Kasuya A, Kobayashi Y, Nagao D, Konno M, Mamykin S, Dmytruk A, Takeda M, Ohuchi N. X-ray absorption of gold nanoparticles with thin silica shell. J Nanosci Nanotechnol **6:** 3503-3506 (2006).

Parkin DM, Bray FI, Devesa SS. Cancer burden in the year 2000. The global picture. Eur J Cancer **37:** S4-S66 (2001).

Partridge SC. Future applications and innovations of clinical breast magnetic resonance imaging. Top Magn Reson Imaging **19:** 171-176 (2008).

Pasqualini JR. Progestins and breast cancer. Gynecol Endocronol **23:** 32-41 (2007).

Patani N, Mokbel K. The utility of MRI for the screening and staging of breast cancer. Int J Clin Pract **62:** 450-453 (2008).

Patel V, Issever AS, Burghardt A, Laib A, Ries M, Majumdar S. MicroCT evaluation of normal and osteoarthritic bone structure in human knee specimens. J Orthop Res **21:** 6-13 (2003).

Patil CA, Bosschaart N, Keller MD, van Leeuwen TG, Mahadevan-Jansen A. Combined Raman spectroscopy and optical coherence tomography for tissue characterization. Opt Lett **33:** 1135-1137 (2008).

Pediconi F, Catalano C, Roselli A, Padula S, Altomari F, Moriconi E, Pronio AM, Kirchin MA, Passariello R. Contrast-enhanced MR mammography for evaluation of the contralateral breast in patients with diagnosed unilateral breast cancer or high-risk lesions. Radiology **243:** 670-680 (2007).

Peele AG, De Carlo F, McMahon PJ, Dhal BB, Nugent KA. X-ray phase contrast tomography with a bending magnet source. Rev Sci Instrum **76:** 083707 (2005).

Penn A, Thompson S, Brem R, Lehman C, Weatherall P, Schnall M, Newstead G, Conant E, Ascher S, Morris E, Pisano E. Morphologic blooming in breast MRI as a characterization of margin for discriminating benign from malignant lesions. Acad Radiol **13:** 1344-1354 (2006).

Petretta M, Costanzo P, Acampa W, Imbriaco M, Ferro A, Filardi PP, Cuocolo A. Noninvasive assessment of coronary anatomy and myocardial perfusion: going toward an integrated imaging approach. J Cardiovascu Med (Hagerstown) **9:** 977-986 (2008).

Pfeiffer F, Bech M, Bunk O, Kraft P, Eikenberry EF, Brönnimann Ch, Grünzweig C, David C. Hard-x-ray dark-field imaging using a grating interferometer. Nat Mater **7:** 134-137 (2008).

Pfeiffer F, Kottler C, Bunk O, David C. Hard x-ray phase tomography with low-brilliance sources. Phys Rev Lett **98:** 1081051-1081054 (2007).

Pfeiffer F, Weitkamp T, Bunk O, David C. Phase retrieval and differential phase-contrast imaging with low-brilliance x-ray sources. Nat Phys **2:** 258-261 (2006).

Pham W, Medarova Z, Moore A. Synthesis and application of a water-soluble near-infrared dye for cancer detection using optical imaging. Bioconjug Chem **16:** 735-740 (2005).

Pharoah PD, Day NE, Duffy S, Easton DF, Ponder BA. Family history and the risk of breast cancer: a systematic review and meta-analysis. Int J Cancer **71:** 800-809 (1997).

"Phase Contrast Technology" www.konicaminolta.com/healthcare/technology/phasecontrast. Accessed 10/8/08.

Phillips KA. Current perspectives on BRCA1- and BRCA2-associated breast cancers. Intern Med J **31:** 349-356 (2001).

Piestrup MA, Wu X, Kaplan VV, Uglov SR. A design of mammography units using a quasimonochromatic x-ray source. Rev Sci Instrum **72:** 2159 (2001).

Pisano ED, Johnson RE, Chapman D, Geradts J, Iacocca MV, Livasy CA, Washburn DB, Sayers DE, Zhong Z, Kiss MZ, Thomlinson WC. Human Breast Cancer Specimens: Diffraction-enhanced Imaging with Histologic Correlation-Improved Conspicuity of Lesion Detail Compared to Digital Radiography. Radiology **214:** 895-901 (2000).

Pisano ED, Yaffe MJ and Kuzmiak CM. Digital Mammography. Lippincott, Williams & Wilkins: Philadelphia (2004).

Pisano ED, Gatsonis CA, Yaffe MJ, Hendrick RE, Tosteson AN, Fryback DG, Bassett LW, Baum JK, Conant EF, Jong RA, Rebner M, D'Orsi CJ. American College of Radiology Imaging Network digital mammographic imaging screening trial: objectives and methodology. Radiology **236:** 404-412 (2005a)

Pisano ED, Gatsonis C, Hendrick E, Yaffe M, Baum JK, Acharyya S, Conant EF, Fajardo LL, Bassett L, D'Orsi C, Jong R, Rebner M; Digital Mammographic Imaging Screening Trial (DMIST) Investigators Group. Diagnostic performance of digital versus film mammography for breast-cancer screening. N Engl J Med **353:** 1773-1783 (2005b)

Pisano ED, Hendrick RE, Yaffe MJ, Baum JK, Acharyya S, Cormack JB, Hanna LA, Conant EF, Fajardo LL, Bassett LW, D'Orsi CJ, Jong RA, Rebner M, Tosteson AN, Gatsonis C; DMIST Investigators Group. Diagnostic accuracy of digital versus film mammography: exploratory analysis of selected population subgroups in DMIST. Radiology **246:** 376-383 (2008).

Plewes DB, Bishop J, Samani A, Sciarretta J. Visualization and quantification of breast cancer biomechanical properties with magnetic resonance elastography. Phys Med Biol **45:** 1591-1610 (2000).

Podgoršak EB. Radiation Physics for Medical Physicists**.** Springer-Verlag: Berlin Heidelberg (2006).

Polikarpov I, Panov V, Bartunik H. Dynamical adjustment of crystal reflectivity by large-amplitude ultrasonic excitation for synchrotron x-ray monochromatization. Journal of Applied Cryst **27:** 453-462 (1994).

Poplack SP, Tosteson TD, Kogel CA, Nagy HM. Digital breast tomosynthesis: initial experience in 98 women with abnormal digital screening mammography. AJR Am J Roentgenol **189:** 616-623 (2007a).

Poplack SP, Tosteson TD, Wells WA, Pogue BW, Meaney PM, Hartov A, Kogel CA, Soho SK, Gibson JJ, Paulsen KD. Electromagnetic breast imaging: results of a pilot study in women with abnormal mammograms. Radiology **243:** 350-359 (2007b).

Port ER, Park A, Borgen PI, Morris E, Montgomery LL. Results of MRI screening for breast cancer in high-risk patients with LCIS and atypical hyperplasia. Ann Surg Oncol **14:** 1051-1057 (2007).

Porter GA, Inglis KM, Wood LA, Veugelers PJ. Effect of obesity on presentation of breast cancer. Annals of Surgical Oncology **13:** 347-332 (2006).

Potischman N, Troisi R. In-utero and early life exposures in relation to risk of breast cancer. Cancer Causes Control **10:** 561-573 (1999).

Poulos A, McLean D, Rickard M, Heard R. Breast compression in mammography: how much is enough? Australas Radiol **47:** 121-126 (2003).

Pramanik M, Ku G, Li C, Wang LV. Design and evaluation of a novel breast cancer detection system combining both thermoacoustic (TA) and photoacoustic (PA) tomography. Med Phys **35:** 2281-2223 (2008).

Prandini N, Lazzeri E, Rossi B, Erba P, Parisella MG, Signore A. Nuclear medicine imaging of bone infections. Nucl Med Commun **27:** 633-644 (2006).

Prasad SN, Houserkova D, Campbell J. Breast imaging using 3D electrical impedance tomography. Biomed Pap Med Fac Univ Palacky Olomouc Czech Repub **152:** 151-154 (2008).

Prince JL and Links JM. Medical Imaging Signals and Systems. Pearson Prentice Hall: Upper Saddle River, NJ (2006).

"Profiles of Breast Cancer Drugs." Imaginis. 8 July 2008 ,http://www.imaginis.com/>.

Protopopov VV. Dark-field phase contrast imaging. U.S. Patent 6,870,896 (2005).

Pu J, Zheng B, Leader JK, Gur D. An ellipse-fitting based method for efficient registration of breast masses on two mammographic views. Med Phys **35:** 487-494 (2008).

Purslow C, Wolffsohn JS. Ocular surface temperature: a review. Eye Contact lens **31:** 117-123 (2005).

Qian J, Li X, Wei M, Gao X, Xu Z, He S. Bio-molecule-conjugated fluorescent organically modified silica nanoparticles as optical probes for cancer cell imaging. Opt Express **16:** 19568-19578 (2008).

Qian W, Song D, Lei M, Sankar R, Eikman E. Computer-aided mass detection based on ipsilateral multiview mammograms. Acad Radiol **14:** 530-538 (2007).

Qiu Y, Sridhar M, Tsou JK, Lindfors KK, Insana MF. Ultrasonic viscoelasticity imaging of nonpalpable breast tumors: preliminary results. Acad Radiol **15:** 1526-1533 (2008).

Quaia E. Microbubble ultrasound contrast agents: an update. Eur Radiol **17:** 1995-2008 (2007).

Rabin O, Manuel Perez J, Grimm J, Wojtkiewicz G, Weissleder R. An x-ray computed tomography imaging agent based on long-circulating bismuth sulphide nanoparticles. Nat Mater **5:** 118-122 (2006).

Rahman WN, Bishara N, Ackerly T, He CF, Jackson P, Wong C, Davidson R, Geso M. Enhancement of radiation effects by gold nanoparticles for superficial radiation therapy. Nanomedicine **5:** 136-142 (2009).

Rajian JR, Carson PL, Wang X. Quantitative photoacoustic measurement of tissue optical absorption spectrum aided by an optical contrast agent. Opt Express **17:** 4879-4889 (2009).

Rampaul RS, Bagnall M, Burrell H, Pinder SE, Evans AJ, Macmillan RD. Randomized clinical trial comparing radioisotope occult lesion localization and wire-guided excision for biopsy of occult breast lesions. Br J Surg **91:** 1575-1577 (2004).

Rapoport N, Gao Z, Kennedy A. Multifunctional nanoparticles for combining ultrasonic tumor imaging and targeted chemotherapy. J Natl Cancer Inst **99:** 1095-1106 (2007).

Rayavarapu RG, Petersen W, Ungureanu C, Post JN, van Leeuwen TG, Manohar S. Synthesis and bioconjugation of gold nanoparticles as potential molecular probes for light-based imaging techniques. Int J Biomed Imaging **2007:** 29817 (2007).

Reed KW, Turman BN, Kaye RJ, Schneider L. "X-ray tube with magnetic electron steering." Patent 6151384 (2000).

Reinikainen H, Paakko E, Suramo I, Paivansalo M, Jauhiainen J, Rissanen T. Dynamics of contrast enhancement in MR imaging and power Doppler ultrasonography of solid breast lesions. Acta Radiol **43:** 492–500 (2002).

Rettenbacher T. Focal liver lesions: role of contrast-enhanced ultrasound. Eur J Radiol **64:** 173-182 (2007).

Reynolds P, Hurley S, Goldberg DE, Anton-Culver H, Bernstein L, Deapen D, Horn-Ross PL, Peel D, Pinder R, Ross RK, West D, Wright WE, Ziogas A. Active smoking, household passive smoking, and breast cancer: evidence from the California teachers study. J Natl Cancer Inst **96:** 29-37 (2004).

Rieger J, Sitter T, Toepfer M, Linsenmaier U, Pfeifer KJ, Schiffl H. Gadolinium as an alternative contrast agent for diagnostic and interventional angiographic procedures in patients with impaired renal function. Nephrol Dial Transplant **17:** 824-828 (2002).

Ries LAG, Melbert D, Krapcho M, Mariotto A, Miller BA, Feuer EJ, Clegg L, Horner MJ, Howlader N, Eisner MP, Reichman M, Edwards BK (eds). SEER Cancer Statistics Review, 1975-2004, National Cancer Institute. Bethesda, MD, http://seer.cancer.gov/csr/1975_2004/, based on November 2006 SEER data submission, posted to the SEER web site (2007).

Richter K, Heywang-Köbrunner SH, Winzer KJ, Schmitt KJ, Prihoda H, Frohberg HD, Guski H, Gregor P, Blohmer JU, Fobbe F, Döinghaus K, Löhr G, Hamm B.

Detection of malignant and benign breast lesions with an automated US system: results in 120 cases. Radiology **205:** 823-830 (1997).

Rigon L, Astolfo A, Arfelli F, Menk RH. Generalized diffraction-enhanced imaging: application to tomography. Eur J Radiol **68:** S3-S7 (2008).

Rocha HS, Lopes RT, Valiante PM, Tirao G, Mazzaro I, Hönnicke MG, Cusatis C, Giles C. Diagnosis of thyroid multinodular goiter using diffraction-enhanced imaging. Nucl Instrum Methods Phys Res A **548:** 175-180 (2005).

Rock CL, Lampe JW, Patterson RE. Nutrition, genetics, and risks of cancer. Annu Rev Public Health **21:** 47-64 (2000).

Rockhill B, Spiegelman D, Byrne C, Hunter DJ, Colditz GA. Validation of the Gail et al. model of breast cancer risk prediction and implications for chemoprevention. J Natl Cancer Inst **93:** 358-366 (2001).

Ronnov-Jessen L, Petersen OW, Bissell MJ. Cellular changes involved in conversion of normal to malignant breast: importance of the stromal reaction. Physiol Rev **76:** 69-125 (1996).

Rosé C, Dose J, Avril N. Positron emission tomography for the diagnosis of breast cancer. Nucl Med Common **23:** 613-618 (2002).

Rosen PP. Rosen's Breast Pathology. 2nd ed. Lippincott Williams & Wilkins: Philadelphia, 2001.

Rosner B, Colditz GA. Nurses' Health Study: log-incidence mathematical model of breast cancer incidence. J Natl Cancer Inst **88:** 359-364 (1996).

Ross JS, Fletcher JA, Linette GP, Stec J, Clark E, Ayers M, Symmans WF, Pusztai L, Bloom KJ. The HER-2/*neu* gene and protein in breast cancer 2003: biomarker and target of therapy. The Oncologist **8:** 307-325 (2003).

Ross JS, Hortobagyi GN. Molecular Oncology of Breast Cancer. Jones & Bartlett Publishers, Sudbury, Massachusetts (2005).

Roy PG, Thompson AM. Cyclin D1 and breast cancer. Breast **15:** 718-727 (2006).

Ruschin M, Timberg P, Båth M, Hemdal B, Svahn T, Saunders RS, Samei E, Andersson I, Mattsson S, Chakrabort DP, Tingber A. Dose dependence of mass and microcalcification detection in digital mammography: free response human observer studies. Med Phys **34:** 400-407 (2007).

Sakamoto JH, Smith BR, Xie B, Rokhlin SI, Lee SC, Ferrari M. The molecular analysis of breast cancer utilizing targeting nanoparticle based ultrasound contrast agents. Technol cancer Res Treat **4:** 627-636 (2005).

Sakka E, Prentza A, Koutsouris D. Classification algorithms for microcalcifications in mammograms (review). Oncol Rep **15:** 1049-1055 (2006).

Samei E, Saunders RS Jr, Baker JA, Delong DM. Digital mammography: effects of reduced radiation dose on diagnostic performance. Radiology **243:** 396-404 (2007).

Sandborg M, Christoffersson JO, Carlsson GA, Almén T, Dance DR. The physical performance of different x-ray contrast agents: calculations using a Monte Carlo model of the imaging chain. Phys Med Biol **40:** 1209-1224 (1995).

Santra S, Yang H, Holloway PH, Stanley JT, Mericle RA. Synthesis of water-dispersible fluorescent, radio-opaque, and paramagnetic CdS:Mn/ZnS quantum dots: a multifunctional probe for bioimaging. J Am Chem Soc **127:** 1656-1657 (2005).

Sapir R, Patlas M, Strano SD, Hadas-Halpern I, Cherny NI. Does mammography hurt? J Pain Symptom Manage **25:** 53-63 (2003).

Sardanelli F, Fausto A, Menicagli L, Esseridou A. Breast vascular mapping obtained with contrast-enhanced MR imaging: implications for cancer diagnosis, treatment, and risk stratification. Eur Radiol **17 Suppl 6:** F48-F51 (2007).

Sardanelli F, Iozzelli A, Fausto A, Carriero A, Kirchin MA. Gadobenate dimeglumine-enhanced MR imaging breast vascular maps: association between invasive cancer and ipsilateral increased vascularity. Radiology **235:** 791-797 (2005).

Sardanelli F, Iozzelli A, Fausto A. MR imaging of the breast: indications, established technique and new directions. Eur Radiol **13 Suppl 3:** N28-N36 (2003).

Sarnelli A, Elleaume H, Taibi A, Gambaccini M, Bravin A. K-edge digital subtraction imaging with dichromatic x-ray sources: SNR and dose studies. Phys Med Biol **51:** 4311-4328 (2006).

Saslow D, Boetes C, Burke W, Harms S, Leach MO, Lehman CD, Morris E, Pisano E, Schnall M, Sener S, Smith RA, Warner E, Yaffe M, Andrews KS, Russell CA; American Cancer Society Breast Cancer Advisory Group. American Cancer Society guidelines for breast screening with MRI as an adjunct to mammography. CA Cancer J Clin **57:** 75-89 (2007).

Saunders RS Jr, Samei E. The effect of breast compression on mass conspicuity in digital mammography. Med Phys **35:** 4464-4473 (2008).

Saunders RS Jr, Samei E, Lo JY, Baker JA. Can compression be reduced for breast tomosynthesis? Monte carlo study on mass and microcalcification conspicuity in tomosynthesis. Radiology **251:** 673-682 (2009).

Schirrmeister H, Kühn T, Guhlmann A, Santjohanser C, Hörster T, Nüssle K, Koretz K, Glatting G, Rieber A, Kreienberg R, Buck AC, Reske SN. Fluorine-18 2-deoxy-2-fluoro-D-glucose PET in the preoperative staging of breast cancer: comparison with the standard staging procedures. Eur J Nucl Med **28:** 351-358 (2001).

Schneider BP, Miller KD. Angiogenesis of breast cancer. J Clin Oncol **23:** 1782-1790 (2005).

Scott BR. "Radiation Sources & Effects in People." www.radiation-scott.org/radsource/3-0.htm. Accessed 10-23-2006.

Seeger H, Wallwiener D, Mueck AO. Statins can inhibit proliferation of human breast cancer cells in vitro. Exp Clin Endocrinol Diabetes **111:** 47-48 (2003).

Seenu V, Pavan Kumar MN, Sharma U, Gupta SD, Mehta SN, Jagannathan NR. Potential of magnetic resonance spectroscopy to detect metastasis in axillary lymph nodes in breast cancer. Magn Reson Imaging **23:** 1005-1010 (2005).

SEER Program (Surveillance, Epidemiology, and End Results) (www.seer.cancer.gov) SEER*Stat Database: Mortality – All COD, Public-Use With State, Total U.S. (1969–2004), National Cancer Institute, DCCPS, Surveillance Research Program, Cancer Statistics Branch, Underlying mortality data provided by NCHS (www.cdc.gov/nchs) (2007).

Senn HJ, Morant R. Chemoprevention of breast and prostate cancers: where do we stand? Ann Oncol **19 Suppl 7:** vii234-vii237 (2008).

Shah N, Gibbs J, Wolverton D, Cerussi A, Hylton N, Tromberg BJ. Combined diffuse optical spectroscopy and contrast enhanced-magnetic resonance imaging for monitoring breast cancer neoadjuvant chemotherapy: a case study. J Biomed Opt **10:** 051503 (2005).

Sharma U, Mehta A, Seenu V, Jagannathan NR. Biochemical characterization of metastatic lymph nodes of breast cancer patients by in vitro 1H magnetic resonance spectroscopy: a pilot study. Magn Reson Imaging **22:** 697-706 (2004).

Shavers VL, Brown ML. Racial and ethnic disparities in the receipt of cancer treatment. J Natl Cancer Inst **94:** 334-357 (2002).

Shaw C, Chen L, Altunbas M, Tu S, Wang TP, Lai CJ, Cheenu Kappadath S, Meng Y, Liu X. Cone beam breast CT with a flat panel detector – simulation, implementation and demonstration. Conf Proc IEEE Eng Med Biol Soc **4:** 4461-4464 (2005).

Shaw DR, Kessel DO. The current status of the use of carbon dioxide in diagnostic and interventional angiographic procedures. Cardiovasc Intervent Radiol **29:** 323-331 (2006).

Shih HA, Couch FJ, Nathanson KL, Blackwood MA, Rebbeck TR, Armstrong KA, Calzone K, Stopfer J, Seal S, Stratton MR, Weber BL. BRCA1 and BRCA2 mutation frequency in women evaluated in a breast cancer risk evaluation clinic. J Clin Oncol **20:** 994-999 (2002).

Shimao D, Kunisada T, Sugiyama H, Ando M. Refraction-enhanced tomosynthesis of a finger joint by x-ray dark-field imaging. Japanese Journal of Applied Physics **46:** L608-L610 (2007).

Shimao D, Kunisada T, Sugiyama H, Ando M. Shift-and-add tomosynthesis of a finger joint by x-ray dark-field imaging: difference due to tomographic angle. Eur J Radiol **68:** S27-S31 (2008).

Shimao D, Sugiyama H, Kunisada T, Ando M. Articular cartilage depicted at optimized angular position of Laue angular analyzer by x-ray dark-field imaging. Appl Radiat Isot **64:** 868-874 (2006).

Shimauchi A, Yamada T, Sato A, Takase K, Usami S, Ishida T, Moriya T, Takahashi S. Comparison of MDCT and MRI for evaluating the intraductal component of breast cancer. AJR Am J Roentgenol **187:** 322-329 (2006).

Shipley JA, Duck FA, Goddard DA, Hillman MR, Halliwell M, Jones MG, Thomas BT. Automated quantitative volumetric breast ultrasound data-acquisition system. Ultrasound Med Biol **31:** 905-917 (2005).

Sickles EA. Breast cancer detection with transillumination and mammography. Am J Roentgenol **142:** 841-844 (1984).

Simon GH, Fu Y, Berejnoi K, Fournier LS, Lucidi V, Yeh B, Shames DM, Brasch RC. Initial computed tomography imaging experience using a new macromolecular iodinated contrast medium in experimental breast cancer. Invest Radiol **40:** 614-620 (2005a).

Simon MS, Korczak JF, Yee CL, Daling JR, Malone KE, Bernstein L, Marchbanks PA, Folger SG, McDonald JA, Norman SA, Strom BL, Deapen D, Ursin G, Burkman RT, Press MF, Schwartz AG, Spirtas R. Racial differences in the familial aggregation of breast cancer and other female cancers. Breast Cancer Res Treat **89:** 227-235 (2005b).

Singh S, Tourassi GD, Baker JA, Samei E, Lo JY. Automated breast mass detection in 3D reconstructed tomosynthesis volumes: a featureless approach. Med Phys **35:** 3626-3636 (2008).

Sinha S, Lucas-Quesada FA, Sinha U, DeBruhl N, Bassett LW. In-vivo diffusion-weighted MRI of the breast: potential for lesion characterization. J Magn Reson Imaging **15:** 693-704 (2002).

Sinha SP, Roubidoux MA, Helvie MA, Nees AV, Goodsitt MM, LeCarpentier GL, Fowlkes JB, Chalek CL, Carson PL. Multi-modality 3D breast imaging with x-ray tomosynthesis and automated ultrasound. Conf Proc IEEE Eng Med Biol Soc **2007:** 1335-1338 (2007).

Sinha S, Sinha U. Recent advances in breast MRI and MRS. NMR Biomed **22:** 3-16 (2009).

Sinkus R, Tanter M, Catheline S, Lorenzen J, Kuhl C, Sondermann E, Fink M. Imaging anisotropic and viscous properties of breast tissue by magnetic resonance-elastography. Magn Reson Med **53:** 372-387 (2005).

Siu KKW, Kitchen MJ, Pavlov KM, Gillam JE, Lewis RA, Uesegi K, Yagi N. An improvement to the diffraction-enhanced imaging method that permits imaging of dynamic systems. Nucl Instrum Methods Phys Res A **548:** 169-174 (2005).

Slamon DJ, Godolphin W, Jones LA, Holt JA, Wong SG, Keith DE, Levin WJ, Stuart SG, Udove J, Ullrich A, Press MF. Studies of the HER-2/neu proto-oncogene in human breast and ovarian cancer. Science **244:** 707-712 (1989).

Slanetz PJ, Edmister WB, Yeh ED, Talele AC, Kopans DB. Occult contralateral breast carcinoma incidentally detected by breast magnetic resonance imaging. Breast J **8:** 145-148 (2002).

Smith A. Full field breast tomosynthesis. Radiol Manage **27:** 25-31 (2005).

Smith IC, Welch AE, Hutcheon AW, Miller ID, Payne S, Chilcott F, Waikar S, Whitaker T, Ah-See AK, Eremin O, Heys SD, Gilbert FJ, Sharp PF. Positron emission tomography using [(18)F]-fluorodeoxy-D-glucose to predict the pathologic response of breast cancer to primary chemotherapy. J Clin Oncol **18:** 1676-1688 (2000).

Smith-Warner SA, Spiegelman D, Yaun SS, van den Brandt PA, Folsom AR, Goldbohm RA, Graham S, Holmberg L, Howe GR, Marshall JR, Miller AB, Potter JD, Speizer FE, Willett WC, Wolk A, Hunter DJ. Alcohol and breast cancer in women: a pooled analysis of cohort studies. JAMA **279:** 535-540 (1998).

Snigirev A, Snigireva I, Kohn V, Kuznetsov S, Schelokov I. On the possibilities of x-ray phase contrast microimaging by coherent high-energy synchrotron radiation. Rev Sci Instrum **66:** 5486-5492 (1995).

Sone S, Kasuga T, Sakai F, Aoki J, Izuno I, Tanizaki Y, Shigeta H, Shibata K. Development of a high-resolution digital tomosynthesis system and its clinical application. Radiographics **11:** 807–822 (1991).

Sones B, Danon Y. Thin metallic crystals for parametric x-ray (PXR) production. Transaction of the American Nuclear Society, Vol 96, p337-339, June 24-28, Boston, MA (2007).

Song KH, Kim C, Maslov K, Wang LV. Noninvasive in vivo spectroscopic nanorod-contrast photoacoustic mapping of sentinel lymph nodes. Eur J Radiol **70:** 227-231 (2009).

Song KH, Stein EW, Margenthaler JA, Wang LV. Noninvasive photoacoustic identification of sentinel lymph nodes containing methylene blue in vivo in a rat model. J Biomed Opt **13:** 054033 (2008).

Soni NK, Hartov A, Kogel C, Poplack SP, Paulsen KD. Multi-frequency electrical impedance tomography of the breast: new clinical results. Physiol Meas **25:** 301-314 (2004).

Sprawls PJ. Physical Principles of Medical Imaging 2nd ed. Aspen Publishers: Gaithersburg, MD (1993).

Stanwell P, Gluch L, Clark D, Tomanek B, Baker L, Giuffrè B, Lean C, Malycha P, Mountford C. Specificity of choline metabolites for in vivo diagnosis of breast cancer using 1H MRS at 1.5 T. Eur Radiol **15:** 1037-1043 (2005).

Stark A, Hulka BS, Joens S, Novotny D, Thor AD, Wold LE, Schell MJ, Melton LJ 3rd, Liu ET, Conway K. HER-2/neu amplification in benign breast disease and the risk of subsequent breast cancer. J Clin Oncol **18:** 267-274 (2000).

Steiner G, Soleimani M, Watzenig D. A bio-electromechanical imaging technique with combined electrical impedance and ultrasound tomography. Physiol Meas **29:** S63-S75 (2008).

Stevens GM, Birdwell RL, Beaulieu CF, Ikeda DM, Pelc NJ. Circular tomosynthesis: potential in imaging of breast and upper cervical spine-- preliminary phantom and in vitro study. Radiology **228:** 569-575 (2003).

Stojadinovic A, Moskovitz O, Gallimidi Z, Fields S, Brooks AD, Brem R, Mucciola RN, Singh M, Maniscalco-Theberge M, Rockette HE, Gur D, Shriver CD. Prospective

study of electrical impedance scanning for identifying young women at risk for breast cancer. Breast Cancer Res Treat **97:** 179-189 (2006).

Stone J, Dite GS, Gunasekara A, English DR, McCredie MR, Giles GG, Cawson JN, Hegele RA, Chiarelli AM, Yaffe MJ, Boyd NF, Hopper JL. The heritability of mammographically dense and nondense breast tissue. Cancer Epidemiol Biomarkers Prev **15:** 612-617 (2006).

Stone N, Matousek P. Advanced transmission Raman spectroscopy: a promising tool for breast disease diagnosis. Cancer Res **68:** 4424-4430 (2008).

Strunk HM, Schild H. Actual clinical use of gadolinium-chelates for non-MRI applications. Eur Radiol **14:** 1055-1062 (2004).

Su CH, Sheu HS, Lin CY, Huang CC, Lo YW, Pu YC, Weng JC, Shieh DB, Chen JH, Yeh CS. Nanoshell magnetic resonance imaging contrast agents. J Am Chem Soc **129:** 2139-2146 (2007).

Sun B, Ranganathan B, Feg SS. Multifunctional poly(D,L-lactide-co-glycolide)/montmorillonite (PLGA/MMT) nanoparticles decorated by Trastuzumab for targeted chemotherapy of breast cancer. Biomaterials **29:** 475-486 (2008).

Sun Y, Zhu P, Yu J, Chen X. Computerized tomography based on DEI refraction information. Comput Med Imaging Graph **31:** 383-389 (2007).

Suortti P, Thomlinson W. Medical Applications of Synchrotron Radiation. Phys Med Biol **48:** R1-R35 (2003).

Suryanarayanan S, Karellas A, Vedantham S, Glick SJ, D'Orsi CJ, Baker SP, Webber RL. Comparison of tomosynthesis methods used with digital mammography. Acad Radiol **7:** 1085-1097 (2000).

Suzuki Y, Yagi N, Uesugi K. X-ray refraction-enhanced imaging and a method for phase retrieval for a simple object. **9:** 160-165 (2002).

Swanson SD, Kukowska-Latallo JF, Patri AK, Chen C, Ge S, Cao Z, Kotlyar A, East AT, Baker JR. Targeted gadolinium-loaded dendrimer nanoparticles for tumor-specific magnetic resonance contrast enhancement. Int J Nanomedicine **3:** 201-210 (2008).

Tada H, Higuchi H, Wanatabe TM, Ohuchi N. In vivo real-time tracking of single quantum dots conjugated with monoclonal anti-HER2 antibody in tumors of mice. Cancer Res **67:** 1138-1144 (2007).

Taira N, Ohsumi S, Takabatake D, Hara F, Takashima S, Aogi K, Takashima S, Inoue T, Sugata S, Nishimura R. Contrast-enhanced CT evaluation of clinically and

mammographically occult multiple breast tumors in women with unilateral early breast cancer. Jpn J Clin Oncol **38:** 419-425 (2008).

Tamimi RM, Hankinson SE, Colditz GA, Byrne C. Endogenous sex hormone levels and mammographic density among postmenopausal women. Cancer Epidemiol Biomarkers Prev **14:** 2641-2647 (2005).

Tanaka T, Honda C, Matsuo S, Noma K, Oohara H, Nitta N, Ota S, Tsuchiya K, Sakashita Y, Yamada A, Yamasaki M, Furukawa A, Takahashi M, Murata K. The first trial of phase contrast imaging for digital full-field mammography using a practical molybdenum x-ray tube. Invest Radiol **40:** 385-396 (2005).

Taouli B, Losada M, Holland A, Krinsky G. Magnetic resonance imaging of hepatocellular carcinoma. Gastroenterology **127:** S144-152 (2004).

Taplin SH, Rutter CM, Lehman CD. Testing the effect of computer-assisted detection on interpretive performance in screening mammography. AJR Am J Roentgenol **187:** 1475-1482 (2006).

Tarhan S, Unlu Z. Magnetic resonance imaging and ultrasonographic evaluation of the patients with knee osteoarthritis: a comparative study. Clin Rheumatol **22:** 181-188 (2003).

Taylor P, Potts HW. Computer aids and human second reading as interventions in screening mammography: two systematic reviews to compare effects on cancer detection and recall rate. Eur J Cancer **44:** 798-807 (2008).

Teh WL, Wilson AR, Evans AJ, Burrell H, Pinder SE, Ellis IO. Ultrasound guided core biopsy of suspicious mammographic calcifications using high frequency and power Doppler ultrasound. Clin Radiol **55:** 390-394 (2000).

Thomas MA, Binesh N, Yue K, DeBruhl N. Volume-localized two-dimensional correlated magnetic resonance spectroscopy of human breast cancer. J Magn Reson Imaging **14:** 181-186 (2001).

Thomas MA, Wyckoff N, Yue K, Binesh N, Banakar S, Chung HK, Sayre J, DeBruhl N. Two-dimensional MR spectroscopic characterization of breast cancer in vivo. Technol Cancer Res Treat **4:** 99-106 (2005).

Thomsen HS, Almen T, Morcos SK. Gadolinium-containing contrast media for radiographic examinations: a position paper. Eur Radiol **12:** 2600-2605 (2002).

Topp KA, O'Brien WD Jr. Anisotropy of ultrasonic propagation and scattering properties in fresh rat skeletal muscle in vitro. J Acoust Soc Am **107:** 1027-1033 (2000).

Torres-Mejía G, De Stavola B, Allen DS, Pérez-Gavilán JJ, Ferreira JM, Fentiman IS, Dos Santos Silva I. Mammographic features and subsequent risk of breast cancer: a comparison of qualitative and quantitative evaluations in the Guernsey Prospective Studies. Cancer Epidemiol Biomarkers Prev **14:** 1052-1059 (2005).

Trokhanova OV, Okhapkin MB, Korjenevsky AV. Dual-frequency electrical impedance mammography for the diagnosis of non-malignant breast disease. Physiol Meas **29:** S331-S44 (2008).

Tromberg BJ, Cerussi A, Shah N, Compton M, Durkin A, Hsiang D, Butler J, Mehta R. Imaging in breast cancer: diffuse optics in breast cancer: detecting tumors in pre-menopausal women and monitoring neoadjuvant chemotherapy. Breast Cancer Res **7:** 279-285 (2005).

Tsai TH, Yang PC. Ultrasound in the diagnosis and management of pleural disease. Curr Opin Pulm Med **9:** 282-290 (2003).

Tse GM, Cheung HS, Pang LM, Chu WC, Law BK, Kung FY, Yeung DK. Characterization of lesions of the breast with proton MR Spectroscopy: comparison of carcinomas, benign lesions, and phyllodes tumors. AJR Am J Roentgenol **181:** 1267-1272 (2003).

Ueda H, Togashi K, Konishi I, Katoaka ML, Koyama T, Fujiwara T, Kobayashi H, Fujii S, Konishi J. Unusual appearances of uterine leiomyomas: MR imaging findings and their histopathologic backgrounds. Radiographics, **19:** S131–S145 (1999).

Umstadter D. "Laser Driven X-ray Systems." Accessed 4-10-2009. www. AccessScience.com (2002).

Unlu MB, Lin Y, Birgul O, Nalcioglu O, Gulsen G. Simultaneous in vivo dynamic magnetic resonance-diffuse optical tomography for small animal imaging. J Biomed Opt **13:** 060501 (2008).

Upton AC; National Council on Radiation Protection and Measurements Scientific Committee 1-6. The state of the art in the 1990's: NCRP Report No. 136 on the scientific basis for linearity in the dose-response relationship for ionizing radiation. Health Phys **85:** 15-22 (2003).

U.S. Cancer Statistics Working Group. *United States Cancer Statistics: 2004 Incidence and Mortality*. Atlanta (GA): Department of Health and Human Services, Centers for Disease Control and Prevention, and National Cancer Institute (2007).

U.S. Department of Health and Human Services. *Bone Health and Osteoporosis: A Report of the Surgeon General.* Rockville, MD: U.S. Department of Health and Human Services, Office of the Surgeon General (2004).

Vachon CM, Pankratz VS, Scott CG, Maloney SD, Ghosh K, Brandt KR, Milanese T, Carston MJ, Sellers TA. Longitudinal trends in mammographic percent density and breast cancer risk. Cancer Epidemiol Biomarkers Prev **16:** 921-928 (2007).

van Breuseghem I. Ultrastructural MR imaging techniques of the knee articular cartilage: problems for routine clinical application. Eur Radiol **14:** 184-192 (2004).

van de Hulst HC. Light Scattering by Small Particles. Dover Publications, Inc: New York (1981).

van den Bos IC, Hussain SM, de Man RA, Zondervan PE, Ijzermans JN, Krestin GP. Primary hepatocellular lesions: imaging findings on state-of-the-art magnetic resonance imaging, with pathologic correlation. Curr Probl Diagn Radiol **37:** 104-114 (2008).

van Engeland S, Karssemeijer N. Combining two mammographic projections in a computer aided mass detection method. Med Phys **34:** 898-905 (2007).

van Esser S, Veldhuis WB, van Hillegersberg R, van Diest PJ, Stapper G, ElOuamari M, Borel Rinkes IH, Mali WP, van den Bosch MA. Accuracy of contrast-enhanced breast ultrasound for pre-operative tumor size assessment in patients diagnosed with invasive ductal carcinoma of the breast. Cancer Imaging **7:** 63-68 (2007).

van Goethem M, Tjalma W, Schelfout K, Verslegers I, Biltjes I, Parizel P. Magnetic resonance imaging in breast cancer. Eur J Surg Oncol **32:** 901-910 (2006).

van Tilborg GA, Mulder WJ, Chin PT, Storm G, Reutelingsperger CP, Nicolay K, Strijkers GJ. Annexin A5-conjugated quantum dots with a paramagnetic lipidic coating for the multimodal detection of apoptotic cells. Bioconjug Chem **17:** 865-868 (2006).

Venkatesh SK, Yin M, Glockner JF, Takahashi N, Araoz PA, Talwalkar JA, Ehman RL. MR elastography of liver tumors: preliminary results. AJR Am J Roentgenol **190:** 1534-1540 (2008).

Viehweg P, Rotter K, Laniado M, Lampe D, Buchmann J, Kölbl H, Heywang-Köbrunner S. MR imaging of the contralateral breast in patients after breast-conserving therapy. Eur Radiol **14:** 402-408 (2004).

Villanueva FS, Wagner WR. Ultrasound molecular imaging of cardiovascular disease. Nat Clin Pract Cardiovasc Med **5 Suppl 2:** S26-32 (2008).

Vincentis GD, Porfiri LM, Betti M, Filippi L, Remediani S, Santo GD, Zaccagnino P, Felice CD, Pieracci M, Cinti MN, Bennati P, Pellegrini R, Pani R. High resolution scintimammography helps in differentiating benign from malignant findings in scintigraphic hot spots. Phys Med **21 Suppl 1:** 87-90 (2006).

Vine DJ, Paganin DM, Pavlov KM, Kraublich J, Wehrhan O, Uschmann I, Forster E. Analyzer-based phase contrast imaging and phase retrieval using a rotating anode x-ray source. Appl Phys Lett **91:** 254110 (2007).

Vogel VG, Costantino JP, Wickerham DL, Cronin WM, Cecchini RS, Atkins JN, Bevers TB, Fehrenbacher L, Pajon ER Jr, Wade JL 3rd, Robidoux A, Margolese RG, James J, Lippman SM, Runowicz CD, Ganz PA, Reis SE, McCaskill-Stevens W, Ford LG, Jordan VC, Wolmark N; National Surgical Adjuvant Breast and Bowel Project (NSABP). Effects of tamoxifen vs raloxifene on the risk of developing invasive breast cancer and other disease outcomes: the NSABP Study of Tamoxifen and Raloxifene (STAR) P-2 trial. JAMA **295:** 2727-2741 (2006).

von Maltzahn G, Park JH, Agrawal A, Bandaru NK, Das SK, Sailor MJ, Bhatia SN. Computationally guided Photothermal tumor therapy using long-circulating gold nanorod antennas. Cancer Res **69:** 3892-3900 (2009).

von Ramm OT, Smith SW. Real time volumetric ultrasound imaging system. J Digit Imaging **3:** 261-266 (1990).

Wagner A, Sachse A, Keller M, Aurich M, Wetzel WD, Hortschansky P, Schmuck K, Lohmann M, Reime B, Metge J, Arfelli F, Menk R, Rigon L, Muehleman C, Bravin A, Coan P, Mollenhauer J. Qualitative evaluation of titanium implant integration into bone by diffraction-enhanced imaging. Phy Med Biol **51:** 1313-1324 (2006).

Wagner A, Aurich M, Sieber N, Stoessel M, Wetzel WD, Schmuck K, Lohmann M, Reime B, Metge J, Coan P, Bravin A, Arfelli F, Rigon L, Menk RH, Heitner G, Irving T, Zhong Z, Muehleman C, Mollenhauer JA. Options and limitations of joint cartilage imaging: DEI in comparison to MRI and sonography. Nucl Instrum Methods Phys Res A **548:** 47-53 (2005).

Wahl RL, Zasadny K, Helvie M, Hutchins GD, Weber B, Cody R. Metabolic monitoring of breast cancer chemohormonotherapy using positron emission tomography: initial evaluation. J Clin Oncol **11:** 2101-2111 (1993).

Wang J, Costantino JP, Tan-Chiu E, Wickerham DL, Paik S, Woolmark N. Lower-category benign breast disease and the risk of invasive breast cancer. J Natl Cancer Inst **96:** 616-620 (2004).

Wang J, Zhu P, Yuan Q, Huang W, Shu H, Chen B, Hu T, Wu Z. Reconstruction of the refractive index gradient by x-ray diffraction-enhanced computed tomography. Phys Med Biol **51:** 3391-3396 (2006a).

Wang X. Line x-ray source for diffraction-enhanced imaging in clinical and industrial applications [dissertation]. Raleigh (NC): North Carolina State University (2006b).

Wang Y, Cheng Z, Li J, Tang J. Gray-scale contrast-enhanced ultrasonography in detecting sentinel lymph nodes: An animal study. Eur J Radiol (2009a eupb ahead of print).

Wang Y, Wang W, Li J, Tang J. Gray-scale contrast-enhanced ultrasonography of sentinel lymph nodes in a metastatic breast cancer model. Acad Radiol **16:** 957-962 (2009b).

Warner E. The role of magnetic resonance imaging in screening women at high risk of breast cancer. Top Magn Reson Imaging **19:** 163-169 (2008).

Weaver DL, Krag DN, Ashikaga T, Harlow SP, O'Connell M. Pathologic analysis of sentinel and nonsentinel lymph nodes in breast carcinoma: a multicenter study. Cancer **88:** 1099-1107 (2000).

Weik JL, Lum SS, Esquivel PA, Tully RJ, Bae WC, Petersen FF, Jaque JM, Reeves ME, Garberoglio CA. The Gail model predicts breast cancer in women with suspicious radiographic lesions. American Journal of Surgery **190:** 526-529 (2005).

Weir HK, Thun MJ, Hankey BF, Ries LA, Howe HL, Wingo PA, Jemal A, Ward E, Anderson RN, Edwards BK. Annual report to the nation on the status of cancer, 1975-2000, featuring the uses of surveillance data for cancer prevention and control. J Natl Cancer Inst **95:** 1276-1299 (2003).

Weissleder R, Tung CH, Mahmood U, Bogdanov A Jr. In vivo imaging of tumors with protease-activated near-infrared fluorescent probes. Nat Biotechnol **17:** 375-378 (1999).

Weitkamp T, Diaz A, David C, Pfeiffer F, Stampanoni M, Cloetens P, Ziegler E. X-ray phase imaging with a grating interferometer. Opt Express **13:** 6296-6304 (2005).

Weitkamp T, David C, Bunk O, Bruder J, Cloetens P, Pfeiffer F. X-ray phase radiography and tomography of soft tissue using grating interferometry. Eur J Radiol **68:** S13-S17 (2008).

Wernick MN, Wirjadi O, Chapman D, Oltulu O, Zhong Z, Yang Y. Preliminary investigation of a multiple-image radiography method. IPL Conference Papers 129-132 (2002).

Wernick MN, Wirjadi O, Chapman D, Zhong Z, Galatsanos NP, Yang Y, Brankov JG, Oltulu O, Anastasio MA, Muehleman C. Multiple image radiography. Phys Med Biol **48:** 3875-3895 (2003).

Wernick MN, Yang Y, Mondal I, Chapman D, Hasnah M, Parham C, Pisano E, Zhong Z. Computation of mass-density images from x-ray refraction-angle images. Phys Med Biol **51:** 1769-1778 (2006).

Wilking N, Rutqvist LE, Carstensen J, Mattsson A, Skoog L. Prognostic significance of axillary nodal status in primary breast cancer in relation to the number of resected nodes. Stockholm Breast cancer Study Group. Acta Oncol **31:** 29-35 (1992).

Wilkins SW, Gureyev TE, Gao D, Pogany A, Stevenson AW. Phase-contrast imaging using polychromatic hard x-rays. Nature **384:** 335-338 (1996).

Winchester DP, Hudis CA and Norton L. Breast Cancer. 2nd ed. BC Decker INC Hamilton, Ontario (2005).

Wink MH, de la Rosette JJ, Grimbergen CA, Wijkstra H. Transrectal contrast enhanced ultrasound for diagnosis of prostate cancer. World J Urol **25:** 367-373 (2007).

Wittry DB, Barbi NC. X-ray crystal spectrometers and monochromators in microanalysis. Microsc Microanal **7:** 124-141 (2001).

Wong SL, Edwards MJ, Chao C, Tuttle TM, Noyes RD, Carlson DJ, Cerrito PB, McMasters KM. Sentinel lymph node biopsy for breast cancer: impact of the number of sentinel nodes removed on the false-negative rate. J Am Coll Surg **192:** 684-689 (2001).

Woo J. "A short history of the development of ultrasound in obstetrics and gynecology." http://www.ob-ultrasound.net/history1.html. March 2008, Accessed Nov-30-2008.

Wratten CR, O'brien PC, Hamilton CS, Bill D, Kilmurray J, Denham JW. Breast edema in patients undergoing breast-conserving treatment for breast cancer: assessment via high frequency ultrasound. Breast J **13:** 266-273 (2007).

Wuang SC, Neoh KG, Kang ET, Pack DW, Leckband DE. Polypyrrole nanospheres with magnetic and cell-targeting capabilities. Macromol Rapid Commun **28**: 816-821 (2007).

Wuang SC, Neoh KG, Kang ET, Pack DW, Leckband DE. HER-2-mediated endocytosis of magnetic nanospheres and the implications in cell targeting and particle magnetization. Biomaterials **29:** 2270-2279 (2008).

Wu WJ, Moon WK. Ultrasound breast tumor image computer-aided diagnosis with texture morphological features. Acad Radiol **15:** 873-880 (2008).

Wu X, Liu H. Clinical implementation of x-ray phase-contrast imaging: theoretical foundations and design considerations. Med Phys **30:** 2169-2179 (2003).

Wu X, Liu H. X-ray phase contrast imaging: phase reconstructions. Conf Proc IEEE Eng Med Biol Soc **2:** 1786-1789 (2005).

Xu RX, Young DC, Mao JJ, Povoski SP. A prospective pilot clinical trial evaluating the utility of a dynamic near-infrared imaging device for characterizing suspicious breast lesions. Breast Cancer Res **9:** R88 (2007).

Xydeas T, Sigmann K, Sinkus R, Krainick-Strobel U, Miller S, Claussen CD. Magnetic resonance elastography of the breast: correlation of signal intensity data with viscoelastic properties. Invest Radiol **40:** 412-420 (2005).

Yagi N, Suzuki Y, Umetani K, Kohmura Y, Yamasaki K. Refraction enhanced x-ray imaging of mouse lung using synchrotron radiation source. Med Phys **26:** 2190-2193 (1999).

Yahara T, Koga T, Yoshida S, Nakagawa S, Deguchi H, Shirouzu K. Relationship between microvessel density and thermographic hot areas in breast cancer. Surg Today **33:** 243-248 (2003).

Yang F, Li L, Li Y, Chen Z, Wu J, Gu N. Superparamagnetic nanoparticle-inclusion microbubbles for ultrasound contrast agents. Phys Med Biol **53:** 6129-6141 (2008a).

Yang F, Li Y, Chen Z, Zhang Y, Wu J, Gu N. Superparamagnetic iron oxide nanoparticle-embedded encapsulated microbubbles as dual contrast agents of magnetic resonance and ultrasound imaging. Biomaterials **30:** 3882-3890 (2009).

Yang G, Rajaram R, Cao G, Sultana S, Lalush D, Lu J, Zhou O. Stationary digital breast tomosynthesis for breast cancer detection. SPIE Newsroom DOI: 10.1117/2.1200802.1042 (2008b).

Yang Q, Khoury MJ, Rodriguez C, Calle EE, Tatham LM, Flanders WD. Family history score as a predictor of breast cancer mortality: prospective data from the Cancer Prevention Study II, United States, 1982-1991. Am J Epidemiol **147:** 652-659 (1998).

Yang SK, Moon WK, Cho N, Park JS, Cha JH, Kim SM, Kim SJ, Im JG. Screening mammography-detected cancers: sensitivity of a computer-aided detection system applied to full-field digital mammograms. Radiology **244:** 104-111 (2007a).

Yang WT, Carkaci S, Chen L, Lai CJ, Sahin A, Whitman GJ, Shaw CC. Dedicated cone-beam breast CT: feasibility study with surgical mastectomy specimens. AJR Am J Roentgenol **189:** 1312-1315 (2007b).

Yap MH, Edirisnghe EA, Bez HE. A novel algorithm for initial lesion detection in ultrasound breast images. J Appl Clin Med Phys **9:** 2741 (2008).

Yeung DK, Yang WT, Tse GM. Breast cancer: in vivo proton MR spectroscopy in the characterization of histopathologic subtypes and preliminary observations in axillary node metastases. Radiology **225:** 190-197 (2002).

Yin H, Liu B, Gao X, Shu H, Gao X, Zhu P, Luo S. Diffraction-enhanced x-ray imaging for observing guinea pig cochlea. Conf Proc IEEE Eng Med Biol Soc **6:** 5699-5701 (2005).

Yoshikawa MI, Ohsumi S, Sugata S, Kataoka M, Takashima S, Kikuchi K, Mochizuki T. Comparison of breast cancer detection by diffusion-weighted magnetic resonance imaging and mammography. Radiat Med **25:** 218-223 (2007).

Young KC, Burch A. Radiation doses received in the UK breast screening programme in 1997 and 1998. Br J Radiol **73:** 278-287 (2000).

Young LW, Parham C, Zhong Z, Chapman D, Reaney MJ. Non-destructive diffraction-enhanced imaging of seeds. J Exp Bot **58:** 2513-2523 (2007).

Yuasa T, Hashimoto E, Maksimenko A, Sugiyama H, Arai Y, Shimao D, Ichihara S, Ando M. Highly sensitive detection of the soft tissues based on refraction contrast by in-plane diffraction-enhanced imaging CT. Nucl Instrum Methods Phys Res A **591:** 546-557 (2008).

Yuasa T, Maksimenko A, Hashimoto E, Akatsuka T, Ando M. Physico-mathematical considerations on x-ray computed tomography based on diffraction-enhanced imaging. Conf Proc IEEE Eng Med Biol Soc **2007:** 4441-4444 (2007).

Yuasa T, Maksimenko A, Hashimoto E, Sugiyama H, Hyodo K, Akatsuka T, Ando M. Hard-x-ray region tomographic reconstruction of the refractive-index gradient vector field: imaging principles and comparisons with diffraction-enhanced-imaging-based computed tomography. Opt Lett **31:** 1818-1820 (2006).

Yu SB, Watson AD. Metal-based x-ray contrast media. Chem Rev **99:** 2353-2378 (1999).

Zagzebski JA. Essentials of Ultrasound Physics. Mosby: St. Louis (1996).

Zakhireh J, Gomez R, Esserman L. Converting evidence to practice: a guide for the clinical application of MRI for the screening and management of breast cancer. Eur J Cancer **44:** 2742-2752 (2008).

Zeng K, Yu H, Zhao S, Fajardo LL, Ruth C, Jing Z, Wang G. Digital tomosynthesis aided by low-resolution exact computed tomography. J Comput Assist Tomogr **31:** 976-983 (2007).

Zhang D, Donovan M, Fajardo LL, Archer A, Wu X, Liu H. Preliminary feasibility study of an in-line phase contrast x-ray imaging prototype. IEEE Trans Biomed Eng **55:** 2249-2257 (2008a).

Zhang Q, Xie J, Lee JY, Zhang J, Boothroyd C. Synthesis of Ag@AgAu metal core/alloy shell bimetallic nanoparticles with tunable shell compositions by a galvanic replacement reaction. Small **4:** 1067-1071 (2008b).

Zhang X, Liu XS, Yang XR, Chen SL, Zhu PP, Yuan QX. Mouse blood vessel imaging by in-line x-ray phase-contrast imaging. Phys Med Biol **53:** 5735-5743 (2008c).

Zhao S, Borden M, Bloch S, Kruse D, Ferrara KW, Dayton PA. Radiation force assisted targeting facilitates ultrasonic molecular imaging. Mol Imaging **3:** 135-148 (2004).

Zheng B, Leader JK, Abrams GS, Lu AH, Wallace LP, Maitz GS, Gur D. Multiview-based computer-aided detection scheme for breast masses. Med Phys **33**, 3135-3143 (2006).

Zhenyu J, Feng F, Ruigang L, Kan W, Xuetao S, Fusheng Y, Xiuzhen D. Study of influencing factors on electrical impedance scanning imaging. Conf Proc IEEE Eng Med Biol Soc **3:** 2910-2913 (2005).

Zhi H, Xiao XY, Yang HY, Wen YL, Ou B, Luo BM, Liang BL. Semi-quantitating stiffness of breast solid lesions in ultrasonic elastography. Acad Radiol **15:** 1347-1353 (2008).

Zhong Z, Chapman D, Menk R, Richardson J, Theophanis S, Thomlinson W. Monochromatic energy-subtraction radiography using a rotating anode source and a bent Laue monochromator. Phys Med Biol **42:** 1751-1762 (1997).

Zhong Z, Thomlinson W, Chapman D, Sayers D. Implementation of diffraction-enhanced imaging experiments: at the NSLS and APS. Nuclear Instruments and Methods in Physics Research A **450**, 556-567 (2000).